Nanostructures of Liquid Crystal Phases

By

Dong Chen

B.S., University of Science and Technology of China, 2006

M.S., University of Colorado at Boulder, 2008

A thesis submitted to the

Faculty of the Graduate School of the

University of Colorado in partial fulfillment

of the requirement for the degree of

Doctor of Philosophy

Department of Physics

2012

This thesis entitled:
Nanostructures of Liquid Crystal Phases
written by Dong Chen
has been approved for the Department of Physics

_____
Noel A. Clark

_____
Joseph E. Maclennan

_____
Matthew A. Glaser

Date _____

The final copy of this thesis has been examined by the signatories, and we find that both the content and the form meet acceptable presentation standards of scholarly work in the above mentioned discipline.

Chen, Dong (Ph.D., Physics)

Nanostructures of Liquid Crystal Phases

Thesis directed by Prof. Noel A. Clark

Bent-core liquid crystals have attracted intense interest in recent years, exhibiting a wide variety of novel structural phenomena involving the interplay of chirality, molecular bend and molecular tilt. Freeze-fracture transmission electron microscopy together with other experimental methods has been used to characterize the nanostructures of bent-core liquid crystal phases in which the molecules undergo complex self-assembly, forming, for example, helical nanofilaments (the B4 phase), disordered focal conics (the DC phase), and layer undulations (the B7 phase) in the bulk. These studies have helped us better understand the complex nature of these and other liquid crystal phases. For example, the investigation of the chirality-preserving growth of the helical nanofilaments in the B4 phase will allow better control of its growth for applications, the discovery of the quasi-ordered toric focal conics of the DC phase at the air/liquid crystal interface opens the way for the development of two-dimensional or even three-dimensional periodic dielectric media for photonic crystal applications, the study of layer undulation defects reveals the detailed molecular arrangement in the B7 phase, and the discovery and characterization of the randomized twist grain boundary phase broads the understanding of chiral liquid crystal phases.

Acknowledgements

I still remember the first time I met with Prof. Noel Clark. At the beginning of my second semester at CU-Boulder, I happened to be the teaching assistant of Prof. Noel Clark's class. When I first met him, he asked me "Are you interested in condense matter?". I answered yes. Then he said "Send me your resume.". After that I joined his group. At that time, I didn't know what liquid crystal is. It was him who has brought me into the world of liquid crystal. I enjoyed his guidance, encouragement, advice and discussions that made my research proceed in the right way. There are a number of other people I wish to thank for their assistance and contributions to make this thesis possible. I would like to thank Joseph Maclennan, for his useful discussion and careful manuscript revision. I have benefited from his comments about this thesis. I would like to thank Matthew Glaser for his wonderful ideas and his support. I am also grateful to the members of my thesis committee for their constructive comments including David Walba, and Leo Radzihovsky in addition to Noel, Joseph and Matthew.

I am grateful to Renfan Shao who teaches me the basic knowledge of liquid crystal. I also am grateful to Arthur Klittnick for his technical help. I am thankful to the graduates in the laboratory for their help: Loren Hough for teaching me freeze-fracture transmission electron microscopy, Chenhui Zhu for teaching me freely suspended film, Yongqiang Shen for teaching me X-ray measurement, Youngwoo Yi for teaching me atomic force microscopy, and Yue Shi for teaching me the high sensitive birefringence detector. I am also thankful to undergraduates Josh working on the microfluidics and Newton working on freeze-fracture transmission electron microscopy together.

Thanks to all the other people in the lab Guanjiu Fang, Ying Wang, Zach Smith, Greg Smith, Cheol Park, Duong Nguyen, Ali Alshomrany, Giuliano Zanchetta and Dong Ki Yoon for making these years easy and happy. I enjoyed good times with them.

To the administrative people: Annett Baumgartner, Nikki Kilbride, Barbara Bowman, and Kathryn Brocko, thank you for your assistants.

I have benefited from interactions with people out of our lab. I own many thanks to Prof. Thomas Giddings for solving the problem of freeze-fracture machine. I thank Eva Körblova and Jacqueline Richardson, Ethan Tsai and Tao Gong in David's group for synthesizing the liquid crystal materials and Quan Zhang in Leo's group for helpful discussion. I thank Anderson Shum in David Weitz's group for teaching me the glass capillary microfluidics.

I also thank Prof. Antal Jakli, Prof. Junji Watanabe, Prof. Hideo Takezoe, Prof. Carsten Tschierske, Prof. Wolfgang Weissflog, and Prof. M. Blanca Ros for their generosity of sharing their materials with us.

Thanks to my friends Ke Zhao, Geluo A, Jixia Dai, Jianhua Cheng and Long He, for making my life in Boulder happy.

Finally, thanks to my family, especially my wife Xiujuan Huang for her support and making my daily life go smoothly. I like my two kids.

CONTENTS

Chapter

TABLES

Table

FIGURES

Figure

Chapter 1

Introduction

1.1 Liquid crystal phases of rod-like molecules

Liquid crystals (LCs) are a state of matter which has properties between those of a conventional liquid and those of a solid crystal. For instance, liquid crystal may flow like a liquid, but its molecules may be oriented in a crystal-like way. In the early days, liquid crystal phases of rod-like molecules have been intensively investigated. If the molecules are achiral, on cooling from the isotropic, the four most common liquid crystal phases formed in rod-like molecules are shown in Figures 1.1.1a-d, respectively.

If the molecule is chiral which means that there is a chiral center with four different groups and the molecule loses the mirror symmetry, the phases usually shown in rod-like molecules are denoted as N^*, SmA^*, SmC^*, where the molecular packing of each phase is shown in Figures 1.1.2a-d, respectively. There are distinct differences between the molecular packing of liquid crystal phases made of achiral rod-like molecule and that made of chiral rod-like molecule. In the N* phase, the chirality of the molecules makes the twist of the director more favorable. In the SmA* phase, the molecular pack is the same as that of the SmA phase. However, with the application of electric field, only the SmA^* phase shows the electroclinic effect, where the molecules tilt away from the layer normal linearly proportional to the electric field when the strength of the electric field is small. For the SmC* phase, there is macroscopic polarization perpendicular to the n-z plane, and the phase is ferroelectric in thin cells.

From the previous discussion, we know that chirality plays an important role in the property of the liquid crystal phases. The symmetry of achiral rod-like molecule is $C_{\infty h}$. When the achiral rod-like molecules are arranged in the SmC phase, the symmetry of the SmC phase is C_{2h}. The symmetry of chiral rod-like molecule is C_{∞}. When the chiral rod-like molecules are arranged in the SmC* phase, the symmetry of the SmC* phase is C_2. Here we will show why polarization is allowed in the SmC* phase but not the SmC phase, using symmetry argument (which is important in analyzing the property of liquid crystal phases) [1]. In the x-y-z coordinates (shown in the inset of Figure 1.1.1d and the inset of Figure 1.1.2d), there is a C_{2h} symmetry along y-axis in the SmC phase, which means the system stays the same under the symmetry operation. For the two fold rotation along the y-axis, we have

$$\begin{bmatrix} P_x \\ P_y \\ P_z \end{bmatrix} = \begin{bmatrix} P_x' \\ P_y' \\ P_z' \end{bmatrix} = \begin{bmatrix} -1 & 0 & 0 \\ 0 & 1 & 0 \\ 0 & 0 & -1 \end{bmatrix} \begin{bmatrix} P_x \\ P_y \\ P_z \end{bmatrix},$$

that is P_x=-P_x=0, P_y=P_y, P_z=-P_z=0. For the mirror reflection where the mirror plane is perpendicular to the y-axis, we have

$$\begin{bmatrix} P_x \\ P_y \\ P_z \end{bmatrix} = \begin{bmatrix} P_x' \\ P_y' \\ P_z' \end{bmatrix} = \begin{bmatrix} 1 & 0 & 0 \\ 0 & -1 & 0 \\ 0 & 0 & 1 \end{bmatrix} \begin{bmatrix} P_x \\ P_y \\ P_z \end{bmatrix},$$

that is P_x=P_x, P_y=-P_y=0, P_z=P_z. Combining these two results, we get P_x=P_y=P_z=0, which means that polarization is not allowed in the SmC phase by symmetry. For the SmC* phase, the symmetry along the y-axis has reduced to C_2. The mirror plane perpendicular to the y-axis has been broken by the chiral nature of the molecules. Under the symmetry operation of the two fold rotation along the y-axis, we have

$$\begin{bmatrix} P_x \\ P_y \\ P_z \end{bmatrix} = \begin{bmatrix} P_x' \\ P_y' \\ P_z' \end{bmatrix} = \begin{bmatrix} -1 & 0 & 0 \\ 0 & 1 & 0 \\ 0 & 0 & -1 \end{bmatrix} \begin{bmatrix} P_x \\ P_y \\ P_z \end{bmatrix},$$

that is $P_x=-P_x=0$, $P_y=P_y$, $P_z=-P_z=0$. Thus, in the SmC* phase, polarization is only allowed along the y-axis, which is always perpendicular to the n-z plane.

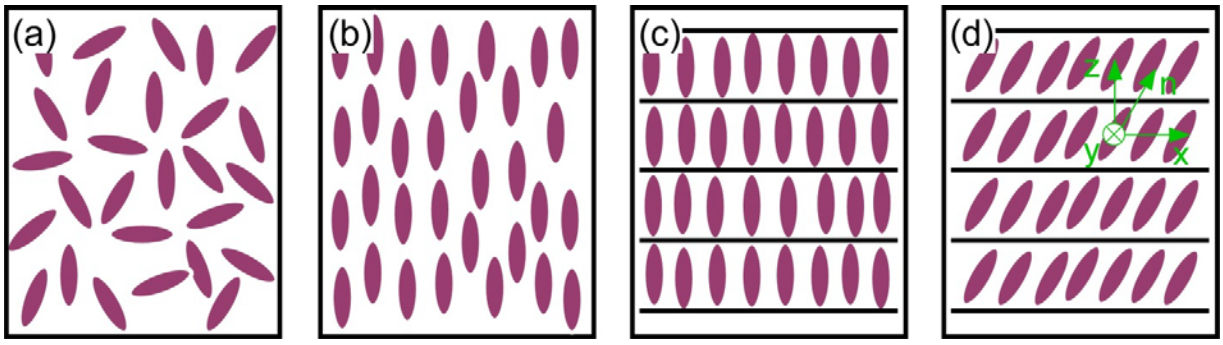

Figure 1.1.1: A simplified sketch of the four most common liquid crystal phases of achiral rod-like molecules. (a) Isotropic (Iso) phase. (b) Nematic (N) phase. (c) Smectic A (SmA) phase. (d) Smectic C (SmC) phase.

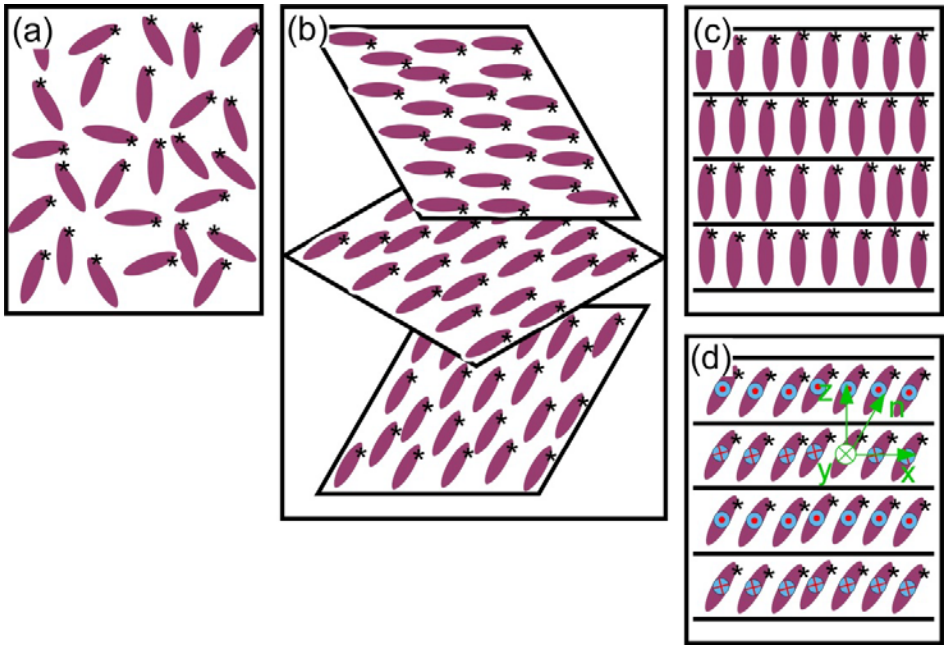

Figure 1.1.2: A simplified sketch of the four most common liquid crystal phases of chiral rod-like molecules. (a) Isotropic (Iso) phase. (b) Nematic* (N*) phase (Cholesteric phase). (c) Smectic A* (SmA*) phase. (d) Smectic C* (SmC*) phase.

1.2 Liquid crystal phases of bent-core molecules

Liquid crystal phases of bent-core molecules have been intensively investigated during the recent years, since the first discovery of ferroelectric in achiral bent-core molecules [2]. As we have discussed in section 1.1, macroscopic polarization is not allowed in the SmC phase of achiral rod-like molecules, because the $C_{\infty h}$ symmetry of the molecule and the C_{2h} symmetry of the phase. However, for bent-core molecules, because of the bent molecular shape, the symmetry of the molecule is C_{2d}. When the achiral bent-core molecules are arranged in tilted smectic layers, the symmetry of the phase is only C_2, which is the same as that of the SmC* phase of chiral rod-like molecules. Thus, for bent-core molecules, even though the molecules are achiral, the tilted smectic layers can be chiral with polarization along the layer plane.

The bent-core liquid crystals exhibit a wide variety of novel structural phenomena involving the interplay of bent-core, molecular tilt and polarization. When the molecules are tilted, the bent-core serves as a chiral center, breaking the mirror symmetry and enabling polarization perpendicular to the n-z plane. Thus, in any chiral, polar phase of bent-core molecules, the molecules are tilted. As shown in Figures 1.2.1a and b, the $SmAP_F$ phase is polar, but since the molecules are not tilted, there is still a mirror plane, σ_v, and the phase is achiral. When the polar molecules are tilted, the mirror symmetry is broken and the phase is chiral, as shown in Figures 1.2.1c and d. Molecular tilt is an unavoidable consequence of the broken symmetry. It is universal in any chiral phase of bent-core molecules. Different combinations of the tilt and polarization directions give the four common smectic phases in bent-core molecules: SmC_AP_A, SmC_SP_S, SmC_AP_S, SmC_SP_A [3].

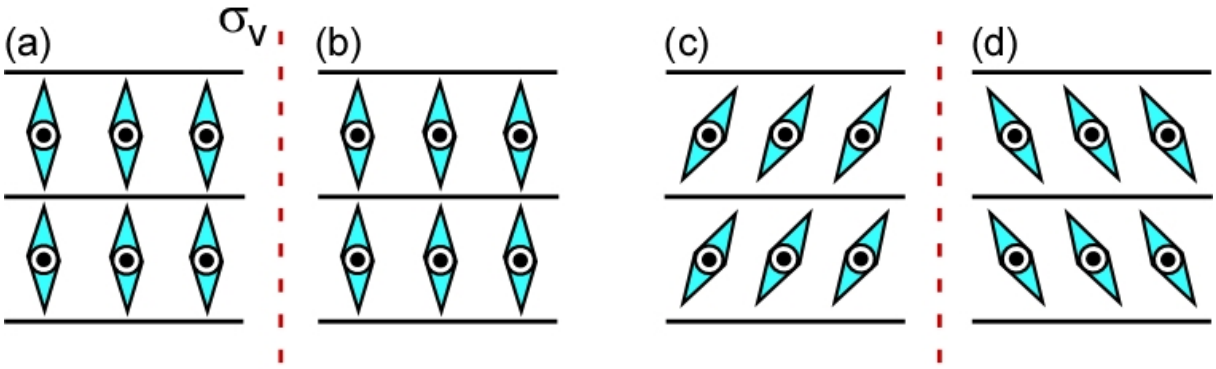

Figure 1.2.1: The interplay of bent core, molecular tilt and polarization in the liquid crystal phases of bent-core molecules. (a) The $SmAP_F$ phase and its mirror image (b). The two states are indistinguishable and the $SmAP_F$ phase is polar but achiral. (c) The SmC_SP_F phase and its mirror image (d). The SmC_SP_F phase has no mirror symmetry and the two states can not be superimposed. The SmC_SP_F phase is therefore polar and chiral. The red dashed line is the reflection plane.

1.3 Layout of the chapters

The interplay of molecular bent core, molecular tilt and polarization has induced a wide variety of novel structural phenomena, unique in the bent-core molecules. In this thesis, we will focus on the microstructures of the liquid crystal phases of bent-core molecules. However, microstructures of other interesting systems will also be described.

Before characterizing the characteristic microstructure of each liquid crystal phase, in Chapter 2, we will first describe some experimental methods which are commonly used to characterize the liquid crystal phases. Useful information on the liquid crystal phases can be obtained from each experimental method. However, combining of all these methods can give a better image of the liquid crystal phase being studied.

The B4 helical nanofilament phase, which is the most complex hierarchical self-assembly in soft matter and the first bent-core liquid crystal phase showing macroscopic chiral structure [4], will be discussed in detail in Chapter 3. We will first demonstrate the chirality-preserving growth of the B4 nanofilaments and then the pre-transitional orientational ordering of rod-like molecules in the helical nanofilament random network. In contrast to the helical nanofilament in the bulk, achiral surface structure of the B4 phase is also observed, due to the confinement of flat surface. Finally, possible applications of the B4 helical nanofilament phase will be discussed.

The dark conglomerate (DC) phase is another phase showing macroscopic left- and right-handed chiral domains, which are made of disordered focal conic domains [5]. In Chapter 4, we will describe the quasi-ordered toric focal conic arrays discovered in the DC phase at the air/liquid crystal interface. Following this, we will emphasize the importance of studying the free surface structures of the liquid crystal phases, by analyzing the free surface structures of the B4,

B7 and DC phases. Thereafter, investigating free surface structures is incorporated in the following chapters when characterizing the microstructures of the liquid crystal phases.

The B7 phase of bent-core molecules is the phase which shows the most beautiful, fantastic optical texture. Polarization-modulated layer undulation has been clarified in the B7 phase [6]. In Chapter 5, we will further discuss the microstructure of the B7 phase by analyzing the defects observed in the B7 layer undulation. At the end, we will briefly discuss the optical texture of the B7 phase and a model is proposed to explain the observed B7 texture.

In chapter 6, we will discuss some microstructures discovered in the low temperature chiral phase (the liquid crystal phase is stable at room temperature and is supposed to be the B4 phase), including the achiral B4 structure of P-12-OPIMB which coexists with the helical nanofilament, the enhanced formation of helical nanofilament of W513 in the mixtures with 8CB, and the disordered B4 phase (or the low temperature DC phase) of W624.

Recently, an interesting chiral phase was discovered in a hockey-stick like molecule, which will be characterized in Chapter 7. This chiral phase, which shows macroscopic chiral domains under decrossed polarizers, appears below a SmA phase and is followed by crystallization. This behavior is different from the DC phase which appears below isotropic or the B4 phase which is stable at room temperature. FFTEM images reveal that the bulk structure of this chiral phase is made of smectic blocks, oriented in different directions, a structure mediated by defects between different blocks. By analogy with the twist grain boundary phase, we call this new phase the randomized twist grain boundary phase.

In Chapter 8 we will summarize all the other microstructures studied (ones not mentioned anywhere else in the thesis) and this chapter will also serve as a gallery of the microstructures of the other liquid crystal phases (ones not mentioned anywhere else in the thesis).

Bibliography

[1] S. T. Lagerwall, and I. Dahl: Ferroelectric liquid crystals. *Mol. Cryst. Liq. Cryst.* 1984, **114**, 151-187.

[2] T. Niori, T. Sekine, J. Watanabe, T. Furukawa, and H. Takezoe: Distinct ferroelectric smectic liquid crystals consisting of banana shaped achiral molecules. *J. Mater. Chem.* 1996, **6**, 1231-1233.

[3] D. R. Link, G. Natale, R. Shao, J. E. Maclennan, N. A. Clark, E. Körblova, and D. M. Walba: Spontaneous formation of macroscopic chiral domains in a fluid smectic phase of achiral molecules. *Science* 1997, **278**, 1924-1927.

[4] L. E. Hough, H. T. Jung, D. Krüerke, M. S. Heberling, M. Nakata, C. D. Jones, D. Chen, D. R. Link, J. Zasadzinski, G. Heppke, J. P. Rabe, W. Stocker, E. Korblova, D. M. Walba, M. A. Glaser, and N. A. Clark: Helical nanofilaments phases. *Science* 2009, **325**, 456-460.

[5] L. E. Hough, M. Spannuth, M. Nakata, D. A. Coleman, C. D. Jones, G. Dantlgraber, C. Tschierske, J. Watanabe, E. Korblova, D. M. Walba, J. E. Maclennan, M. A. Glaser, and N. A. Clark: Chiral isotropic liquids from achiral molecules. *Science* 2009, **325**, 452-456.

[6] D. A. Coleman, J. Fernsler, N. Chattham, M. Nakata, Y. Takanishi, E. Körblova, D. R. Link, R.-F. Shao, W. G. Jang, J. E. Maclennan, O. Mondainn-Monval, C. Boyer, W. Weissflog, G. Pelzl, L.-C. Chien, J. Zasadzinski, J. Watanabe, D. M. Walba, H. Takezoe, and N. A. Clark: Polarization-modulated smectic liquid crystal phases. *Science* 2003, **301**, 1204-1211.

Chapter 2

Experimental Techniques

2.1 Introduction

In the study of liquid crystal phases, there are several commonly used experimental techniques, such as differential scanning calorimetry, x-ray diffraction, depolarized transmission light microscopy, freely suspended film, freeze-fracture transmission electron microscopy, nuclear magnetic resonance and so on. All these experimental methods are powerful tools for characterizing the liquid crystal phases. On the other hand, there is no single experimental method which can fully characterized the liquid crystal phases, and each experiment method only focus on some particular property of the liquid crystal phases. Only a combination of all these methods can give a clear, unambiguous picture of the liquid crystal phases investigated. As most of the experimental techniques have been described in detail somewhere else, here we only give a brief description of each method and focus on what information we can obtain from each method and how we can analyze the liquid crystal phases from those experimental results.

2.2 Differential scanning calorimetry (DSC)

DSC is a thermoanalytical technique in which the difference in the amount of heat required to increase the temperature of a sample and reference is measured as a function of temperature. Both the sample and reference are maintained at nearly the same temperature throughout the experiment. Generally, the temperature program for a DSC analysis is designed such that the sample holder temperature increases linearly as a function of time. The reference sample should have a well-defined heat capacity over the range of temperature to be scanned. The basic principle underlying this technique is that when the sample undergoes a physical transformation such as phase transitions, more or less heat will need to flow to it than the reference to maintain both at the same temperature. By observing the difference in heat flow between the sample and reference, differential scanning calorimeters are able to measure the amount of heat absorbed or released during such transitions. With DSC, one is able to observe very subtle phase changes, such as glass transitions. Thus, DSC is the one of the most common technique used to detect the phase transitions of the liquid crystal materials, as it is possible to observe the small energy changes that occur due to phase transitions. The type of phase transition can sometime be determined from the DSC peaks. Usually, for first order phase transition, the DSC peak is sharp and strong, while for second order phase transition, the DSC peak is broad and weak. DSC scans are also good for determining the change of phase transitions when materials are confined in a finite volume [1]. Advanced DSC, such as high sensitivity DSC [2], is also powerful in characterizing the phase transition.

2.3 X-ray diffraction (XRD)

X-ray diffraction is based on the elastic scattering of x-rays from the electron clouds of the individual atoms in the system. Bragg's law gives the angles for coherent scattering from the lattices of those atoms. X-ray diffraction can be carried out on unoriented liquid crystal phases, where the materials are filled into a glass capillary by capillary force and then cooled to the desired temperature for the liquid crystal phase. Sometimes, in order to achieve direct, actual structural information, x-ray diffractions are performed on macroscopically well oriented samples, for example, for characterizing the cybotactic nematic phase [3]. For liquid crystal phases, we usually divide the x-ray reflection peaks into two categories: small angle x-ray reflection peaks (q~0.2 $Å^{-1}$), which are usually the coherent scattering peaks from periodic liquid crystal layers or periodic liquid crystal lattices (for example, the hexagonal lattice for some columnar liquid crystal phase), and wide angle x-ray reflection peaks (q~2 $Å^{-1}$), which are usually the constructive scattering peaks from intralayer molecular packing.

Besides the conventional x-ray diffraction, some advanced x-ray scattering methods have also been used to explore the structure of the liquid crystal phases in detail, for example, the unambiguously identification of the SmC_α phase using resonant x-ray scattering [4].

For our XRD experiments, XRD experiments on powder samples were carried out using a Huber four-circle goniometer on beamline X10A of the National Synchrotron Light Source at Brookhaven National Laboratory. This beamline uses a double-bounce Si monochromator and a Ge 111 analyzer to obtain a wavevector resolution δq=0.0005 $Å^{-1}$ full width at half maximum. Powder samples were in 1 mm diameter glass capillaries in a temperature controlled chamber.

2.4 Depolarized transmission light microscopy (DTLM)

DTLM is one of the most popular tools used to characterize the liquid crystal phases and phase sequences. By cooling down the sample from isotropic, we can observe the optical texture of each liquid crystal phase and the change of optical texture when the sample undergoes a phase transition. Because most characteristic liquid crystal textures are associated with their unique molecular arrangements (or liquid crystal lattices) and corresponding defect structures, by analyzing the liquid crystal texture, people sometimes can immediately determine the type and the structure of the phase. However, this requires some experience with the optical texture of each liquid crystal phase, and thus, we refer the reader to a useful book on this subject [5].

Here we present an example of analyzing the liquid crystal phase based on the optical texture. As shown in Figure 2.4.1a, the liquid crystal phase is characteristic of the focal conic texture, with dark brushes parallel to the polarizers. The cell geometry is shown in Figure 2.4.1b. As we know, in typical focal conic domains, the layer normal is axially outwards from the center, as shown in Figure 2.4.1c. In any regions, where it's dark under crossed polarizers, the principle optical axis in that region is parallel to the polarizers. In the case of Figure 2.4.1a, the dark bushes are along the layer normal, indicating that the principle optical axis is parallel to the layer normal everywhere in the focal conic domains. Base on this conclusion, where principle optical axis is parallel to the layer normal, we propose that the phase can only be either smectic A phase (including De Vries phase) or smectic C_A phase.

In order to further characterize the molecular arrangements in this liquid crystal phase, an electric field is usually applied to the cell to study the electro-optic behavior of the phase, as shown in Figure 2.4.2a. The dark brushes rotate about 45° with respect to the polarizers,

indicating that the principle optical axis is 45° tilted with respect to the layer normal in the focal conic domains, as modeled in Figure 2.4.2b. Though we can unambiguously determine the molecular arrangement in those focal conic domains under electric field, there are still two possibilities for the ground state of the phase, the De Vries phase and the smectic C_A* phases. We will show in the following section that by observing a freely suspended film the ground state of the phase can further be identified.

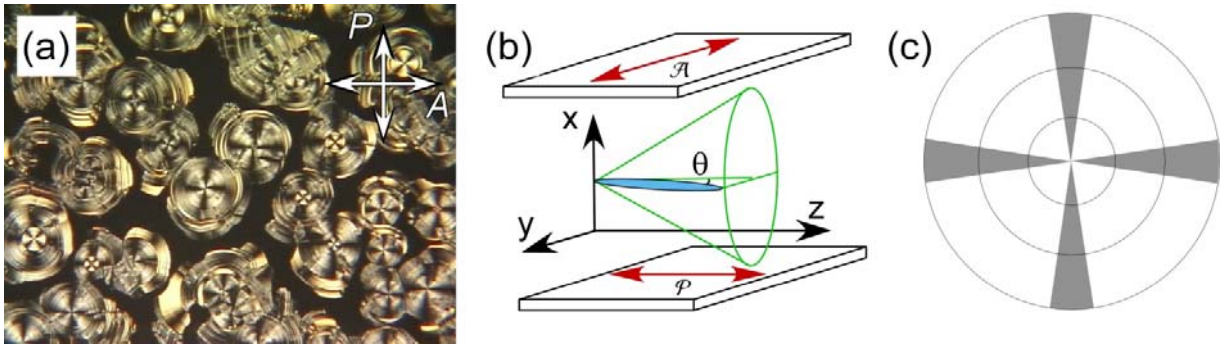

Figure 2.4.1: DTLM image of the liquid crystal phase under crossed polarizers without electric field and the model. (a) DTLM image of W639, a chiral, rod-like molecule, without electric field under crossed polarizers at T=90°C. (b) Cell geometry with one example of tilted, rod-like molecule. (c) Layering of the focal conic domains.

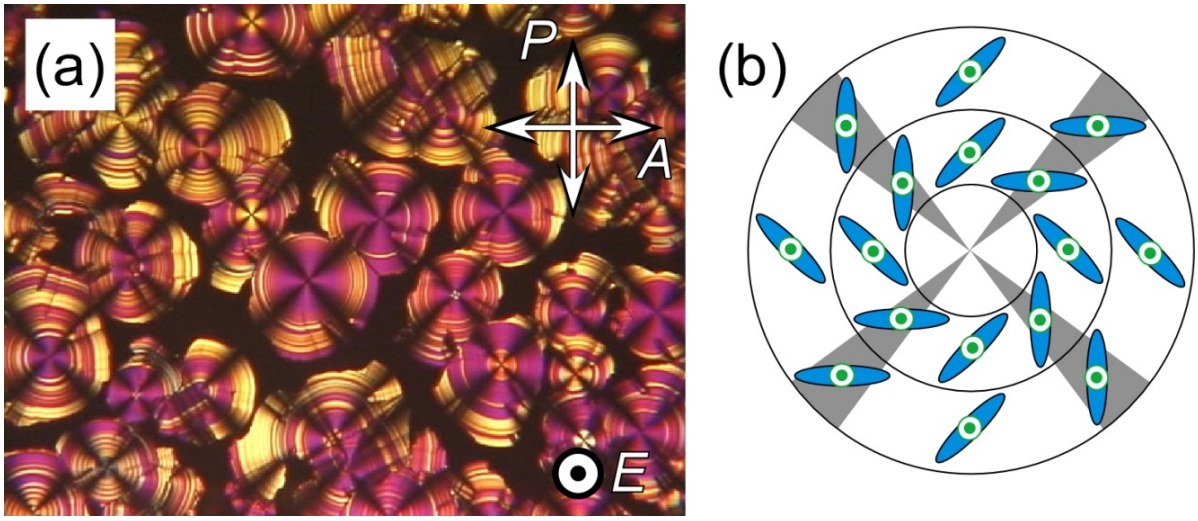

Figure 2.4.2: DTLM image of the liquid crystal phase under crossed polarizers with electric field and the model. (a) DTLM image of W639, a chiral, rod-like molecule, with electric field under crossed polarizers at T=90°C. (b) Layering of the focal conic domains and the corresponding molecular arrangement with electric field.

2.5 Freely suspended film

Because many liquid crystal phases form smectic layers, freely suspended film of those liquid crystal phases can easily be made, by drawing the materials across an opening. Those freely suspended films are assumed to show the bulk property of the liquid crystal phases, as there is no influence from the surface anchoring such as in the cell, and are widely used in liquid crystal studies. The freely suspended film by itself is an interesting system, as it is on the border line between 2D and 3D systems. A lot of interesting phenomena have been observed in this system, such as the crossover between 2D and 3D fluid dynamics [6] and the layer by layer phase transition [7].

Following the optical texture study in section 2.4, here we will analyze the freely suspended film of the liquid crystal phase. As shown in Figure 2.5.1a, under an in-plane electric field of E=55 V/mm, there is odd-even effect with slightly decrossed polarizer and analyzer, where odd-numbered layers with lateral polarization orient perpendicular to electric field (dark regions) and even-numbered layers with longitudinal polarization orient parallel to the electric field (bright regions). The net polarizations along the molecular longitudinal and lateral directions in odd- and even-numbered layers are shown in Figure 2.5.1b. Usually, air induces polarization at the air/liquid crystal interface, for example, with net polarization pointing along the molecular long axis [8]. This kind of longitudinal polarization is smaller than the lateral polarization and become weaker away from the interface. In even-numbered layers, the lateral polarization canceled out, there is only net longitudinal polarization and molecules align parallel to the electric field. In odd-numbered layers, the lateral polarization dominates (no net longitudinal polarization) and molecules align perpendicular to the electric field. By including this observation, we can now conclude that the ground state of W639 studied here is SmC_A*.

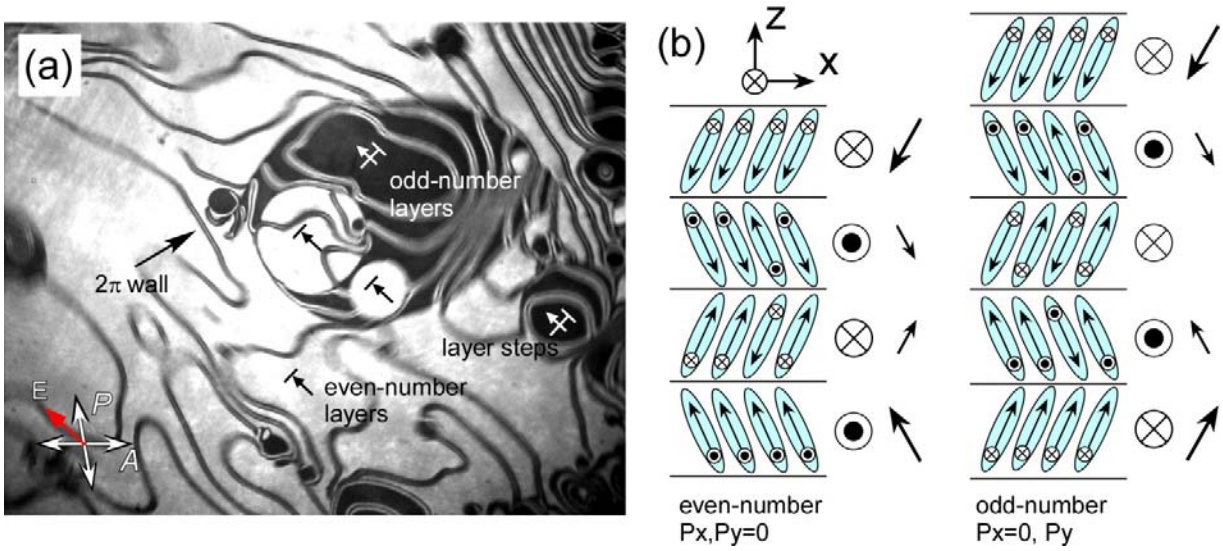

Figure 2.5.1: Odd-even effect observed in the freely suspended film of the anticlinic, antiferroelectric phase. (a) The odd-even effect in the freely suspended film of W639 at T=88°C. (b) The underlying molecular arrangements of the odd-even effect.

2.6 Freeze-fracture transmission electron microscopy (FFTEM)

Freeze fracture transmission electron microscopy (FFTEM) is one of the most powerful tools to directly visualize the microstructure of the liquid crystal phase. FFTEM experiments were carried out by sandwiching the sample between 2 mm by 3 mm glass planchettes (Figure 4.6.1a, which were previously cleaned using detergent and then acetone but are otherwise untreated), and then cooling from the isotropic or heating from the crystal phase to a selected temperature of the liquid crystal phase, the phase being confirmed by optical microscopy. The samples were then rapidly quenched to T<-180°C by immersion in liquid propane, fractured in vacuum at -140°C, and then coated with 2 nm of platinum deposited at 45° and then with 25 nm of carbon deposited at 90°. After dissolving the liquid crystal, the Pt-C replicas are placed in the TEM, where the topographic structure of the fracture plane may be observed. Smectic layer surfaces are generally smooth but have occasional layer steps that are distinct and can be identified unambiguously.

We have also extended the FFTEM method to investigate some liquid crystal phase under electric field. In this case, the samples are sandwich between ITO glasses of 2 mm by 3 mm, connected by fine hair-like wires, as shown in Figure 4.6.1b. Electric field can be applied through the wires to the ITO electrodes and the samples can be quenched under electric field. After quenching, the electric field is turned off and the wires are removed, then the following procedure is the same as conventional FFTEM.

To the conventional FFTEM method, there are also some variations. Free surface transmission electron microscopy (FSTEM) is the method we have developed to investigate the self-assembly of liquid crystal phases at the air/liquid crystal interface. For this method, all

samples are prepared on clean glass substrates, as shown in Figure 4.6.1c. Due to the dewetting of liquid crystal materials from the glass surface, the samples will usually form a small dome on top of the substrate. At the same time, the samples are much thicker than those sandwiched between two glasses, and thus the polarity associated with the glass substrate has little effect on the structure at the free surface. However, the boundary conditions imposed by the air/liquid crystal interface play an important role in the self-assembly at the surface. All samples are cooled from the isotropic to the desired phase, with the phase being confirmed by optical microscope, and are rapidly quenched by immersion in liquid propane. Then the samples are coated with 2 nm of platinum deposited at 45° and with 25 nm of carbon deposited at 90° at room temperature. In conventional FFTEM, after quenching, the samples are fractured and coated at -140°C to avoid any recrystallization. However, in order to visualize the free surface, we need to coat the samples at room temperature to get rid of the ice crystals which usually condense on the surfaces of cold samples when transferring them to the fracturing and coating machine. We have confirmed that no recrystallization happens during the short time that the samples are warmed to room temperature for coating. After dissolving the liquid crystal, the Pt-C replicas are placed in the TEM, where the topography of the liquid crystal surface may be observed. TEM images are interpreted with the understanding that regions of the surface facing the platinum shadowing beam appear dark, while those facing away are bright.

Freeze cutting transmission electron microscopy (FCTEM) is another variation on the conventional FFTEM. For FFTEM, the fracturing process is uncontrollable and usually the cells are fractured along one of the glass substrates. Freeze cutting transmission electron microscopy provides a controllable investigation of any plane below the free surface, by cutting a hemispherical-shaped sample drop with a sharp knife. For this method, sufficient samples are

placed on a copper holder where they form a hemispherical drop on top of the holder, as shown in 2.6.1d. After quenching the sample, the sample holder is placed in the fracture machine, where there is a sharp knife to cut the hemispherical sample to a desired depth. The following procedure is then the same as conventional FFTEM.

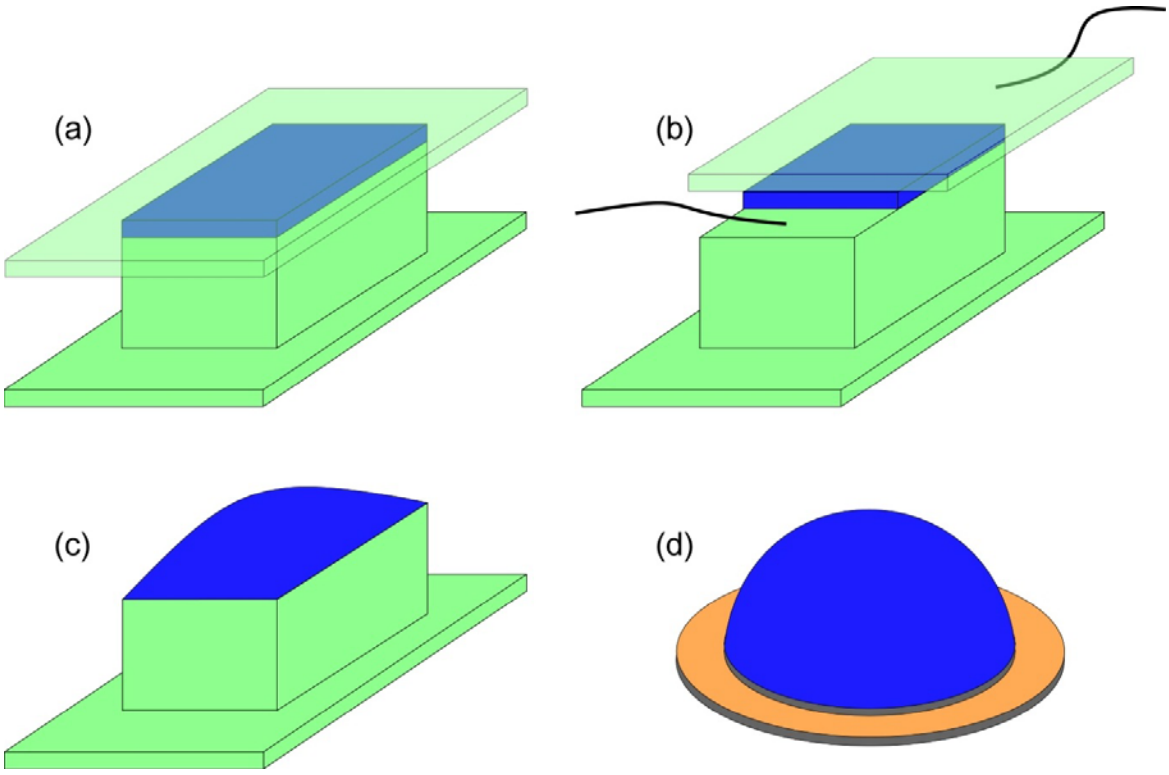

Figure 2.6.1: Sample preparations for FFTEM and its variations. (a) Samples are sandwiched between glass planchettes of 2 mm by 3 mm for FFTEM. (b) Samples are sandwiched between glass planchettes with electrodes when investigating the microstructure of the liquid crystal phases under electric field. (c) Samples placed on the glass planchette for free surface transmission electron microscopy and no fracturing is needed to image the free surface topography of the liquid crystal phase. Due to the dewetting of liquid crystal materials from the glass surface, the samples will usually form a small dome on top of the substrate. (d) Samples are place on a copper holder and form hemispherical drop on the sample holder for freeze cutting transmission electron microscopy.

2.7 Nuclear magnetic resonance (NMR)

NMR spectroscopy is one of the principal techniques used to obtain physical, chemical, electronic and structural information about molecules due to the chemical shift, the Zeeman effect and so on, on the resonant frequencies of the nuclei present in the sample. It is a powerful technique that can provide detailed information on the topology, dynamics and three-dimensional structure of molecules in solution and the solid state. Those information obtained from NMR sometimes is critical to understand the liquid crystal phases, for example, the NMR study of the B4 phase of the symmetrical molecule P-9-OPIMB, which reveals double peaks of the C=O group indicating the conformational chirality of the molecules in the B4 phase [9].

Bibliography

[1] K. Takekoshi, K. Ema, H. Yao, Y. Takanishi, J. Watanabe, and H. Takezoe: Appearance of a liquid crystalline nematic-isotropic critical point in a mixture system of rod- and bent-shaped molecules. *Phys. Rev. Lett.* 2006, **97**, 197801/1-4.

[2] H. Nagayama, Y. Sasaki, F. Araoka, K. Ema, K. Ishikawa, and H. Takezoe: Discrete and sequential formation of helical nanofilaments in mixtures consisting of bent- and rod-shaped molecules. *Soft Matter* 2011, **7**, 8766-8769.

[3] O. Francescangeli, F. Vita, F. Fauth, and E. T. Samulski: Extraordinary magnetic field effect in bent-core liquid crystals. *Phys. Rev. Lett.* 2011, **107**, 207801/1-5.

[4] P. Mach, R. Pindak, A.-M. Levelut, P. Barois, H. T. Nguyen, C. C. Huang, and L. Furenlid: Structural characterization of various chiral smectic-C phases by resonant x-ray scattering. *Phys. Rev. Lett.* 1998, **81**, 1015-1018.

[5] Ingo Dierking: *Textures of liquid crystals*. Wiley-Vch, 2003.

[6] Z. H. Nguyen, M. Atkinson, C. S. Park, J. E. Maclennan, M. A. Glaser, and N. A. Clark: Crossover between 2D and 3D fluid dynamics in the diffusion of islands in ultrathin freely suspended smectic films. *Phys. Rev. Lett.* 2010, **105**, 268304/1-4.

[7] R. Geer, T. Stoebe, C. C. Huang, R. Pindak, J. W. Goodby, M. Cheng, J. T. Ho, and S. W. Hui: Liquid-hexatic phase transitions in single molecular layers of liquid-crystal films. *Nature* 1992, **355**, 152-154.

[8] D. R. Link, N. A. Clark, B. I. Ostrovskii, and E. A. Soto Bustamante: Bilayer-by-bilayer antiferroelectric ordering in freely suspended films of an achiral polymer-monomer liquid crystal mixture. *Phys. Rev. E* 2000, **61**, R37-R40.

[9] D. M. Walba, L. Eshda t, E. Körblova, and R. K. Shoemaker: On the nature of the B4 banana phase: crystal or not a crystal? *Crystal Growth & Design* 2005, **5**, 2091-2099.

Chapter 3

B4 Phase: Novel Self-Assembly of Helical Nanofilaments

3.1 Introduction

Chirality has been one of the most attractive themes in chemistry since Pasteur's famous experiment showing the handedness of tartaric acid [1]. Understanding how chirality arises is important from the perspective of science as well as technology. In biology, for example, several models have been proposed to address the fundamental question of how enantiomerically pure solutions or crystals might have emerged from a presumably racemic prebiotic world [2, 3, 4].

While quite common in crystals, spontaneous chirality was only recently reported in fluids of achiral molecules, with macroscopic chiral conglomerate domains observed in stacked fluid layers of banana-shaped, achiral liquid crystal molecules. Indeed, mesogens with bent cores and one or two flexible tails exhibit a wide variety of novel structural phenomena involving the interplay of chiral, polar, and liquid crystalline order [5, 6], including the first manifestation of ferroelectricity in a smectic phase of achiral molecules [7]. The strong local preference for layering, coupled with the bent shape of the molecules, leads to two spontaneous, symmetry-breaking instabilities: polar molecular orientational ordering and molecular tilt [8]. These instabilities combine to drive the formation of chiral layered phases such as the B2 and B7 [9, 10].

It has been shown recently that in both the dark conglomerate and B4 phases of banana-shaped molecules there is a preference for the smectic layers to have saddle-splay curvature [11, 12]. This tendency is attributed to the orthogonal tilt directions of the two molecular half-arms, which causes dilation in one half-layer and compression in the other. This produces a frustrated state that can be relieved by saddle-splay curvature, a response that accommodates both the chirality and the layering. While the dark conglomerate phase is composed of disordered focal conic domains, the B4 phase forms helical nanofilaments. Even though NOBOW is an achiral molecule, in a mechanism common to many bent-core phases, spontaneous symmetry breaking results in the B4 phase being chiral. However, the B4 is unique so far in being the only bent-core phase with a macroscopically chiral structure, the twisted filament. The hierarchical self-assembly of the nanofilament phase is shown in Figure 3.1.1. The macroscopic chirality of the dark conglomerate phase is maintained by the local chiral organization of the molecules and the long-range continuity of the smectic layers. However, the establishment of macroscopic chirality in the B4 phase, which is composed of distinct left- or right-handed helical filaments, has remained a mystery.

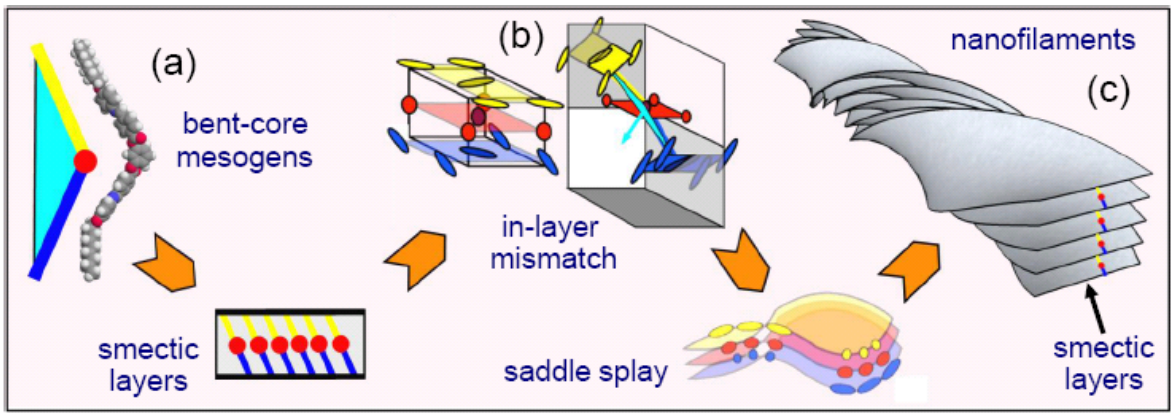

Figure 3.1.1: Hierarchical self-assembly of the nanofilament phase. (a) The hierarchical self-assembly of the nanofilament phase starts with bent-core mesogenic molecules, which form well-defined smectic layers with in-plane hexatic order, macroscopic polarization, and tilt of the molecular planes, making them chiral. (b) In this geometry, the half-molecular tilt directions on either side of the layer mid-plane are nearly orthogonal. The projections onto the layer mid-plane of the lattices formed by the core arms (yellow and violet) do not match, resulting in a local preference for saddle-splay layer curvature and driving the formation of twisted nanofilaments (c).

3.2 Chirality-preserving growth of helical filaments in the B4 phase of bent-core liquid crystals

The observation of unusually large chiral domains (of mm dimensions) in the depolarized transmission light microscopy (DTLM) in mixtures of the rod-shaped mesogen 5CB or 8CB with NOBOW has led to their being intensively investigated [13, 14, 15]. Freeze-fracture transmission electron microscopy (FFTEM) images show individual twisted nanofilaments, allowing the direct measurement of the filament diameter and helix pitch, which we find to be independent of the 8CB concentration (Table 3.2.1). Precision x-ray diffraction measurements show that the smectic layer spacing in the B4 nanofilaments is also independent of the 8CB concentration [15]. In addition to reflections from the B4 filaments, the diffraction pattern shows at lower temperatures a separate Bragg peak from the 8CB smectic A layers, with a spacing d≈33 Å at temperature T≈33°C, also independent of the 8CB concentration. This suggests that NOBOW is insoluble in the 8CB, indicating an essentially complete phase separation of the two components once the B4 forms, with NOBOW forming nanofilaments and 8CB occupying the space between them. The chemical structure and the phase behavior of 8CB/NOBOW mixtures are shown in Figure 3.2.1. The linear reduction of the Iso–B4 transition temperature of NOBOW with increasing 8CB concentration corresponds to classical freezing point depression, where the latent heat obtained from fitting the slope of this phase boundary, $\Delta H_{Iso\text{-}B4}\approx 51$ kJ/mol, matches the value $\Delta H_{Iso\text{-}B4}\approx 53$ kJ/mol obtained from the extrapolation of the DSC data. The overall picture that emerges from these structural studies is of a strongly nano-segregated mixture of NOBOW filaments of diameter D≈36 nm, with 8CB in nano-sized pores whose average dimension decreases as the 8CB

concentration is reduced. At smaller 8CB concentrations, the confinement of the 8CB smectic in the random environment of NOBOW filaments leads to a broadening of the thermal anomalies associated with its Iso-N and N-SmA phase transitions [15] similar to what is observed in 5CB [16], indicating that 8CB is interacting with the filament surfaces and that orientational or layer ordering of the 8CB is limited to smaller and smaller volumes. In this case, the 8CB/NOBOW system can be well understood in terms of "nano-phase separation", with the 8CB filling the volume between dilute, random networks of NOBOW B4 helical filaments. In the scenario of nano-phase segregation, the phase diagram of the NOBOW/8CB mixtures is generalized in Figure 3.2.2.

The mixtures also provide a good platform for investigating the development of chirality in the B4 phase, as in neat NOBOW the B4 phase grows in from the B2 and it is difficult to distinguish the nucleation events. In the mixtures, the B4 phase appears directly from the isotropic, forming large chiral domains in which we can directly observe the growth of the phase. In addition, because of the dilution with 8CB, each chiral domain comprises a network of individual B4 filaments where we can visualize how new helical nanofilaments branch off from existing ones. More importantly, phase segregation combined with spontaneous nanoscale self-assembly of the B4 helical nanofilaments offers the possibility for a wide variety of novel materials. Understanding the nucleation and growth behavior of the B4 helical nanofilament in the blends will help in their application such as nano-heterogeneous media.

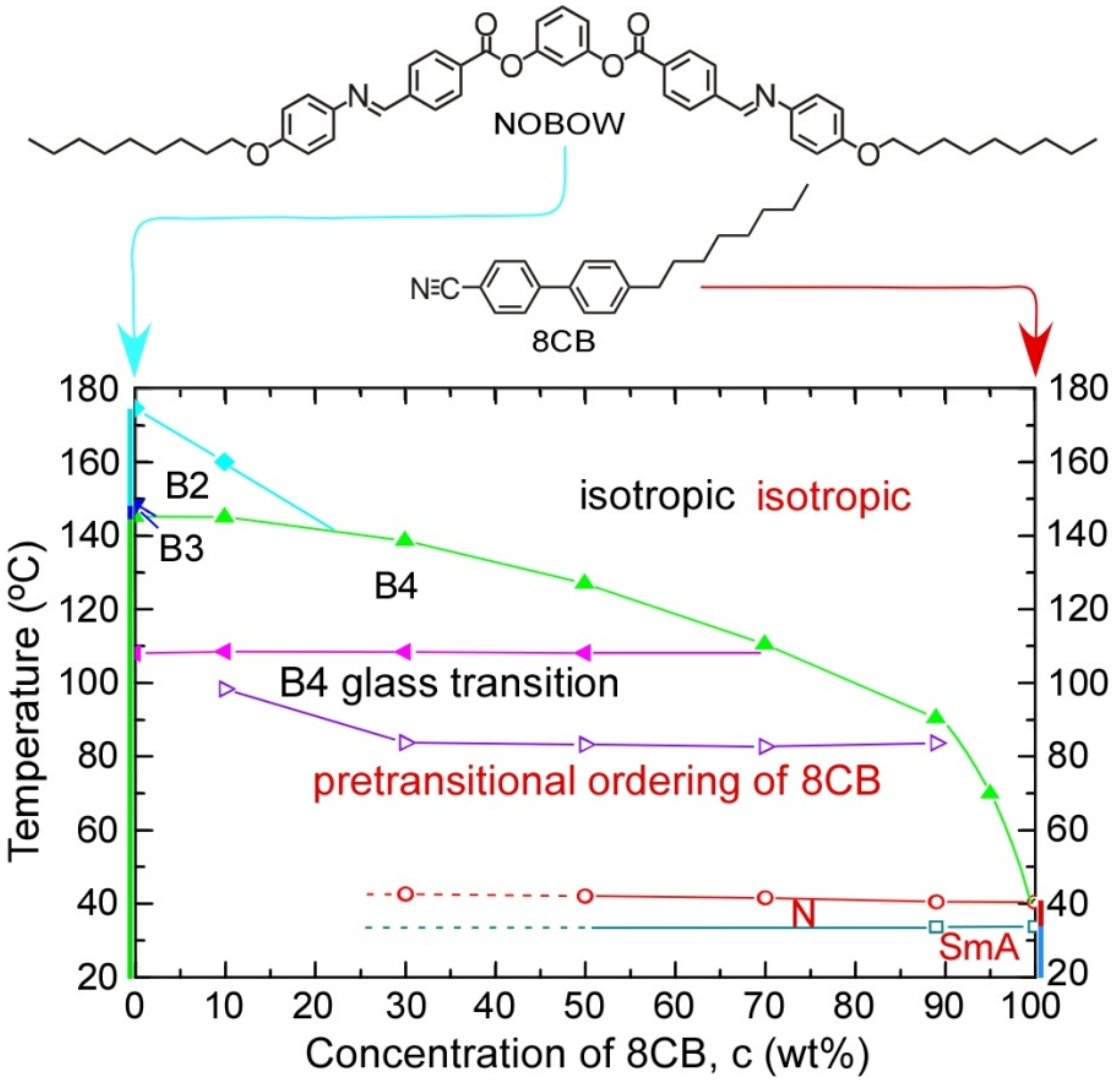

Figure 3.2.1: Phase diagram of the binary system derived from differential scanning calorimetry (DSC) and DTLM observations. The phase sequences of the pure materials on cooling are for NOBOW: Iso(175ºC)B2(147ºC)B3(143ºC)B4 and for 8CB: Iso(40ºC)N(33ºC)SmA. Mixtures of NOBOW with 8CB form a single, homogeneous phase only in the high temperature, isotropic range. At lower temperatures, the NOBOW B4 phase-separates into a network of helical nanofilaments, leaving the 8CB to fill the interstitial spaces (NOBOW phases shown in black, 8CB phases in red). As the concentration of 8CB is increased, the NOBOW B2 and B3 phases disappear and the transition to the B4 phase is depressed, decreasing approximately linearly with 8CB concentration. The linear reduction of the NOBOW Iso-B4 transition corresponds to conventional freezing point depression. The DSC peak around 83°C observed in the mixtures (open purple triangles) arises from local pre-transitional orientational ordering of 8CB around the surface of NOBOW B4 helical nanofilaments, which will be discussed in detail in Section 3.3 of this chapter.

8CB Concentration	0%	30%	50%	75%	95%
Helix Pitch p (nm)	217±6	221±4	218±6	217±3	216±6
Filament Width w (nm)	37±2	37±3	37±2	36±3	38±8

Table 3.2.1: Helical B4 filament characteristics in 8CB/NOBOW mixtures. The helix pitch p and filament width w were measured as a function of composition from freeze-fracture transmission electron microscopy images as indicated in Figure 3.2.5a. The uncertainties correspond to the standard deviation obtained from five measurements of each mixture. The helix structure shows little dependence on the 8CB concentration.

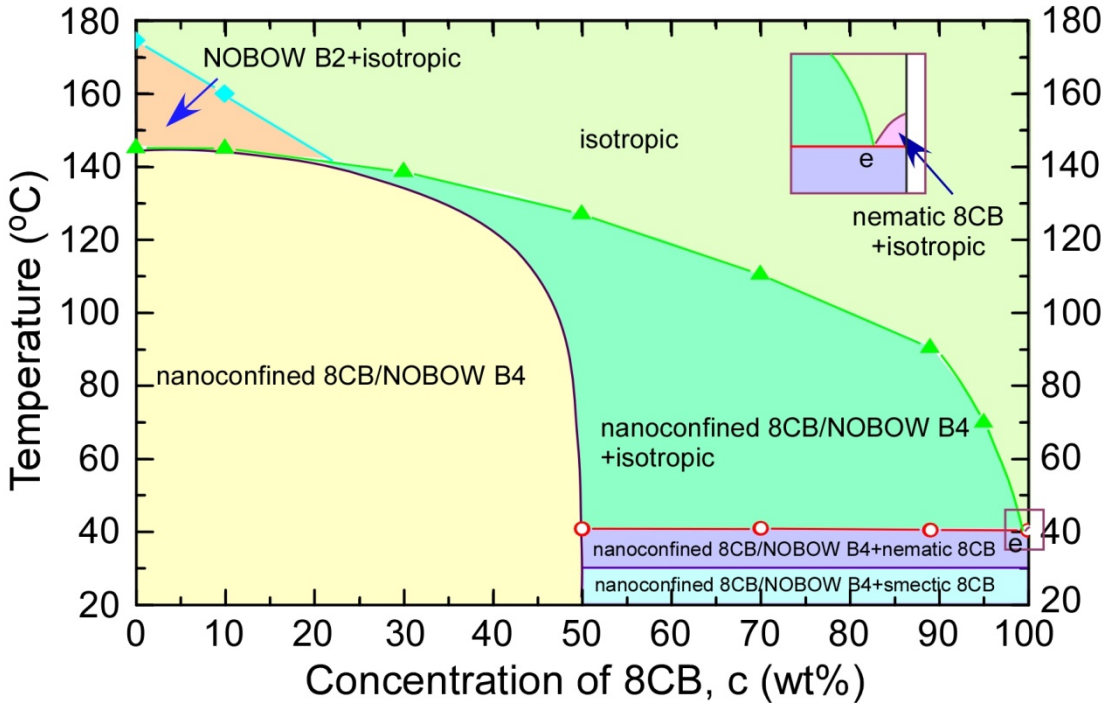

Figure 3.2.2: Simplified phase diagram of binary mixtures of NOBOW and 8CB. Mixtures of NOBOW with 8CB form a single, homogeneous phase only in the high temperature, isotropic range, while at lower temperatures the NOBOW B4 phase totally phase-separates from 8CB. When the 8CB concentration is low, the 8CB is nano-confined in the random network formed by NOBOW B4 helical nanofilaments, while at higher 8CB concentration there are also domains of bulk 8CB. For nanoconfined 8CB, as 8CB is microscopically, homogeneously mixed with the NOBOW B4 nanofilaments and this 8CB has lost its bulk features [15, 16], we show it as a single phase on the diagram ("nanoconfined 8CB/NOBOW B4"). The eutectic point e is very close to the pure 8CB Iso–N transition in the NOBOW/8CB mixtures, as shown in the inset.

The chirality of the mixtures was investigated by combining depolarized transmission light microscopy (DTLM), which reveals the macroscopic texture and optical activity, with freeze-fracture transmission electron microscopy (FFTEM), which shows the chirality of individual nanofilaments. For DTLM, 4 μm thick cells with rubbed polyimide alignment layers were filled with isotropic LC through capillary force. In pure NOBOW samples, the B4 phase comes in below the B2, and shows a uniform bluish color under crossed polarizers, with the texture resolved into left- and right-handed chiral domains when the polarizers are decrossed [12]. In mixtures with more than c=25% 8CB, measured in wt%, the B4 phase appears directly from the isotropic melt, at temperatures far above the clearing point of 8CB. When the B4 phase first appears, large homochiral domains of many millimeter across with random handedness grow out from distinct nuclei until they fill the available volume in the cell. For an 8CB/NOBOW mixture with c=50%, conventional optical activity is observed in the B4 phase. The sample is dark when viewed between crossed polarizers, because of its low birefringence, while uncrossing the polarizers by 5° reveals that each nucleation domain has a random but well defined handedness which is maintained as it grows. Eventually the cell is filled with distinct left- and right-handed chiral domains, distinguished by their opposite optical activity (Figures 3.2.3a and b). When the illumination is very strong, we can see using crossed polarizers that each region with uniform chirality comprises a single domain with a pattern of birefringence corresponding to a local optic axis pointing radially outward from the nucleation center (Figure 3.2.3c). This birefringence reflects anisotropy in the B4 filament organization as the phase grows out from the nucleation site. At high concentrations of NOBOW (for example, 1-c=50%), the B4 phase grows in as domains with smooth circular

boundaries, which eventually become parabolic when different domains meet. As the NOBOW concentration is decreased, the B4 phase growth morphology changes from circular to fractal domains. In mixtures with a low concentrations of NOBOW (for example, 1-c=11%), a fantastic dendritic texture is observed when the B4 phase nucleates and grows within the isotropic 8CB medium (Figure 3.2.3d), with the chirality of the phase revealed by its optical activity (Figures 3.2.3e and f). When the sample is subsequently cooled so the 8CB goes from isotropic to nematic, the 8CB in the vicinity of the NOBOW dendrites becomes aligned by the B4 filaments (Figure 3.2.3g), while further from the NOBOW domains the 8CB is planar-aligned by the glass surface. A sufficiently strong applied electric field causes the 8CB component to orient along the field direction, while the NOBOW shows no response (Figure 3.2.3h, bottom left). Figure 3.2.3i shows the optical texture, when 8CB changes from nematic to smectic. The layer normal tends to be parallel to the rubbing direction and yet is affected by the B4 helical nanofilaments presented. These optical observations all confirm that the chiral NOBOW domains grow from distinct nucleation sites and that the chirality is maintained as the domains grow.

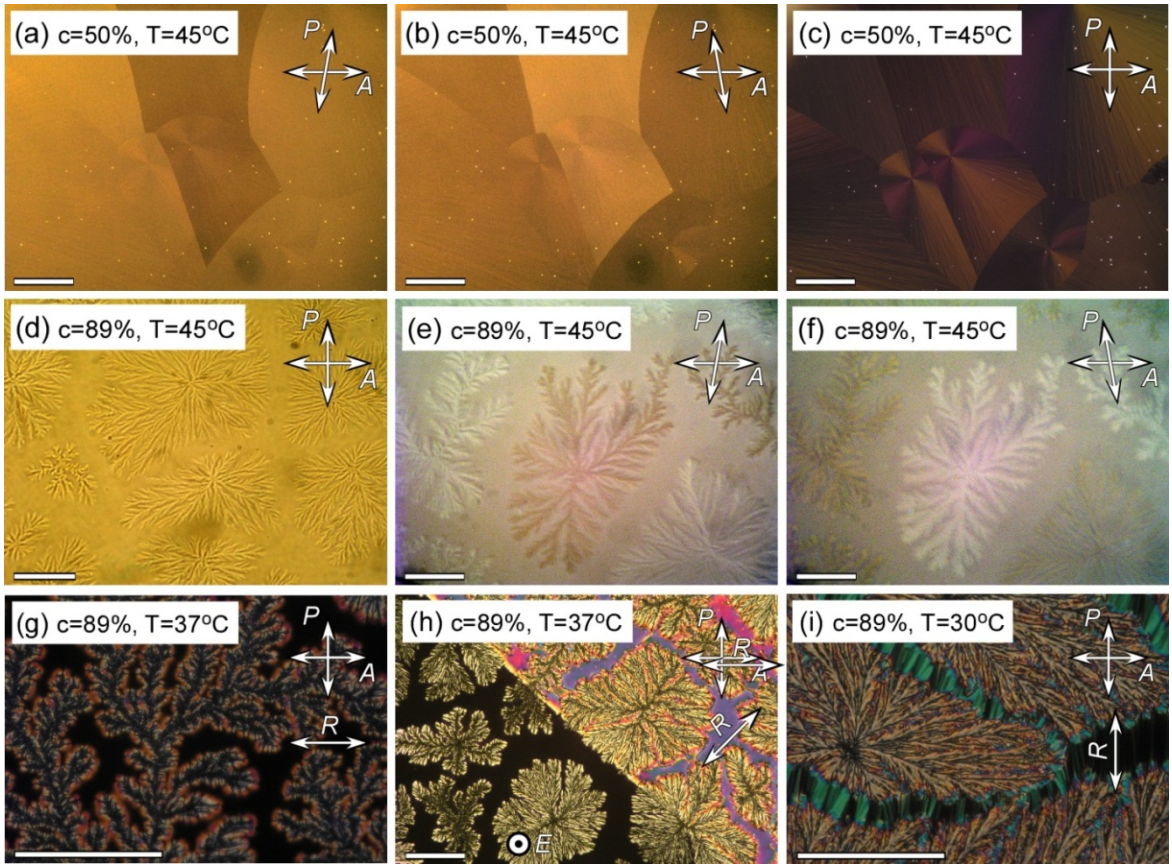

Figure 3.2.3: Depolarized transmission light microscopy (DTLM) images of 8CB/NOBOW mixtures in 4 μm thick planar-aligned cells. (a)-(c) show a c=50% 8CB/NOBOW mixture at 45°C, where the 8CB is isotropic and the NOBOW is in the B4 phase: (a), (b) Left- and right-handed chiral domains can be observed when the polarizers are decrossed. The sample is dark between crossed polarizer and analyzer, with negligible birefringence under regular illumination. (c) With much stronger illumination, we see that each chiral region comprises a single domain with radial local optic axis orientation. (d)-(i) show a c=89% 8CB/NOBOW mixture at different temperatures: (d) Dendritic domains of the B4 phase can be distinguished from the interspersed isotropic 8CB medium (T=45°C), due to an index mismatch at their interface. (e), (f) The dendritic domains are chiral, as evidenced by the opposite optical activity revealed with decrossed polarizers. (g) When 8CB transitions from isotropic to nematic (T=37°C), the 8CB is locally aligned by the NOBOW B4 dendrites, with the alignment extending about 2 μm from the B4 boundaries, giving them a thin magenta outline. The details of this alignment are still under investigation. Far from the NOBOW dendrites, 8CB is planar-aligned by the glass surface. (h) In an applied electric field of 10 V/μm (lower left half of the image), the 8CB aligns with the field, giving homeotropic orientation and optical extinction, while the dendritic B4 regions do not respond. (i) When 8CB changes from nematic to smectic, the layer normal tends to be parallel to the rubbing direction and yet is affected by the B4 helical nanofilaments presented. The scale bar is 100 μm in all images, and the double-headed arrow indicates the planar alignment direction. The contrast in (a), (b), (d), (e) and (f) was enhanced using Adobe Photoshop.

In the absence of preferred nucleation sites, B4 domains are expected to nucleate homogeneously. If we assume that each domain starts as a spherical cluster of radius r which liberates a latent heat $-G_v$ (energy/volume) during formation, but which must pay the cost γ (energy/area) of creating the surface interfacing with the surrounding isotropic material, then the change in free energy in forming such a cluster is $W=-4/3\pi r^3 G_v+4\pi r^2\gamma$. These bulk and interfacial energies are sketched in Figure 3.2.4a, where we see that below a critical radius $r_c=2\gamma/G_v$ it costs free energy to add molecules to the B4 cluster (green curve in Figure 3.2.4a). We expect the surface tension γ at the interface to depend on such properties of the B4 filaments as the smectic layer spacing d, the filament width w, and the helix pitch p. The smectic layer spacing in the B4 filaments is independent of the 8CB concentration [15], and the helix pitch and width, shown in Table 3.2.1, are also invariant. It therefore seems reasonable to assume that γ stays the same through the whole concentration range. However, the magnitude of the normalized latent heat of the I–B4 transition which is essentially equivalent to G_v, shown in Figure 3.2.4b, decreases significantly as the NOBOW concentration goes down. This implies that the critical radius for nucleation of the B4 phase increases as the NOBOW is progressively diluted. Since the Iso-B4 phase transition is above 100°C in the mixtures, NOBOW molecules undergo rapid diffusion in the isotropic phase and are able to reach the site of nucleation quickly enough to promote growth. In this scenario, the nucleation rate is limited by the average number of critical clusters, while the critical radius r_c is enhanced in the mixtures and only very few nuclei can reach the critical radius r_c, aided for example by thermal fluctuations or super cooling. Another factor which may also contribute to the formation of large chiral domains in the mixtures is that the increased

coexistence range of the Iso and B4 phases in the mixtures leads to a reduction in the effective cooling rate. In practice, it is much easier to get large homochiral domains in the mixtures than in pure NOBOW. An example of domain nucleation and growth is shown for a c=50% 8CB/NOBOW mixture in Figures 3.2.4c-e.

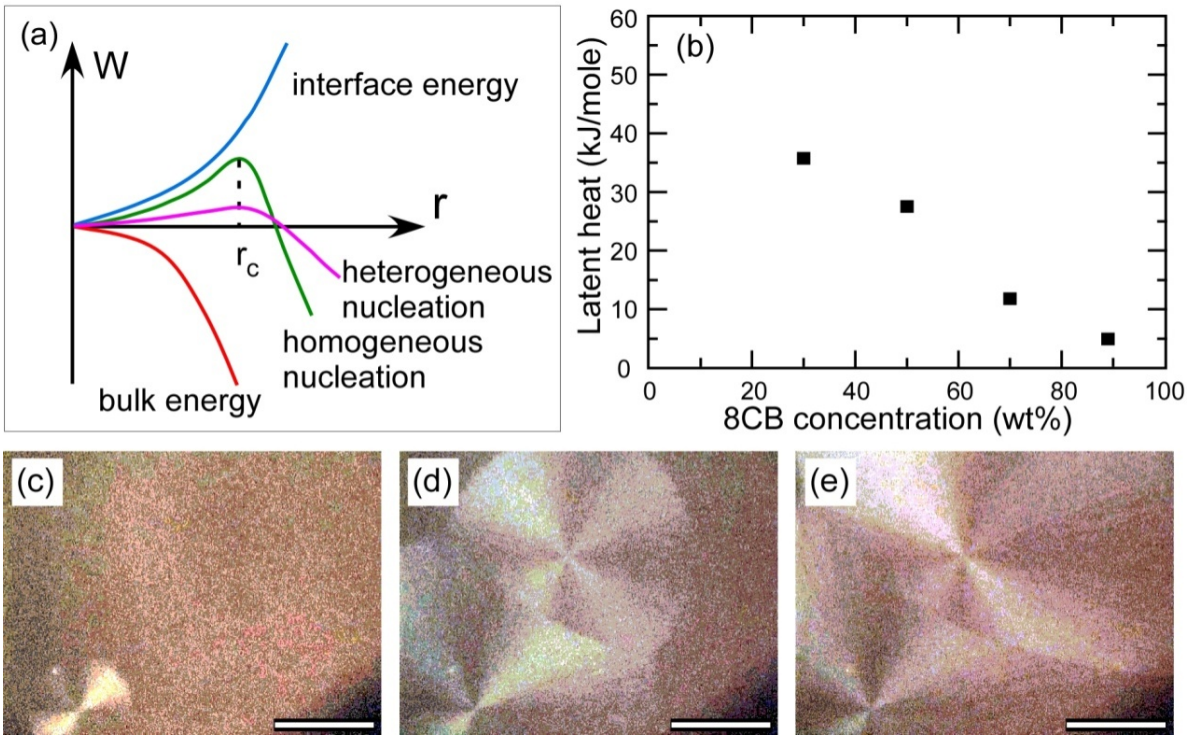

Figure 3.2.4: Energetics and real-time observation of chiral domain nucleation and growth of NOBOW B4 phase in 8CB/NOBOW mixtures. (a) The competition between the energy gained by creating a new volume of B4 ($-4/3\pi r^3 G_v$, red curve) and the cost of surface tension ($4\pi r^2 \gamma$, blue curve) results in a finite energy barrier to homogeneous nucleation (green curve) and a critical radius r_c. For heterogeneous nucleation, for example in the case of chiral doping, the critical radius r_c is the same as for homogeneous nucleation, but the energy barrier of domains with the same chirality as the dopant is reduced (magenta curve). (b) The normalized latent heat of the NOBOW Iso-B4 phase transition decreases as the concentration of NOBOW is reduced. (c), (d) and (e) DTLM images showing the nucleation and growth of B4 domains in a c=50% 8CB/NOBOW mixture in a 4 μm cell at 128°C at one second intervals. The scale bar is 100 μm in all images, and the growth velocity is around 0.1 μm/ms. The contrast has been enhanced using Adobe Photoshop.

The degeneracy of left- and right-handed chiral domains of a liquid crystal phase can be lifted in a variety of ways [8, 17, 18, 19, 20, 21, 22]. For example, an imbalance of chirality can be produced by an external chiral stimulus, such as weak chiral doping giving strong "sergeants-and-soldiers" enantio-selection of B4 chirality [8, 17], chiral surface treatments with polyimide layers possessing chiral side chains [18], growth from a twisted nematic [19] or chiral B2 phase [20], illumination with circularly polarized light [21], or using a nonchiral polymer network template to achieve a macroscopically chiral structure [22]. These effects can be understood in the general context of heterogeneous nucleation theory. For example, in the case of chiral doping, the critical radius for nucleation remains unchanged while the energy barrier that must be overcome for heterogeneous nucleation of domains of the same chirality as the dopant is greatly reduced, facilitating nucleation (magenta curve, Figure 3.2.4a).

Freeze-fracture transmission electron microscopy (FFTEM), which enables visualization of structure on nanometer length scales, reveals many details of the local layer organization in the B4 phase. Our observations of 8CB/NOBOW mixtures confirm that the B4 phase is made of individual helical filaments [12], and show unambiguously that these occur with both left- and right-handed twist, illustrated in Figures 3.2.5a and c. We propose that the handedness of the B4 helices determines the global chirality of the macroscopic, homochiral domains observed in DTLM such as those shown in Figure 3.2.3, with homochiral filaments organizing collectively into locally ordered arrays of coherent twist, extending over visible length scales to form macroscopic chiral domains. In many hundreds of B4 FFTEM images of a variety of samples, a consistent feature of the B4 filaments is that they are of the same

handedness over large areas. No mixing of left- and right-handed helical filaments has ever been observed, even in images covering many square microns. This is consistent with the optical observation that the B4 domains are large, homochiral, and have distinct boundaries, as seen in Figure 3.2.3. The twist sense of the helical filaments depends on the layer chirality of the tilted, polar bent-core molecules, sketched in Figures 3.2.5b and d. Because of the in-plane hexagonal ordering of the molecules [12], the molecular arms dilate along the tilt direction, with the top and bottom arms (modeled as elastic slabs in Figures 3.2.5b and d, top right) tilting in orthogonal directions. In order to relieve the stress induced by the mismatch of the top and bottom core arms of the banana molecules, saddle-splay curvature of the layers is adopted. When coupled with the polarization of the phase (the saddle-splay curvature itself is achiral), the structure is chiral and favors one sign of helical twist of the nanofilament, either left-handed (Figure 3.2.5b) or right-handed (Figure 3.2.5d). In other words, twist of the filaments (structural chirality) is a consequence of the local layer chirality resulting from the interplay of molecular polarization and tilt.

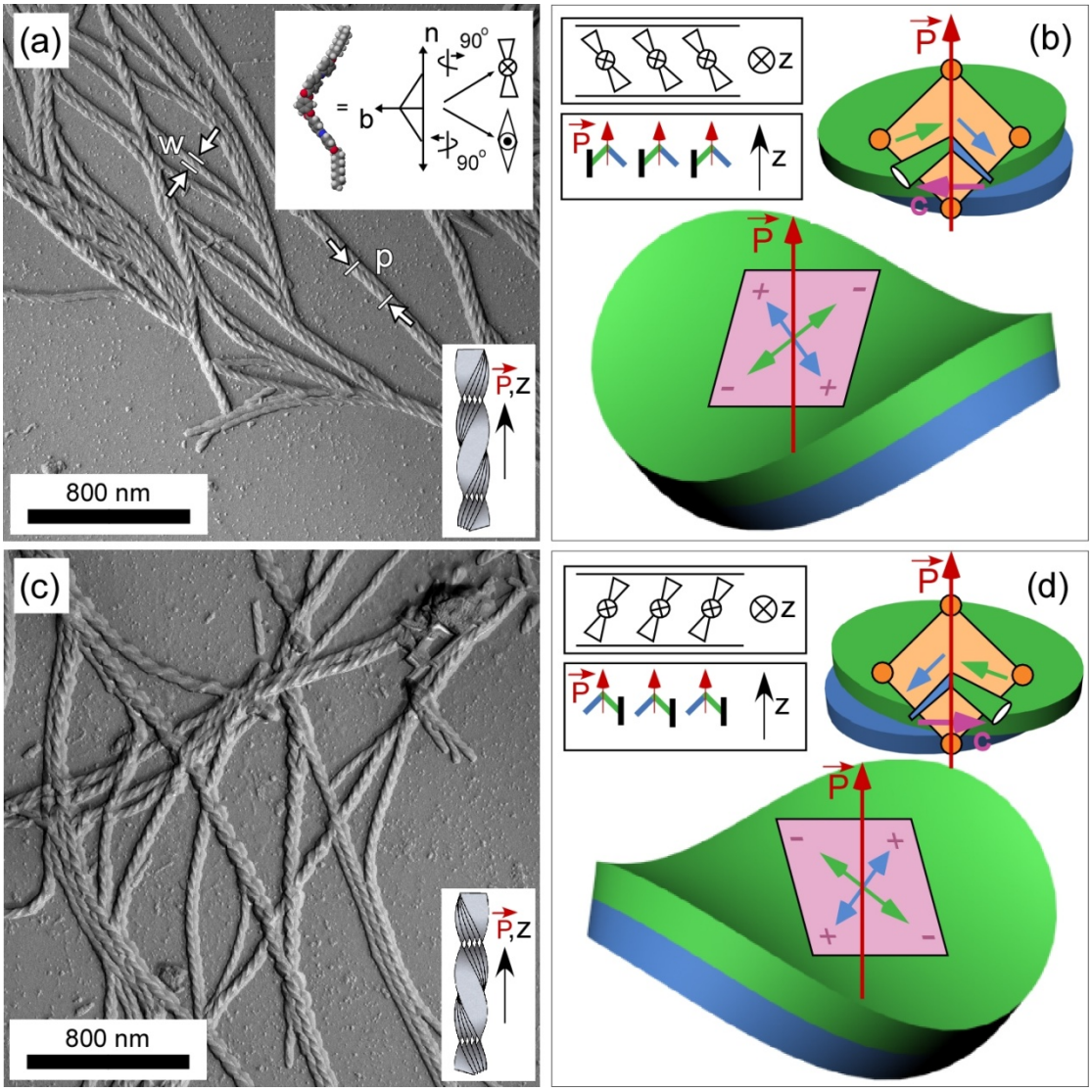

Figure 3.2.5 Left- and right-handed B4 filaments and their corresponding molecular organization. FFTEM images of a c=75% 8CB/NOBOW mixture quenched at 37°C reveal large homochiral regions with either (a) left- or (c) right-handed helices. Such images suggest that the macroscopic chiral domains of the B4 phase seen in the optical microscope comprise exclusively left- or right-handed helical filaments. The inset in (a) shows the convention for molecular director **n** and molecular bow direction **b** of bent-core molecules, with the polarization **P** along **b**. The handedness of the helices is determined by the corresponding layer chirality, as shown in (b) and (d). Each molecular arm can be viewed as being an elastically isotropic slab, which dilates along the molecular tilt direction and compresses perpendicular to the molecular tilt direction due to the hexagonal in-plane ordering [11, 12]. Because the tilt directions of the top and bottom molecular arms are orthogonal, the two elastic slabs adopt saddle-splay curvature to relieve the intra-layer mismatch. The local layer chirality, determined by the polarization and molecular tilt, results in distinct regions with orthogonal saddle-splay and opposite signs of filament twist. The filament width w and pitch p measured in different mixtures are shown in Table 3.2.1.

The unusual size of the homochiral domains, and our ability to make direct observations of domain growth in the mixtures, prompt us to speculate a mechanism of filament growth in which their handedness is preserved. If each filament nucleated and grew individually from the isotropic, random mixtures of left- and right-handed filaments would be expected. Since the filaments are all left- or right-handed over large areas, the nucleation and growth process is chirality-preserving, with the chirality of new filaments determined by filaments already present. We propose that the helicity in each domain is preserved through a growth process starting from a single nucleus, rather than forming each filament individually with a random handedness. In general, an isotropic NOBOW molecule can either attach to the ends of an existing B4 filament to make it longer, or attach to the side of the filament to make it wider, or form a new layer on the filament surface. However, x-ray reflections from the B4 smectic layers show diffuse peaks, indicating layer correlations over distances of only 40 nm, implying that the nanofilament thickness is limited to about eight smectic layers. Although the layers show only short-range order, they are robust, giving several harmonics in the x-ray reflection pattern [12]. Thus we first focus on growth that makes the filaments wider, arguing that the final filament width is determined by the elastic energy of the layers.

As we have mentioned previously, saddle-splay curvature is adopted in order to relieve the stress induced by the mismatch of the top and bottom core arms of the banana molecules [11, 12], which leads to a preferred value of saddle-splay curvature. For the NOBOW B4 helical nanofilament, when modeled as a collection of twisted, isotropic, elastic slabs (Figures 3.2.5b and d), the elastic energy density of a filament is given, to quadratic order of the principal curvatures σ' and σ'', by $f_E = K/2(\sigma' + \sigma'')^2 - \overline{K}(\sigma'\sigma'') + G(\sigma'' - \sigma')$, where

K and $\overline{K}$ are the Frank elastic constants for mean and Gaussian curvature respectively, and G drives curvature in response to the frustrated internal in-plane layer strain β [12]. In the model proposed by Matsumoto et al. [23], the n^{th} twisting layer surface of a helical B4 nanofilament is given by $x\sin(qz) \pm y\cos(qz) = nd$, where d is the layer spacing and p=2π/q the helix pitch. The $\pm$ sign gives left- or right-handed twist respectively. For a left-handed twisting central layer, the coordinates of any point on the layer are given by $\vec{r} = (s\cos(qz), -s\sin(qz), z)$, where s is the displacement from the helix axis, shown in Figure 3.2.6a. Following Kamien's procedure for determining the curvature [24], the principal curvatures as a function of s are $\sigma=\sigma'=-\sigma''=q/(1+q^2s^2)$, where p=2π/q is the helix pitch and s is the displacement from the helix axis. For a minimal surface such as the B4 helical filament, the elastic energy cost is given by $f_E^m = \overline{K}(\sigma - \sigma_o)^2$, where $\sigma_o = 1/R_p = G/\overline{K}$ gives the preferred curvature [12]. However, in a thermotropic smectic, where the layers are constrained to have constant spacing, the preferred saddle-splay arrangement cannot be maintained over long distances. Therefore as previously calculated, the principal curvature σ of the central layer of the filament varies as a function of s, as $\sigma=q/(1+q^2s^2)$, where p=2π/q is the helix pitch and s is the displacement from the helix axis. Figure 3.2.6b shows how the curvature decreases towards the outside of a helical filament with preferred curvature $\sigma=\sigma_o$ at s=0. As the sample is cooled into the B4 range, the ribbon can lower its free energy by gaining Gibbs energy G_v, releasing latent heat. The energy density gained during growth obtained by considering the cost of elastic energy and the gain of Gibbs energy, can be expressed as $f = f_E^m - G_v$, so that the energy gained per unit length of a filament central layer of width w and thickness d becomes

$$F = \int_V (f_E^m - G_v)\, dV = d\int_A (f_E^m - G_v) dA = d\int_{-w/2}^{w/2}\int_0^1 (f_E^m - G_v)\sqrt{1+s^2q^2}\, ds dz$$

$$= d\int_{-w/2}^{w/2} (f_E^m - G_v)\sqrt{1+s^2q^2}\, ds = d\int_{-w/2}^{w/2} (\overline{K}(\sigma-\sigma_o)^2 - G_v)\sqrt{1+s^2q^2}\, ds$$

$$= d\int_{-w/2}^{w/2} \left(\overline{K}\left(\frac{q}{1+q^2s^2} - \sigma_o\right)^2 - G_v\right)\sqrt{1+s^2q^2}\, ds$$

$$= d\overline{K}\int_{-w/2}^{w/2} \left[\left(\frac{q}{1+q^2s^2} - \sigma_o\right)^2 - \frac{G_v}{\overline{K}}\right]\sqrt{1+s^2q^2}\, ds \qquad \text{(Eq. 3.2.1)}$$

where the principal curvature as a function of s is $\sigma = q/(1+q^2s^2)$ and the integration element can be expressed as $dA = \sqrt{1+s^2q^2}\, ds dz$. Here, we have neglected the surface tension term ($\propto r^2$) as it is small compared to the bulk terms ($\propto r^3$) in the growth process. This normalized linear energy density is plotted as a function of scaled filament pitch and width in Figure 3.2.6c. Analytical minimization using Mathematica yields $w_{max}/R_p \approx 1.4$ and $p/R_p \approx 5.6$ when $G_v R_p^2/\overline{K} = 0.1$. For p=217 nm, a typical helix pitch observed in the FFTEM images, we predict a preferred maximum filament width w_{max}=54 nm, which is similar to what is observed experimentally (confirming that $G_v R_p^2/\overline{K} = 0.1$ is a good estimate of the dimensionless constant, which will be used again in the energy density argument below). In our model, the high elastic energy cost makes the growth of filaments beyond w_{max} unfavorable. We propose that for this reason, filaments eventually split, lowering the overall elastic energy while continuing to gain Gibbs energy as more material is added to the filaments. Examples of such filament bifurcation are shown in the FFTEM images of Figures 3.2.6d and e, with a cross-section of the bifurcating filament sketched in Figure 3.2.6f. The layer chirality is preserved as the filament grows wider. When the filament branches into two filaments, the two new filaments twist in phase with each other. Further examples of

branching are shown in Figures 3.2.6g and h, while Figure 3.2.6i depicts an array of collectively organized filaments in this filament growth scenario.

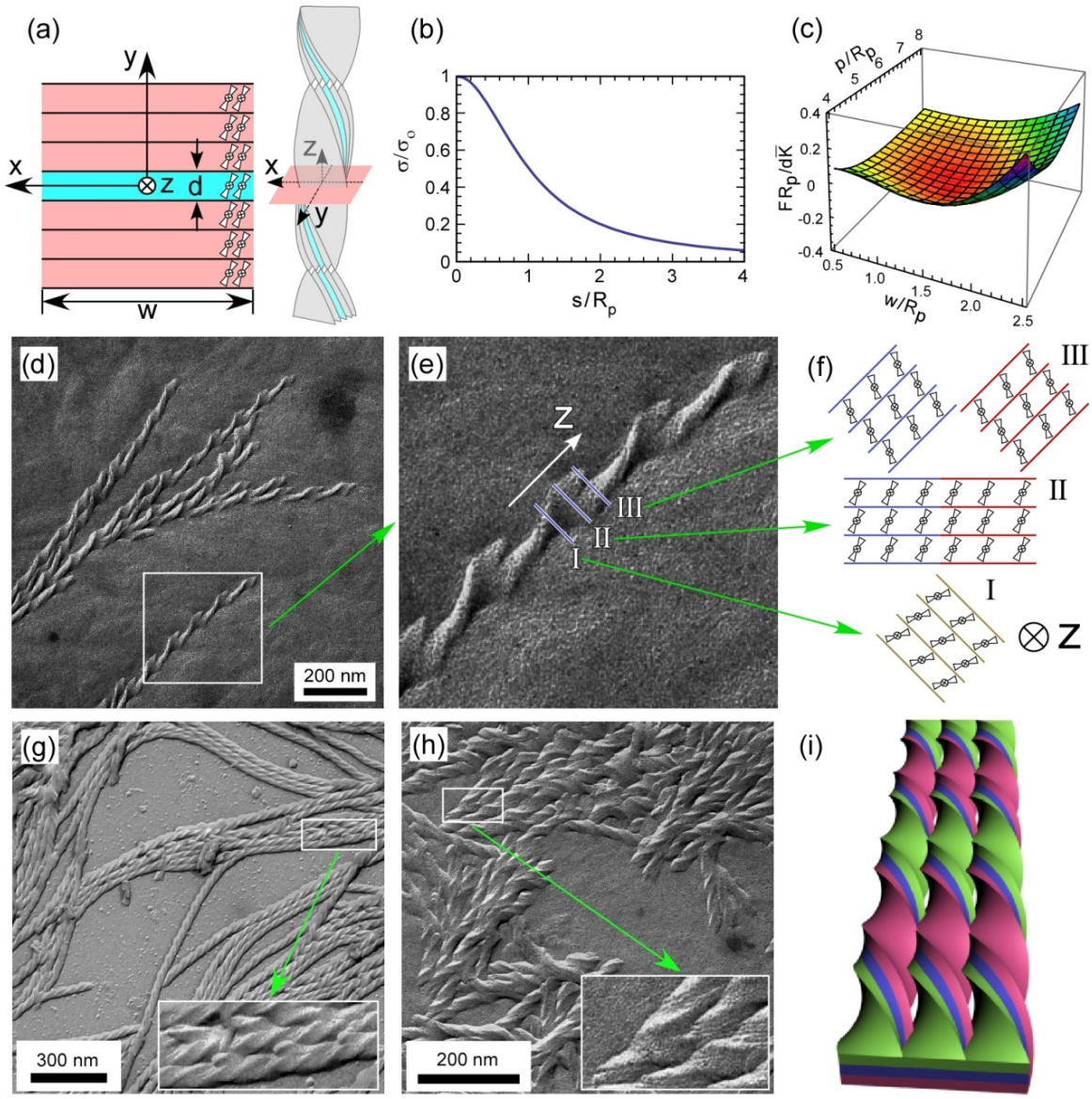

Figure 3.2.6: Chirality-preserving growth of helical B4 filaments. (a) Cross section (pink plane) of a helical filament, showing the filament width along x, thickness along y, and length along z. The molecules are tilted, with the polarization oriented along z, the helix axis. d is the smectic layer spacing. (b) Normalized principal curvature of the central layer of the filament (shaded blue in (a)) as a function of normalized distances from the helix axis assuming the preferred curvature $\sigma=\sigma_o$ at s=0. Away from the helix axis, the layers deviate from the ideal shape, at the cost of higher elastic energy. (c) Normalized energy gained per unit length of filament central layer as a function of scaled width and pitch given by Eq. 3.2.1. Minimization of the energy assuming $G_v R_p^2/\overline{K} = 0.1$ gives a filament thickness $w_{max}/R_p \approx 1.43$

and pitch $p/R_p \approx 5.57$. Above the critical filament width w_{max} in this model, the reduction of the Gibbs energy achieved by growing wider can not compensate for the associated increase in the elastic energy. (d) FFTEM image showing chirality-preserving dendritic growth of helical filaments. New filaments branch from the center of an existing one to form a pair of filaments with the same twist. The region in the white box is enlarged in (e) to show helix branching more clearly. (f) Cross-sections of the helical filament near the branching area as marked in (e). Since the molecular organization is preserved during widening, both the chirality and the twist of the branched filaments are the same as the original one, and neighboring helices are naturally phase coherent. (g) FFTEM image of a c=75% 8CB/NOBOW mixture, showing the remanents of neighboring filaments above, most of which have been removed by fracture (magnified in the inset). (h) FFTEM image of pure NOBOW showing filament branching. The inset shows the layer edges and surfaces in a branching region. (i) Model of a bundle of homochiral, phase-coherent, helical B4 nanofilaments.

The preceding analysis is based on minimizing the total free energy per unit length of the central layer of the filament, which yields a finite filament width w. We now extend these arguments by considering the kinetics of filament growth, showing that local variations in the elastic energy determine the growth velocity profile of the filament tip and lead to spontaneous bifurcation. As discussed above, the energy density gained during filament growth is given by

$$f = f_E^m - G_v = \bar{K}(\sigma - \sigma_o)^2 - G_v = \bar{K}\left(\frac{q}{1+q^2s^2} - \sigma_o\right)^2 - G_v$$

$$= \bar{K}\sigma_o^2\left[\left(\frac{q/\sigma_o}{1+q^2s^2} - 1\right)^2 - \frac{G_v}{\bar{K}\sigma_o^2}\right]$$

$$= \bar{K}\sigma_o^2\left[\left(\frac{q/\sigma_o}{1+(q/\sigma_o)^2(s/R_p)^2} - 1\right)^2 - \frac{G_v R_p^2}{\bar{K}}\right] \qquad \text{(Eq. 3.2.2)}$$

where the principal curvature as a function of s is $\sigma = q/(1+q^2s^2)$ and the preferred curvature can be expressed as $\sigma_o = 1/R_P = G/\bar{K}$. Figure 3.2.7a shows the normalized energy density as a function of normalized distance from the helix axis for three different helix pitches and the corresponding preferred, final filament radii, assuming $G_v R_p^2/\bar{K} = 0.1$. In all cases, $f<0$ for small s/R_p, favoring growth when the filaments are thin, and $f>0$ for large s/R_p, where the

elastic energy cost is larger than the Gibbs energy gained, and the growth terminates, which gives the final radius of the filament. The final filament radius (r_1, r_2, r_3) increases with q, indicating that the filaments twisted more tightly can gain more free energy by increasing their width. Since the growth velocity normal to the Iso/B4 interface, $v_n(s)$, is linearly proportional to the energy density gained (the energetic driving force) and is thus a function of the radial displacement s: $v_n=0$ when $f>0$ and when $f<0$, the velocity profile is of the form

$$v_n(s/R_p) \propto |f_E^m - G_v| = 0.1 - \left(\frac{q/\sigma_o}{1+(q/\sigma_o)^2(s/R_p)^2} - 1\right)^2 \text{ μm/ms.} \qquad \text{(Eq. 3.2.3)}$$

We have chosen the constant of proportionality (not shown) to be 1 μm/ms to match typical experimental velocities, which are around 0.1 μm/ms. Figure 3.2.7b shows the velocity profiles for $q=\sigma_o$ and $q=1.2\sigma_o$. In order to illustrate how the velocity field leads to bifurcation of the filament tip, we have computed the advance of the tip in time using $z(t+\Delta t)=(v_n/\cos\theta)*\Delta t+z(t)$, where θ is the inclination of the filament tip (Figure 3.2.7c), starting from a plane front. When $q=\sigma_o$, the steady state tip is parabolic in shape and the tip has a constant growth velocity $v_n(s/R_p=0)$ (magenta curves in Figure 3.2.7c). When $q>\sigma_o$, the growth velocity along z at the two sides ("shoulders") of the filament v_s is much larger than that at the filament center line v_c (see Figures 3.2.7b and c), and the two sides of the filament grow much faster than the center, eventually causing the tip to bifurcate (blue curves in Figure 3.2.7c). This result is consistent with experimental observations that the tip front is parabolic and the filaments always bifurcate symmetrically about the center. In this scenario, heterogeneous nucleation and directional growth of helical filaments at the edge of a cell (Figure 3.2.7d), giving macroscopically aligned helical nanofilaments, is one of the easiest way of obtaining aligned helical nanofilaments.

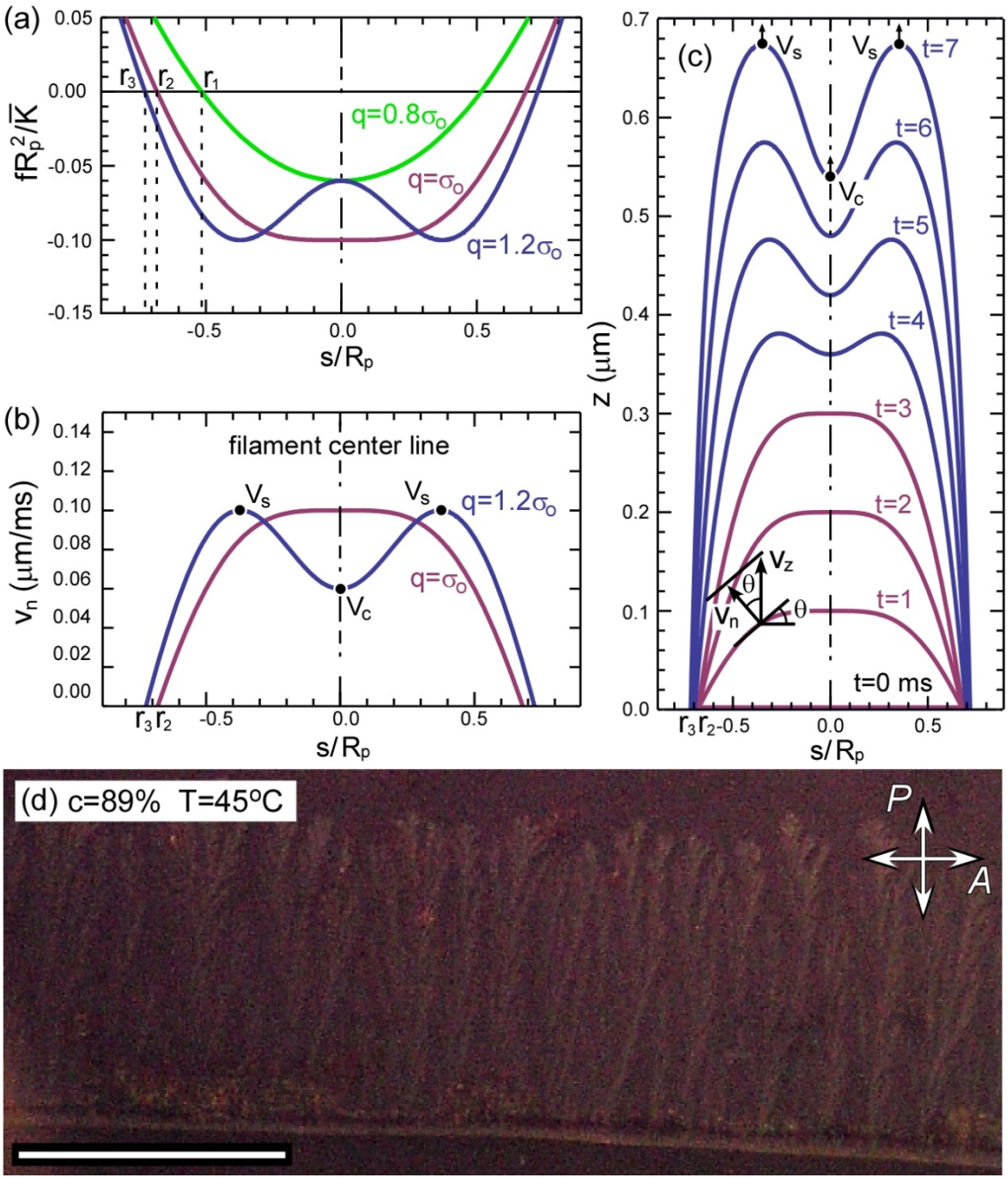

Figure 3.2.7: Kinetic analysis of filament tip growth. (a) Normalized energy density gained during growth as a function of normalized distance from the helical axis for different q, shown in the plot. When the helical twist pitch ($p=2\pi/q$) is large, growth occurs fastest along the helix axis (s=0). Below a critical twist pitch $p=2\pi/q<2\pi/\sigma_o$, however, more energy is released per volume by growth of the off-axis "shoulders" of the filament tips and these regions therefore grow faster. The corresponding final filament radii r are indicated at left. (b) Velocity profile v_n as a function of normalized distance from the helix axis for $q=\sigma_o$ and $q=1.2\sigma_o$. (c) Analytic simulation of filament tip growth, starting from a planar growth front, first using the velocity profile assuming $q=\sigma_o$ (magenta curves), and then the profile for $q=1.2\sigma_o$ (blue curves), which leads to tip bifurcation. (d) Heterogeneous nucleation and directional growth of helical filaments at the edge of a cell (bottom of image), giving macroscopically aligned helical nanofilaments. The scale bar is 50 μm.

From the above discussion, we know that NOBOW B4 helical nanofilaments in the mixtures are quite robust, expelling 8CB and forming nanofilaments identical to those seen in pure NOBOW, which means that in the NOBOW/8CB system, the NOBOW B4 phase is totally phase-separated from the 8CB on the molecular scale. On the other hand, through the bifurcation of growing filaments, the B4 phase forms a random network of homochiral filaments. At low concentration of 8CB (below c=50%), 8CB is microscopically (tens of nm in scale), homogeneously mixed with this random network [15] and no bulk 8CB is observed in this regime. Such phase segregation on the molecular scale combined with mixing on the microscopic scale makes the system ideal for a wide variety of novel materials. For example, the chiral boundary condition presented by the B4 helical nanofilaments enables nematic 5CB (achiral rod-like molecule) to fill space with a chiral director field, which strongly enhances the non-linear optical rotation [14].

The B4 phase is one of the most complex hierarchical self-assemblies known in soft materials. We have directly observed and characterized chirality-preserving growth of the B4 helical nanofilaments in NOBOW/8CB mixtures. The alignment of bent-core liquid crystal phases in general has been a challenging and interesting topic, and understanding the nucleation and growth behavior of the helical nanofilaments in the B4 phase suggests novel ways of achieving macroscopic alignment of those nanofilaments. As shown in Figures 3.2.8a and b, the B4 phase shows a strong birefringence under DTLM when the sample is sheared in the B2 phase [25]. FFTEM images (Figures 3.2.8c and d) show unambiguously the macroscopically aligned nanofilaments, which accounts for the anisotropic optical index observed under DTLM. The helical nanofilaments can also be aligned effectively over large

areas along one global direction by heterogeneous nucleation, for example using directional growth at the edge of a cell, as shown in Figure 3.2.7d.

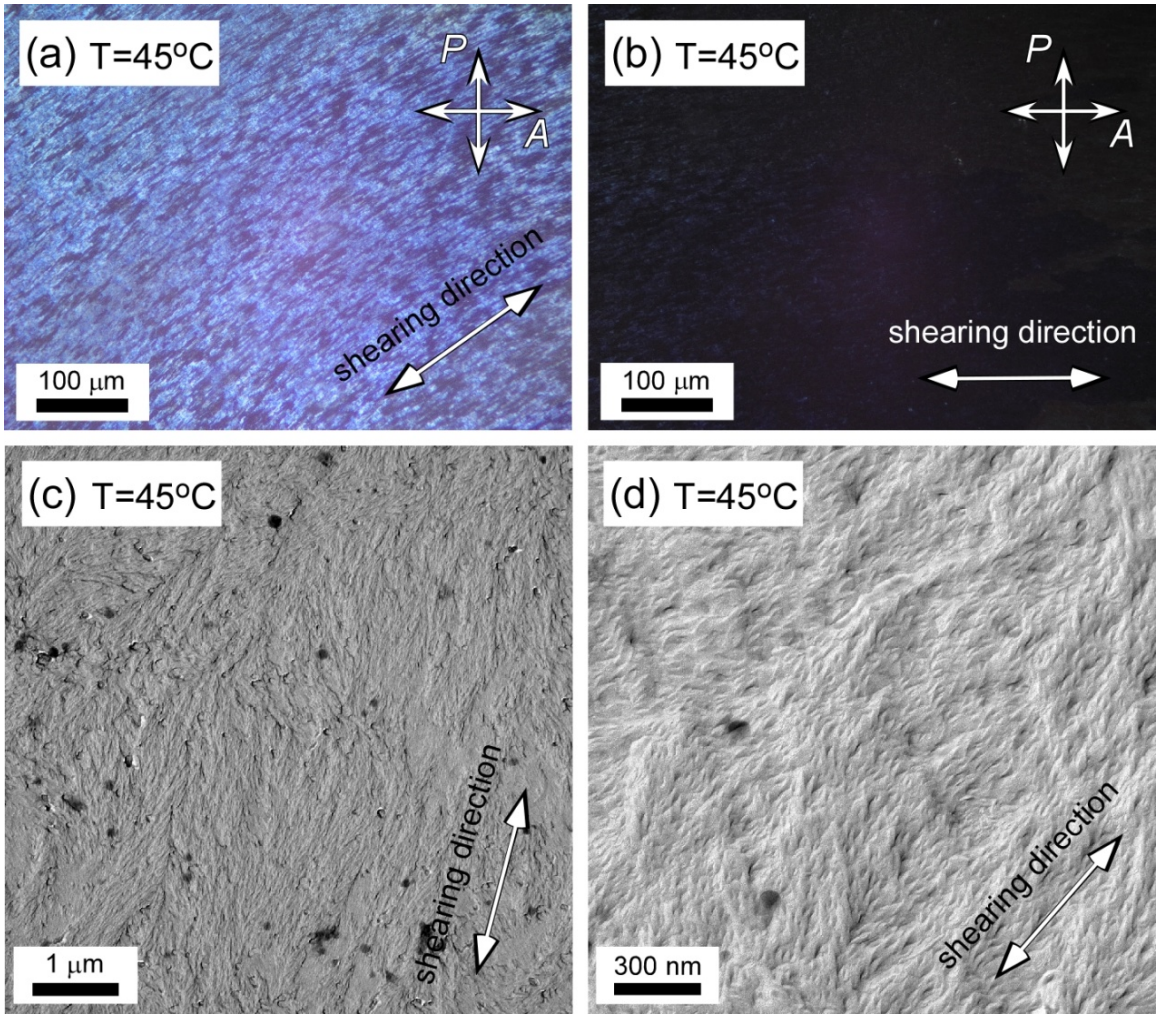

Figure 3.2.8: DTLM and FFTEM images showing macroscopically aligned B4 helical filaments of pure NOBOW sheared in the B2 phase at T=165°C before cooling to the B4 phase. (a) The sheared B4 phase shows a strong birefringence when the shearing direction is at 45° to the polarizer, and extinguish (b) when the shearing direction is along the analyzer. (c), (d) FFTEM images showing the macroscopic alignment of helical nanofilaments along the shearing direction at low and high magnification respectively.

In a summary, freeze-fracture transmission electron microscope images confirm that the B4 helical filaments of NOBOW observed in mixtures with 8CB, a calamitic mesogen which is not soluble in the B4 phase, are structurally identical to those seen in pure NOBOW. Adding 8CB results in the formation of large homochiral domains, allowing the nucleation and growth of individual B4 chiral domains to be characterized. The constraint of constant smectic layer spacing in the B4 banana phase prevents the establishment of globally uniform saddle-splay curvature in the twisted filaments, with the local curvature of the smectic layers deviating from the preferred value as you move away from the helix axis. In order to lower the Gibbs free energy by continued growth without accumulating excess elastic energy, filaments that reach a certain width exhibit spontaneous branching. As each filament has specific layer chirality, an existing filament and all of its branches are naturally homochiral with the layers of adjacent filaments twisting in phase. This kind of spontaneous nanoscale self-assembly of the B4 helical nanofilaments offers the possibility for a wide variety of novel materials.

3.3 Pre-transitional orientational ordering of a calamitic liquid crystal by helical nanofilaments of a bent-core mesogen: Surface interaction and large surface effect.

Mixtures of liquid crystals (LCs) sometimes yield new phases and may show phase sequences not present in any of the individual components [26]. In many cases, desirable liquid crystalline properties and phases with broad temperature ranges can be obtained more easily by mixing compounds of different shapes and properties than by performing systematic variations in the synthesis of pure compounds.

Mixtures of bent-core and calamitic (rod-shaped) mesogens are particularly interesting systems for exploring the role of molecular shape in determining liquid crystal ordering. Transitions between the B2 banana phase and mesophases more typically found in calamitic compounds, e.g. the phase sequence SmA-SmC-B2, have been reported in pure bent-core mesogens [27]. The experiments indicate that an essential condition for such phase sequences is a change of the molecular conformation as a function of temperature. Studies of the binary mixtures of bent-core and calamitic mesogens have led to the observation of the phase sequences SmA-B2, SmC-B2, and N-SmA-SmC-B2 [28]. The calamitic/bent-core binary system reported by Pratibha et al. [29, 30] shows an orientational transition of bent-core molecules, which, at low concentration (3 to 4 mol%), order within the smectic layers of the rod-like molecules with the director orthogonal to the layer normal and display a biaxial smectic A_2 (SmA_{2b}) phase. Rod-like chiral dopants have also been used to control the proportion of left- and right-handed chiral domains in thin cells of achiral bent-core compounds [31].

In the 3.2 section of this chapter, we have characterized the chirality preserving-growth of the helical nanofilaments in the 8CB/NOBOW mixtures. In this section, we will probe in detail the interaction of the helical nanofilaments of the NOBOW B4 phase with 8CB molecules. We find that there is substantial pre-alignment of the 8CB by the B4 helical nanofilaments far above the 8CB bulk isotropic-nematic transition temperature, which we believe must be due to a thin film of 8CB adsorbed to the nanofilament surface. DSC and NMR experiments provide clear evidence for the existence of an adsorbed 8CB film on the nanofilament surfaces above the 8CB Iso-N transition, as we shall discuss below.

8CB/NOBOW mixtures of concentration c, where c is the wt% of 8CB in the mixture, were prepared in the range $0\% < c < 100\%$. The differential scanning calorimetry (DSC) data shows an additional peak at $T \approx 83°C$ (Figure 3.3.1a), more than 40°C above the clearing point of pure 8CB, which appears neither in pure NOBOW nor in pure 8CB. At the same time, the normalized latent heat of the bulk 8CB Iso-N transition at $T \approx 40°C$ in the mixtures (black triangles in Figure 3.3.1b) is substantially reduced compared with that of pure 8CB. This strongly indicates that some fraction of 8CB is pre-aligned by the NOBOW B4 helical nanofilaments, inducing orientational ordering of 8CB at elevated temperature. Indeed, in mixtures which are almost 8CB, with few B4 nanofilaments available to pre-align the 8CB, the normalized latent heat of the bulk 8CB Iso-N transition approaches the bulk value, while the contribution from pre-aligned 8CB becomes very small (Figure 3.3.1b). The pre-alignment transition of the 8CB is not noticeable in the depolarized transmitted light microscope, presumably because any additional birefringence from pre-transitional orientational ordering of the 8CB is averaged out by the global orientational disorder of the

B4 nanofilaments. However, nuclear magnetic resonance (NMR) provides a sensitive alternative probe of the local orientational ordering of the 8CB molecules.

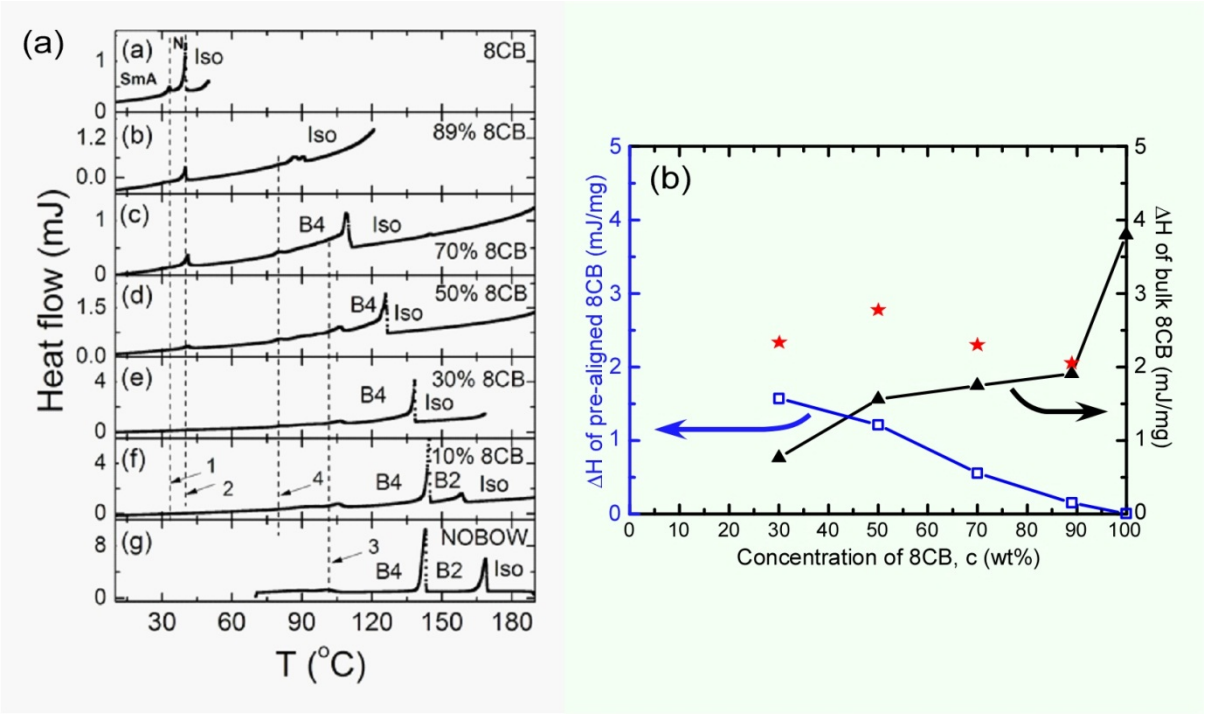

Figure 3.3.1: DSC scans and pre-alignment of 8CB indicated by the DSC scans. (a) DSC scans of 8CB/NOBOW mixtures (c=10%, 30%, 50%, 70% and 89%), pure 8CB, and pure NOBOW obtained on cooling [15]. Dashed lines 1, 2, and 3 mark the pure 8CB N-SmA transition, the pure 8CB Iso-N transition, and the pure NOBOW B4 glass transition, respectively. Dashed line 4 marks the pre-alignment of 8CB by NOBOW B4 helical nanofilament in the mixture. As the 8CB concentration increases, the transition temperature of NOBOW Iso-B2 transition and Iso-B4 transition decreases due to freezing point depression. The 8CB nematic range is observed to broaden slightly as the NOBOW concentration increases. (c) Normalized latent heat of the 8CB bulk Iso-N transition (T≈40°C, black triangles) and that of 8CB pre-aligning around the B4 filament surfaces (T≈83°C, blue squares) in a series of 8CB/NOBOW mixtures. The latent heat of the surface-pre-aligned 8CB increases as the concentration of B4 filaments increases, with a corresponding decline for that of the bulk 8CB Iso-N transition. The red stars show the sum of the 8CB bulk Iso-N transition and pre-aligned latent heats in the mixtures.

Solid-state NMR spectra were acquired using a Varian Inova 400 spectrometer equipped with an extended variable-temperature 4 mm cross-polarization, magic-angle-spinning (CPMAS) probe, operating at 100.63 MHz for ^{13}C observation. CPMAS spectra were acquired using a 90º pulse of 3.4 μs, a typical MAS spinning frequency of 11 kHz, with a Hartmann-Hahn spin locking field of 71.5 kHz for both ^{1}H and ^{13}C. Typical cross-polarization contact times were 4.0 ms, and TPPD ^{1}H decoupling was applied during acquisition. Single-pulse ^{13}C MAS NMR was done using a 3.5 μs 90º excitation pulse. The relaxation delay was 3.0 s for all experiments. Actual sample temperatures were calibrated using the ^{207}Pb chemical shift of lead nitrate, as described in [32]. Using careful matching of air-flows and spinning-speeds with the calibration standard, we were able to achieve reproducible sample temperatures of ±2ºC.

In CPMAS NMR, the observed ^{13}C NMR signal arises via the heteronuclear, first-order dipole-dipole coupling between the ^{1}H nuclei and the ^{13}C nuclei. In a rapidly-tumbling, isotropic environment, this interaction is zero, and the cross-polarization (CP) mechanism vanishes. Therefore, the observation of a ^{13}C NMR signal via CP indicates that the molecule is either tumbling slowly on the NMR/dipolar-coupling timescale (~10–100 kHz), or that the molecular motion is anisotropic in nature. In addition, in CPMAS experiments, only the proton nuclei need to relax between transient acquisition, and in condensed phases, ^{1}H spin-lattice relaxation time-constants (T_1) are generally significantly smaller than ^{13}C, often by one or more orders of magnitude. In a single-pulse, magic-angle-spinning (MAS) spectrum, all of the net ^{13}C magnetization present in the sample is excited by the pulse; however, in rigid solids, the T_1 relaxation time is so long that no signal is observed under signal averaging

unless very long relaxation delay times are used. In this work, when performing single-pulse MAS NMR, only highly mobile molecules having solution-like T_1 relaxation behavior are observed with significant intensity.

To illustrate this, in the c=75% 8CB/NOBOW mixture observed with the sample at T≈80°C, above the Iso-N transition temperature of pure 8CB but still well below the clearing point of NOBOW, the single pulse spectrum (Figure 3.3.2a) is predominantly from 8CB, both bulk and pre-aligned, except at small chemical shift where there is some signal from the NOBOW tails, which are more mobile than the cores. Using this isotropic liquid-phase ^{13}C data, it is possible to assign nearly all of the resonances of the 8CB molecule, assisted by the predicted ^{13}C NMR shifts using the ACD/Labs NMR software (version 12.0). Fortuitously, in the NMR spectrum, the two strongest 8CB peaks (around 29 and 126 ppm, marked by red stars in Figure 3.3.2) do not significantly overlap with the NOBOW spectrum, and can easily be distinguished in the CPMAS NMR spectrum in Figure 3.3.2b. When subtracting an appropriately scaled single pulse NMR signal (Figure 3.3.2a) from the CPMAS NMR signal (Figure 3.3.2b), we obtain the CPMAS NMR spectrum of pure NOBOW (Figure 3.3.2c), which is consistent with that reported in [32].

We recorded a series of CPMAS NMR spectra while cooling the c=30% 8CB/NOBOW mixture, shown in Figure 3.3.3. As expected, at high temperature all of the 8CB is isotropic and the spectrum is purely from the NOBOW B4 phase (Figure 3.3.3a). At slightly lower temperature, the two strongest 8CB peaks appear (Figure 3.3.3b, marked by red stars), indicating that there is anisotropic 8CB which is orientationally ordered far above the Iso–N

transition of bulk 8CB. On further cooling, the 8CB peaks persist all the way down to room temperature (Figures 3.3.3c-f). To analyze the 8CB peak intensity quantitatively as a function of temperature, we first normalize each scan by setting the integrated intensity of the two peaks around 68 ppm to a value of 100, for they are due only to NOBOW and are independent of 8CB below the NOBOW clearing point. As shown in Figures 3.3.3g and h, 8CB signals appear at T≈93°C, a temperature that is slightly higher than that obtained by DSC, indicating the onset of orientational ordering of 8CB around the nanofilament surfaces. On further cooling, the 8CB signal strength increases steadily, indicating that the orientational ordering of 8CB is progressively enhanced. When the sample is cooled through the bulk 8CB Iso–N transition (blue dashed line in Figures 3.3.3g and h), there is a large increase of the 8CB signal as the remaining 8CB becomes nematic.

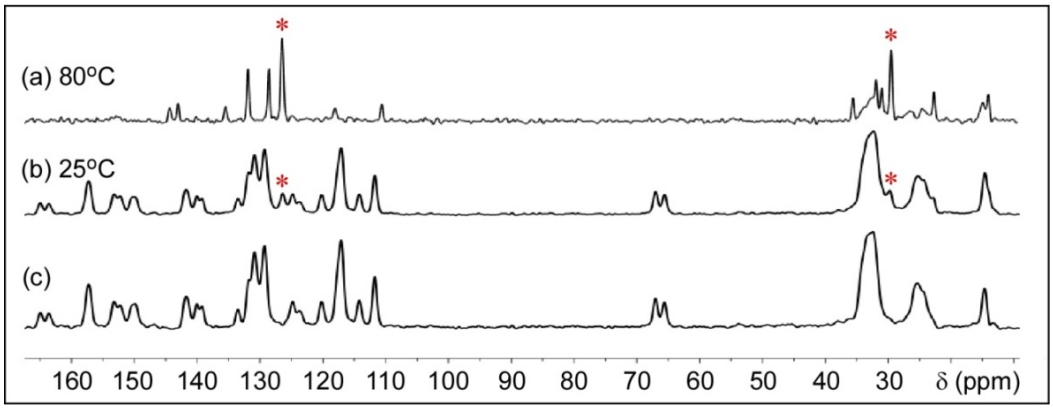

Figure 3.3.2: Single pulse and CPMAS NMR spectra of a c=30% 8CB/NOBOW mixture. (a) The single pulse NMR spectrum taken at T≈80°C is dominated by the 8CB signal. At low chemical shift there is some signal from the tails of NOBOW, which are more mobile than their cores. (b) The CPMAS NMR spectrum at T≈25°C shows both NOBOW and 8CB peaks. Fortuitously, the two strongest peaks from 8CB do not overlap significantly with the NOBOW spectrum (marked with red stars). (c) The NOBOW spectrum obtained by subtracting the scaled single pulse signal (a) from the CPMAS signal (b) agrees well with the spectrum of pure NOBOW reported previously [32].

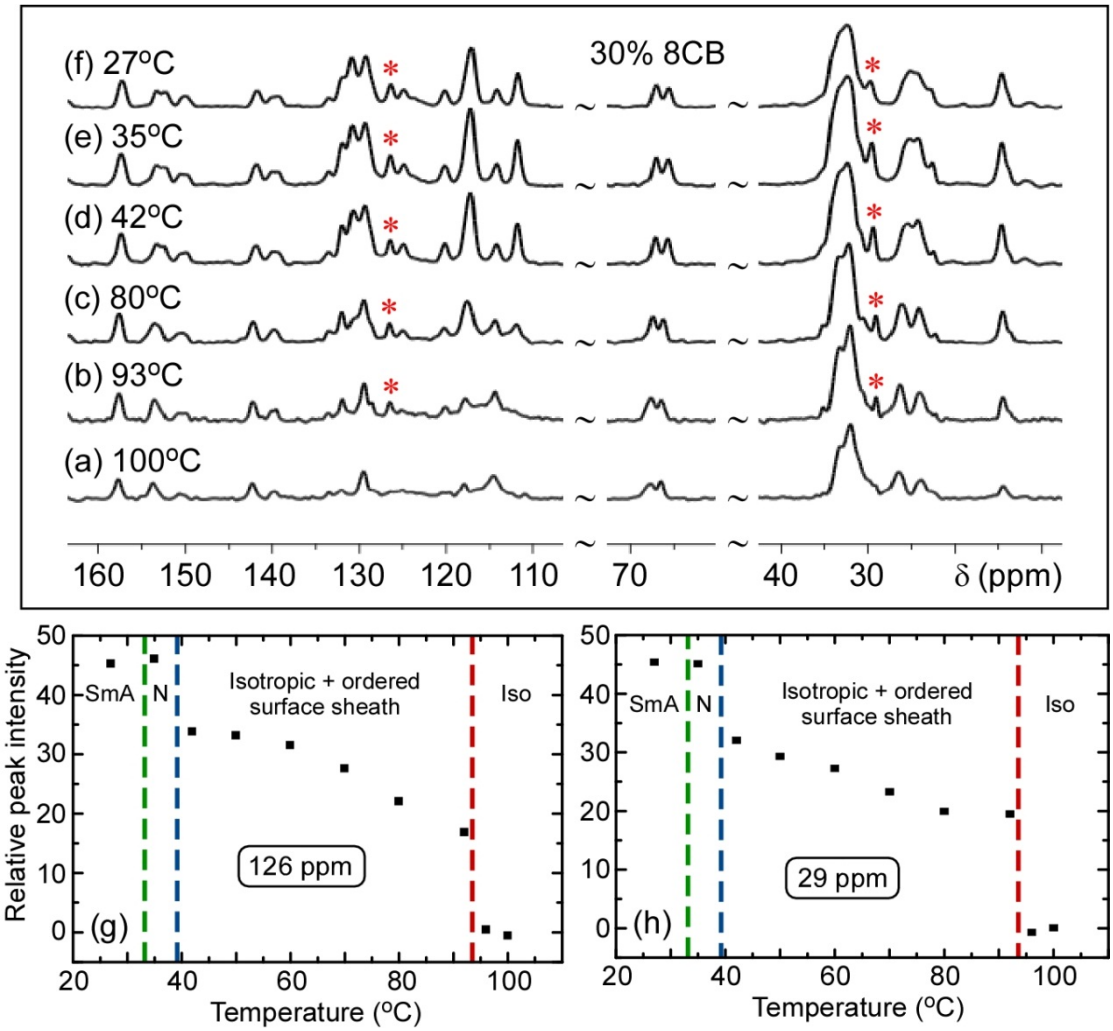

Figure 3.3.3: CPMAS NMR spectra of a c=30% 8CB/NOBOW mixture at different temperatures. (a) At high temperature, there is no contribution from 8CB and the spectrum is the same as that of pure NOBOW [32]. (b) 8CB peaks (indicated by red stars) appear on cooling, indicating the presence of anisotropic 8CB far above the bulk 8CB Iso–N transition. (c)-(f) show the 8CB signal persisting all the way down to room temperature. (g), (h) Relative intensities of 8CB peaks around 126 ppm and 29 ppm respectively, obtained by setting the integrated intensity of the NOBOW peaks near 68 ppm to a value of 100 in each scan and then subtracting the high temperature isotropic background. On cooling, the anisotropic 8CB signal first appears at about T≈93°C (red line) as a first order transition, which is slightly higher than the temperature predicted by DSC (around T≈83°C). This may be due to the different environment of the NMR sample holder. The 8CB peak intensities increase slightly on further cooling, with a strong enhancement of the NMR signal below the 8CB bulk Iso-N transition temperature (T≈39°C, blue line).

The CPMAS NMR spectra of the c=70% 8CB/NOBOW mixture are qualitatively different from those of the c=30% 8CB/NOBOW mixture. At high temperature (Figure 3.3.4a), well below the NOBOW Iso-B4 transition, there is no signal either from NOBOW or 8CB, even though the NOBOW is in the B4 phase. This is because there are fewer B4 filaments than in the c=30% 8CB/NOBOW mixture and those that are present are mobile, floating around in the 8CB medium, with no orientational order. As the sample is cooled and the B4 filaments become more rigid, the NOBOW signal begins to appear, together with 8CB peaks (Figures 3.3.4b-f). As before, we observe 8CB peaks in the CPMAS NMR spectra at temperatures far above the bulk 8CB Iso-N transition temperature, confirming the pre-transitional orientational ordering of 8CB by the B4 filaments. The simultaneous appearance of the 8CB and NOBOW signals on cooling indicates a strong dependence of 8CB pre-alignment on the presence of the B4 filaments.

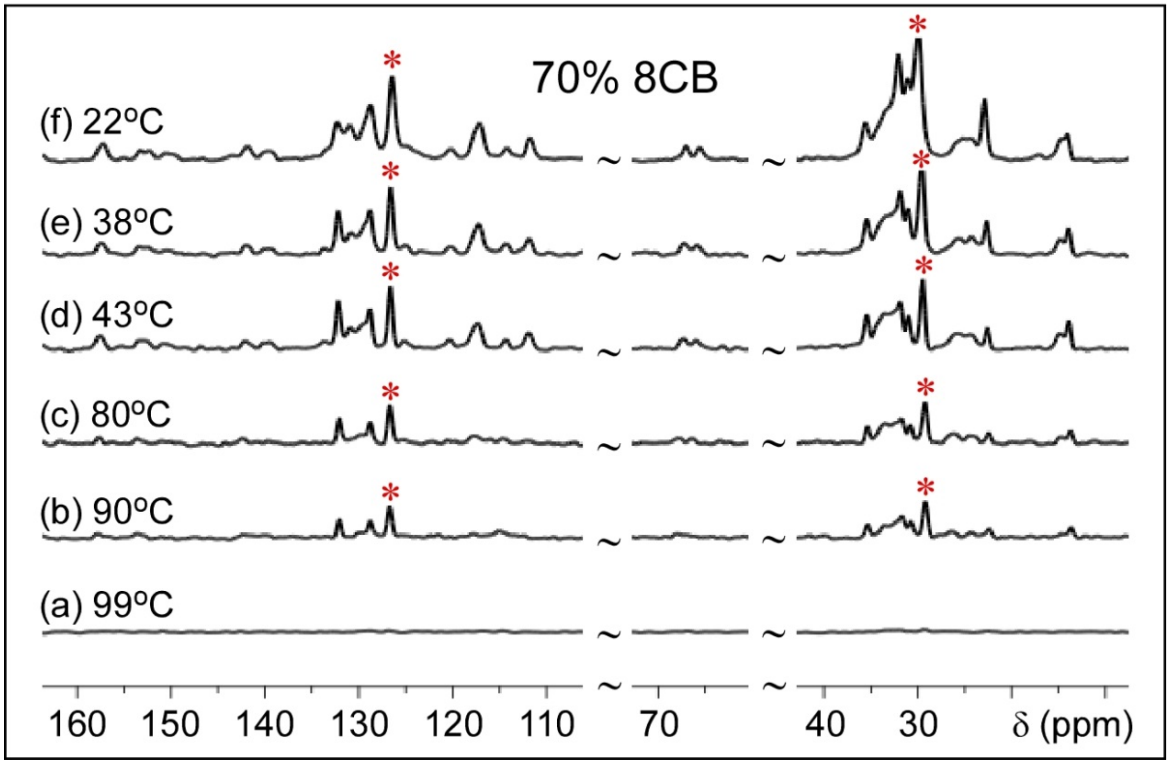

Figure 3.3.4: CPMAS NMR spectra of a c=70% 8CB/NOBOW mixture at different temperatures. (a) At high temperature but well below the NOBOW Iso-B4 transition, the B4 nanofilaments are mobile and float around in the isotropic 8CB solution, resulting in no NMR signal either from 8CB or from NOBOW. (b) At slightly lower temperature, the B4 filaments become more rigid and both B4 and 8CB peaks (the latter marked with red stars) appear. (c)-(f) On further cooling, both the B4 and 8CB signals become more intense.

In contrast to pure NOBOW, where smectic layer edges are seen in FFTEM images of the helical nanofilaments (right inset, Figure 3.3.5a), no layer edges are visible in the mixtures with 8CB (Figure 3.3.5a, magnified in the left inset), consistent with the idea that each B4 filament in the mixture is coated by an aligned layer of 8CB (Figure 3.3.5b), with the 8CB molecules adhering to the filament at some fixed orientation relative to the local NOBOW smectic layering. We can use the latent heat data to obtain a quantitative estimate of the thickness of the ordered 8CB coating. We approximate the helical B4 filaments as cylinders and assume that only 8CB in a thin layer around each filament is pre-aligned

(Figure 3.3.5b). We expect that a substantial fraction of the 8CB can be pre-aligned because the surface area to volume ratio of the B4 filaments is large ($\approx 10^8$ m^{-1}). Assuming that the latent heat release per 8CB molecule is the same for molecules orientationally ordering at the nanofilament surface or becoming nematic in the bulk liquid crystal, the ratio of $\Delta H_{pre\text{-}align}$, the latent heat release at the pre-alignment transition, to $\Delta H_{I\text{-}N}$, that of the bulk 8CB Iso-N phase transition, as a function of 8CB concentration c, depends only on the relative volumes of the surface (red region) and bulk (blue region) 8CB:

$$\Delta H_{ratio} = \frac{\Delta H_{pre-align}}{\Delta H_{I-N}} = \frac{a(1-c)}{c-a(1-c)} \quad \text{where} \quad a = \frac{\rho_{8CB}}{\rho_{NOBOW}} \left(\frac{r_{total-}^2 r_{NOBOW}^2}{r_{NOBOW}^2} \right).$$

The best fit to the ratios obtained by DSC at different 8CB concentrations is $a \approx 0.29$, shown in Figure 3.3.5c. Assuming similar liquid crystal densities ($\rho_{NOBOW} \approx \rho_{8CB} \approx 1$ g/cm^3) and taking a typical bare filament radius measured from FFTEM images ($r_{NOBOW} \approx 18$ nm), we obtain $r_{total} \approx 20.4$ nm, implying that 8CB is pre-aligned in a sheath about 2.4 nm thick around the nanofilaments. Several factors may cause this simple model to underestimate the thickness of the pre-aligned 8CB sheath. First, the aggregation of filaments, as seen in Figure 3.3.5a, reduces the overall exposed filament surface area and thus reduces the measured $\Delta H_{pre\text{-}align}$. Second, the orientational ordering of the 8CB may well occur inhomogeneously on the nanofilaments, given that the chemical potential of the smoothly helixing smectic ribbon surfaces are different from that of the exposed layer edges. Finally, we see from Figure 3.3.1b that the latent heat sum $\Delta H_{pre\text{-}align} + \Delta H_{I\text{-}N}$ in the mixtures (red stars in Figure 3.3.1b) is noticeably smaller than $\Delta H_{I\text{-}N}$ of pure 8CB Iso-N transition, implying that the pre-alignment latent heat release per molecule is in fact smaller than that of the bulk Iso-N transition.

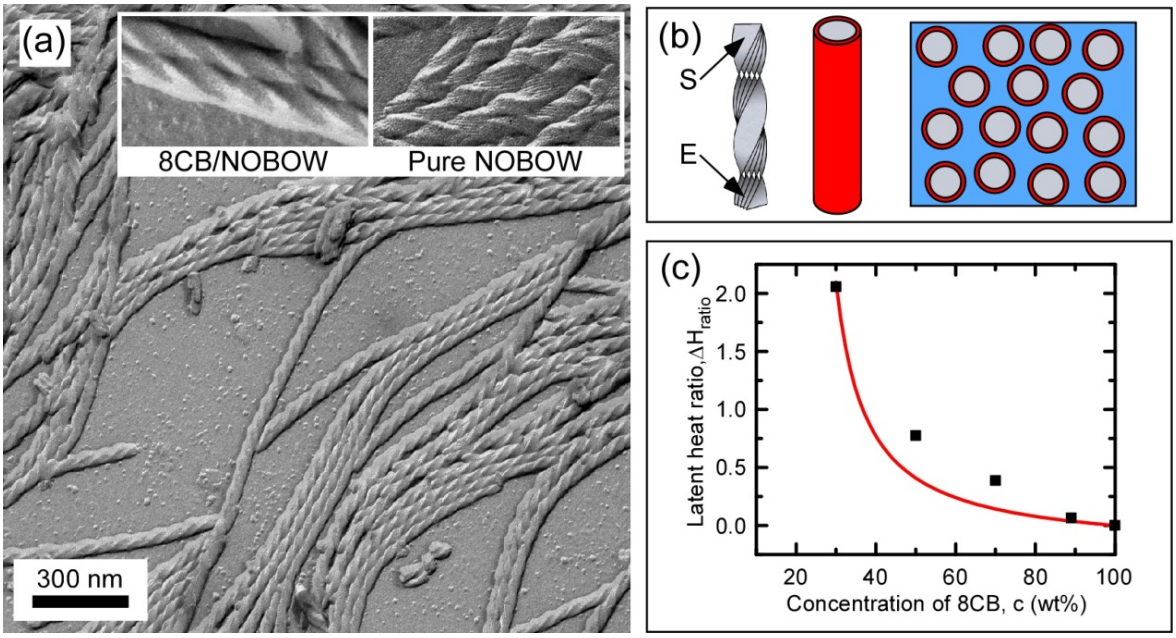

Figure 3.3.5: Structural model for the pre-alignment of 8CB by NOBOW B4 helical nanofilaments. (a) FFTEM image of c=75% 8CB/NOBOW mixture quenched at T≈37°C and then fractured at T≈-140°C. The image shows helical filaments of the NOBOW B4 phase near the glass surface (magnified in the left inset). No layer edges are visible, suggesting that the filaments are smoothly coated with 8CB, in contrast with pure NOBOW (right inset), where layer edges are easily identified. (b) In our model, the filaments are approximated as cylinders (grey region), with pre-aligned 8CB forming a thin sheet around each cylinder (red region) and the rest of the 8CB being isotropic (blue region). (c) Analysis of the latent heat ratios of pre-aligned to bulk 8CB Iso-N transition, $\Delta H_{ratio}=\Delta H_{pre\text{-}align}/\Delta H_{I\text{-}N}$, as a function of 8CB concentration implies that a 2.4 nm thick layer of 8CB is pre-aligned around each filament.

The elevated temperature of the pre-alignment indicates that the 8CB/NOBOW surface interaction is strong, and its appearance as a transition over a rather narrow temperature range indicates that some kind of well defined interfacial complex is being formed. Although roughly the pre-alignment can be viewed as a coating of a cylindrical filament by a uniform layer of 8CB, in actuality the filaments present two quite distinct surfaces to the 8CB, the layer surfaces S, and the layer edges E in Figure 3.3.5b. Since the S and E surfaces most likely have very different adsorption characteristics for 8CB, it is likely that only one surface

subset, the S or the E, is involved in the pre-alignment. A requirement for the pre-alignment appearing as a well-defined transition is a well-defined and repeatable nanostructure of the adsorption surface. Figure 3.3.5a shows that the filaments grow in a very regular way, suggesting that they provide an appropriate transition substrate. As noted above, the fact that the layer edges of filaments of pure NOBOW are visible in the FFTEM image but not in those of filaments of a NOBOW/8CB mixture (inset, Figure 3.3.5a), may indicate that the pre-alignment is occurring on the layer edges, a mode that would be consistent with the strong adsorption of 8CB on aromatic graphite [33] and polyimide [34] surface. On the other hand, it is well known that smectic layers at interfaces are molecularly smooth and exhibit a wide variety of surface induced phase transitions, including the formation of smectic layers at the isotropic-air and isotropic-solid interfaces. At this point, however, the precise molecular adsorption mechanism in the pre-aligned layer is not known. The pre-aligned 8CB sheath might resemble liquid crystal films at the air/water interface [35, 36, 37, 38] or pre-wetting films of 8CB on silicon substrates [39, 40], where a smectic-like trilayer organization, comprising a tilted, polar monolayer of 8CB with a thickness of 8 Å, covered by a 32 Å bilayer, is energetically favored, even in the isotropic phase. Alternatively, the nanofilament layer edges, clearly visible in the FFTEM images of pure NOBOW, should present a highly anisotropic organic surface to the surrounding 8CB molecules, similar to that found on rubbed polymer surfaces commonly used to align liquid crystals. Such surfaces impose planar alignment of the liquid crystals and induce nm thick aligned surface layers in the isotropic phase [41, 42].

In a summary, on cooling the isotropic mixture, the NOBOW component phase

separates, forming a dilute, random network of helical nanofilaments in the B4 phase with isotropic 8CB material filling the interstitial volume. At lower temperature, but still far above the bulk isotropic–nematic transition of pure 8CB, a significant fraction of the 8CB becomes pre-aligned on the filament surfaces, due to the relatively large surface area of the NOBOW filaments. The pre-transitional orientational ordering of 8CB far above its bulk Iso-N transition has been unambiguously verified by NMR spectroscopy. We propose that this pre-transitional ordering is induced by short-range interactions of the polar 8CB molecules with the NOBOW filaments, leading to the formation of an adsorbed film of orientationally frozen 8CB around each filament.

3.4 Structure of the B4 liquid crystal phase near a glass surface: Suppression of the structural chirality

The formation of chiral smectic phases has been a key feature of achiral, banana-shaped molecules, with spontaneous symmetry breaking originally described in the B2 phase of P-9-OPIMB, also known as NOBOW. The first observation of macroscopic chiral domains was also in the B4 phase of P-9-OPIMB homologs [43], where large left- and right-handed chiral domains can be distinguished under decrossed polarizers. These domains immediately suggested some kind of helical structure [44] and it has since been confirmed that left- and right-handed helical nanofilaments are the structural basis of the B4 phase [12]. The bent-core molecules form well-defined smectic layers with in-plane hexatic order, the coupling of macroscopic polarization and tilt of the molecular planes making the layers chiral. In this geometry, the half-molecular tilt directions above and below the layer mid-plane are nearly orthogonal, so that the projections onto the layer mid-plane of the lattices formed by the core arms do not match and there is a local preference for saddle-splay layer curvature that drives the formation of twisted nanofilaments. These nanofilaments are internally crystalline but their mesoscopic organization is liquid crystalline. The existence of helical nanofilaments in the B4 phase has been verified unambiguously by freeze-fracture transmission electron microscopy (FFTEM) images, such as those in Figures 3.4.1a and b. In section 3.2 of this chapter, we have proposed that the formation of macroscopic chiral domains of the B4 phase proceeds through the nucleation and chirality-preserving growth of individual helical nanofilaments, with single filaments bifurcating when they exceed a critical width.

Although macroscopic chiral domains have also been observed in the dark conglomerate,

a fluid phase of disordered focal conics [11], the B4 is unique in being the only bent-core phase with a macroscopically chiral structure, the twisted filaments. While the dark conglomerate usually appears on cooling directly from the isotropic and changes to crystal at lower temperature [45, 46, 47, 48], the B4 filaments are quite stable and robust, with the properties of the phase preserved even on cooling to room temperature and in mixtures with calamitic LCs (Figure 3.4.1b), making B4 materials of potential use for chiral-optic materials.

Because of their twisted conformation, helical filaments cannot completely fill space near the interface with a flat substrate or make full contact with such a surface. This implies that the structure of the B4 phase must be modified at a liquid crystal/glass interface. In this section, FFTEM is used to reveal the surface structure of the B4 phase of bent-core materials in the P-n-OPIMB homologous series, as shown in Figure 3.4.1c, and to explore the 3D arrangement of the smectic layers near a liquid crystal/glass interface. Our experiments reveal a rich diversity of surface structures that will help us better understand the complex nature of the B4 bent-core liquid crystal phase.

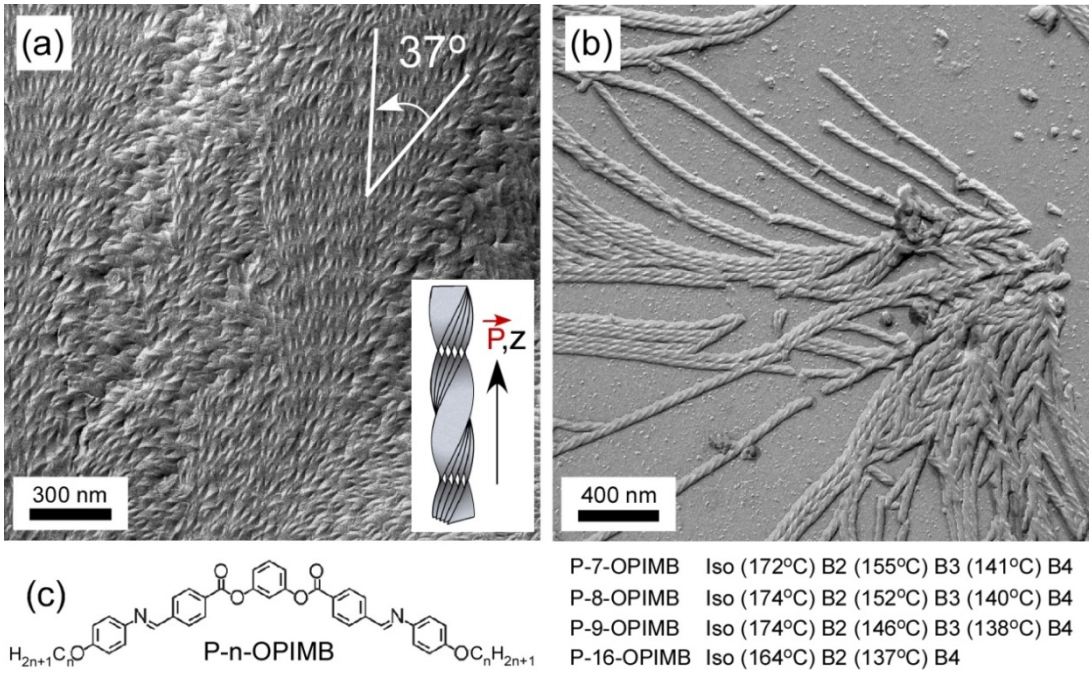

Figure 3.4.1: Self-assembly of B4 helical nanofilaments and chemical structures and phase sequences of P-n-OPIMB liquid crystals. (a) Helical nanofilaments of the B4 phase of P-8-OPIMB quenched at room temperature observed by FFTEM. The angle between the helix axis z and the helix groove direction is about 37º. (b) Helical nanofilaments of the B4 phase of P-9-OPIMB observed by FFTEM in a c=75% 8CB/P-9-OPIMB mixture quenched at 37°C. (c) Chemical structures and phase sequences on cooling of the P-n-OPIMB materials investigated.

An FFTEM image of P-8-OPIMB fractured near one of the glass planchettes (Figure 3.4.2a) reveals the topography of the B4 phase at different heights above the glass substrate. The upper right part of Figure 3.4.2a shows the typical bulk texture of densely packed B4 helical filaments, growing on top of layer undulation stripes, the B4 surface structure seen in the rest of the image. Unlike the layer undulations observed in the B7 phase, which are a direct consequence of layer thickness variations associated with polarization modulation [10], or the periodically flattened semi-cylinders observed in thin smectic films frustrated between two interfaces imposing antagonistic anchoring [49], Figure 3.4.2a shows different topography at different distances from the glass substrate. When the fracture plane is close to the glass (at lower right) we see alternating curved and flat regions, while further away from

the glass (at lower left), the surface topography appears as undulations with a periodicity of around 100 nm. The surface structure manifested near the liquid crystal/glass interface can be modeled as a 1D parabolic focal conic (PFC) array of smectic layers. PFCs are a variant of conventional focal conics (if the two foci of an ellipse are infinitely far from each other, the shape of the ellipse near one of the foci approaches a parabola). PFC domains have been observed in many other systems, for example, in dilated smectic A cells [50] and in cholesteric liquid crystal cells with an electric field applied along the twist axis [51]. A 1D PFC array can be constructed from a set of parabolas with their foci along the liquid crystal/glass interface (Figure 3.4.2b). The focus is colinear with the line defect (the structure is translationally invariant along this line) at the interface, which in most cases minimizes the elastic free energy of the system [49]. Due to the fluidity of the B4 phase at high temperature, the line defects can locally anneal into ordered, one-dimensional arrays at the liquid crystal/glass interface. Near the glass (the lower right part of Figure 3.4.2a), the equidistant parabolas are separate and the layers are alternately curved (within the parabolas) and flat (outside the parabolas) as sketched in Figure 3.4.2c. Further from the glass (the lower left part of Figure 3.4.2a), the adjacent parabolas overlap and periodic undulations of the layers are observed, with the layers curving around the line defects within the envelope of each parabola as indicated in Figure 3.4.2b. By measuring the widths of two undulating regions at different heights, we can compute the form of the parabola. Since the height difference between the regions with 50 nm and 68 nm wide curved layers shown in Figure 3.4.2a is approximately 10 nm (calculated from the width of the shadowed step between the two regions), the parabola is described by $u - 1/(4a) = av^2$ with $a \approx 0.019\ nm^{-1}$.

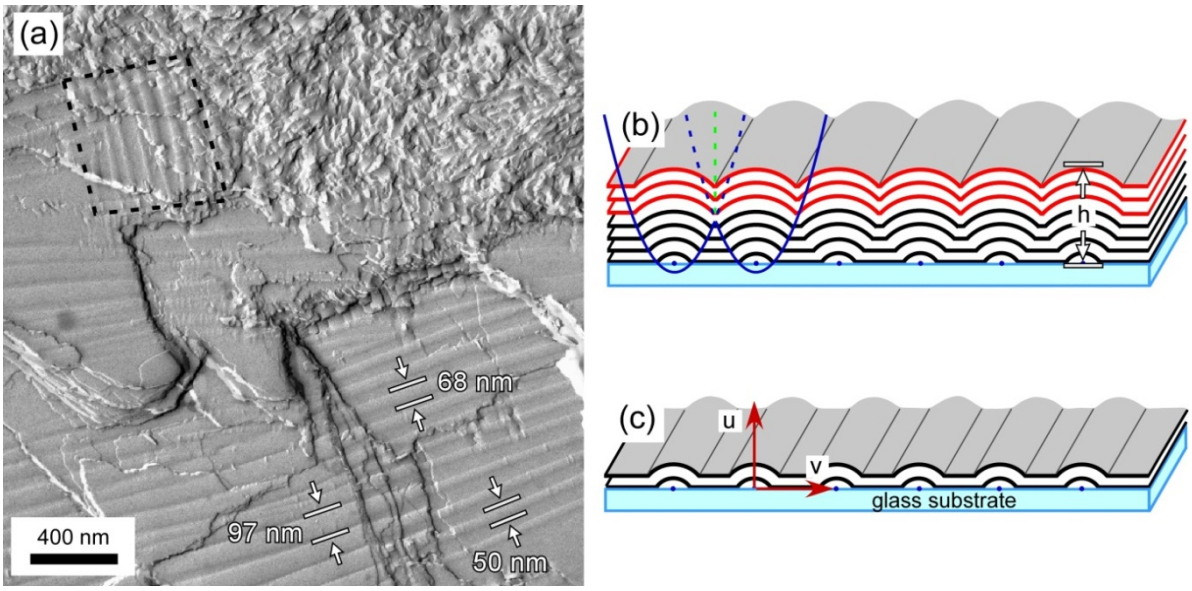

Figure 3.4.2: Parabolic focal conic surface structure of the B4 phase of P-8-OPIMB near the liquid crystal/glass interface quenched at room temperature. (a) FFTEM image showing the topography of the B4 phase fractured at different heights above the liquid crystal/glass interface. The lower half shows the parabolic focal conic array near the glass, with the lower right closer to the interface and the lower left further away. The region marked at upper left shows a PFC array oriented almost orthogonal to that in the lower half. The rest of the upper half shows the typical self-assembly of helical filaments of the B4 phase in the bulk. (b) and (c) Model of the surface topography of the PFC array fractured at different heights h. The curves are parabolas with their foci at the glass substrate. The smectic layers curve around the focus within each parabola and become flat outside, giving alternating curved and flat regions. With each additional layer, the curved regions become wider until the parabolas overlap and the layers show homogeneous, periodic undulations.

Because the glass is essentially untreated, the surface anchoring is very weak, with no clear preference for either homeotropic or planar anchoring of the director. The crucial element inducing the B4 surface structure is thought to be the flat geometry of the substrate, which suppresses the formation of helical nanofilaments at the glass. However, we believe that the in-plane molecular ordering of the PFC array is the same as that in the bulk nanofilaments, for above a certain distance from the glass substrate, helical nanofilaments do appear, growing continuously on top of the undulating layers. The elastic energy density of

the PFC is given, to quadratic order of the two principal curvatures σ′ and σ′′ of the layers, by $f_E = K/2(\sigma' + \sigma'')^2 - \bar{K}(\sigma'\sigma'') + G(\sigma'' - \sigma')$, where K and $\bar{K}$ are respectively the Frank elastic constants for mean and Gaussian curvature, and G drives curvature in response to the frustrated internal in-plane layer strain β [12]. The minimum of the elastic energy density, shown in Figure 3.4.3, is obtained when $\sigma' = -\sigma'' = G/\bar{K}$ (the minimal surface), leading to the adoption of saddle-splay curvature. As the distance from the glass increases, the confining influence of the glass surface on the layers becomes weaker, and the undulating structure of the surface layers eventually transitions to the characteristic bulk helical nanofilament structure, seen in Figure 3.4.2a. The PFC surface structure is estimated to penetrate no more than 100 nm into the bulk.

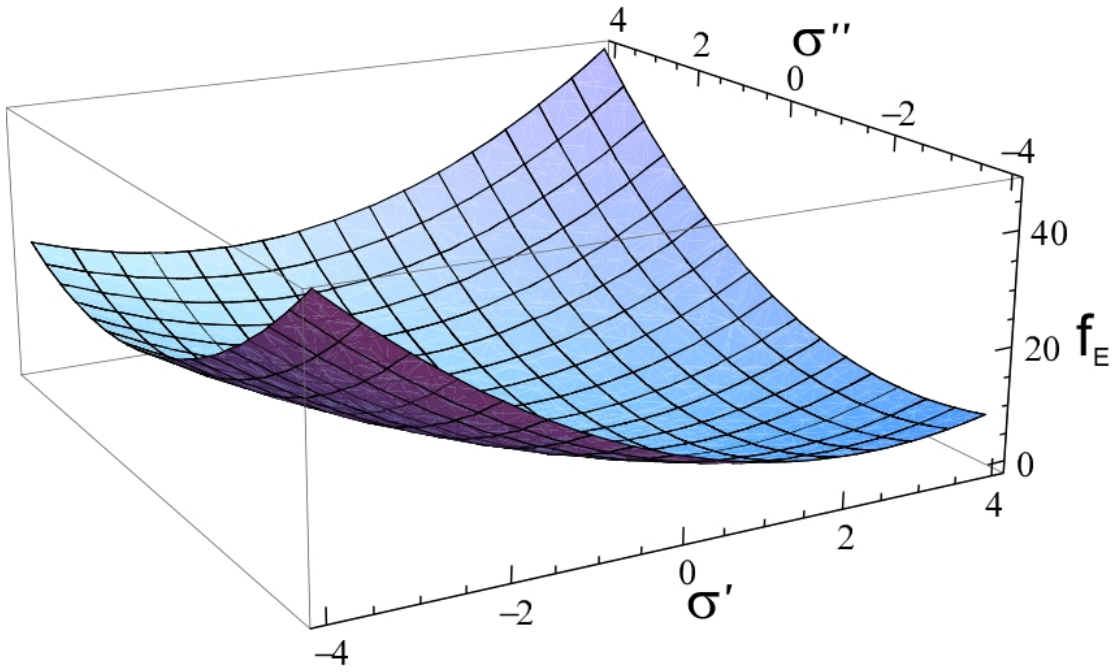

Figure 3.4.3: Elastic energy density $f_E = K/2(\sigma' + \sigma'')^2 - \bar{K}(\sigma'\sigma'') + G(\sigma'' - \sigma')$ of the smectic layers as a function of σ′ and σ′′ with K=2, $\bar{K}$=1 and G=1. The energy is minimized when $\sigma' = -\sigma'' = G/\bar{K}$ (minimal surface). For K=2, $\bar{K}$=1 and G=1, the minimum is obtained when σ′=–σ′′=1. The elastic energy cost intrinsically drives the layers to adopt the saddle-splay curvature in the B4 phase.

The surface undulations in any given FFTEM images are typically not uniformly aligned along one direction but adopt two degenerate orientations at right angles, as can be seen in Figures 3.4.2a and 3.4.4a. This appears to be due to the independent formation of new PFC arrays, which nucleate heterogeneously and grow perpendicular to the edges of existing arrays as shown in the inset of Figure 3.4.4a. We have also observed bamboo-like surface structures growing from the boundaries of PFC arrays (shown in Figure 3.4.4a) or nucleating independently (shown in Figures 3.4.4b and 3.4.5). We propose that this structural variant is made of layers nested in toric focal conic (TFC) domains, with the axial defect line lying at the liquid crystal/glass interface and the circular defect line normal to the glass (see the inset of Figure 3.4.4b). A characteristic feature of the bamboo-like structure is that the radial growth is self-limiting, ceasing when the layers extend far away from the axial defect line, as seen in Figure 3.4.4b. Similar elastic energy arguments to those limiting the height of the PFC arrays can be applied here. As a smectic layer grows away from the axial defect line, it becomes flatter. Since the layers intrinsically prefer to be curved, this costs more and more elastic energy and eventually the growth terminates. The disordered, fractal-like arrangement of the bamboo-like structure (compared with the ordered PFC arrays) may be a manifestation of quenched disorder, which would occur if they formed at lower temperature and were unable to anneal into ordered arrays. Disordered surface structures with worm-like textures, shown in Figures 3.4.6a and b, have also been observed near the glass substrate.

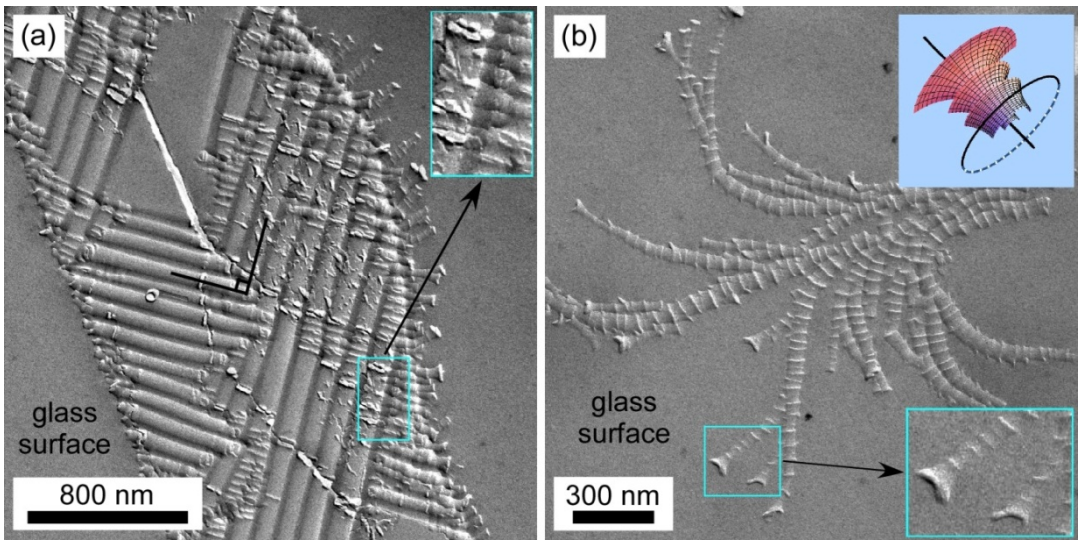

Figure 3.4.4: Nucleation and growth of the toric focal conic structure near the liquid crystal/glass interface in the B4 phase of P-7-OPIMB quenched at room temperature and observed by FFTEM. (a) Coexistence of parabolic focal conic arrays essentially orthogonal to each other is commonly observed (the smooth regions on either side of the PFC arrays are bare glass). This is a result of the nucleation and growth of new PFC arrays at the edges of existing ones (magnified in the inset). (b) Toric focal conics in the B4 phase. This bamboo-like structure, which is also visible along the right boundary of the PFC arrays in (a), is made of toric focal conics with their axial defect lines lying along the glass. A model of the layers is shown in the upper inset, with the straight line and the circle representing the line defects. As the layers further from the surface grow, they become flatter (magnified in the lower inset). The reduced curvature raises the elastic energy and inhibits the structure from growing further.

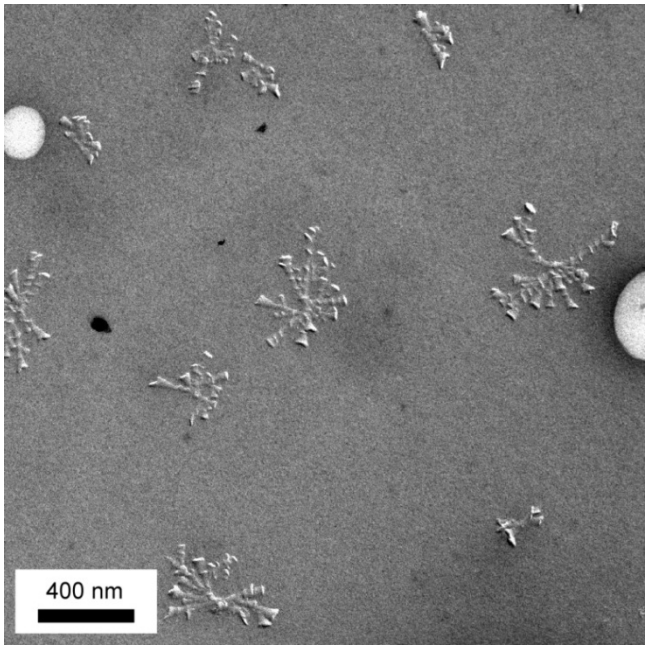

Figure 3.4.5: Nucleation and growth of the bamboo-like surface structure of P-7-OPIMB in the B4 phase near the liquid crystal/glass interface quenched at room temperature.

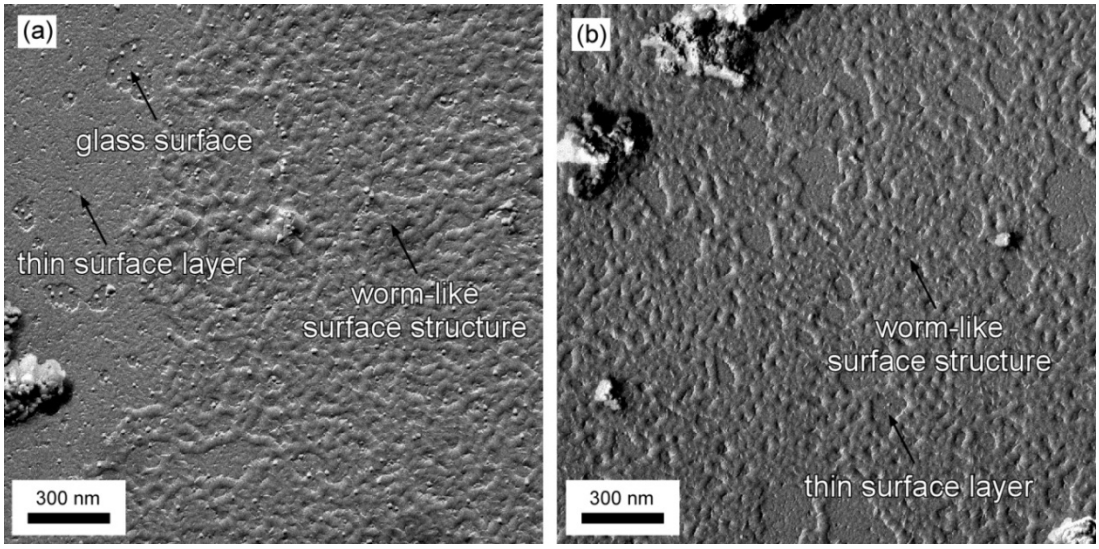

Figure 3.4.6: FFTEM images of P-16-OPIMB quenched at 160°C in the B4 phase. (a) and (b) show a disordered, worm-like surface structure. The thin surface layer seen here and in Figure 3.4.8 may be another (as yet unidentified) kind of B4 surface structure. The small "pits" in the images are artifacts due to ice crystals which condensed on the liquid crystal surface after fracturing.

The topology in both the B4 and dark conglomerate phases of bent-core liquid crystals is driven by the tendency for the layers to adopt saddle-splay curvature, which leads to the formation of minimal surface that can be realized in the form of helicoid and catenoid. Though the catenoid (Figure 3.4.7a) and helicoid (Figure 3.4.7b) are adjoint structures/topologies, with the same local mean and Gaussian curvatures at equivalent points on the saddle-splay surfaces, the reason why the bulk B4 phase prefers the shape of helicoids, forming helical nanofilaments with structural chirality [12], while the shape of catenoids dominates in the dark conglomerate phase, with the layers forming disordered focal conics in the bulk [11] or quasi-ordered toric focal conics at the free surface (Chapter 4), is still a mystery. The observation of toric focal conics at B4 surfaces suggests (Figures 3.4.4, 3.4.5 and 3.4.6) that focal conics may be thermodynamically close to helical nanofilaments in the B4 phase and might be observed under the right conditions in bulk B4.

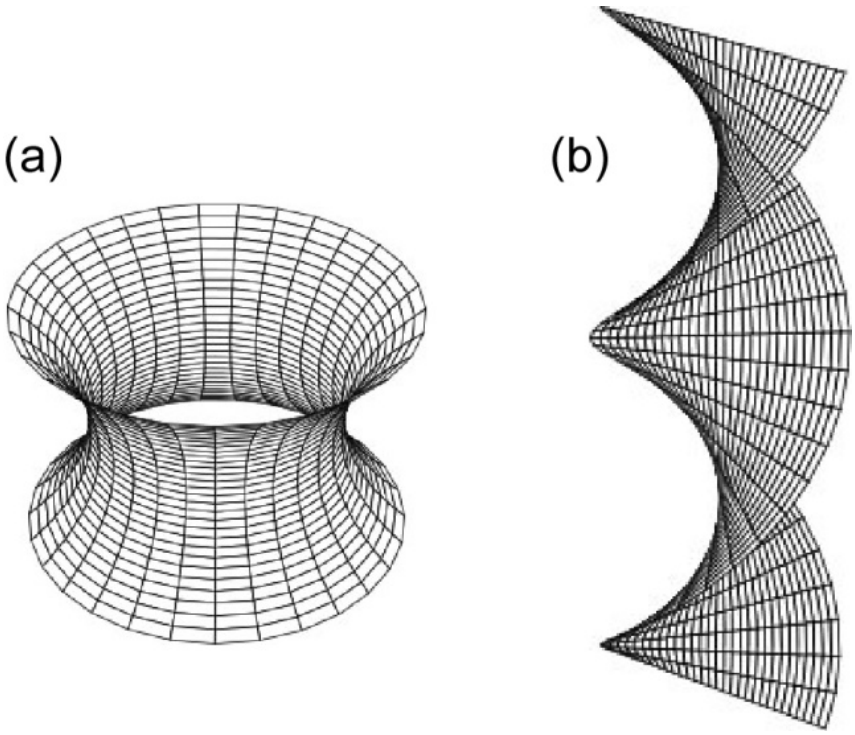

Figure 3.4.7: Model of catenoid (a) and helicoid (b), both of which are minimal surfaces. The catenoid and helicoid are adjoint, sharing the same local mean and Gaussian curvatures at equivalent points on the saddle-splay surfaces. The catenoid is, however, macroscopically achiral while the helicoid is macroscopically chiral.

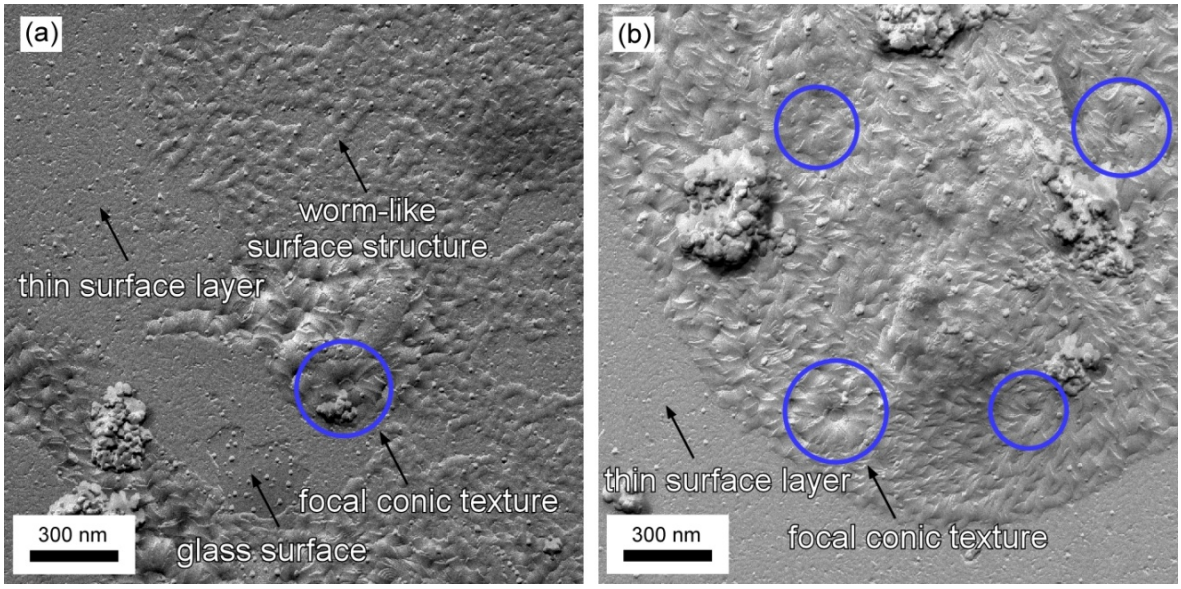

Figure 3.4.8: FFTEM images of P-16-OPIMB quenched at 160°C in the B4 phase. (a) and (b) show toric focal conic structures (enclosed by blue circles), each with the axial defect line perpendicular to the substrate and the circular defect line lying on the glass surface.

The transition from the B4 surface structure to bulk helical nanofilaments is illustrated in Figure 3.4.9a. The filaments appear to be smoothly connected to the underlying PFC arrays, and show characteristic flame-tip-like texture (Figures 3.4.9a and b). The filaments make an angle of about 38º with respect to the PFC stripe direction, essentially matching the angle between the helix axis and the helical groove (~37º, shown in Figure 3.4.1a). Careful examination of the filaments in Figure 3.4.9b reveals a broken symmetry: the filaments all have the same twist sense (i.e., they are homochiral) and rotate clockwise from the undulation stripes in this case. Although layer twist is suppressed at the glass surface, the smectic layers are nevertheless chiral (the molecules are polar and tilted, as indicated in Figure 3.4.9c) and we propose that this chirality is inherited by the helical filaments growing above, leading them to be homochiral and uniformly oriented with respect to the undulation stripes. The projection of the periodicity of the PFC array along the helix axis z of the nanofilaments is about 106 nm (Figure 3.4.9b), which is approximately the half-pitch of a filament ($p/2 \approx 108$ nm). The B4 filaments growing on top of the undulating layers thus appear to align their grooves epitaxially along the curved surface layers, as sketched in Figure 3.4.9c. This alignment is also observed when nanofilaments grow on the bamboo-like surface structure, as shown in Figure 3.4.10.

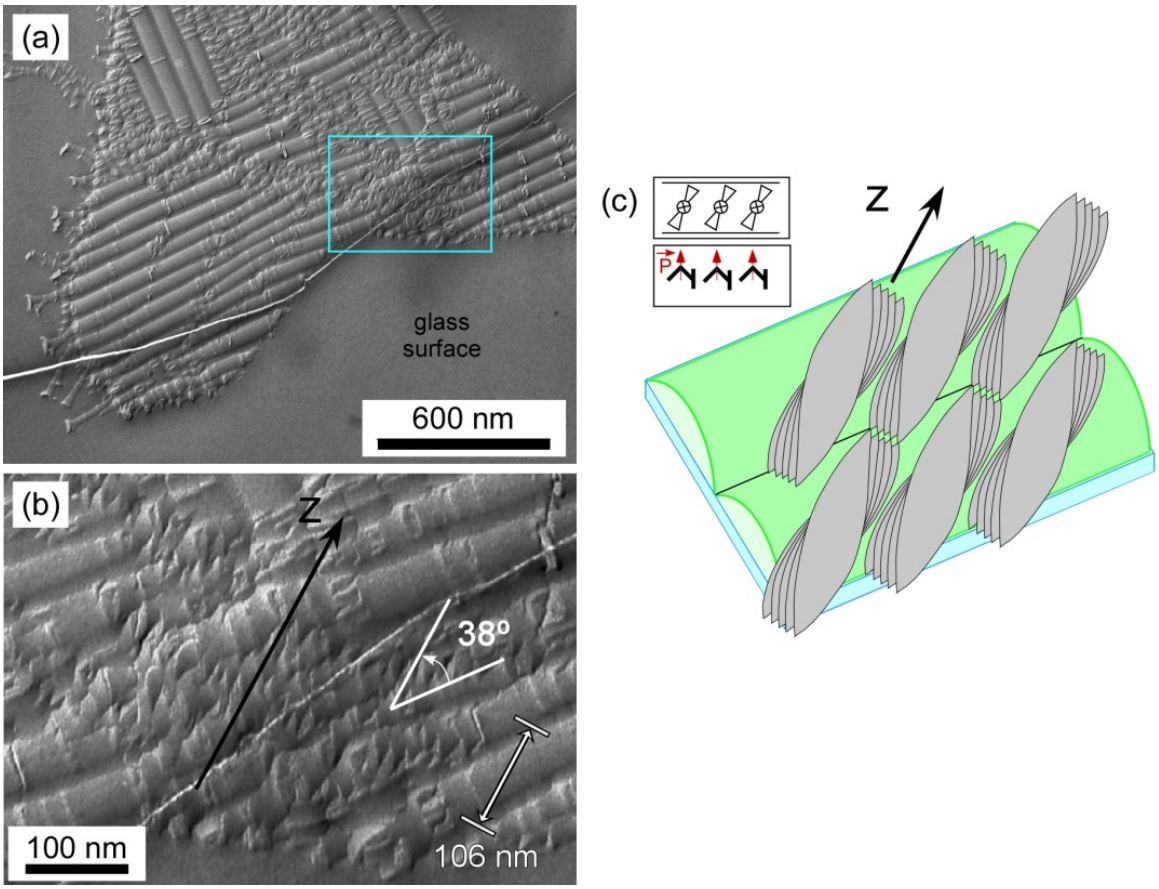

Figure 3.4.9: Homochiral helical nanofilaments growing on top of parabolic focal conic surface arrays in the B4 phase of P-7-OPIMB quenched at room temperature. (a) FFTEM image showing PFC arrays near the glass and helical nanofilaments above them, as well as bamboo-like toric focal conics at the left boundary. (b) Details of the region indicated in (a). Smectic layers forming on top of the undulated surface layers twist into helical nanofilaments. The nanofilaments grow with an orientation of about 38º from the direction of the undulation stripes and have a characteristic flame-tip-like texture. The projection of the periodicity of the PFC array along the helix axis z of the nanofilament is about 106 nm, matching the half-pitch of the filament. (c) Cartoon of the transition from undulating surface layers to bulk helical filaments. The inset shows the molecular polarization and molecular tilt which give layer chirality shared in the untwisted surface layers and the twisted nanofilaments.

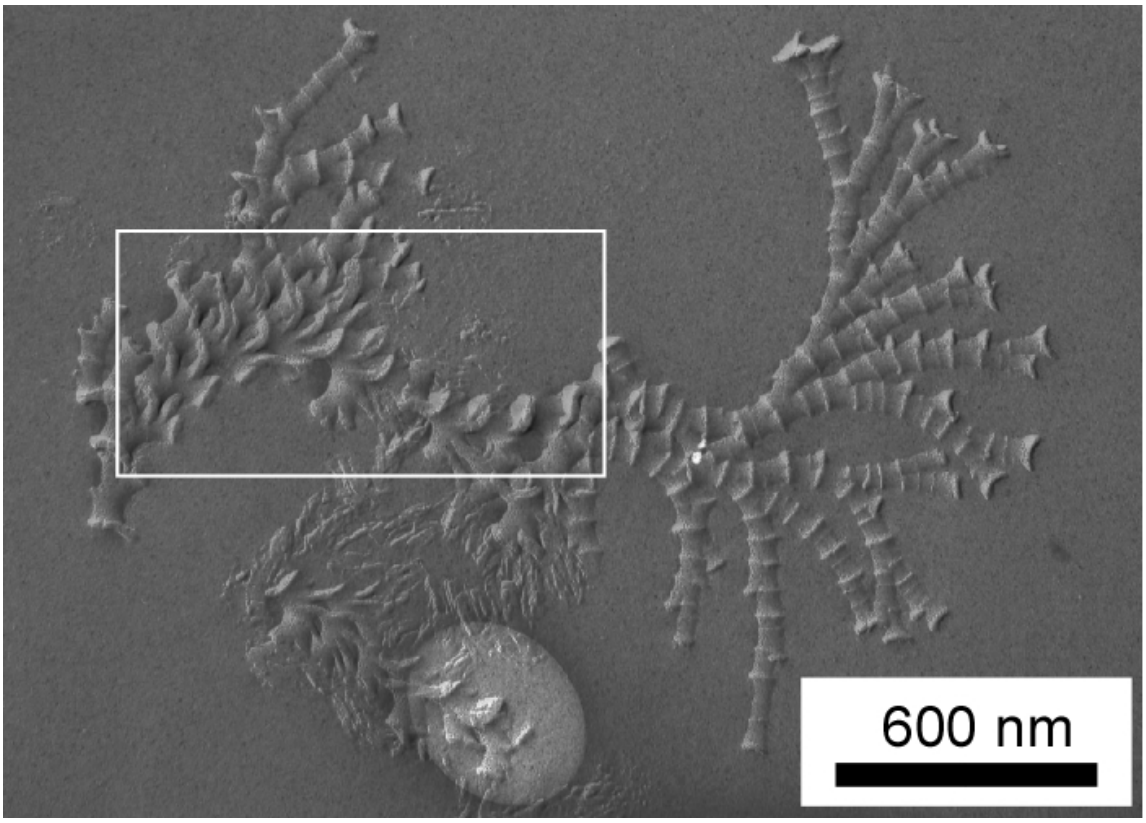

Figure 3.4.10: Homochiral helical nanofilaments (enclosed by white box) formed on top of the bamboo-like surface structure in the B4 phase of P-7-OPIMB. The sample is quenched at room temperature.

In a summary, freeze-fracture transmission electron microscopy images reveal the diverse topology of the B4 liquid crystal phase of mesogens in the P-n-OPIMB homologous series near the liquid crystal/glass interface. One-dimensional, periodic parabolic focal conic arrays are manifested as smectic layer undulations near the glass. Nucleation and growth of toric focal conic surface structures is also observed. Although the growth of twisted nanofilaments, the usual manifestation of structural chirality in the B4 phase, is suppressed near the surface, the smectic layers are intrinsically chiral. Further from the glass substrate, the layers evolve to the familiar twisted structure of the bulk, with homochiral helical nanofilaments nucleating smoothly on top of the underlying layers and growing epitaxially

with the helix groove aligned along the crests of the curved layers. This observation suggests that it may be possible to align B4 helical nanofilaments along one global direction using topographically patterned substrates.

3.5 Nanoconfined systems prepared by helical nanofilament network of bent-core liquid crystal

Porous materials are widely used in the chemical industry as catalysts and catalyst supports for chemical reactions, or as templates for materials fabrication [52, 53, 54, 55]. Nanoconfined systems prepared using these porous materials are also of rich fundamental scientific interest, with new physics often resulting from the finite-size effects, the varying dimensionality, and the surface forces [56]. Molecules confined within narrow pores, a few molecular diameters across, can exhibit a wide range of physical behavior, as a large fraction of the confined molecules will experience a reduction in the number of nearest-neighbor molecules. Conventional nanoporous materials have crystalline or regular pore structure (e.g. aluminosilicates, aluminophosphates) and amorphous pore structure (e.g. porous glasses, silica aerogel). Preparation of nanoconfined system in conventional nanoporous materials usually involves infiltrating the isotropic material by capillary force. However, even a small number of defects in the host material may interrupt the interconnected pore structure, making complete filling difficult. Collapse of the porous structure may also happen.

From the discussion of previous sections, we know that the B4 phase of bent-core molecules is a recently characterized helical nanofilaments phase [12]. Though, made of achiral bent-core molecule, the B4 phase forms distinct left- and right-handed chiral domain under depolarized transmission light microscopy and helical structure is proposed in the B4 phase [44]. In the B4 phase, bent-core mesogenic molecules organize into layered smectic liquid crystal phases in which there is a strong inherent tendency for saddle splay deformation of the molecular layers due to intra-layer mismatch. Growth of the B4 phase is limited to left-

or right-handed helical nanofilaments, which accounts for the left- and right-handed chiral domains. On the other hand, due to the constraint of constant layer spacing and preferred layer curvature, helical nanofilaments of the B4 phase is limited to about eight smectic layers (40 nm) and only diffuse peaks are observed in the x-ray reflections from the smectic layers. Although the layers show only short-range order, they are robust, giving several harmonics in the x-ray reflection pattern.

In the study of mixtures of bent-core molecules and rod-like molecules [13], people get a better understanding of the B4 helical nanofilament phase. Those helical nanofilaments are quite robust, expelling 8CB in the NOBOW/8CB mixtures and forming nanofilaments identical to those seen in pure NOBOW, which means that in the NOBOW/8CB system, the NOBOW B4 phase is totally phase-separated from the 8CB on the molecular scale [15]. On the other hand, through the bifurcation of growing filaments, the B4 phase forms a random network of homochiral helical nanofilaments. At low concentration of 8CB (above c=50%, weight percent of NOBOW in the mixture), 8CB is microscopically (tens of nm in scale), homogeneously mixed with this random network and no bulk 8CB is observed in this regime. Such phase segregation on the molecular scale combined with mixing on the microscopic scale makes the helical nanofilaments network ideal for preparing nanoconfined systems. Rich property has emerge from the nanoconfined systems prepare by the helical nanofilaments network [16, 14], for example, the appearance of a liquid crystalline nematic-isotropic critical point of 5CB in the mixture system of P-8-OPIMB/5CB.

In this section, we explore the feasibility of preparing nano-confined systems through the phase separation process by cooling down mixtures of NOBOW with other materials and

we will also characterize the 3D random network structure formed by the B4 helical nanofilaments. Mixtures of NOBOW with different materials, e. g. 8CB (rod-like molecule, forming SmA phase), JR6-65C (discotic molecule, forming hexagonal columnar phase) [57, 58], M6R8 (rod-like monomer, forming SmA phase) in PM6R8 (rod-like polymer, forming bilayer SmC phase) [59, 60] and P3HT (polymer, forming crystal nano whisker) [61, 62], are investigated. In all these systems, the components mix completely in the isotropic range, but phase separate when cooled down.

The chemical structures and phase sequences of the materials investigated here are shown in Figure 3.5.1. All of the mixtures with NOBOW have similar phase behavior, where the NOBOW bent-core molecules undergo self-assembly of helical nanofilaments, as shown in Figure 3.5.2a. The phase diagram of the mixtures, based on x-ray diffraction (XRD) and depolarized transmission light microscopy (DTLM) observations, can be simplified and generalized as in Figure 3.5.2b. All the mixtures form a single, homogeneous phase in the high temperature, isotropic range. At large concentrations of NOBOW, upon cooling, the NOBOW B4 phase first appears, separating from the isotropic medium, to form a random network of the helical nanofilaments. Those helical nanofilaments are quite robust and are identical to those in pure NOBOW, as the peak position and FWHM of their x-ray diffraction in different mixtures are essentially invariant, as shown in Table 3.5.1, indicating no other molecule dissolves in the B4 helical nanofilaments. Subsequently, the investigated phase is nanoconfined in this network and undergoes the phase transition upon further cooling. As the concentration of NOBOW decreases, there may be coexistence of nanoconfined and bulk phase of the investigated material, due to the low concentration of helical nanofilaments or

the bulk phase of investigated material may appears first. The eutectic point e depends on the property of the investigated materials. Below, we will describe the behavior of those mixtures in detail.

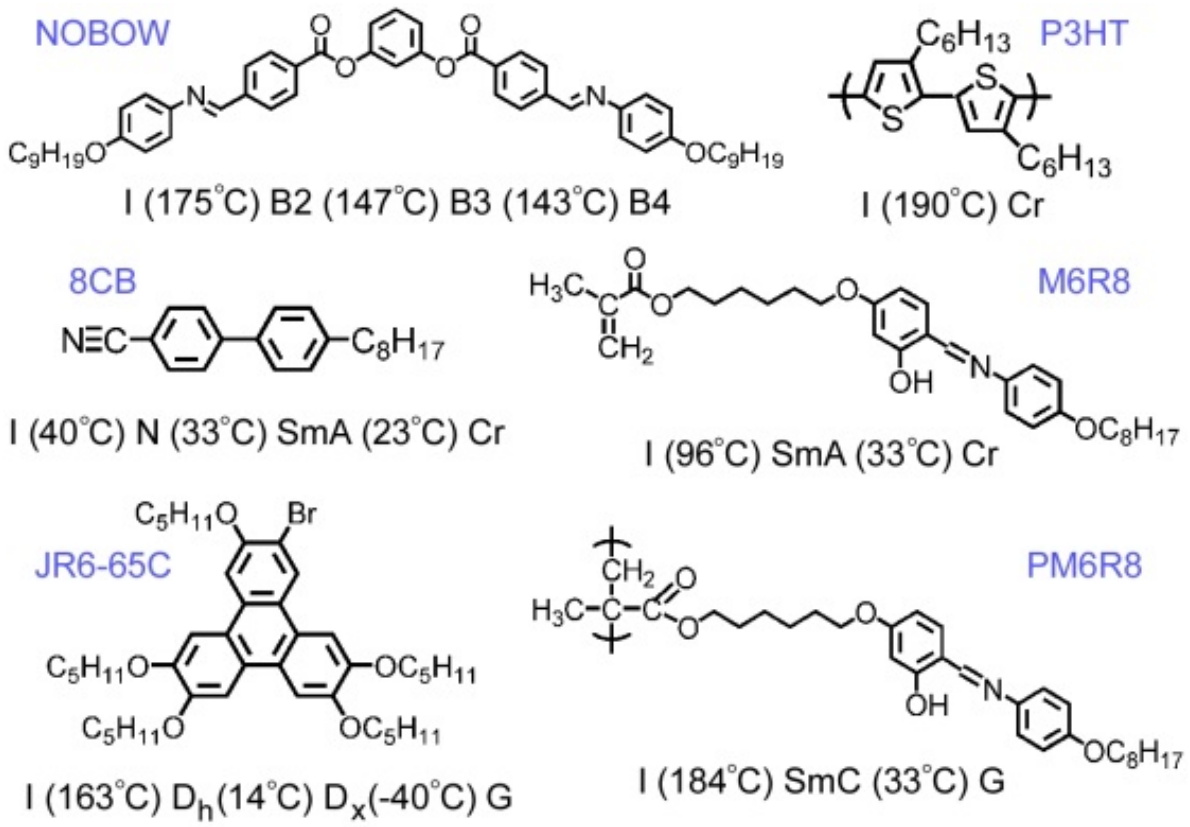

Figure 3.5.1: Chemical structures and phase sequences of the materials NOBOW, 8CB, JR6-65C, P3HT, M6R8 and PM6R8. I, isotropic; Cr, Crystal; G, glass; D_h, hexagonal discotic; D_x, unidentified discotic.

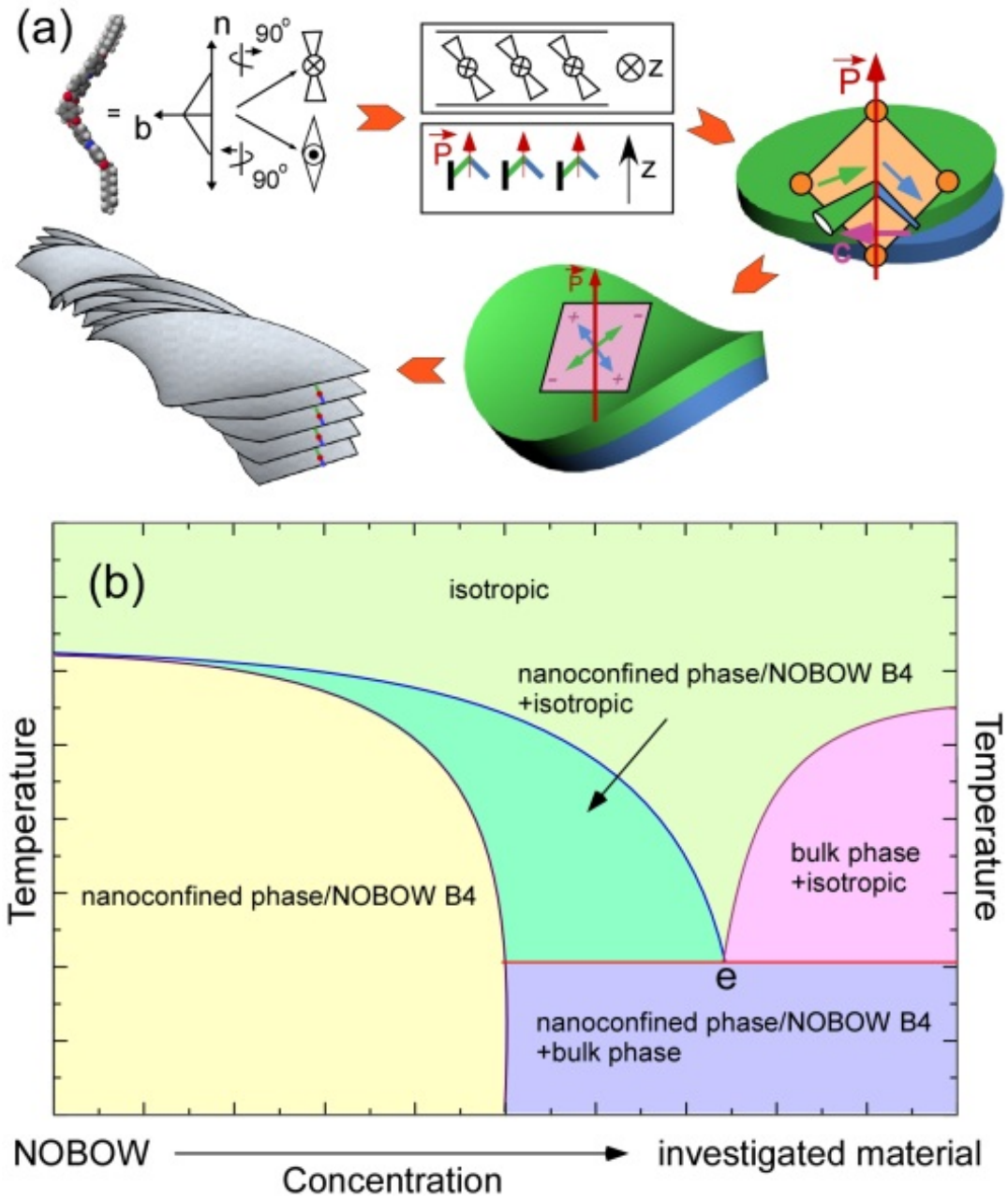

Figure 3.5.2: Formation of nanoconfined system through the self-assembly of helical nanofilaments in the mixtures. (a) Self-assembly of helical nanofilaments. The bent-core molecules form well-defined smectic layers, while the coupling of macroscopic polarization and tilt of the molecular planes makes the layers chiral. Due to the in-plane hexatic order, each half-layer dilates along the tilt direction of their molecular arm while the tilt directions of molecular arms above and below the layer mid-plane are nearly orthogonal. This kind of intra-layer mismatch results in a local preference for saddle-splay layer curvature and driving the formation of twisted nanofilaments. (b) Simplified, generalized phase diagram of the mixture of NOBOW with other materials investigated here derived from x-ray diffraction (XRD) and DTLM observations.

Mixture of NOBOW with other materials	c=50% with 8CB	c=41% with JR6-65C	c=49% with 90%M6R8 in PM6R8	c=50% with 77%M6R8 in PM6R8	c=50% with P3HT
Temperature (°C)	70	76	69	69	68
Peak Position (A^{-1})	0.13100	0.13096	0.13139	0.13164	0.13102
FWHM (A^{-1})	0.01159	0.01095	0.01021	0.01158	0.00707

Table 3.5.1: Peak position and FWHM of B4 helical nanofilaments' x-ray diffraction around 70°C in different mixtures of NOBOW with other materials. Peak position and FWHM of NOBOW B4 phase were measured by fitting the XRD peak using Lorentz function. The peak position of NBOW B4 phase is essentially invariant in different mixtures and is the same as that in pure NOBOW, indicating no molecule mixes in the B4 helical nanofilament. FWHM is also identical in different mixtures.

Columnar phases comprising of supermolecular assemblies of disk-shaped molecules show the potential application as semiconductor, for electron can travel along the columnar axis. Recently, triphenylene based discotics have emerged as a new class of fast photoconductive materials, due to their photoconductivity and high charge carrier mobilities [63]. However, the columnar phase range of those materials is typically very narrow, due to the C_3 symmetry of the molecules, which have a large chance of optimal packing leading to crystallization. JR6-65C is a discotic mesogen synthesized to broaden the phase range and increase the mobility of the electrons by limiting or biasing the molecular rotation within the columns, which leads to fewer degrees of rotational freedom within the column and results in higher overall order in the mesophase. They possess a single electron-withdrawing group (and consequently a large dipole moment) connected directly to the polyaromatic core. Figure 3.5.3a shows the XRD scan of the hexagonal columnar phase (D_h phase) in pure JR6-65C. The peak from the hexagonal ordering is pretty much resolution-limited, indicating long-range order in the bulk. However, in the mixture of c=60% NOBOW/JR6-65C (c is the

weight percent of NOBOW in the mixture), the peak from JR6-65C columnar phase can only be fitted by two Lorentz peaks (shown in Figure 3.5.3b), one resolution-limited and one diffuse, which indicates that some portion of the D_h phase is nanoconfined by the NOBOW nanofilament network. By integrating the areas of the two peaks, we can calculate the portion of the bulk (area~0.188) and nanoconfined phase (area~0.728), which means that 79.5% of the columnar phase is nanoconfined. Due to the confinement, the peak position in the mixture shift by (0.1 Å) relative to that in pure material, which is minor in affecting the property of the D_h phase. To see the phase behavior of the mixture more clearly, the periodicities of the NOBOW B4 phase and JR6-65C D_h phase as a function of temperature are shown in Figure 3.5.3c. The two components mix well in the high temperature isotropic range. On cooling, NOBOW first phase separates, forming the helical nanofilament network. Afterwards, the isotropic discotic molecules of JR6-65C transition into the columnar phase, with some of them confined in the nanofilament network. In contrast to the binary system of NOBOW/8CB, where all 8CB is nanoconfined above c=50%, there is still bulk D_h phase (20.5%) in c=60% mixture, indicating that the hexagonal ordering is more resistant to the disturbance introduced by the nanofilament network than the smectic layering. In order to get a clearer picture of the nanoconfined system, Figure 3.5.3d shows the helical nanofilament network of the NOBOW B4 phase under crossed polarizers, while the JR6-65C is still isotropic. When further cooling down the mixture, the D_h phase of JR6-65C appears as tiny white spots when confined in the porous network (Figure 3.5.3e).

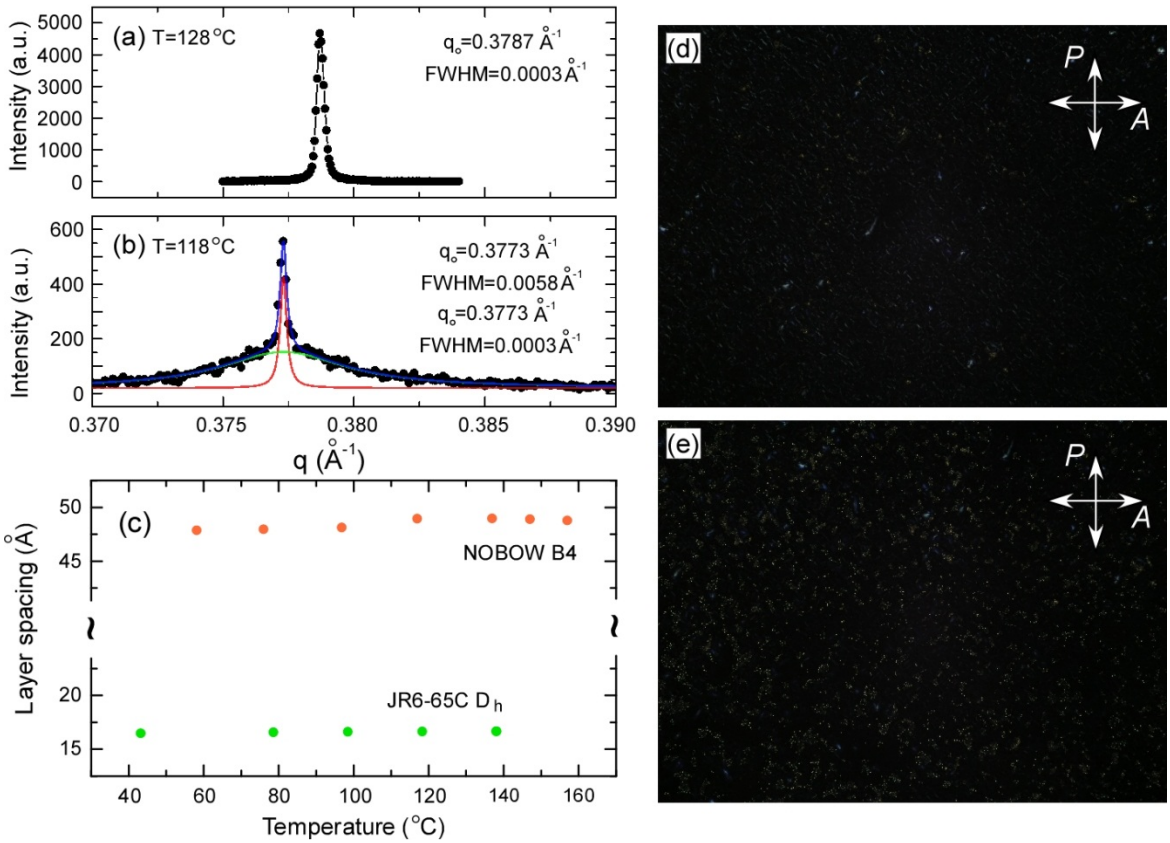

Figure 3.5.3: Binary mixture of NOBOW/JR6-65C. (a) XRD of pure JR6-65C showing the resolution-limited peak of the hexagonal columnar phase (D_h). (b) XRD scan of a c=60% NOBOW/JR6-65C mixture. The peak from the JR6-65C columnar phase is fitted by two Lorentz peaks, one resolution-limited (bulk component) and one diffuse (nanoconfined component). (c) Layer spacing of the NOBOW B4 phase and JR6-65C D_h phase in a c=60% NOBOW/JR6-65C mixture. They are essentially independent of temperature. On cooling, NOBOW B4 phase first forms the random helical nanofilament network from the isotropic. Afterwards, the discotic molecules of JR6-65C change to the columnar phase. (d) DTLM image of the NOBOW B4 phase in a c=80% NOBOW/JR6-65C mixture at T=100°C, where JR6-65C is isotropic. (e) DTLM image of a c=80% NOBOW/JR6-65C mixture at T=60°C, where the nanoconfined JR6-65C columnar phase contributes to the tiny white spots.

PM6R8 is a peculiar polymeric mesogen, forming a bilayer antiferroelectric smectic C phase, though the molecule itself is achiral [59]. The molecular packing of this bilayer antiferroelectric smectic C phase has been clearly elucidated in mixtures of the monomer M6R8 in PM6R8, using freely suspended films [60]. Here ternary mixtures of NOBOW with M6R8 in PM6R8 are prepared. On one hand, we will further testify the stability of the formation of the NOBOW B4 helical nanofilaments in the present of the polymer. On the other hand, we will show how the pore size of the nanofilament network can be modified by introducing e.g. polymer, other than changing the NOBOW concentration. The bulk SmA peak of 90% M6R8 in PM6R8 is shown in Figure 3.5.4a, which is almost resolution-limited. In a ternary mixture of c=49% NOBOW/90% M6R8 in PM6R8, the NOBOW B4 layering peak is similar to pure NOBOW (Table 3.5.1) in spite of the presence of the polymer, further confirming the robust formation of the helical nanofilaments. As expected, the SmA phase of M6R8 is nanoconfined in the network of NOBOW nanofilaments. The XRD layering peak shown in Figure 3.5.4b is very diffuse and the SmA layers of M6R8 have a finite correlation length of ξ~122 Å or about 4 layers. By increasing the concentration of PM6R8, we can reduce the correlation length of the SmA phase further to 39 Å, corresponding to just one layer, which means that the ordering of smectic layer is limited to the neighboring layer, as shown in Figure 3.5.4c in a mixture of c=50% NOBOW/77% M6R8 in PM6R8.

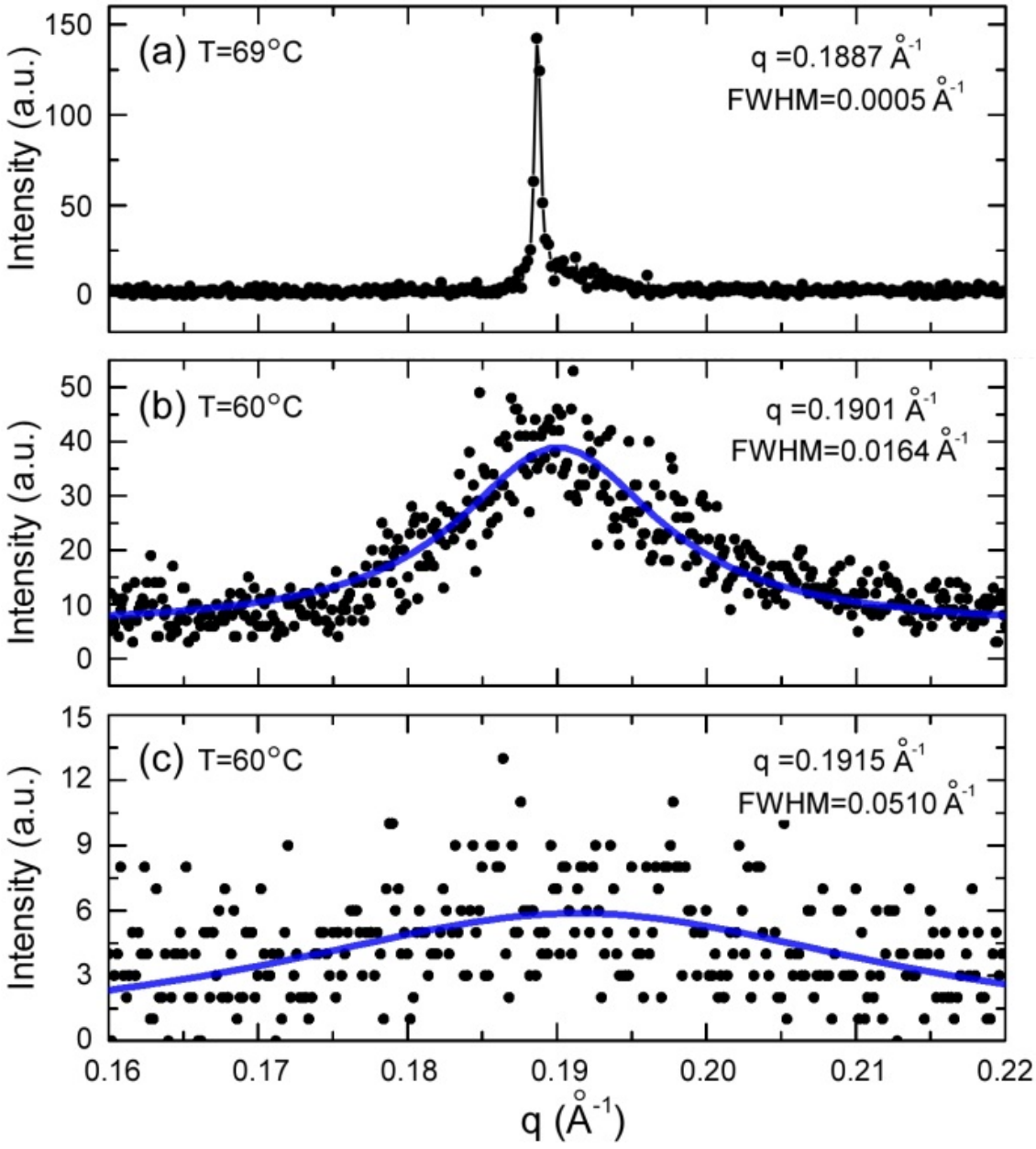

Figure 3.5.4: XRD of 90% M6R8 in PM6R8, c=49% NOBOW/90% M6R8 in PM6R8 and c=50% NOBOW/77% M6R8 in PM6R8 mixtures. (a) XRD scan of 90% M6R8 in PM6R8 showing almost resolution-limited SmA peak of M6R8. (b) A diffuse SmA peak of M6R8 is detected in a c=49% NOBOW/90% M6R8 in PM6R8 mixture. (c) Only a very weak, broad SmA peak of M6R8 is observed in a mixture of c=50% NOBOW/77% M6R8 in PM6R8. The high temperature SmC peak of PM6R8 is too weak to be detected in the ternary mixtures.

P3HT is one of the most widely used materials in organic photo voltaic. P3HT is not a mesogen but in a solvent forms a suspension of crystalline nano whiskers [62], which are similar to the B4 helical nanofilaments, except twisting. Figure 3.5.5a show the XRD scan of pure P3HT, which has a diffuse peak around q~0.30 $Å^{-1}$, due to the finite width of the nanowires (finite ordering). However, different from other systems, where the peak is usually broadened in the mixture as the phase is nanoconfined in the random network of the B4 helical nanofilaments and the ordering is only limited to a very short range, the peak from P3HT crystal phase in the mixture is sharper than that in the pure sample, which may associate with the change of surface tension in the mixture, as shown in Figure 3.5.5b. To understand this, the phase diagram of a c=50% NOBOW/P3HT mixture is shown in Figure 3.5.5c. The binary mixture mixes well in the high temperature isotropic range. Upon cooling, instead of the NOBOW B4 phase, P3HT first separates from the isotropic, forming crystals of nano whiskers. The same peak position of pure P3HT and NOBOW/P3HT mixture indicates that all NOBOW molecules are expelled from the P3HT. After that, only NOBOW molecules left, and they undergo I-B2 and B2-B4 phase transitions, which shows the B2 peak at high temperature and the B4 peak at low temperature. So there is no nanoconfinement in this case but complete phase separation.

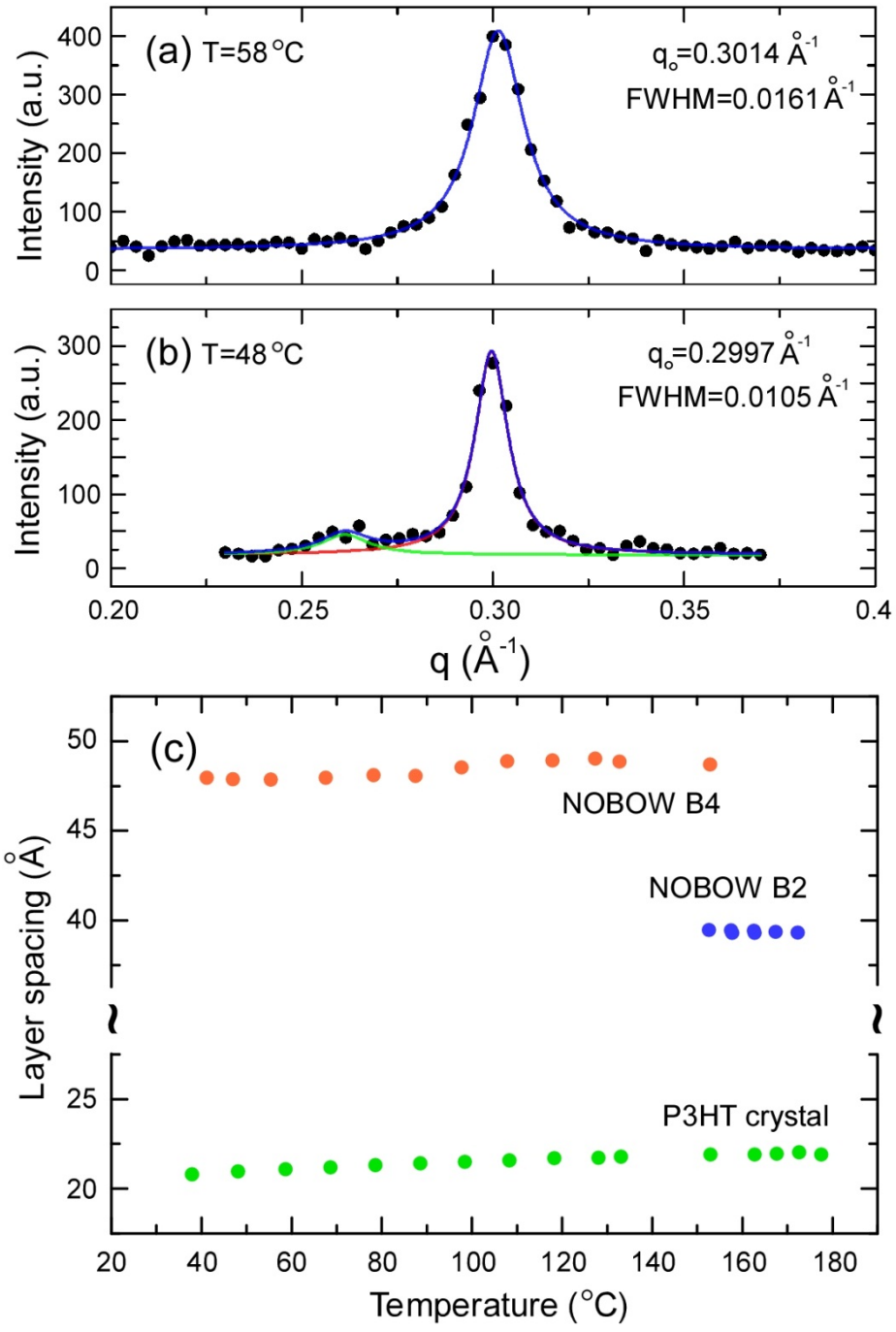

Figure 3.5.5 XRD of the binary mixture of NOBOW/P3HT. (a) XRD scan of pure P3HT. The peak of P3HT crystal phase is diffuse even in a pure sample. (b) XRD scan of a c=50% NOBOW/P3HT mixture. The P3HT peak is sharper in the mixture. The small peak to the left of the P3HT crystal layering peak is the second harmonic of the NOBOW B4 phase. (c) Layer spacing of NOBOW B2 and B4 phases and P3HT crystal phase in a c=50% NOBOW/P3HT mixture. The layer spacings are essentially independent of temperature.

From the above discussion, we know that the simple method can prepare the designated nanoconfined system. However, we need to characterize the 3D structure of the helical nanofilament random network. Nucleation and growth of the helical nanofilaments have been characterized. Individual nucleation and growth event has also been detected by highly sensitive DSC [64, 65] and it has been proposed that asymmetry in viscoelastic property plays an important role in the nano scale phase separation [66]. An example of the nucleation and growth of the helical nanofilaments is shown in Figure 3.5.6a. Because the influence of the helical nanofilaments, 8CB is randomly aligned, contributing the bright color. Places where 8CB is aligned by the glass substrate appear dark. In order to get an overview of the structure of the helical nanofilament random network, Figures 3.5.6b and 3.5.6c shows the formation of the helical nanofilaments in a reservoir of hexadecane. The helical nanofilament random networks appear as sol-gel macroscopically. In the microscopic scale, as shown in Figure 3.5.6d, we can identify individual helical nanofilament. Figure 3.5.6e, shows individual helical nanofilament near the glass substrate, where the network forms via bifurcation growth of helical nanofilaments. Figure 3.5.6f shows the pores formed in the bulk, where the material is expelled to the interstitial volume. Complementary to Figure 3.5.6f, Figure 3.5.6g shows a plane where most helical nanofilaments intersect the fracture plane normally or obliquely. The results provide a direct confirmation of nano-phase separation in the binary system, with the NOBOW B4 helical nanofilaments forming a dilute random network uniformly distributed in the bulk and the 8CB filling the interstitial volume. A global picture emerged from those images is that through the bifurcation growth of helical nanofilaments, the helical nanofilament forms a three-dimensional porous structure.

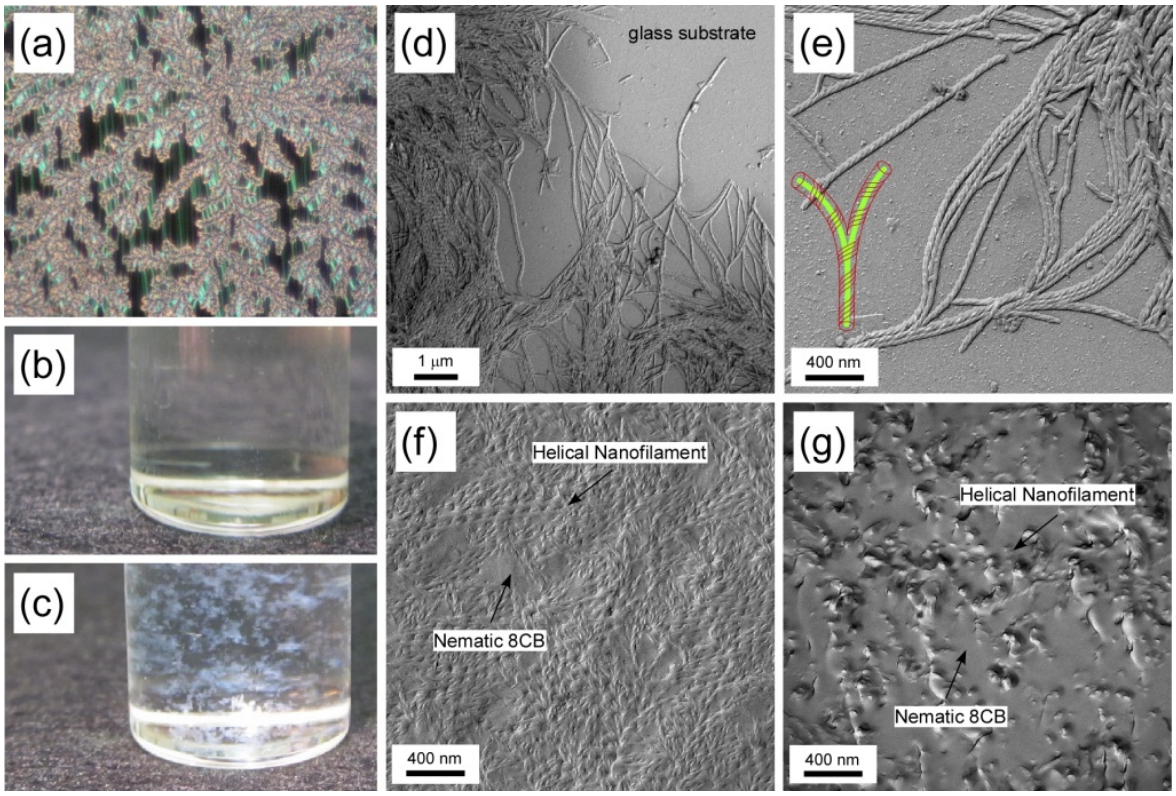

Figure 3.5.6: 3D structure of helical nanofilament random network. (a) Fractal growth of helical nanofilaments in a c=11% NOBOW/8CB mixture at T=30°C. (b) A c=6.5*10^{-3} wt% NOBOW/hexadecane mixture shows clear isotropic blend at T=100°C (c) At room temperature, NOBOW phase separates from hexadecane and forming random network of helical nanofilament, appearing as white, gel-like stuff. (d) FFTEM image of a c=25% NOBOW/8CB mixture quenched at T=37°C, showing the bulk texture of nanoconfined 8CB within the helical nanofilament network. (e) FFTEM image of a c=25% NOBOW/8CB mixture quenched at T=37°C, showing individual helical nanofilament near the glass substrate. Inset is a model of the chirality-preserving growth of helical nanofilaments, where local variations in the elastic energy determine the growth velocity profile of the filament tip and lead to spontaneous bifurcation. (f) An example of a nanoconfined system of a c=25% NOBOW/8CB mixture, where we see a random network of NOBOW B4 helical nanofilaments with 8CB filling the interstitial volume. (g) FFTEM image of a c=25% NOBOW/8CB mixture obtained after quenching an open hemispherical sample at T≈80°C and cutting it deep into the bulk. Randomly oriented helical imprints of the NOBOW B4 phase are uniformly distributed in the bulk, while the isotropic 8CB appears as smooth regions between the helical imprints.

The nanoconfined system prepared with 8CB confined in silica aerogel has been well studied [67]. Therefore, we use the same method described in [68] to further investigate the phase property of the material confined by the helical nanofilament network. The background- and bulk portion-subtracted peaks I(δq) of a c=60% NOBOW/JR6-65C mixture plotted versus $|\delta q|=|q-q_o|$ is shown in Figure 3.5.7. The peaks can be fitted using $I(\delta q)=\chi/[1+(\xi\delta q)^{1+\kappa}]$ quite well as shown in the images. When $\xi\delta q>>1$, the I(δq) tails fall as $\delta q^{-(1+\kappa)}$ with $\kappa\sim1.028$, which is slightly larger than 1 and is indicative of a small crossover to anomalous elasticity in the nanoconfined systems.

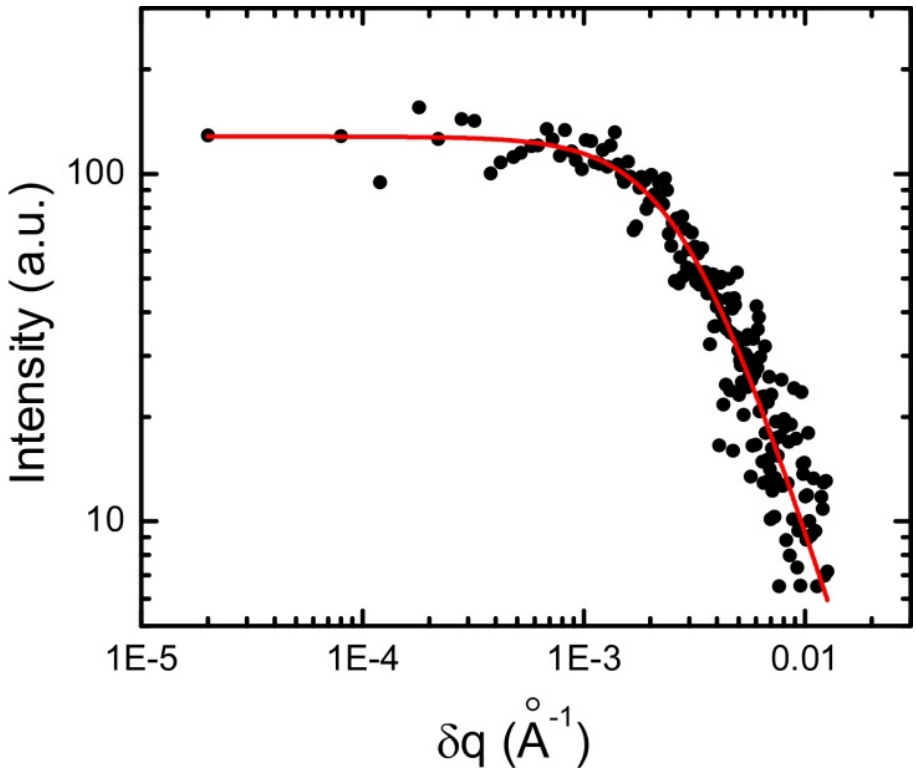

Figure 3.5.7: Background- and bulk portion-subtracted peaks I(δq) plotted versus $|\delta q|=|q-q_o|$ of a c=60% NOBOW/JR6-65C mixture. The symmetry, i.e. the overlap of the $\delta q>0$ and $\delta q<0$ points, indicates suppression of the bulk divergence of $\xi_{||}/\xi$. Fit to $I(\delta q)=\chi/[1+(\xi\delta q)^{1+\kappa}]$ is excellent with $\chi\sim128.2$,$\xi\sim352.3$, $\kappa\sim1.028$.

Compared with conventional porous materials, there are several advantages of preparing nanoconfined systems using this method: (1) The pore size of the helical nanofilament random network can be easily changed by preparing different concentration of the mixtures, or by adding e.g. polymers. (2) The preparation process is simple, where the isotropic blend is cooled down to a desired temperature. There is no problem of filling the material or porous structure collapsing. (3) The isotropic blends can be filled in any three-dimensional structure, e. g. it can be modified to prepare pseudo two-dimensional nanoconfined system such as in cells. (4) The chiral boundary condition presented by the B4 helical nanofilaments is unique and novel phenomena may appear from this, for example, enables nematic 5CB (achiral rod-like molecule) to fill space with a chiral director field, which strongly enhances the non-linear optical rotation [14]. (5) The chirality of the B4 phase or the chiral boundary condition presented by the B4 helical nanofilament can be tuned by chiral dopants [17]. (6) These helical nanofilaments can be used as templates for making porous chiral selector materials if the chiral boundary condition is strong enough to direct the chemical reaction.

In a summary, the B4 phase of bent-core liquid crystals is one of the most complex hierarchical self-assemblies in soft materials, with the molecules forming helical nanofilaments. We have mixed several materials with NOBOW in order to study their behavior in the nanoconfined environment presented by the nanofilament network. All systems studied are completely miscible at high temperature, where they are isotropic. In mixtures rich in NOBOW, the B4 phase separates from the solution upon cooling, forming random networks of helical nanofilaments, leaving the remaining isotropic material in the interstitial volumes. This kind of nano phase segregation resulting from the spontaneous

nanoscale self-assembly of the nanofilaments offers a novel way of preparing nanoconfined fluid systems, e.g. the formation of nanoconfined systems prepared by cooling down isotropic mixtures of the B4 material with other materials. Different kinds of nanoconfined systems prepared in this way have been described.

Bibliography

[1] L. Pasteur: Recherches sur les relations qui peuvent existerentre la forme cristalline, la composition chimique et le sens de la polarisation rotatoire. *Ann. Chim. Phys.* 1848, **24**, 442-459.

[2] D. K. Kondepudi, R. J. Kaufman, and N. Singh: Chiral symmetry breaking in sodium chlorate crystallization. *Science* 1990, **250**, 975-976.

[3] J. M. McBride, and J. C. Tully: Physical chemistry: Did life grind to a start? *Nature* 2008, **452**, 161-162.

[4] W. L. Noorduin, T. Izumi, A. Millemaggi, M. Leeman, H. Meekes, W. J. P. Van Enckevort, R. M. Kellogg, B. Kaptein, E. Vlieg, and D. G. Blackmond: Emergence of a single solid chiral state from a nearly recemic amino acid derivative. *J. Am. Chem. Soc.* 2008, **130**, 1158-1159.

[5] H. Takezoe, and Y. Takanishi: Bent-core liquid crystals: Their mysterious and attractive world. *Jpn. J. Appl. Phys.* 2006, **45**, 597-625.

[6] R. A. Reddy, and C. Tschierske: Bent-core liquid crystal: Polar order, superstructural chirality and spontaneous desymmetrisation in soft matter systems. *J. Mater. Chem.* 2006, **16**, 907-961.

[7] T. Niori, T. Sekine, J. Watanabe, T. Furukawa, and H. Takezoe: Distinct ferroelectric smectic liquid crystals consisting of banana shaped achiral molecules. *J. Mater. Chem.* 1996, **6**, 1231-1233.

[8] D. R. Link, G. Natale, R. Shao, J. E. Maclennan, N. A. Clark, E. Körblova, and D. M. Walba: Spontaneous formation of macroscopic chiral domains in a fluid smectic phase of achiral molecules. *Science* 1997, **278**, 1924-1927.

[9] D. M. Walba, E. Körblova, R. Shao, J. E. Maclennan, D. R. Link, M. A. Glaser, and N. A. Clark: A ferroelectric liquid crystal conglomerate composed of racemic molecules. *Science* 2000, **288**, 2181-2184.

[10] D. A. Coleman, J. Fernsler, N. Chattham, M. Nakata, Y. Takanishi, E. Körblova, D. R. Link, R.-F. Shao, W. G. Jang, J. E. Maclennan, O. Mondainn-Monval, C. Boyer, W. Weissflog, G. Pelzl, L.-C. Chien, J. Zasadzinski, J. Watanabe, D. M. Walba, H. Takezoe, and N. A. Clark: Polarization-modulated smectic liquid crystal phases. *Science* 2003, **301**, 1204-1211.

[11] L. E. Hough, M. Spannuth, M. Nakata, D. A. Coleman, C. D. Jones, G. Dantlgraber, C. Tschierske, J. Watanabe, E. Korblova, D. M. Walba, J. E. Maclennan, M. A. Glaser, and N. A. Clark: Chiral isotropic liquids from achiral molecules. *Science* 2009, **325**, 452-456.

[12] L. E. Hough, H. T. Jung, D. Krüerke, M. S. Heberling, M. Nakata, C. D. Jones, D. Chen, D. R. Link, J. Zasadzinski, G. Heppke, J. P. Rabe, W. Stocker, E. Korblova, D. M. Walba, M. A. Glaser, and N. A. Clark: Helical nanofilaments phases. *Science* 2009, **325**, 456-

460.

[13] Y. Takanishi, G. J. Shin, J. C. Jung, S.-W. Choi, K. Ishikawa, J. Watanabe, H. Takezoe, and P. Toledano: Observation of very large chiral domains in a liquid crystal phase formed by mixtures of achiral bent-core and rod molecules. *J. Mater. Chem.* 2005, **15**, 4020-4024.

[14] T. Otani, F. Araoka, K. Ishikawa, and H. Takezoe: Enhanced optical activity by achiral rod-like molecules nanosegregated in the B4 structure of achiral bent-core molecules. *J. Am. Chem. Soc.* 2009, **131**, 12368-12372.

[15] C. Zhu, D. Chen, Y. Shen, C. D. Jones, M. A. Glaser, J. E. Maclennan, and N. A. Clark: Nanophase segregation in binary mixtures of a bent-core and a rodlike liquid-crystal molecule. *Phys. Rev. E* 2010, **81**, 011704/1-5.

[16] K. Takekoshi, K. Ema, H. Yao, Y. Takanishi, J. Watanabe, and H. Takezoe: Appearance of a liquid crystalline nematic-isotropic critical point in a mixture system of rod- and bent-shaped molecules. *Phys. Rev. Lett.* 2006, **97**, 197801.

[17] F. Araoka, Y. Takanishi, H. Takezoe, A. Kim, B. Park, and J. W. Wu: Electrogyration effect in a chiral bent-core molecular system. *J. Opt. Soc. Am. B* 2003, **20**, 314-320.

[18] K. Shiromo, D. A. Sahade, T. Oda, T. Nihira, Y. Takanishi, K. Ishikawa, and H. Takezoe: Finite enantiomeric excess nucleated in an achiral banana mesogens by chiral alignment surfaces. *Angew. Chem. Int. Ed.* 2005, **44**, 1948-1951.

[19] S.-W. Choi, S. Kang, Y. Takanishi, K. Ishikawa, J. Watanabe, and H. Takezoe: Intrinsic chirality in a bent-core mesogen induced by extrinsic chiral structures. *Angew. Chem. Int. Ed.* 2006, **45**, 6503-6506.

[20] H. Niwano, M. Nakata, J. Thisayukta, D. R. Link, H. Takezoe, and J. Watanabe: Chiral memory on transition between the B2 and B4 phases in a achiral banana-shaped molecular system. *J. Phys. Chem. B* 2004, **108**, 14889.

[21] S.-W. Choi, T. Izumi, Y. Hoshino, Y. Takanishi, K. Ishikawa, J. Watanabe, and H. Takezoe: Circular-polarization-induced enantiomeric excess in liquid crystals of an achiral, bent-shaped mesogen. *Angew. Chem. Int. Ed.* 2006, **45**, 1382–1385.

[22] A. Jákli, G. G. Nair, C. K. Lee, R. Sun, and L. C. Chien: Macroscopic chirality of a liquid crystal from nonchiral molecules. *Phys. Rev. E* 2001, **63**, 061710/1-5.

[23] E. A. Matsumoto, G. P. Alexander, and R. D. Kamien: Helical nanofilaments and the high chirality limit of smectics A. *Phys. Rev. Lett.* 2009, **103**, 257804/1-4.

[24] R. D. Kamien: The geometry of soft materials: A primer. *Rev. Mod. Phys.* 2002, **74**, 953-971.

[25] The angular dependence of the birefringence was first reported by A. Rastegar, G. Wulterkens, H. Verscharen, Th. Rasing, G. Heppke: A shear cell for aligning and measuring birefringence of bow-shaped (banana) liquid crystals. *Review of Scientific*

Instruments **2000**, 71, 4492/1-5.

[26] See, for example, G. Pelzl, S. Diele, K. Ziebarth, W. Weissflog, and D. Demus: Filled smectic A phases in binary liquid-crystalline systems of terminal-nonpolar compounds. V. Smectic A phases with unusually high ratio of the layer spacing and the average molecular length. *Liquid Crystals* 1990, **8**, 765-773.

[27] W. Weissflog, L. Kovalenko, I. Wirth, S. Diele, G. Pelzl, H. Schmalfuss, and H. Kresse: SmA-SmC-B2 polymorphism in an achiral cyano substituted banana-shaped mesogens. *Liquid Crystals* 2000, **27**, 677-681.

[28] M. W. Schröder, S. Diele, G. Pelzl, N. Pancenko, and W. Weissflog: Transitions between the B2 phase and more usual smectic phases in binary systems of banana-shaped with calamitic mesogens. *Liquid Crystals* 2002, **29**, 1039-1046.

[29] R. Pratibha, N. V. Madhusudana, B. K. Sadashiva: On some liquid crystalline phases exhibited by compounds made of bent-core molecules and their mixtures with rod-like molecules. *Pramana* 2003, **61**, 405-415.

[30] R. Pratibha, N. V. Madhusudana, B. K. Sadashiva: An orientational transition of bent-core molecules in an anisotropic matrix. *Science* 2000, **288**, 2184-2187.

[31] J. Thisayukta, H. Niwano, H. Takezoe, and J. Watanabe: Effect of chiral dopant on a helical Sm1 phase of banana-shaped N-n-O-PIMB molecules. *J. Mater. Chem.* 2001, **11**, 2717-2721.

[32] D. M. Walba, L. Eshdat, E. Körblova, and R. K. Shoemaker: On the nature of the B4 banana phase: Crystal or not a crystal. *Crystal Growth & Design* 2005, **5**, 2091-2099.

[33] D. L. Patrick, and T. P. Beebe: Substrate defects and variations in interfacial ordering of monolayer molecular films on graphite. *Langmuir* 1994, **10**, 298-302.

[34] M. Oh-e, S.-C. Hong, and Y. R. Shen: Polar ordering at an interface between a liquid crystal monolayer and a rubbed polyimide. *J. Phys. Chem. B* 2000, **104**, 7455-7461.

[35] J. Xue, C. S. Jung, and M. W. Kim: Phase transitions of liquid-crystal films on an air-water interface. *Phys. Rev. Lett.* 1992, **69**, 474-477.

[36] M. N. G. Mul, J. A. Mann: Multilayer formation in thin films of thermotropic liquid crystals at the air-water interface. *Langmuir* 1994, **10**, 2311-2316.

[37] M. Ibn-Elhaj, H. Riegler, H. Möhwald, M. Schwendler, and C. A. Helm: X-ray reflectivity study of layering transitions and the internal multilayer structure of films of three-block organosiloxane amphiphilic smectic liquid crystals at the air-water interface. *Phys. Rev. E* 1997, **56**, 1844-1852.

[38] M. Harke, M. Ibn-Elhaj, H. Möhwald, H. Motschmann: Polar ordering of smectic liquid crystals within the interfacial region. *Phys. Rev. E* 1998, **57**, 1806-1811.

[39] L. Xu, M. Salmeron, and S. Bardon: Wetting and molecular orientation of 8CB on

silicon substrates. *Phys. Rev. Lett.* 2000**, 84**, 1519-1522.

[40] S. Bardon, R. Ober, M. P. Valignat, F. Vandenbrouck, A. M. Cazabat, and J. Daillant: Organization of cyanobiphenyl liquid crystal molecules in prewetting films spreading on silicon wafers. *Phys. Rev. E* 1999, **59**, 6808-6817.

[41] H.Yokoyama, S. Kobayashi, and H. Kamei: Effect of substrate surfaces on the formation of nematic phase at the isotropic-nematic transition. *Appl. Phys. Lett.* 1982, **41**, 438-440.

[42] H. Yokoyama, S. Kobayashi, and H. Kamei: Measurement of director orientation at the nematic-isotropic interface using a substrate-nucleated nematic film. *Mol. Cryst. Liq. Cryst.* 1984, **107**, 311-331.

[43] T. Sekine, T. Niori, J. Watanabe, T. Furukawa, S. W. Choi, and H. Takezoe: Spontaneous helix formation in smectic liquid crystals comprising achiral molecules. *J. Mater. Chem.* 1997, **7**, 1307-1309.

[44] J. Thisayukta, H. Takezoe, and J. Watanabe: Study on helical structure of B4 phase in a achiral banana-shaped molecule. *Jpn. J. Appl. Phys.* 2001, **40**, 3277-3287.

[45] G. Heppke, D. D. Parghi, and H. Sawade: Novel sulphur-containing banana-shaped liquid crystal molecules. *Liq. Cryst.* **2000**, *27*, 313-320.

[46] J. Thisayukta, Y. Nakayama, S. Kawauchi, H. Takezoe, and J. Watanabe: Distinct formation of a chiral smectic phase in achiral banana-shaped molecules with a central core based on a 2,7-dihydroxynaphthalene unit. *J. Am. Chem. Soc.* 2000, **122**, 7441-7448.

[47] A. Eremin, S. Diele, G. Pelzl, and W. Weissflog: Field-induced switching between states of opposite chirality in a liquid-crystalline phase. *Phys. Rev. E* 2003, **67**, 020702/1-3.

[48] J. Ortega, C. L. Folcia, J. Etxebarria, N. Gimeno, and M. B. Ros: Interpretation of unusual textures in the B2 phase of a liquid crystal composed of bent-core molecules. *Phys. Rev. E* 2003, **68,** 011707/1-4.

[49] J.-P. Michel, E. Lacaze, M. Alba, M. de Boissieu, M. Gailhanou, and M. Goldmann: Optical gratings formed in thin smectic films frustrated on a single crystalline substrate. *Phys. Rev. E* 2004, **70**, 011709/1-12.

[50] Ch. S. Rosenblatt, R. Pindak, N. A. Clark, and R. B. Meyer: The parabolic focal conic: A new smectic A defect. *Journal de Physique* 1977, **38**, 1105-1115.

[51] B. I. Senyuk, I. I. Smalyukh, and O. D. Lavrentovich: Undulations of lamellar liquid crystals in cells with finite surface anchoring near and well above the threshold. *Phys. Rev. E* 2006, **74**, 011712/1-13.

[52] J. S. Beck, J. C. Vartuli, W. J. Roth, M. E. Leonowicz, C. T. Kresge, K. D. Schmitt, C. T-W. Chu, D. H. Olson, E. W. Sheppard, S. B. McCullen, J. B. Higgins, and J. L. Schlenker: A new family of mesoporous molecular sieves prepared with liquid crystal templates. *J. Am. Chem. Soc.* 1992, **114**, 10834-10843.

[53] C. T. Kresge, M. E. Leonowicz, W. J. Roth, J. C. Vartuli, and J. S. Beck: Ordered mesoporous molecular sieves synthesized by a liquid crystal template mechanism. *Nature* 1992, **359**, 710-712.

[54] A. Corma: From microporous to mesoporous molecular sieve materials and their use in catalysis. *Chem. Rev.* 1997, **97**, 2373-2419.

[55] T. Asefa, M. J. MacLachlan, N. Coombs, and G. A. Ozin: Periodic mesoporous organosilicas with organic groups inside the channel walls. *Nature* 1999, **402**, 867-871.

[56] L. D. Gelb, K. E. Gubbins, R. Radhakrishnan, and M. Sliwinska-Bartkowiak: Phase separation in confined systems. *Rep. Prog. Phys.* 1999, **62**, 1573-1659.

[57] J. A. Rego, S. Kumar, I. J. Dmochowski and H. Ringsdorf: Synthesis of novel mixed tail triphenylene discotic liquid crystals the search for higher order. *Chem. Commun.* 1996, 1031-1032.

[58] J. A. Rego, S. Kumar, and H. Ringsdorf: Synthesis and characterization of fluorescent, low-symmetry triphenylene discotic liquid crystals: Tailoring of mesomorphic and optical properties. *Chem. Mater.* 1996, **8**, 1402-1409.

[59] E. A. Soto Bustamante, S. V. Yablonskii, B. I. Ostrovskii, L. A. Beresnev, L. M. Blinov, and W. Haase: Antiferroelectric achiral mesogenic polymer. *Chem. Phys. Lett.* 1996, **260**, 447-452.

[60] D. R. Link, N. A. Clark, B. I. Ostrovskii, and E. A. Soto Bustamante: Bilayer-by-bilayer antiferroelectric ordering in freely suspended films of an achiral polymer-monomer liquid crystal mixture. *Phys. Rev. E* 2000, **61**, R37-R40.

[61] H. Sirringhaus, P. J. Brown, R. H. Friend, M. M. Nielsen, K. Bechgaard, B. M. W. Langeveld-Voss, A. J. H. Spiering, R. A. J. Janssen, E. W. Meijer, P. Herwig, and D. M. de Leeuw: Two-dimensional charge transport in self-organized, high-mobility conjugated polymers. *Nature* 1999, **401**, 685-688.

[62] J. A. Lim, F. Liu, S. Ferdous, M. Muthukumar, and A. L. Briseno: Polymer semiconductor crystals. *Materials Today* 2010, **13**, 14-24.

[63] D. Adam, P. Schuhmacher, J. Simmerer, L. Häussling, K. Siemensmeyer, K. H. Etzbach, H. Ringsdorf, and D. Haarer: Fast photoconduction in the highly ordered columnar phase of a discotic liquid crystal. *Nature* 1994, **371**, 141-143.

[64] H. Nagayama, Y. Sasaki, F. Araoka, K. Ema, K. Ishikawa, and H. Takezoe: Discrete and sequential formation of helical nanofilaments in mixtures consisting of bent- and rod-shaped molecules. *Soft Matter* 2011, **7**, 8766-8769.

[65] Y. Sasaki, H. Nagayama, F. Araoka, H. Yao, H. Takezoe, and K. Ema: Distinctive thermal behavior and nanoscale phase separation in the heterogeneous liquid-crystal B4 matrix of bent-core molecules. *Phys. Rev. Lett.* 2011, **107**, 237802/1-4.

[66] H. Tanaka: Unusual phase separation in a polymer solution caused by asymmetric

molecular dynamics. *Phys. Rev. Lett.* 1993, **71**, 3158-3161.

[67] N. A. Clark, T. bellini, R. M. Malzbender, B. N. Thomas, A. G. Rappaport, C. D. Muzny, D. W. Schaefer, and L. Hrubesh: X-ray scattering study of smectic ordering in a silica aerogel. *Phys. Rev. Lett.* 1993, **71**, 3505-3508.

[68] T. Bellini, L. Radzihovsky, J. Toner, and N. A. Clark: Universality and scaling in the disordering of a smectic liquid crystal. *Science* 2001, **294**, 1074-1079.

Chapter 4

Interface Structure of the Dark Conglomerate Phase

4.1 Introduction

Bent-core mesogens have become a major topic of liquid crystal research in recent years, with many new phases and interesting phenomena and properties being discovered and reported [1, 2, 3]. The dark conglomerate (DC) phase, which appears in some bent-core materials immediately below the isotropic phase, is optically isotropic and exhibits spontaneous macroscopic chirality. The phase has a characteristic texture, appearing dark under crossed polarizers and revealing left- and right-handed chiral domains when the polarizers are decrossed [4, 5, 6, 7, 8, 9, 10, 11], properties that early researchers suggested could be evidence of disordered layering and a locally chiral organization of the molecules [4, 11]. The DC phase was recently described as the first known spontaneously chiral isotropic fluid phase of achiral molecules, resembling a lyotropic sponge phase [12, 13] with the entire volume filled with smectic layers and exhibiting both chiral and polar molecular ordering as broken symmetries [14]. Bent-core smectic layers have a tendency to exhibit spontaneous saddle-splay curvature which, if strong enough, disorders the planar layering of the smectic phase into equilibrium, complex random arrays of focal conic defects which are macroscopically isotropic and at the same time macroscopically chiral. The strong tendency for saddle-splay layer deformation in the DC phase is attributed to the orthogonal tilt

directions of the two molecular half-arms ($\mathbf{a}_1$ and $\mathbf{a}_2$ in Figure 4.1.1a), which causes dilation in one half-layer and compression in the other, producing a frustrated state that can be relieved by saddle-splay curvature [14, 16] (Figure 4.1.1b). The birefringence of the DC phase is small because of orientational averaging of the optic axis, and the optical rotation is a manifestation of the local chiral organization of the molecular director and polarization couple [15] and long-range continuity of the smectic layering. While layer curvature motifs of the focal conic domains are expected to be a characteristic feature of this phase, until now, only amorphous/disordered focal conic domains have been observed.

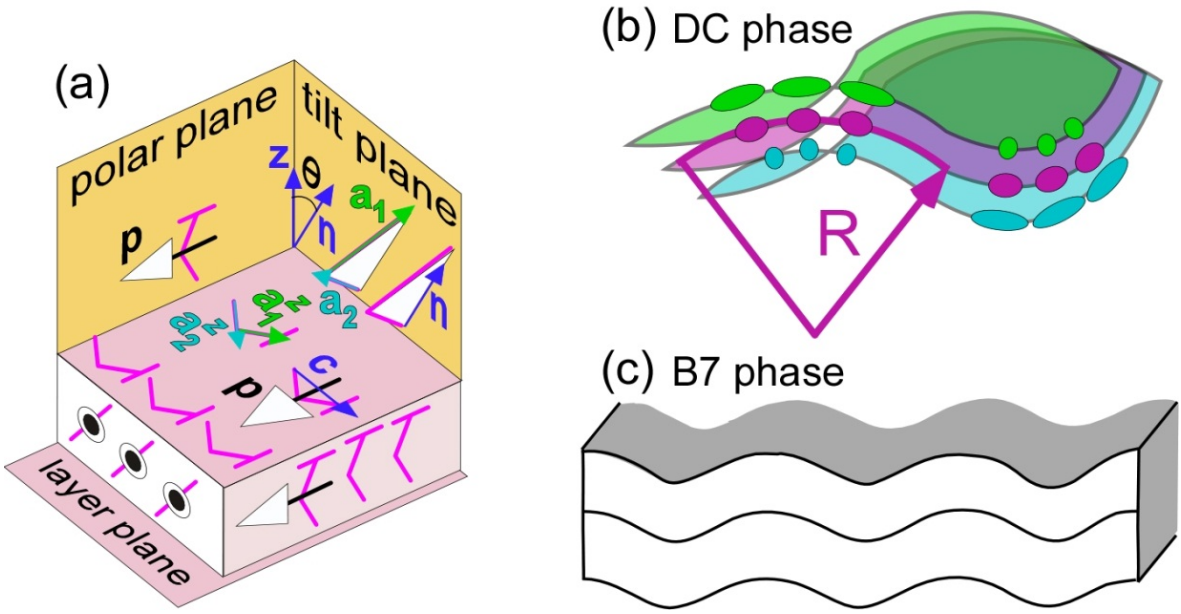

Figure 4.1.1: Phase features of the bent-core liquid crystals. (a) The smectic phase is formed from the stacking of fluid layers of bent-core molecules, where the molecular long axis (**n**) is tilted (by an angle θ) relative to the layer normal (**z**). In addition, polar order of the molecules leads to a macroscopic polarization (**p**) orthogonal to **n** and **z**. The projections of the half-molecular arms ($\mathbf{a}_1$ and $\mathbf{a}_2$) onto the layer plane ($\mathbf{a}_1^z$ and $\mathbf{a}_2^z$) are nearly perpendicular. The four B2 subphases, SmC_SP_S, SmC_SP_A, SmC_AP_S and SmC_AP_A, consist of the four possible bilayer alternations of direction of **p** and **c**. (b) In the DC phase, the intralayer structural mismatch drives the layers to adopt saddle-splay curvature [14]. (c) In the B7 phase, the layer undulations are associated with the formation of periodic polarization splay stripes [30].

4.2 Characterizing the DC phase of Ib

In this section, we present freeze fracture transmission electron microscopy (FFTEM), x-ray diffraction (XRD), and transmission light microscopy (TLM) data showing that focal conic domains in the DC phase of a 4,4′-diphenylmethane (Ar-CH_2-Ar) based bent-core liquid crystal material, compound **Ib** in reference [17], self-assemble into fairly ordered arrays under a variety of conditions. The chemical structure and phase sequence of this compound are shown in Figure 4.2.1a. The aggregation of liquid crystal materials into ordered structures via self-assembly is one of the most exciting interdisciplinary research areas in condensed matter physics, the best known examples being the cholesteric blue phases, which are lattices of nematic disclinations, and the twist grain boundary (TGB) phases, which are periodically twisted assemblies of smectic blocks. This class of materials has potential applications in optoelectronics, biological membranes, and in the creation of nano-patterning templates [18, 19, 20, 21, 22, 23, 24].

The textures observed in the polarized light microscope are typical of the DC phase. On cooling from the isotropic phase, the material appears dark under crossed polarizer and analyzer, with negligible birefringence. Left- and right-handed chiral domains are observed when the polarizers are decrossed, as shown in Figures 4.2.1b and c. On heating from the crystal phase, a texture with both dark and highly birefringent regions appears, shown in Figure 4.2.1d. We will show below that on heating there is coexistence of the DC and B7 phases, with the birefringence due to the B7 domains.

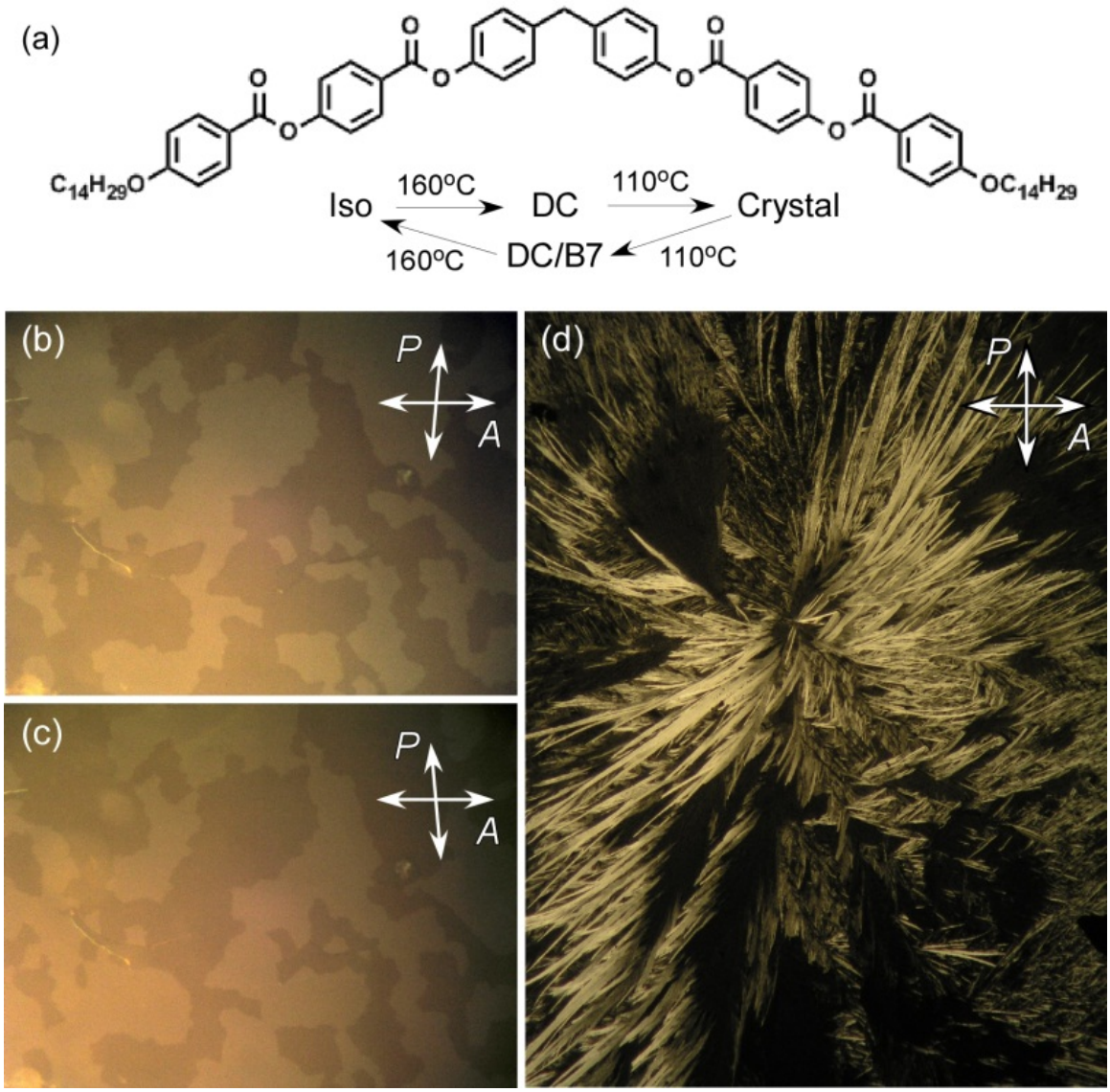

Figure 4.2.1: Transmission light microscope images of the dark conglomerate phase of **Ib** at 140°C. (a) Phase sequence of the bent-core liquid crystal **Ib**. (b, c) Typical texture of left- and right-handed chiral domains observed with decrossed polarizers on cooling. Note that the contrast is greatly enhanced here. When the polarizers are crossed, the cell becomes uniformly dark. (d) On heating from the crystal phase, the cell shows both dark and birefringent domains. Transmission electron microscopy suggests that this is due to the coexistence of the DC (dark) and B7 (birefringent) phases.

X-ray scattering, shown in Figures 4.2.2a-c, shows a diffuse Bragg reflection peak, reflecting the short-range layer ordering, and prominent 2^{nd} and 3^{rd} harmonics. The profile and peak center observed on cooling (blue circles) and heating (black squares) are essentially identical, and each harmonic can be fitted to a single Lorentzian (red curves in Figures 4.2.2a-c) after background subtraction. This kind of disorder strongly resembles the short-range smectic ordering of 8CB (octylcyanobiphenyl, a liquid crystal forming compound) incorporated into the pores of a silica aerogel [25, 26]. In this case, the electron density-density correlation function is a simple exponential, $<\rho(0)\rho(r)>=\exp(-r/\xi)$, with ξ the correlation length, analogous to the time correlation function of the random telegrapher's wave [26]. When the correlations are short-ranged and isotropic, the powder x-ray scattering intensity I(q) (the static structure factor) is proportional to the Fourier transform of the correlation function, yielding a Lorentzian line shape. The peak center and the full width at half maximum (FWHM) of the XRD scans are given in Figure 4.2.2d. The higher harmonics reveal how the local layer ordering deviates from being perfectly periodic: since the peak width increases with the harmonic order, we may conclude that phase fluctuation effects are the principal contribution to the disordering in the DC phase, as in other bulk smectics [27].

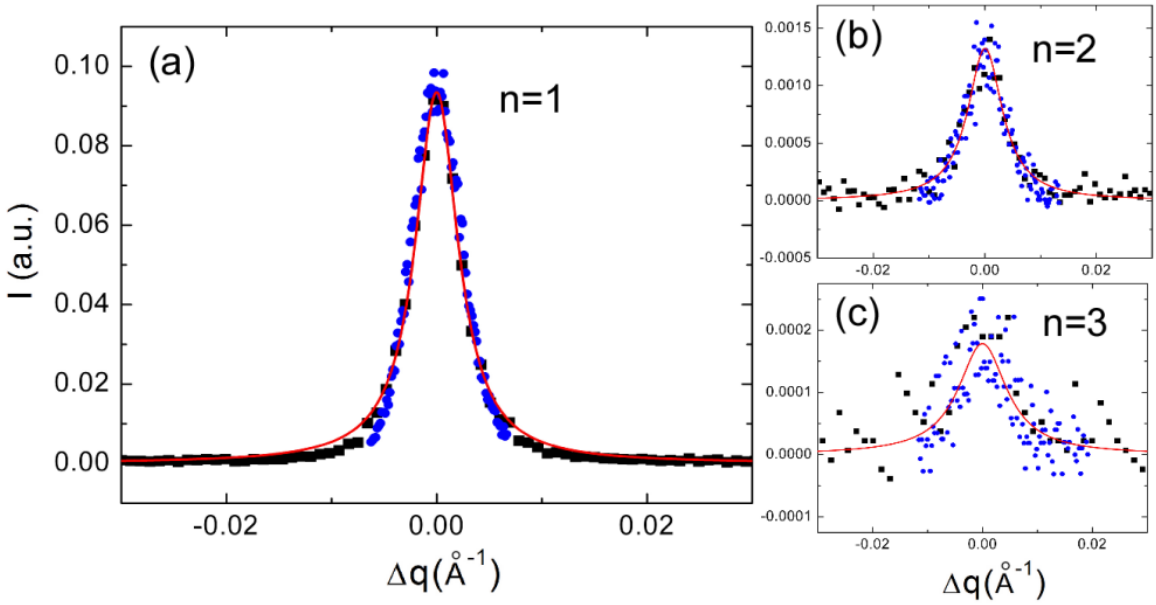

(d)

order	n=1	n=2	n=3
Peak Center (Å^{-1})	0.1384	0.2774	0.4169
FWHM (Å^{-1})	0.0050	0.0076	0.0107

Figure 4.2.2: X-ray scattering from a powder sample of **Ib**. (a) X-ray diffraction pattern from a sample cooled from isotropic to 143°C (blue dots) and heated from crystal to 148°C (black squares). In addition to diffuse Bragg scattering from the smectic layers (n=1), 2nd and 3rd harmonics are also observed (b and c). The profile and peak center position observed on cooling and heating are essentially identical and show little dependence on temperature. In this case, we fit the combined scattering patterns on cooling and heating with a single Lorentzian (red curves in (a)-(c)), after subtracting the background signal and centering all peaks on Δq=0. The peak center and full width at half maximum (FWHM) of the fitted harmonics are indicated in (d). The FWHM increases as the harmonic order goes up, indicating that phase fluctuation effects are the main contribution to disorder in the DC phase.

Freeze fracture transmission electron microscopy (FFTEM) is a powerful imaging technique that enables direct visualization of the layer structure of smectic liquid crystals [14, 28]. Several samples of compound **Ib** in the DC phase with different thermal history were prepared, and the layer structure was studied at both glass (Figure 4.2.3) and air (Figure 4.2.5) surfaces, and along bulk fracture planes (Figure 4.2.4). The transmission electron microscopy (TEM) images shown here have been inverted, so that regions facing the platinum shadowing direction appear bright, i.e., the topography appears as if illuminated by oblique light. Figure 4.2.3a shows a cooled sample fractured near the glass/liquid crystal interface, where the layer normal tends to orient parallel to the glass surface. As we can see from this image, which is similar to those obtained previously, the bulk DC phase is typically made of disordered focal conic domains. At higher magnification (Figure 4.2.3b), well-defined local smectic layers can be observed, both as faint lines where the layers terminate normal to the surface, and as smooth, saddle-shaped domains. This saddle-splay topology is consistent with the model proposed to explain the underlying layer organization of this phase [14], as shown in Figure 4.2.3c. Figures 4.2.4a and b show further examples of the saddle-splay topography with layers in the bulk fracture plane at random orientations.

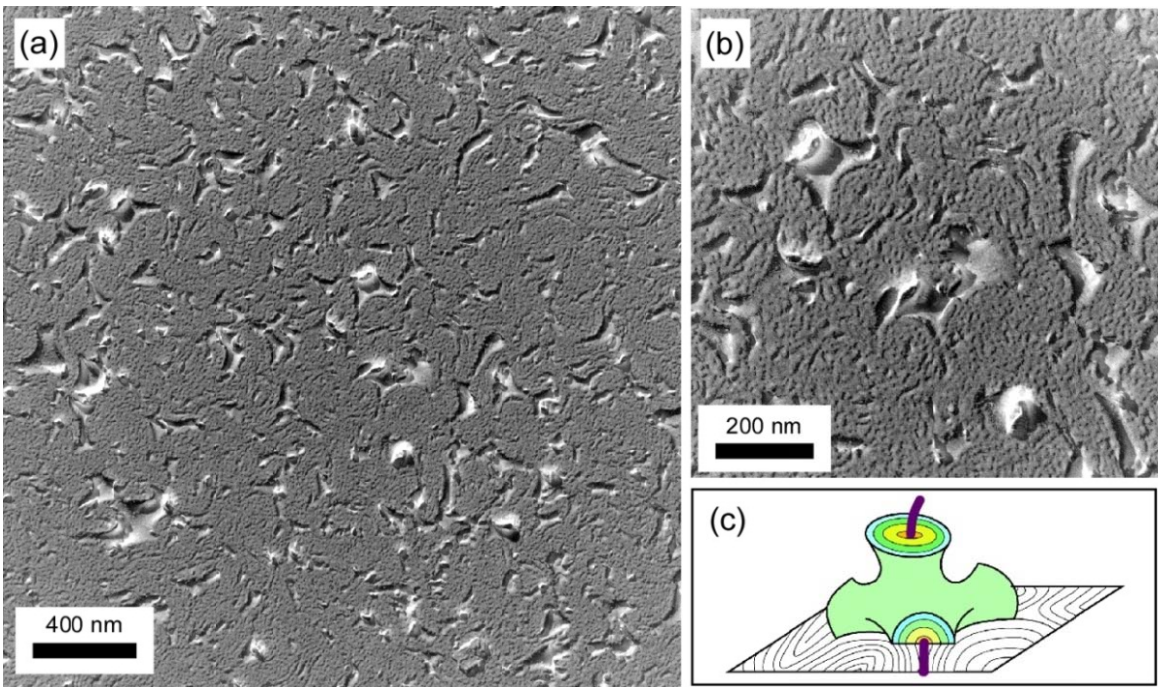

Figure 4.2.3: FFTEM images of the dark conglomerate phase. This sample was quenched after cooling from the isotropic to 140°C, and then fractured at the glass/liquid crystal interface. (a) Disordered focal conic structure characteristic of the DC phase. (b) At higher magnification, we can clearly identify curved layers with saddle-splay topology, corresponding to the model of the local smectic layer orientation shown in (c).

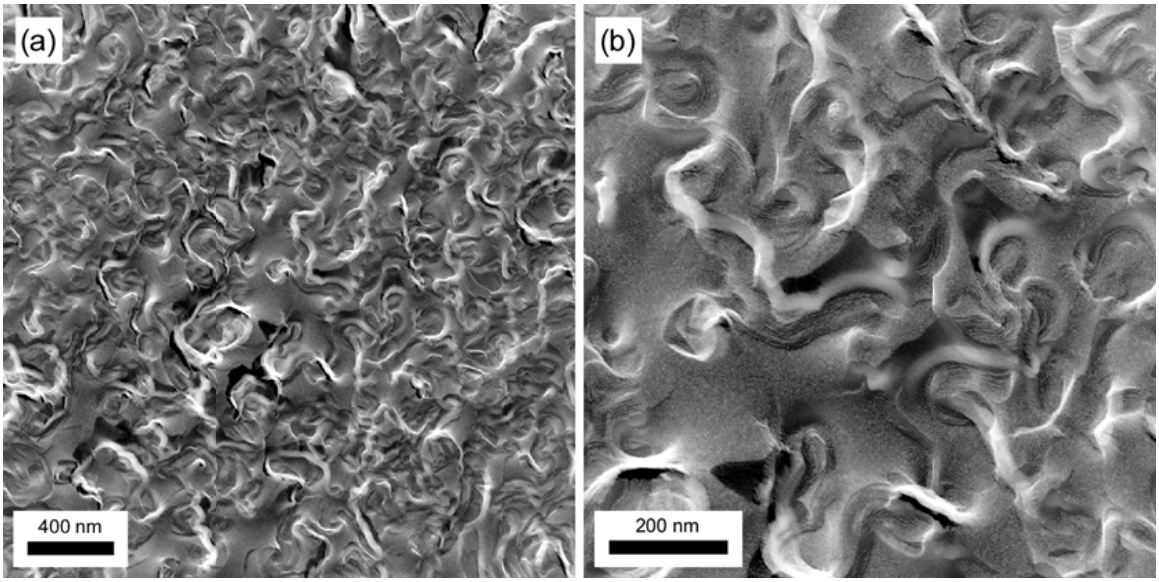

Figure 4.2.4: Freeze fracture transmission electron microscope (FFTEM) images of the dark conglomerate (DC) phase of compound **Ib** quenched after cooling from the isotropic to 140°C, and then fractured in the bulk. (a) A disordered structure is observed, with smooth, saddle-shaped layer surfaces and smectic layer steps. (b) Higher magnification reveals regions where curved smectic layers intersect the fracture plane obliquely.

TEM images of the air/liquid crystal interface obtained on cooling from the isotropic phase reveal with remarkable clarity a well-ordered array of toric focal conic defects (TFCDs) that provide direct confirmation of the plumber's nightmare model of the DC phase (Figure 4.2.5a). Generally, air imposes strong homeotropic alignment at free liquid crystal surfaces, forcing smectic layers to form parallel to the surface [29]. The bulk preference for saddle-splay curvature in the DC phase is then accommodated at the surface by the formation of TFCDs. The internal fluidity of the phase allows these TFCDs to anneal into a quasi-ordered array, essentially forming a hexagonal close-packed structure with a periodicity of about 400 nm, correspond to the minimum elastic free energy [14]. Focal conic domains with negative Gaussian curvature have been proposed as a general model for the spatial organization of the DC phase [14]. The topology of the focal conic domains at different depths is shown in Figure 4.2.5b. The cross section of the surface structure in Figure 4.2.5a is depicted in the top image of Figure 4.2.5b. This surface structure should penetrate to some extent into the bulk and possible example of ordered FCDs below the surface is shown in the middle image of Figure 4.2.5b. Where space is filled predominantly with this type of focal conic domains with hexagonal close packing, the plumber's nightmare structure of Schoen's GW surface describes the three dimensional crystalline structure of the TFCDs well. This kind of order may be lost in the bulk, especially when the sample is very thick. The bottom image in Figure 4.2.5b shows disordered focal conic domains deep in the bulk, the conventional disordered plumber's nightmare structure. It is clear from typical TEM images, such as those shown in Figures 4.2.3 and 4.2.4, that the saddle-splay structure in a cooled sample is much less ordered in the bulk than at a free surface.

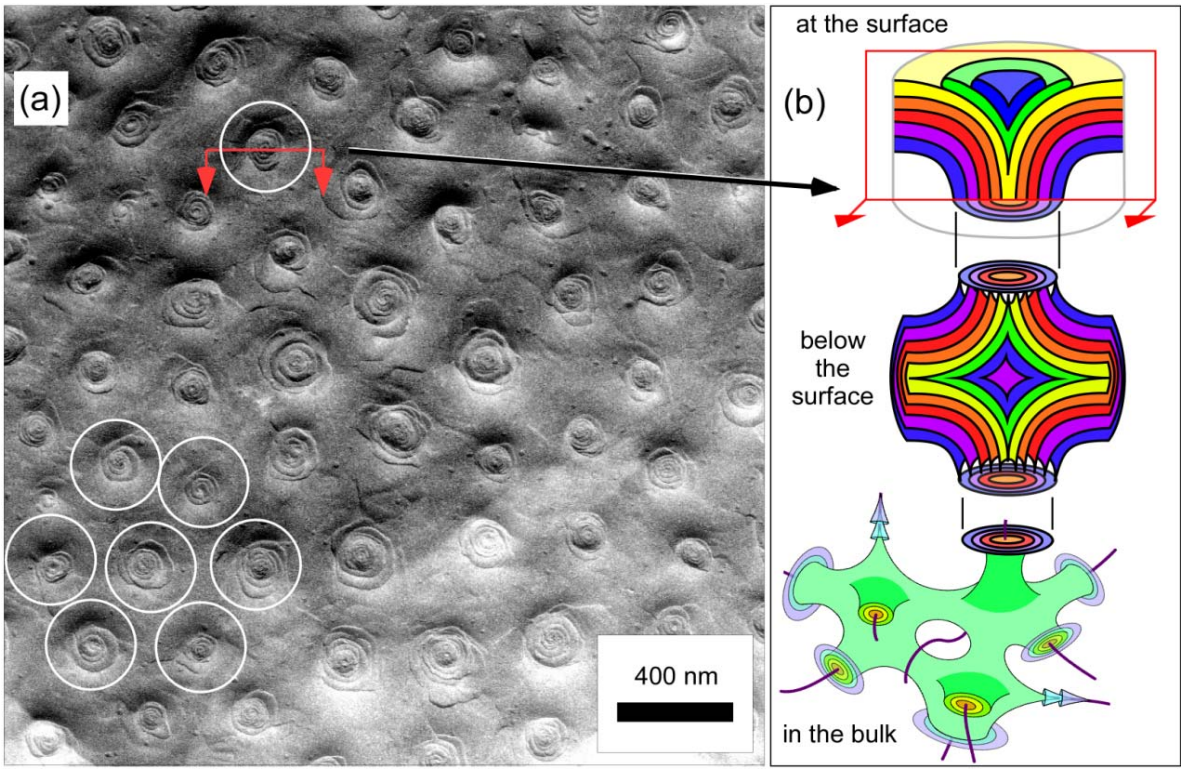

Figure 4.2.5: TEM image of the DC phase at the free surface of a drop of liquid crystal material placed on a glass cover slip that was quenched after cooling from isotropic to 140°C. (a) Toric focal conic domains (TFCDs) self-assemble into a fairly regular, hexagonal close-packed structure. The small "pits" in the image are artifacts due to ice crystals which condensed on the liquid crystal surface while the quenched sample was being transferred to the shadowing machine. (b) Topology of the focal conic domains at different depths. The top image shows a cross section of the toric focal conics at the free surface. The middle image shows a cross section of possible ordered toric focal conic domains some distance below the surface, which can be modeled by plumber's nightmare structure (Schoen's GW surface) to construct a three dimensional crystalline structure with six-fold symmetry. The bottom image shows disordered focal conic domains deep in the bulk, organized in the conventional disordered plumber's nightmare structure.

As in most bent-core systems, however, the morphology and phase of compound **Ib** depend on the thermal trajectory. The bulk DC structure seen on heating, shown in Figure 4.2.6a (expanded in Figure 4.2.6b), is much more regular than that observed on cooling, and strongly resembles the ordered structure observed at the air/liquid crystal interface on cooling (Figure 4.2.5a). The layers are highly curved, with features characteristic of saddle-splay topology and periodicity similar to that seen on cooling. In addition, B7 regions, identifiable by their characteristic layer undulations (Figure 4.1.1c) [30], here with periodicity p~60 nm (see Figure 4.2.7), are seen in coexistence with DC regions. However, in the regions with typical DC texture the layers are locally smooth and there is no evidence of layer undulations, which, if the undulations had the same periodicity as on flat surfaces, would be apparent on the saddle-splay topography of Figure 4.2.6. As noted above, the optical texture obtained on heating from the crystal phase, shown in Figure 4.2.1d, shows both birefringent and dark regions. This is due to the coexistence of the highly birefringent B7 phase and the isotropic DC phase. The coexistence of these two phases is also observed in the three materials investigated in reference [14], with the two textures even overlaid in **CITRO**, where distinct saddle-shaped domains are decorated with B7 layer undulations. It seems that the saddle-splay curvature driven by the intra-layer structural mismatch and the layer undulations associated with periodic polarization splay stripes are independent of each other and may occur either separately or simultaneously.

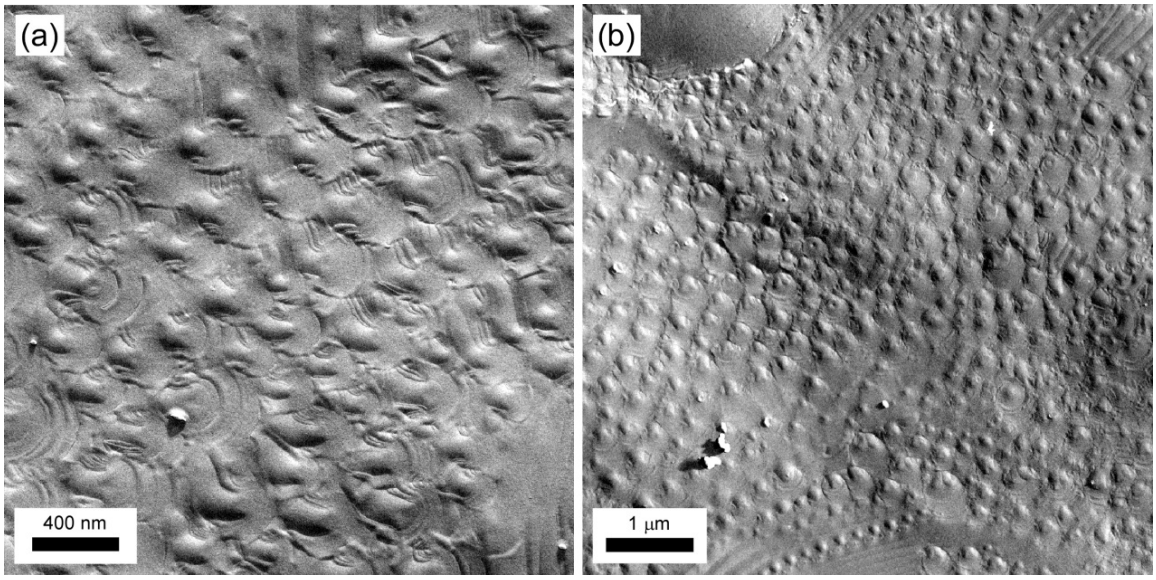

Figure 4.2.6: FFTEM images of the dark conglomerate phase. The sample was quenched after heating from the crystal phase to 140°C, and then fractured in the bulk. (a) As with the cooled sample in Figure 4.2.4, features characteristic of saddle-splay topology are observed, with the curved layers forming an ordered structure reminiscent of the toric focal conic domains of Figure 4.2.5. (b) Instead of the amorphous arrangement seen on cooling from the isotropic phase, the saddle-splay regions are quite well ordered here, with hexagonal close-packing.

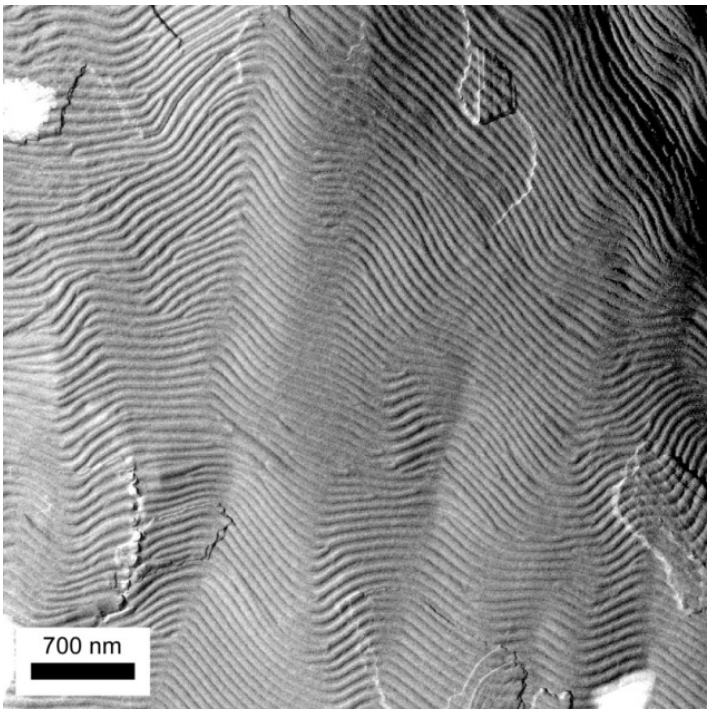

Figure: 4.2.7: FFTEM image of the B7 phase quenched after heating from the crystal phase to 140°C, and then fractured in the bulk. The smectic layers are oriented parallel to the fracture plane and show typical B7 layer undulations. Several layer steps can also be identified in this image.

In a summary, it has been shown previously that the DC phase energetically prefers smectic layers with saddle-splay deformation and that focal conic domains (FCDs) with negative Gaussian curvature, characterize the spatial organization of the DC phase in this case [14]. However, the observation of globally disordered FCDs on cooling may arise from some sort of quenched disorder which stabilizes a glassy array of focal conics. In the present study of a 4,4′-diphenylmethane based bent-core material, at the air/liquid crystal interface, because of the homeotropic alignment imposed by air, the intrinsic preference for saddle-splay curvature and the fluidity of the liquid crystal phase, the FCDs anneal into a quasi-ordered array, which may be thermodynamically preferred. On heating from the crystal phase, the ordering of the FCDs is also enhanced in the bulk, and B7 regions are seen in coexistence with the DC structure. The absence of quenched disorder at the air/liquid crystal interface, and in the bulk upon heating into the DC phase, suggests that the bulk ordering of the DC phase is thermodynamically close by and that under the right conditions three dimensional periodic focal conic arrays may be achievable in this phase, which opens the way for the development of two-dimensional or even three-dimensional periodic dielectric media for photonic crystal applications.

4.3 Topography of the B4, B7 and DC phases at the air/liquid crystal interface

Bent-core liquid crystal molecules have attracted intense interest due to the interplay of chirality, molecular bend and molecular tilt [31] and have exhibited a set of peculiar phases named as B1-B8, none of which exists in rod-like liquid crystals. Among these phases, the B4 (helical nanofilament driven by saddle-splay curvature), B7 (layer undulation driven by polarization modulation), and DC phases (disordered focal conic driven by saddle-splay curvature) are particular interesting, forming fantastic, complex microstructures [14, 16, 30]. Though the structural bases of these phases have already been clarified and researchers have directly observed these structural elements in the bulk by freeze-fracture transmission electron microscopy (FFTEM), not much attention has been paid to the surface structures of these phases. At the air/liquid crystal interface, there is no confinement on the liquid crystal and the molecules are free to flow in response to the internal stress raised during the formation of the liquid crystal phase. Usually liquid crystal molecules prefer to align homeotropically at the interface. This kind of alignment by nature is homogeneous everywhere and imposes rotational and translational symmetry at the interface. Combined with the fluidity of the liquid crystal phase, the bulk structure will compromise and anneal into more ordered structure at the interface. We have observed a variety of different surface topographies, some of which are totally different from the bulk structures, confirming that the intrinsic fluidity of the liquid crystal phases and homeotropic alignment at the air/liquid crystal interface enhances the self-assembly of bent-core molecules.

In this section, we will describe the surface topographies of the B4, B7 and DC phases of bent-core molecules at the air/liquid crystal interface. Though these phases have different

structures, they are correlated with each other. For example, the layer undulations of the B7 phase can be observed in the disordered focal conics of the DC phase [14], both the B4 and DC phases are driven by intra-molecular mismatch [14, 16], and the ground states of the B4, B7 and DC phases are supposed to be synclinic and ferroelectric. Studies of the surface topography will help people further understand the microstructure of these phases and demonstrate the potential application of periodic surface structures as two-dimensional or even three-dimensional photonic crystals. The prerequisite for applications, however, is understanding the type, size and spatial distribution of the defect domains at the surface, a topic which will be discussed in detail in this section.

Surface structure of the B4 phase

The B4 phase is one of the most complex hierarchical self-assemblies known in soft materials. The chemical structure and phase sequence of NOBOW is shown in Figure 4.3.1a, and the surface topography of the B4 phase at the air/liquid crystal interface in Figure 4.3.1b. Individual helical nanofilaments can clearly be identified at the surface. Locally, helical nanofilaments form coherent, homochiral arrays, which can be well understood in terms of the chirality-preserving growth of the filaments (section 3.2 in Chapter 3). The measured filament width w=35 nm and half pitch p=115 nm are consistent with that in the bulk (for example, Figure 3.2.5 in Chapter 3, showing conventional FFTEM images where the samples are fractured before coating and the replicas show the structure in the bulk). B4 helical nanofilaments appear to be quite robust, with the structure retained from the bulk to the surface.

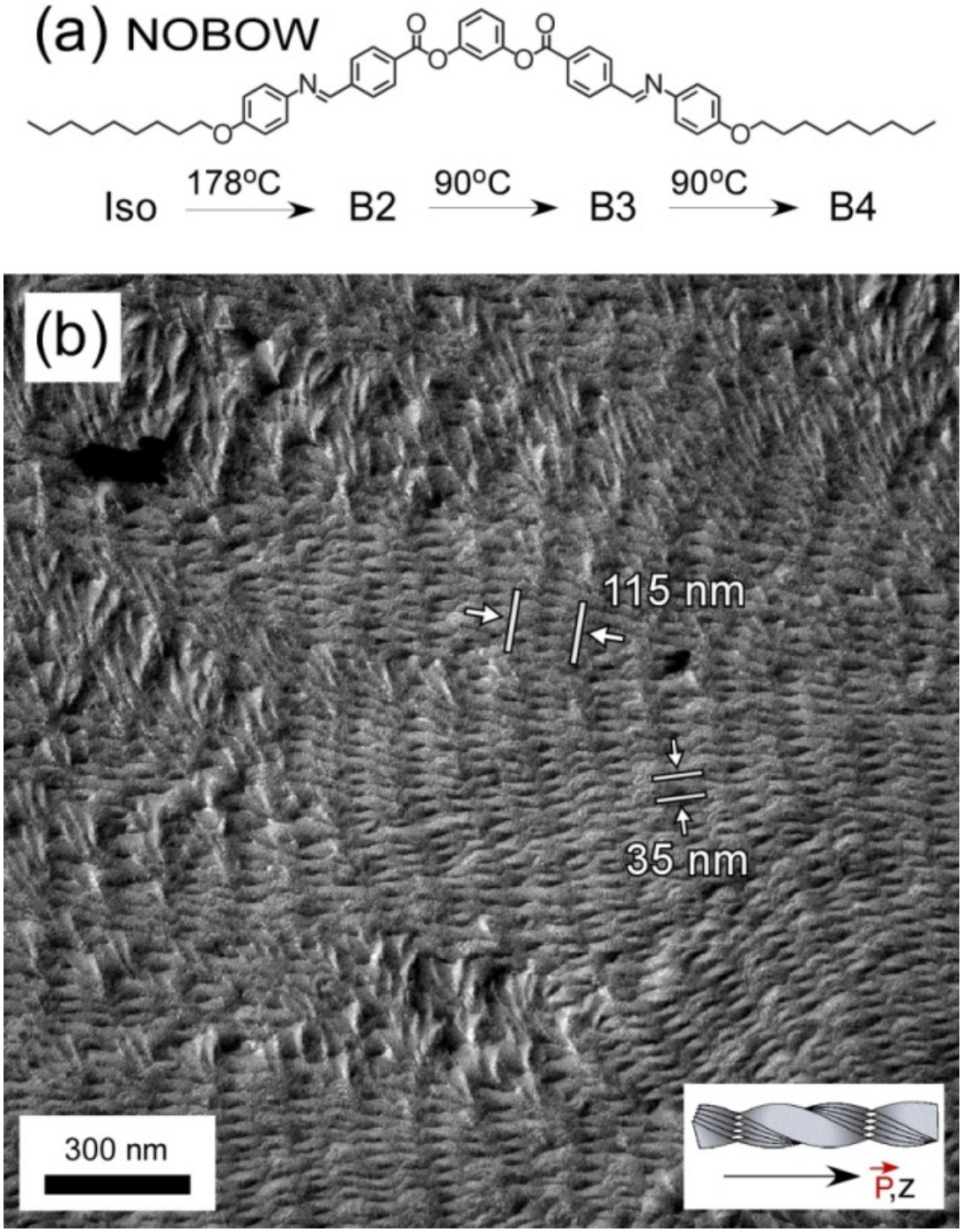

Figure 4.3.1: Helical nanofilaments of NOBOW in the B4 phase. (a) Chemical structure and phase sequence of NOBOW. (b) TEM image of NOBOW B4 phase quenched at 140°C, showing an array of homochiral helical nanofilaments. The inset shows a model of a single twisting helical nanofilament. The measured filament width w is 35 nm and half pitch p is 115nm.

Surface structure of the B7 phase

In order to investigate the surface topography of the B7 phase, we prepared samples of MHOBOW (Figure 4.3.2a). The layer undulations appear as narrow, faint lines between the layer steps, which appear as wide, dark lines, as shown in Figure 4.3.2b. The polarization modulation coupled layer undulations in the B7 phase have been clarified and layer undulations have been directly observed in the FFTEM images (for example, Figure 5.2.2 in Chapter 5). However, FFTEM images of MHOBOW fractured in the bulk only show smooth, sinusoidal layer undulations and so far there has been no direct evidence that the sinusoidal layer undulations correspond to individual polarization modulation stripes, the fine structure of the B7 phase. At the air/liquid crystal interface, a characteristic feature of the layer undulations is that their grooves all go along the layer edges, which means that the polarization modulation stripes tend to anneal along the layer edges during formation. This strongly supports the notion that the layer undulations are made of individual polarization modulation stripes, as the stripes have the property of layering at the layer edges, as modeled in Figure 4.3.2c.

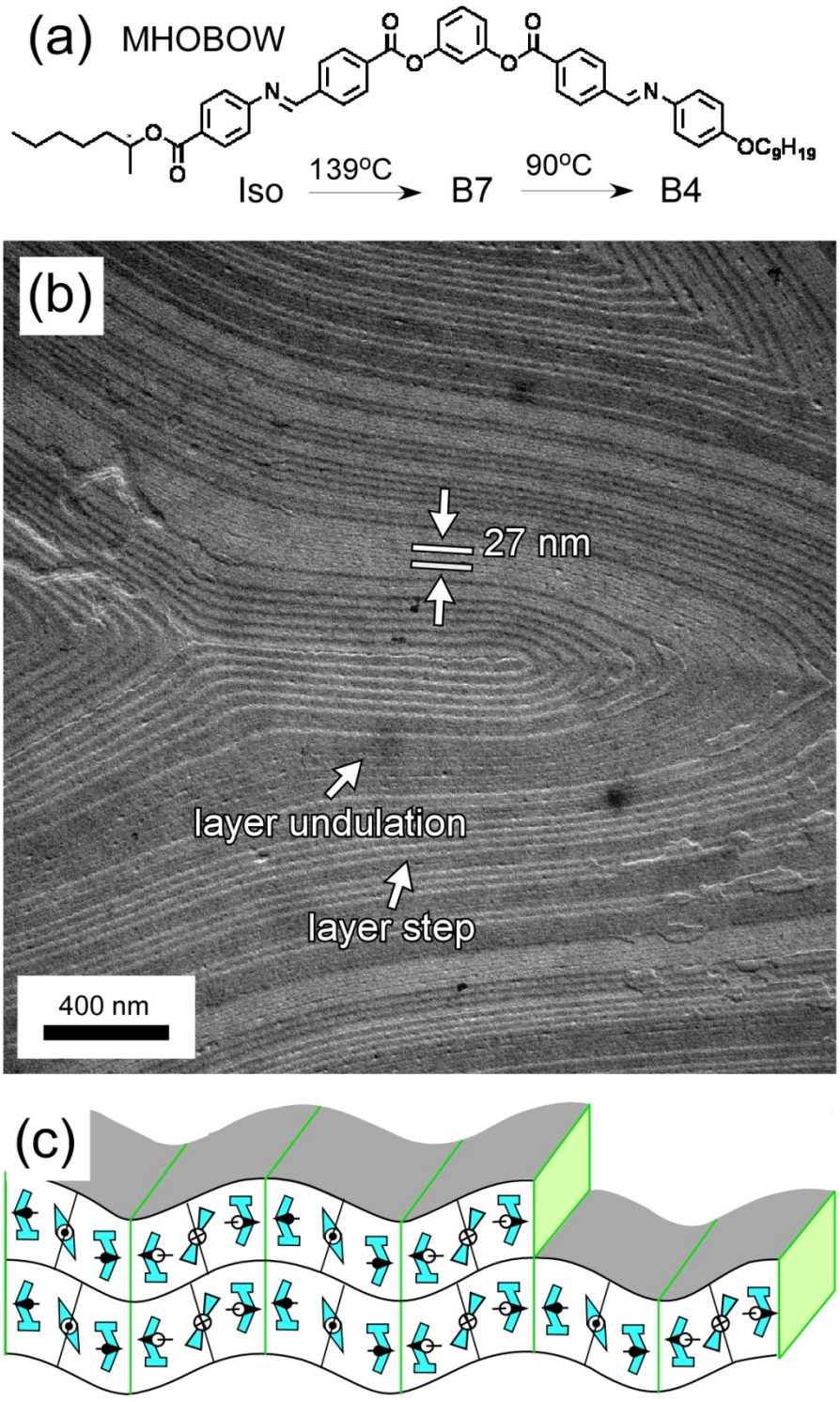

Figure 4.3.2: Layer undulations of MHOBOW in the B7 phase. (a) Chemical structure and phase sequence of MHOBOW. (b) TEM image of MHOBOW in the B7 phase quenched at 130°C. Both layer undulations (narrow, faint lines) and layer steps (wide, dark lines) can be distinguished, where the grooves of layer undulations tend to be parallel to the layer steps. The measured periodicity of the layer undulations is 27 nm. (c) Model showing layer undulations made of individual polarization modulation stripes whose edges coincides with the layer steps. The green lines represent defect walls between different polarization modulation stripes.

Surface structure of the dark conglomerate phase

The dark conglomerate (DC) phase, a chiral, isotropic liquid, shows globally-disordered focal conic domains in the bulk (for example, Figure 4.2.4 in Chapter 4). At the air/liquid crystal interface, due to the homeotropic alignment, the fluidity of the liquid crystal phase, and a preference for saddle-splay curvature, toric focal conic domains self-assemble into a quasi-ordered hexagonal lattice (section 4.2 in Chapter 4). This kind of surface topography is a common feature of the DC phase, having been observed in many materials which form the DC phase, such as W508, shown in Figure 4.3.3. Indentifying the DC phase through the surface structure is much easier than through the bulk structure as some other phases (such as the B2) may also show the focal conic structure in the bulk. Calamitic molecules have been known to form toric focal conic arrays in microchannels. This requires planar alignment at the bottom interface and homeotropic alignment at the top, constraints which can be reconciled by adopting a toric topology, forming toric focal conic domains with two-dimensional order. In the case of the DC phase of bent-core molecules, there is no effect from the surface polarity of the substrate. The periodicity of toric focal conic domains in the DC phase (several hundred nm) is much smaller than those in rod-like liquid crystals (several μm), and, since it is in the visible light range, they could be used as optical gratings.

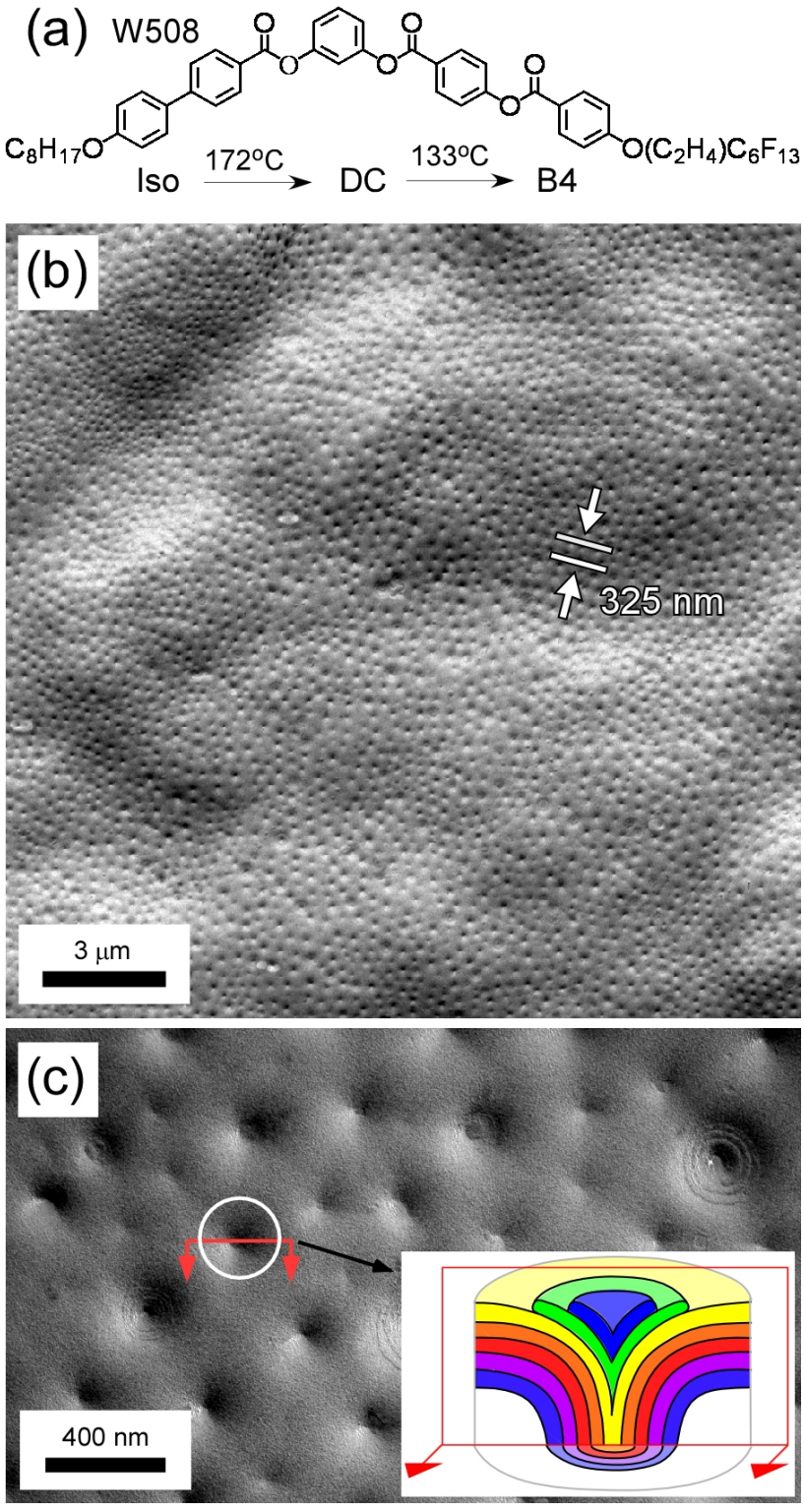

Figure 4.3.3: Toric focal conics of W508 in the DC phase. (a) Chemical structure and phase sequence of W508. (b) TEM image of the DC phase quenched at 160°C. Due to the homeotropic alignment of the air interface, the fluidity of the DC phase, and the preference for saddle-splay curvature, a sub-micron array of toric focal conics covers the entire surface. The measured distance between neighboring toric focal conics is 325 nm. (c) Higher magnification of the surface structure, with the inset showing a cross-section of a TFC below the surface.

We previously reported the formation of quasi-ordered toric focal conic array in the DC phase of the compound **Ib** (chemical structure and phase sequence shown in Figure 4.3.4a) at the air/liquid crystal interface (section 4.2 in Chapter 4). In a further study of this material, we have found that at the surface, in addition to the quasi-ordered toric focal conic domains, other surface topographies are also observed. As shown in Figures 4.3.4b and d, for example, we see one-dimensional and two-dimensional layer undulation patterns. The one-dimensional layer undulation is different from B7 layer undulations (Figure 4.3.2) in that the valleys and peaks are different, i.e., the undulation is not sinusoidal. The one-dimensional layer undulation can be modeled as a one-dimensional parabolic focal conic array, as shown in Figure 4.3.4c. Sometimes, the two-dimensional layer undulations form a fairly regular lattice which can be modeled as a two-dimensional parabolic focal conic array (inset, Figure 4.3.4d). Parabolic focal conic arrays have been observed before, for example in dilated SmA cells [32], however, they form only under external stimulus in rod-like materials. The reason that parabolic focal conic arrays form spontaneously at the free surface of bent-core materials is unknown, but is presumably driven by the complex interplay of molecular polarization, bend, and tilt.

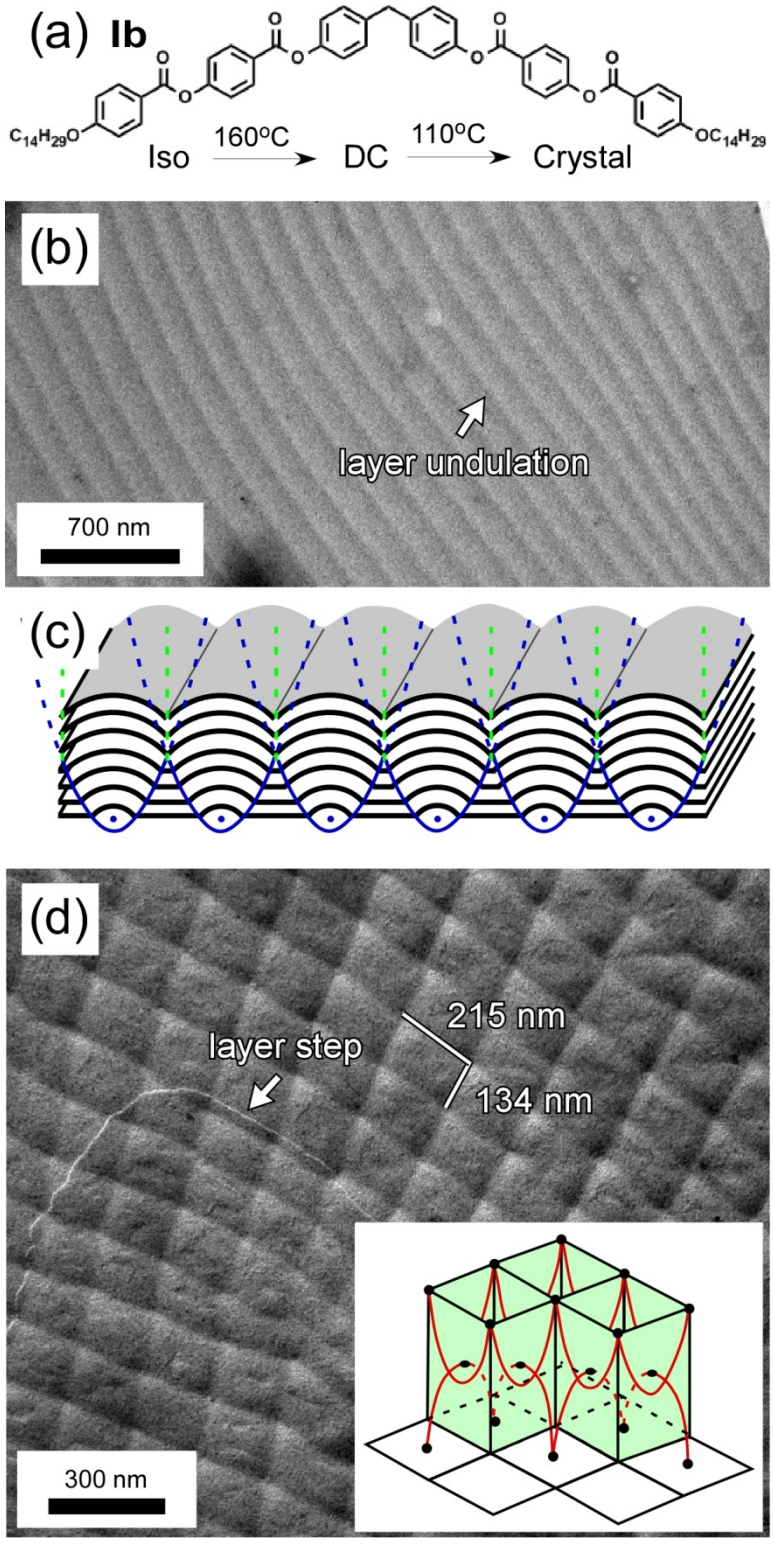

Figure 4.3.4: Parabolic focal conics of **Ib** in the DC phase. (a) Chemical structure and phase sequence of **Ib**. (b) TEM image of the DC phase quenched at 140°C, showing a one-dimensional layer undulation pattern. (c) Model of (a) as a one-dimensional parabolic focal conic array. (d) TEM image of the DC phase showing a periodic, two-dimensional layer undulation pattern, modeled in the inset as a two-dimensional parabolic focal conic array. The measured periodicities of the two-dimensional layer undulation are 215 nm and 134 nm respectively.

In all the current preparation, we investigated the surface structures on samples at least 500 μm thick. In this case, the homeotropic aligning field of the air/liquid crystal interface is the main influence on the surface structure, the glass substrate being too far from the surface to be important. In thin films, on the scale of 1 μm, more interesting self-assembled structures are expected to emerge from the bent-core molecules, as the surface alignment from the substrate and from the air interface compete. The examples shown here suggest that there are still lots of interesting surface structures waiting to be discovered. The self-assembly of surface structures with unique rheological and optical properties could potentially be exploited to make novel materials.

In a summary, the surface structures of the B4, B7 and DC phases of bent-core molecules have been described. In these phases, bent-core molecules undergo complex self-assembly, forming helical nanofilaments (the B4 phase), layer undulations (the B7 phase) and disordered focal conics (the DC phase) in the bulk. Complementary to freeze-fracture transmission electron microscopy (FFTEM) images which reveal the bulk structure of these phases, the surface structures give insight into the underlying structural bases of these phases, and show novel examples of self-assembly, due to the fluidity of the phases and the homeotropic alignment of the interface. The combination of bulk and surface studies is a powerful approach to characterize the liquid crystal phases. In addition, the regularity of the surface structures suggests that they could be used to make novel optical materials such as dielectric arrays, as the defect domains at the surface structure possess unique optical properties.

Bibliography

[1] H. Takezoe, and Y. Takanishi: Bent-core liquid crystals: Their mysterious and attractive world. *Jpn. J. Appl. Phys.* 2006, **45**, 597-625.

[2] R. A. Reddy, and C. Tschierske: Bent-core liquid crystals: Polar order, superstructural chirality and spontaneous desymmetrisation in soft matter systems. *J. Mater. Chem.* 2006, **16**, 907-961.

[3] J. Etxebarria, and M. B. Ros: Bent-core liquid crystals in the route to functional materials. *J. Mater. Chem.* 2008, **18**, 2919-2926.

[4] G. Heppke, D. D. Parghi, and H. Sawade: Novel sulphur-containing banana-shaped liquid crystal molecules. *Liq. Cryst.* 2000, **27**, 313-320.

[5] J. Thisayukta, Y. Nakayama, S. Kawauchi, H. Takezoe, and J. Watanabe: Distinct formation of a chiral smectic phase in achiral banana-shaped molecules with a central core based on a 2,7-dihydroxynaphthalene unit. *J. Am. Chem. Soc.* 2000, **122**, 7441-7448.

[6] H. N. S. Murthy, and B. K. Sadashiva: Banana-shaped mesogens: Effect of lateral substituents on seven-ring esters containing a biphenyl moiety. *Liq. Cryst.* 2002, **29**, 1223-1234.

[7] G. Dantlgraber, A. Eremin, S. Diele, A. Hauser, H. Kresse, G. Pelzl, and C. Tschierske: Chirality and macroscopic polar order in a ferroelectric smectic liquid-crystalline phase formed by achiral polyphilic bent-core molecules. *Angew. Chem. Int. Ed.* 2002, **41**, 2408-2412.

[8] A. Eremin, S. Diele, G. Pelzl, and W. Weissflog: Field-induced switching between states of opposite chirality in a liquid-crystalline phase. *Phys. Rev. E* 2003, **67**, 020702/1-3.

[9] R. A. Reddy, and B. K. Sadashiva: Influence of fluorine substituent on the mesomorphic properties of five-ring ester banana-shaped molecules. *Liq. Cryst.* 2003, **30**, 1031-1050.

[10] J. Etxebarria, C. L. Folcia, J. Ortega, and M. B. Ros: Induction of ferroelectricity in the B2 phase of a liquid crystal composed of achiral bent-core molecules. *Phys. Rev. E* 2003, **67**, 042702/1-4.

[11] J. Ortega, C. L. Folcia, J. Etxebarria, N. Gimeno, and M. B. Ros: Interpretation of unusual textures in the B2 phase of a liquid crystal composed of bent-core molecules. *Phys. Rev. E* 2003, **68,** 011707/1-4.

[12] B. A. DiDonna, and R. D. Kamien: Smectic phases with cubic symmetry: The splay analog of the blue phase. *Phys. Rev. Lett.* 2002, **89**, 215504/1-4.

[13] M. Kleman, and O. Lavrentovich: *Soft matter physics: An introduction*. Springer-Verlag, New York, 2003.

[14] L. E. Hough, M. Spannuth, M. Nakata, D. A. Coleman, C. D. Jones, G. Dantlgraber, C. Tschierske, J. Watanabe, E. Körblova, D. M. Walba, J. E. Maclennan, M. A. Glaser, and

N. A. Clark: Chiral isotropic liquids from achiral molecules. *Science* 2009, **325**, 452-456.

[15] L. E. Hough, and N. A. Clark: Layer-scale optical chirality of liquid-crystalline phases. *Phys. Rev. Lett.* 2005, **95**, 107802/1-4.

[16] L. E. Hough, H. T. Jung, D. Krüerke, M. S. Heberling, M. Nakata, C. D. Jones, D. Chen, D. R. Link, J. Zasadzinski, G. Heppke, J. P. Rabe, W. Stocker, E. Körblova, D. M. Walba, M. A. Glaser, and N. A. Clark: Helical nanofilament phases. *Science* 2009, **325**, 456-460.

[17] N. Gimeno, J. Barberá, J. L. Serrano, M. B. Ros, M. R. de la Fuente, I. Alonso, and C. L. Folcia: Terminal chains as a tool to modulate the properties of bent-core liquid crystals. *Chem. Mater.* 2009, **21**, 4620-4630.

[18] D. K. Yoon, M. C. Choi, Y. H. Kim, M. W. Kim, O. D. Lavrentovich, and H. T. Jung: Internal structure visualization and lithographic use of periodic toric holes in liquid crystals. *Nature Mater.* 2007, **6**, 866-870.

[19] G. M. Whitesides, and B. Grzybowski: Self-assembly at all scales. *Science* 2002, **295**, 2418–2421.

[20] C. D. Rosa, C. Park, E. L. Thomas, and B. Lotz: Microdomain patterns from directional eutectic solidification and epitaxy. *Nature* 2000, **405**, 433-437.

[21] E. Vekris, V. Kitaev, D. D. Perovic, J. S. Aitchison, and G. A. Ozin: Visualization of stacking faults and their formation in colloidal photonic crystal films. *Adv. Mater.* 2008, **20**, 1110–1116.

[22] R. A. Segalman, H. Yokoyama, and E. J. Kramer, *Adv. Mater.*, 2001, **13**, 1152–1155.

[23] S. O. Kim, H. H. Solak, M. P. Stoykovich, N. J. Ferrier, J. J. de Pablo, and P. F. Nealey: Epitaxial self-assembly of block copolymers on lithographically defined nanopatterned substrates. *Nature* 2003, **424**, 411-414.

[24] J. Y. Cheng, A. M. Mayes, and C. A. Ross: Nanostructure engineering by templated self-assembly of block copolymers. *Nat. Mater*. 2004, **3**, 823–828.

[25] N. A. Clark, T. Bellini, R. M. Malzbender, B. N. Thomas, A. G. Rappaport, C. D. Muzny, D. W. Schaefer, and L. Hrubesh: X-ray scattering study of smectic ordering in a silica aerogel. *Phys. Rev. Lett*. 1993, **71**, 3505-3508.

[26] G. P. Crawford, and S. Zumer: *Liquid crystals in complex geometries*. Taylor & Francis, London, 1996.

[27] C. R. Safinya, D. Roux, G. S. Smith, S. K. Sinha, P. Dimon, N. A. Clark, and A. M. Bellocq: Steric interactions in a model multimembrane system: A synchrotron x-ray study. *Phys. Rev. Lett.* 1986, **57**, 2718-2721.

[28] M. J. Costello, R. Fetter, and M. Hochli: Simple procedures for evaluating the cryofixation of biological samples. *Journal of Microscopy-Oxford* 1982, **125**, 125-136.

[29] P. G. de Gennes and J. Prost: *The physics of liquid crystals*. Oxford Univ. Press, New York, 2nd edition, 1993.

[30] D. A. Coleman, J. Fernsler, N. Chattham, M. Nakata, Y. Takanishi, E. Körblova, D. R. Link, R.-F. Shao, W. G. Jang, J. E. Maclennan, O. Mondainn-Monval, C. Boyer, W. Weissflog, G. Pelzl, L.-C. Chien, J. Zasadzinski, J. Watanabe, D. M. Walba, H. Takezoe, and N. A. Clark: Polarization-modulated smectic liquid crystal phases. *Science* 2003, **301**, 1204-1211.

[31] D. R. Link, G. Natale, R. Shao, J. E. Maclennan, N. A. Clark, E. Körblova, and D. M. Walba: Spontaneous formation of macroscopic chiral domains in a fluid smectic phase of achiral molecules. *Science* 1997, **278**, 1924-1927.

[32] Ch. S. Rosenblatt, R. Pindak, N. A. Clark, and R. B. Meyer: The parabolic focal conic: A new smectic A defect. *Journal de Physique* 1977, **38**, 1105-1115.

Chapter 5

B7 Layer Undulation Defects: An Exotic System

5.1 Introduction

Bent-core mesogens have become a major topic of liquid crystal research in recent years, with many interesting phases and properties, deriving from the interplay of molecular bend, molecular tilt and molecular polarization [1]. Alternative combinations of the polar direction and the molecular tilt direction gives the four basic bilayer phases named SmC_AP_A, SmC_AP_F, SmC_SP_A, and SmC_SP_F, respectively. All these phases have been found in bent-core mesogens and have been extensively studied. The SmC_SP_F phase shows three interesting, distinct thermodynamic states, the B4 phase, the DC phase and the B7 phase, where the B4 phase is made of helical nanofilaments, the DC phase is dominated by disordered focal conics, and the B7 phase is composed of polarization modulation stripes coupled layer undulations. These microstructures are stable in the sense of being local minima in the free energy. In this chapter, we will mainly discuss the B7 phase. On slowly cooling the isotropic liquid, helical filaments of the B7 phase appear and coalesce to form a variety of beautiful optical textures, such as striped focal conics, chessboard-like textures, banana-leaf-like textures and ribbon-like textures [2, 3]. A stack of synclinic, ferroelectric layers could in principle lower its free energy by organizing the molecules in a polarization-splay-modulated state, as sketched in Figure 5.1.1a. The periodic supermolecular-scale polarization modulation stripes coupled to layer undulations have been directly confirmed by the freeze fracture transmission electron microscopy (FFTEM) images of

the B7 phase [2]. X-ray scattering patterns which show multiple satellite peaks around the first-order layer reflection peak also indicate the two-dimensional periodic structures, the smectic layers (along the layer normal) and the layer undulations (along the layer plane). While under a threshold electric field, the transition between the polarization modulated state and the ferroelectric state of flat layers has been observed through the microbeam x-ray diffraction. After removal of the electric field, the ferroelectric state of flat layers thermally returns to the polarization modulated state [4].

There are still many mysteries about the B7 phase. For example, the first successful drawing of filaments from a liquid crystal bath of bent-core materials has been with the B7 phase [5]. The formation of stable freely standing filaments in the B7 liquid crystal phase against the Raleigh-Plateau instability is a fascinating and challenging phenomenon found in complex, non Newtonian liquids [6, 7]. The mechanical properties of the B7 freely standing filaments have also been characterized [8].

Though the use of topology and geometry to understand the physical world is commonplace, we will show below that exploiting the topological defects of the layer undulations paves the way for a novel understanding of the B7 phase. In general, macroscopic polarization in the liquid crystal phase costs very high energy and polarization splay is preferred to avoid any macroscopic polarization. This polarization splay can be accommodated by adopting a texture having a series of stripes when there are proper defect structures between them. As shown in Figure 5.1.1a, the macroscopic polarization is relieved by the polarization splay with the polarization spreading out from the center of the stripe. Because of the stronger layer fluctuation near the defect walls, the layers dilate at the boundaries. This kind of layer expansion at the polarization stripe boundary is frustrated, where the space cannot be fully filled by the layers, as shown in Figure 5.1.1b. In

order to establish a uniform layer pitch along **s**, the layers at the center of the stripe must be tilted. Based on the different combinations of the molecular tilt direction and the molecular polarization direction, there are four kinds of polarization splay stripes, as shown in Figures 5.1.1c-f, with layers displace down in Figures 5.1.1c and e and layers displace up in Figures 5.1.1d and f. In this case, even though the layer spacing at the center of the stripe is smaller than those at the boundary, the smectic layers have a uniform layer pitch along $\vec{s}$. Each polarization modulation stripe is coupled to a half pitch of the layer undulation. Because there are four kinds of polarization modulation stripes, the detailed arrangement of the polarization modulation stripes in the layer undulation is still very complicated. Investigation of the B7 layer undulation defects will help us better understand how the polarization modulation stripes are arranged in the layer undulation. The chemical structure and phase sequence of the material investigated are shown in Figures 5.1.2a-c.

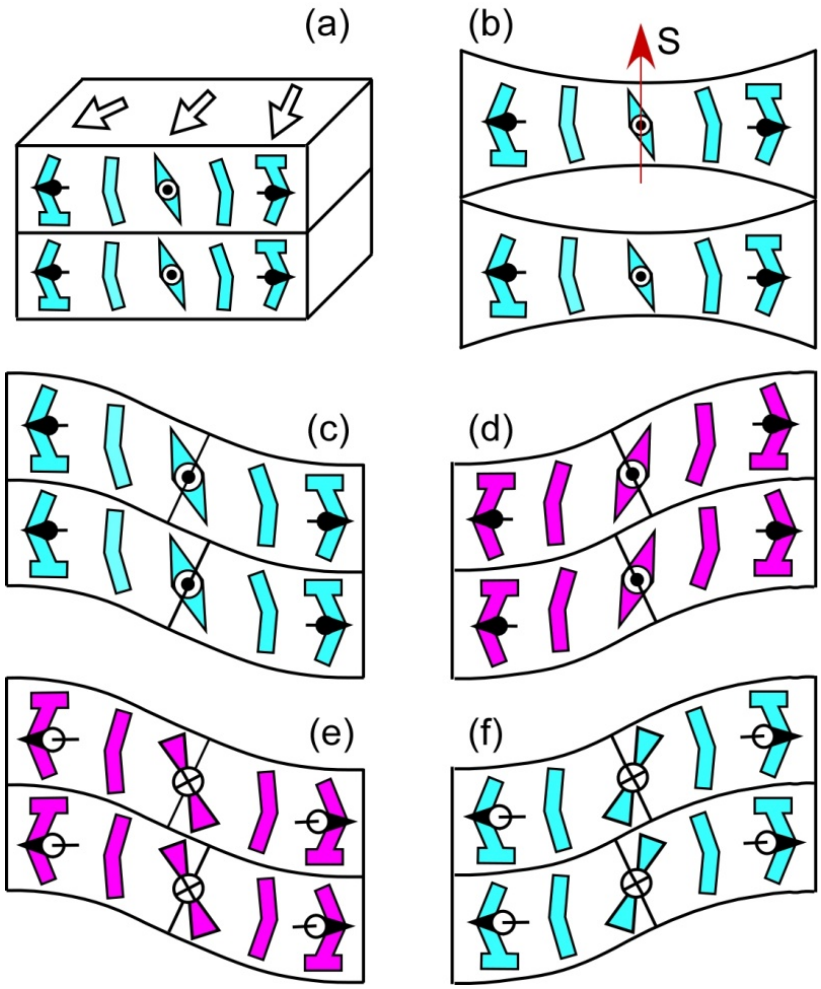

Figure 5.1.1: Model of polarization modulation stripes driven by the polarization splay. (a) In order to escape any macroscopic polarization, the polarization tends to splay within the layers. This kind of polarization splay can be accommodated by adopting a texture having a series of stripes when there are proper defect structures at the boundary of each stripe. (b) Because of the stronger layer fluctuation near the defect walls, the layers dilate at the boundaries. This kind of layer expansion at the stripe boundary is frustrated, which can be relieved by forming the polarization modulation stripes. (c)-(f) The four kinds of polarization modulation stripes of different molecular tilt and polarization direction. In all cases, the layer spacing at the center of the stripe is smaller than those at the boundary, while the layer pitch along $\vec{s}$ is uniform. Tees indicate the projection of the bent-core molecules, where the bar indicates the end near to the reader.

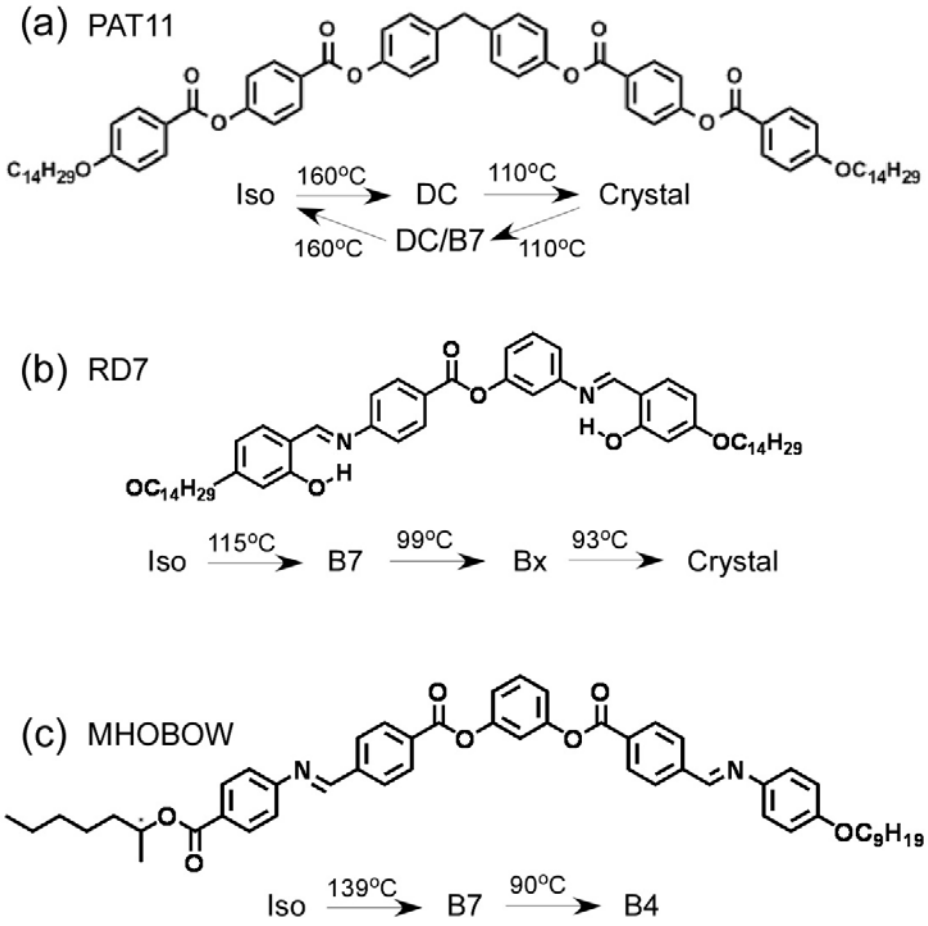

Figure 5.1.2: Chemical structure and phase sequence of PAT11, RD7, MHOBOW.

5.2 B7 layer undulation defects

Though the layer undulation of the B7 phase has been confirmed by the FFTEM images for a long time, there is still no direct evidence, supporting the model that the layer undulation is made of individual polarization modulation stripes. The FFTEM image and free surface TEM image shown in Figures 5.2.1a and b respectively show that each polarization modulation stripe has a distinct boundary and strongly support the model that the layer undulation is made of individual polarization modulation stripes. In both images, the layer steps appear as wide lines while the narrow lines show the layer undulation in the layer plane. Interestingly, as shown in Figure 5.2.1a, the fractured layer steps tend to go along the edges of the polarization modulation stripes, which indicates that the polarization modulation stripes have a distinct boundary. Consistent with the FFTEM image, the TEM image of the B7 phase at the air/liquid crystal interface show that each layer edge coincides with the boundary of the polarization modulation stripes, as shown in Figure 5.2.1b. This means that during the formation of the layer undulation, the boundaries of the polarization modulation stripes naturally anneal along the layer edges. This also indicates that in the B7 phase, the molecules first self-assemble into smectic layers and then the layer undulation develops. This is consistent with the argument below on the spiral patterns of the layer undulation.

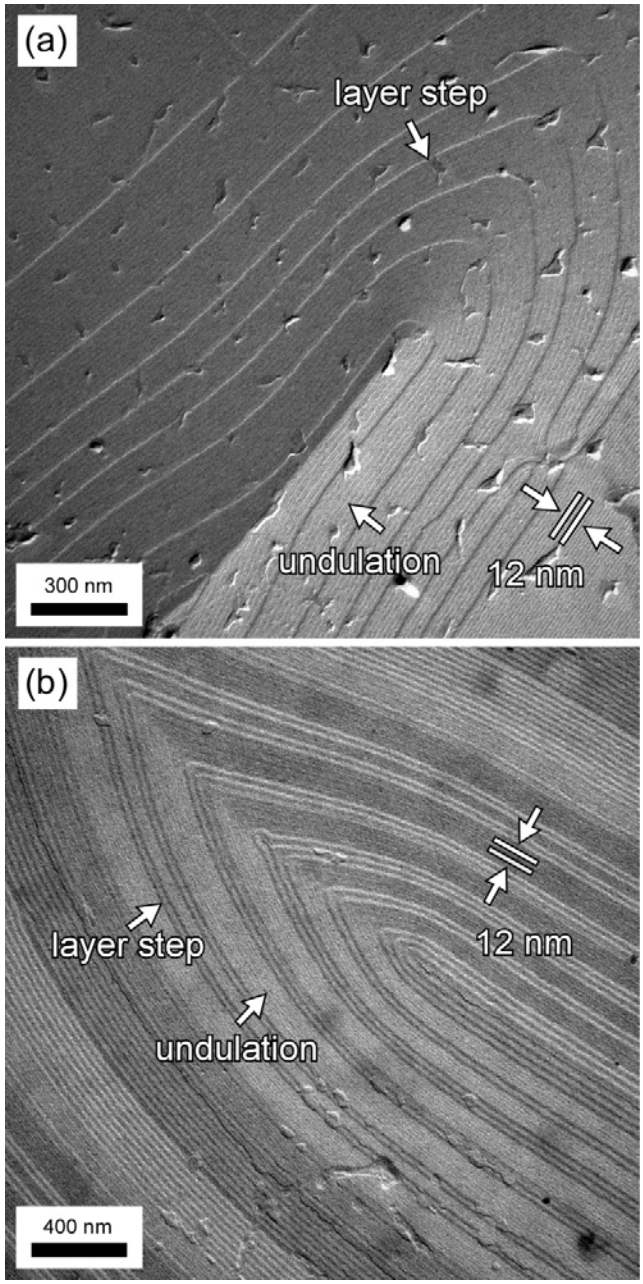

Figure 5.2.1: FFTEM image and free surface TEM image of the B7 layer undulations. (a) FFTEM image of RD7, showing the bulk topography of the B7 phase. (b) Free surface TEM image of MHOBOW, showing the topography of the B7 phase at the air/liquid crystal interface. In both images, the smectic layers are parallel to the image plane. The wide lines indicate the layer steps while the narrow lines show the layer undulations. As shown in (a), the fractured layer steps mostly run along the edges of the polarization modulation stripes. While in (b), at the air/liquid crystal surface, the boundaries of the polarization modulation stripes anneal along the layer steps.

In the study of the B7 layer undulation, we find that the layer undulation shows undulation defects (e.g. the dislocation and the disclination defects) analogous to those observed in the layered system. The typical topography of the B7 layer undulation is shown in Figure 5.2.2a, where the layer plane is parallel to the fracture plane with occasional layer steps and the layer undulation is in the layer plane. Two different kinds of edge dislocations can be observed in the layer undulation, corresponding to the annihilation of the undulation peak and the annihilation of the undulation valley, respectively (examples are highlighted in the white boxes). The regions around the edge dislocations are very smooth. Therefore, it's reasonable to assume that the polarization direction and the molecular tilt undergo a continuous change around the undulation defects, as modeled in Figures 5.2.2b and c. This assumption puts a strong constraint on the possible configuration of the polarization direction and the molecular tilt for the undulation peak and the undulation valley, and requires that neighboring polarization modulation stripes have opposite polarization directions and molecular tilts. The two possible configurations for the undulation peak are shown in Figures 5.2.2d-e and the two possible configurations for the undulation valley are shown in Figures 5.2.2f-g. In a macroscopic region of the layer undulation, the edge dislocation can happen anywhere between any two adjacent polarization modulation stripes, that is the annihilation of any undulation peak or any undulation valley. Therefore, there are only two possible molecular arrangements in the layer undulation, as shown in Figures 5.2.2h and i, respectively. Though the adjacent polarization modulation stripes are of opposite polarization directions and opposite molecular tilts, the layer undulation are macroscopically chiral, either left-handed (Figure 5.2.2h, $\vec{z}x\vec{n} = \vec{p}$) or right-handed (Figure 5.2.2i, $\vec{z}x\vec{n} = -\vec{p}$). We will show below that the layer undulation coupled with the layer chirality forms the clockwise or anticlockwise spiral pattern.

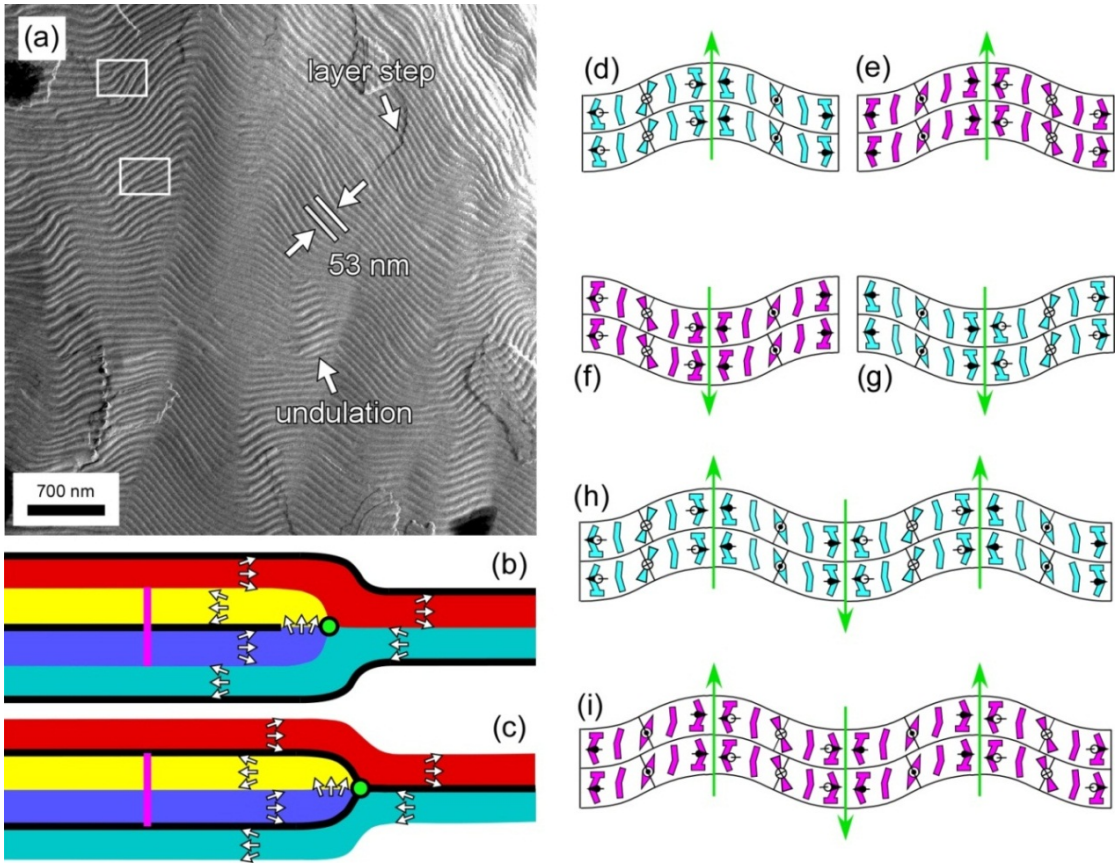

Figure 5.2.2: Edge dislocations of the B7 layer undulation. (a) FFTEM image of **Ib** with layers parallel to the fracture plane. Occasional layer steps can be distinguished in the image and the measured periodicity of the layer undulation is p≈53 nm. Examples of the edge dislocations are highlighted using the white boxes. The smooth appearance of the regions near the dislocation lines suggests the continuous change of the polarization direction and the molecular tilt around the undulation defect. Under this assumption, (b) shows the possible polarization direction in each polarization modulation stripe near the edge dislocation where a layer undulation peak disappears. The polarization directions of neighboring stripes are always in the opposite direction with each other. The peaks of the layer undulation are marked with thick dark lines. The valleys of the layer undulation are the boundaries where two different color polarization modulation stripes meet. The dislocation line is marked by the green dot. (c) shows the possible polarization direction in each polarization modulations stripe near the edge dislocation where a layer undulation valley disappears. Based on the four kinds of polarization splay stipe shown in Figures 5.1.1c-f, under the constraint of continuous change of the polarization direction and the molecular tilt around the layer undulation defects, there are two kinds of molecular arrangement for the undulation peak, as shown in (d) and (e) with the green arrow pointing up, and two kinds of molecular arrangement for the undulation valley, as shown in (f) and (g) with the green arrow pointing down. To ensure the annihilation of any undulation peak or undulation valley (any neighboring polarization modulation stripes), there are only two possible molecular arrangements in the layer undulation, as modeled in (h) and (i), respectively, both of which are macroscopically chiral.

Figure 5.2.3a shows the clockwise and anticlockwise spiral patterns formed by the layer undulation where the layer plane is parallel to the fracture surface with the layer undulation superimposed into the layer surface. There are distinct boundaries between different spiral patterns, indicating some repulsion force at the boundaries between neighboring layer undulation domains, even between clockwise and clockwise spirals. The formation of the spiral structure which usually starts from the center indicates that the layer and the layer undulation of the B7 phase develop independently at the I-B7 phase transition [9]. In the B7 phase, the flat layer structure forms first. Then the layer undulation nucleates and grows, which forms the spiral pattern. When different spiral patterns meet each other, the width of the polarization modulation stripe is compressed due to the repulsion from neighboring layer undulation domains. As discussed in the previous paragraph, the layer undulation of the B7 phase is made of polarization modulation stripes of same chirality and the layer undulation is macroscopically chiral. The appearance of clockwise and anticlockwise spiral patterns is also a direct indication of the chiral nature of the smectic layers in the B7 phase, a result we obtained from the analysis of the undulation defects. Although the transfers of the microscopic level (molecular) chirality to the macroscopic level (structural) chirality have been known for a long time and different macroscopic chiral structures formed by chiral molecules have been reported, for example the cholesteric phase, the blue phase, the TGB phase and so on formed of chiral rod-like molecules. Though the sample used here is racemic, the layers of the B7 phase are still chiral (layer chirality). Therefore the chiral spiral pattern is induced by the layer chirality not the molecular chirality. This is a second example where the layer chirality transfers to the macroscopic chirality, e.g. the clockwise and anticlockwise spiral patterns in the B7 phase. The first example is the

helical nanofilament of the B4 phase of achiral bent-core molecules, which is made of left- and right-handed helical nanofilaments.

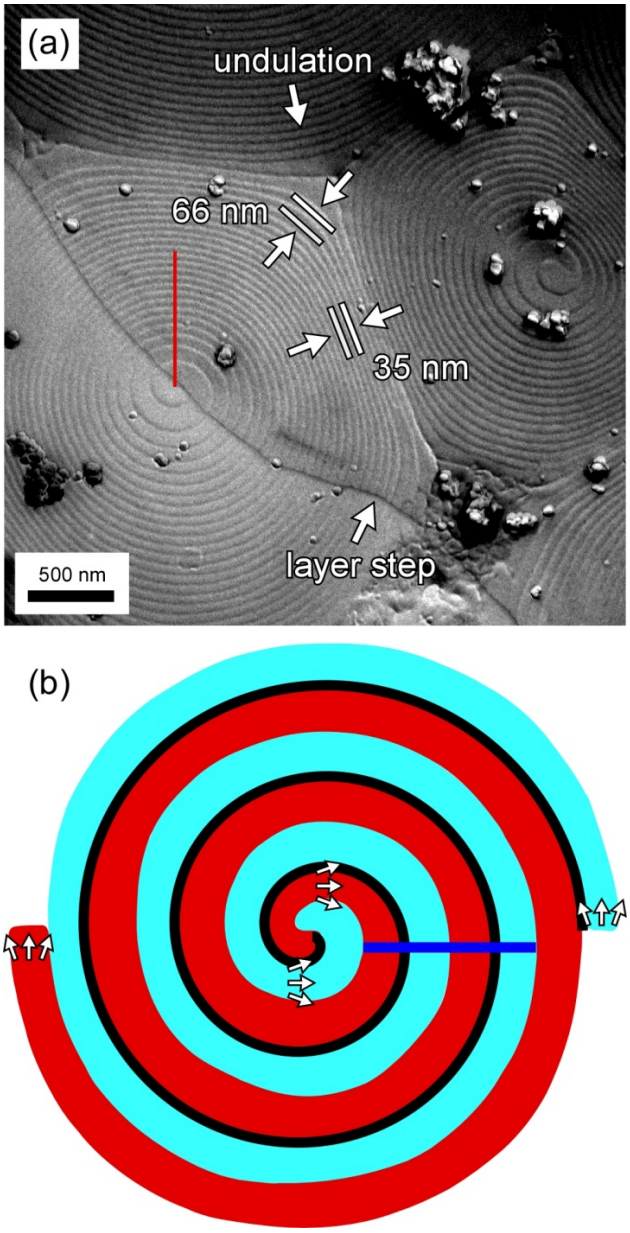

Figure 5.2.3: Clockwise and anticlockwise spiral patterns formed by the layer undulations. (a) Spiral texture of the layer undulation showing different chiral signs, clockwise or anticlockwise. It seems that in the B7 phase it first forms the flat layers, and then the layer undulations appear via a nucleation and growth process. (b) Model of the spiral structure with the white arrows representing the polarization direction and the dark lines showing the undulation peaks.

The most commonly observed one-dimensional, periodic layer undulation pattern can develop far from the spiral center, as shown in Figure 5.2.4. Usually, the morphology of the layer undulation strongly depends on the environment, e.g. the confinement from neighboring layer undulation domains. The spiral pattern shown in Figure 5.2.4a is deformed along one direction, where there is no constraint from neighboring undulation domains, and the layer undulation develops into one-dimensional, periodic stripe. The transition from the spiral structure to the periodic stripe is mediated through a disclination line, as modeled in Figure 5.2.4b. Therefore, the most commonly observed one-dimensional, periodic layer undulation originates from the spiral pattern and is part of the spiral structure. In other words, all these layer undulations are macroscopically chiral, which is a manifestation of chirality transfer from layer chirality (microscopic) to structural chirality (macroscopic).

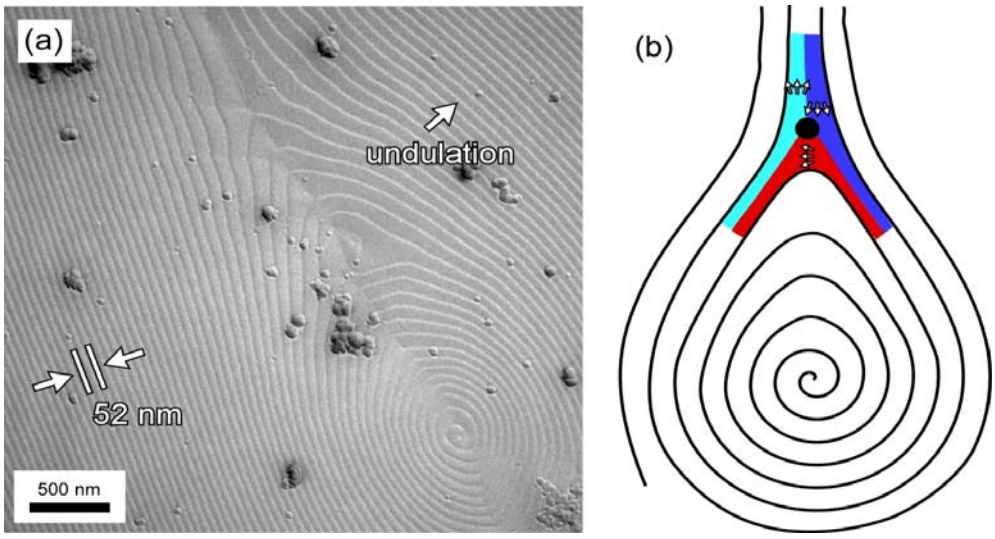

Figure 5.2.4: Deformed spiral pattern of the B7 layer undulation. (a) The spiral conformation of the layer undulation can be deformed upon the surrounding environment. One-dimensional, periodic layer undulation pattern can be obtained far from the spiral center. (b) Model of the deformed spiral structure showing the polarization direction of each polarization modulation stripe near the disclination defect.

As we notice in Figure 5.2.5a, the width of the polarization modulation stripe becomes narrower and narrower away from the spiral center, due to the repulsion from neighboring layer undulation domains. In order to investigate the elastic property of the polarization modulation stripe, the width of the polarization modulation stripe as a function of distance away from the spiral center is shown in Figure 5.2.5. When it is close to the spiral center, the width of the stripe undergoes an exponential decrease as it moves away from the center. When it is far away from the spiral center, the width of the stripe stays constant which means that they cannot be compressed anymore. This behavior indicates that the polarization modulation stripe may be treated as an elastic stripe when considering the elastic energy of the B7 phase.

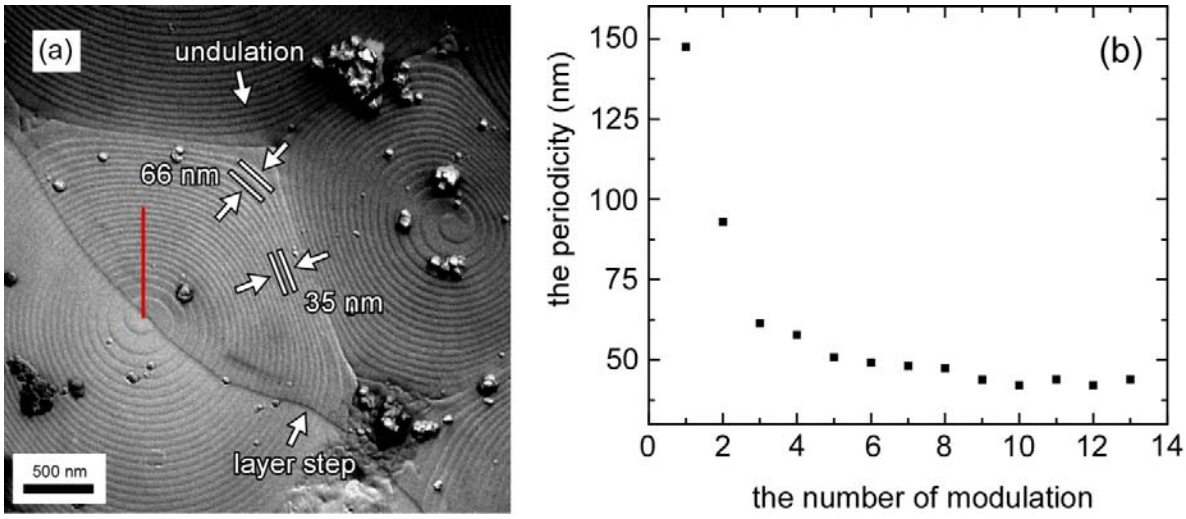

Figure 5.2.5: The elasticity of the layer undulation. (a) Clockwise and anticlockwise spiral patterns of the layer undulations (Figure 5.2.3a is reproduced here for convenience). (b) The width of the polarization modulation stripes as a function of distance away from the spiral center.

In a summary, in bent-core liquid crystal phases, the strong local preference for layering, coupled with the bent shape of the molecules, leads to two spontaneous symmetry-breaking instabilities: polar molecular orientational ordering and molecular tilt. These instabilities combine to produce chiral, layered phases including the B2, B7 and so on. The B7 phase is the best known liquid crystal phase with two dimensional periodicities, the layers and the layer undulations, where the layer undulation is associated with the formation of periodic polarization splay stripes. Investigation of the defects of the layer undulation gives insight into the molecular organization of the polarization splay stripes in the B7 phase. The polarization direction and the molecular tilt of the B7 layer undulation can be determined through the analysis of the defect structure. Though neighboring polarization modulation stripes are of opposite polarization directions and opposite molecular tilts, the layers are macroscopically chiral. This kind of layer chirality is expressed through the formation of clockwise and anticlockwise spiral patterns.

5.3 The texture of the B7 phase: Helical filaments of the smectic layers

As mentioned before, the B7 phase shows extremely beautiful optical textures among all the other liquid crystal phases. In this section, we will discuss the texture of the B7 phase and seek the possible organization of the smectic layers behind those textures. So far, various optical textures have been observed in the B7 phase, such as the chessboard texture, banana-leaf-like texture and so on. However, the most interesting phenomenon of the B7 phase is the formation of different kinds of helical filaments from the isotropic medium. Examples of the helical filaments in the B7 phase are shown in Figures 5.3.1a-d. The helical filaments show different optical textures under crossed polarizers. The step by step filament growth in the B7 phase is also highlighted in Figures 5.3.1a-d. The picture emerged from this growth morphology is that the filament twists as it grows, forming alternative black and white spots. Though previous studies indicate that the helical filaments consist of concentric smectic layers [10], we propose that the helical filaments are formed by twisted ribbons of smectic layers within the isotropic medium and that the ribbons of smectic layers are the fundamental structural basis of the B7 texture, as the ribbons form in the early stage of the Iso-B7 phase transition and these ribbons eventually coalesce to form e.g. the chessboard texture and so on. The appearance of twisting ribbons of smectic layers is also a direct indication of the chiral nature of the smectic layers in the B7 phase as discussed in the previous section. Below, we will show how the textures observed in the B7 phase can be constructed by the twisting ribbons of smectic layers and the evidence that supporting the idea.

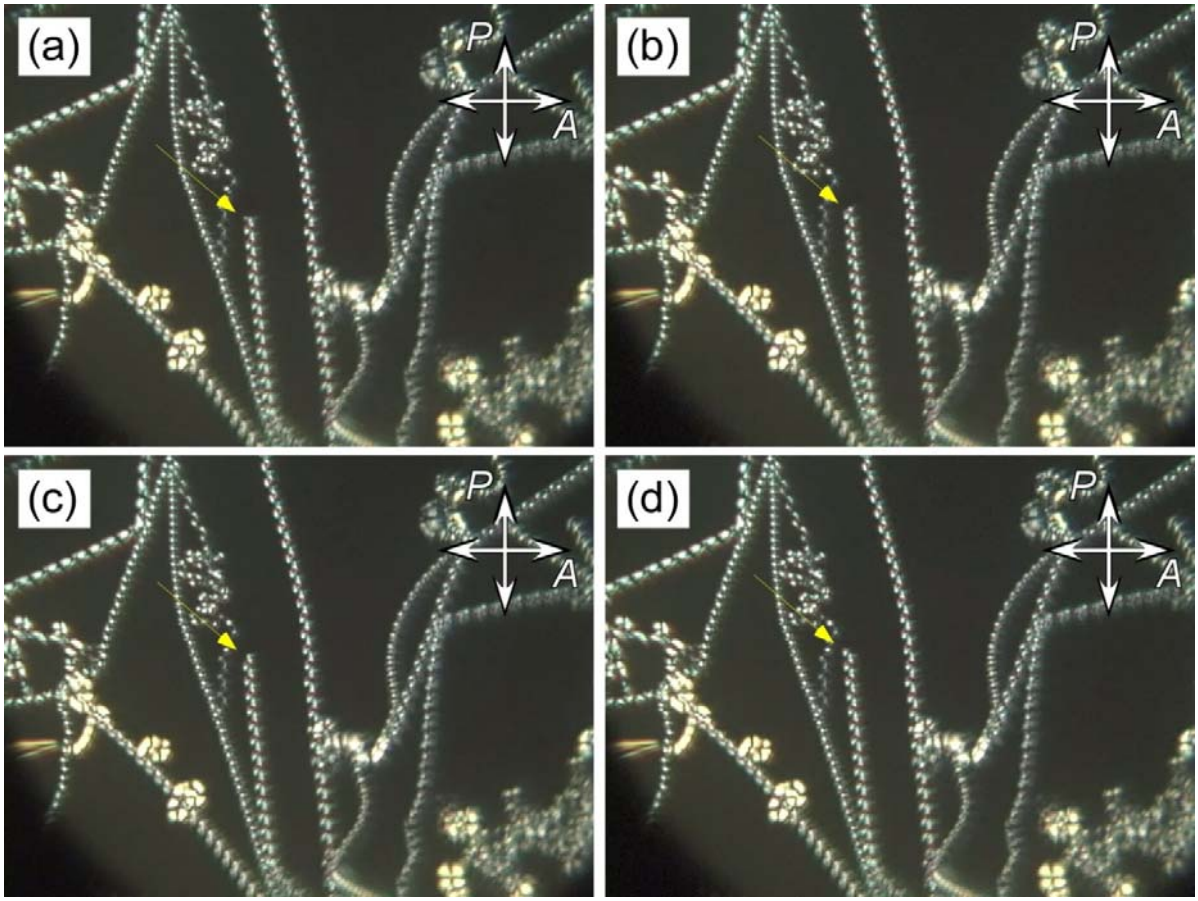

Figure 5.3.1: Step by step filament growth in the B7 phase. (a), (b), (c) and (d) Sequence of DTLM images, showing the step by step filament growth in the B7 phase. The filament tip is highlighted using the yellow arrow in each image.

Figures 5.3.2a and b show the commonly observed chessboard texture and ribbon texture of the B7 phase, respectively. Besides those high birefringent textures, low birefringence regions are observed coexistent with them in the B7 phase (Figure 5.3.2b, upper right, and Figure 5.3.2c). Those textures are overall of very low birefringence and appear grey under crossed polarizers. As we have proposed, all these textures can be constructed from the twisting ribbons of smectic layers. Models of single twisting ribbons and double twisting ribbons of the smectic layers in the B7 phase are shown in Figure 5.3.2d. The directors of the molecules have been shown along each ribbon. Under crossed polarizers, the single twisting ribbon appears as alternative bright and dark spots, as the directors of the molecules in the smectic layers change periodically. When the single twisting ribbons are arranged in arrays, the chessboard texture is obtained when neighboring twisting ribbons are 180° out phase. For the double twisting ribbons, because of the almost orthogonal molecular tilt directions in those two ribbons, the double twisting ribbons overall have a very low birefringence. Therefore, any texture composed of double twisting ribbons has a very low birefringence. The remaining question is why these helical filaments only exist in the B7 phase or what drives the formation of twisting ribbons of smectic layers in the B7 phase. People has observed the spontaneous formation of striped and labyrinthine textures of the c-director in freely suspended polar smectic $SmCP_F$ films, which indicates a negative effective bend constant [11]. The formation of helical filament may be attributed to the special elastic constant of the B7 phase. The phenomena we observed in the B2 phase of NOBOW in a c=10% 8CB/NOBOW mixture (c is the weight percent of 8CB in the mixture) can help us better understand this.

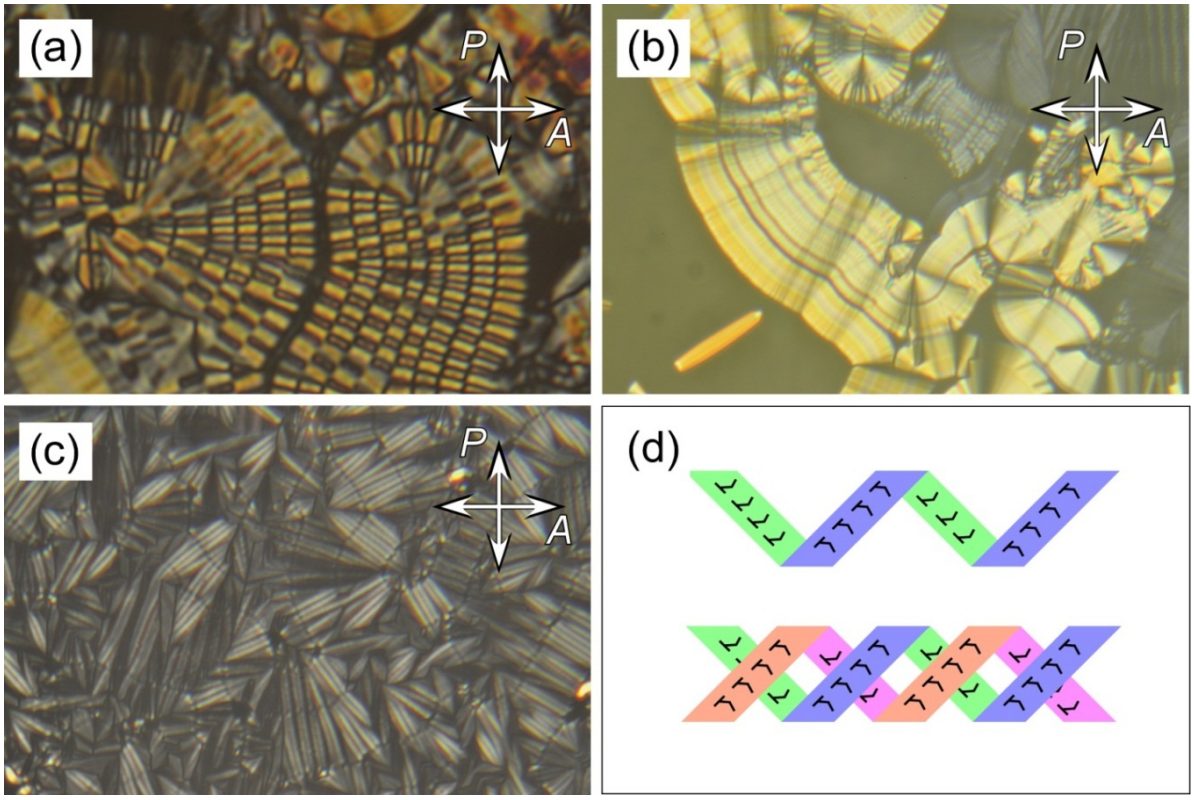

Figure 5.3.2: Different kinds of optical textures of the MHOBOW B7 phase taken at T=125°C, cooling from isotropic at 0.01°C/min. (a) The chessboard texture of the B7 phase. (b) The ribbon texture of the B7 phase. (c) The low birefringent texture of the B7 phase. (d) Single twisting ribbons of smectic layers and double twisting ribbons in the B7 phase with the molecular director shown along each ribbon.

In the B2 phase, smectic layers usually organized in the focal conic structure. Therefore, the B2 phase usually shows the typical focal conic texture. However, the optical textures of the B2 phase of a c=10% 8CB/NOBOW mixture don't look like the conventional focal conic texture, but strongly resemble the texture observed in the B7 phase, as shown in Figures 5.3.3a-d. As discussed in Chapter 3, due to the freezing point depression, with low concentrations of 8CB, the I-B2 phase transition of NOBOW is depressed in the mixture. However, 8CB is insoluble in the B2 phase of NOBOW. On cooling from the isotropic, NOBOW first phase separates and form the B2 phase. However, the smectic layers of the B2 phase formed in the mixture behave totally differently from that of the pure sample and optical textures similar as those in the B7 phase have been observed. The underlying reason is still unknown. It seems that in the mixture the surface tension has changed and it plays an important role in the formation of the B7 like textures.

In a summary, we have shown the fantastic textures of the B7 phase. Twisting ribbons of smectic layers has been proposed as the structural basis of the B7 texture. The various B7 textures can be constructed from the twisting ribbons of the smectic layers. A B7 like texture is observed in the B2 phase of a c=10% 8CB/NOBOW mixture. This phenomenon indicates that the surface tension of the smectic layer plays an important role in forming those twisting ribbons of smectic layers.

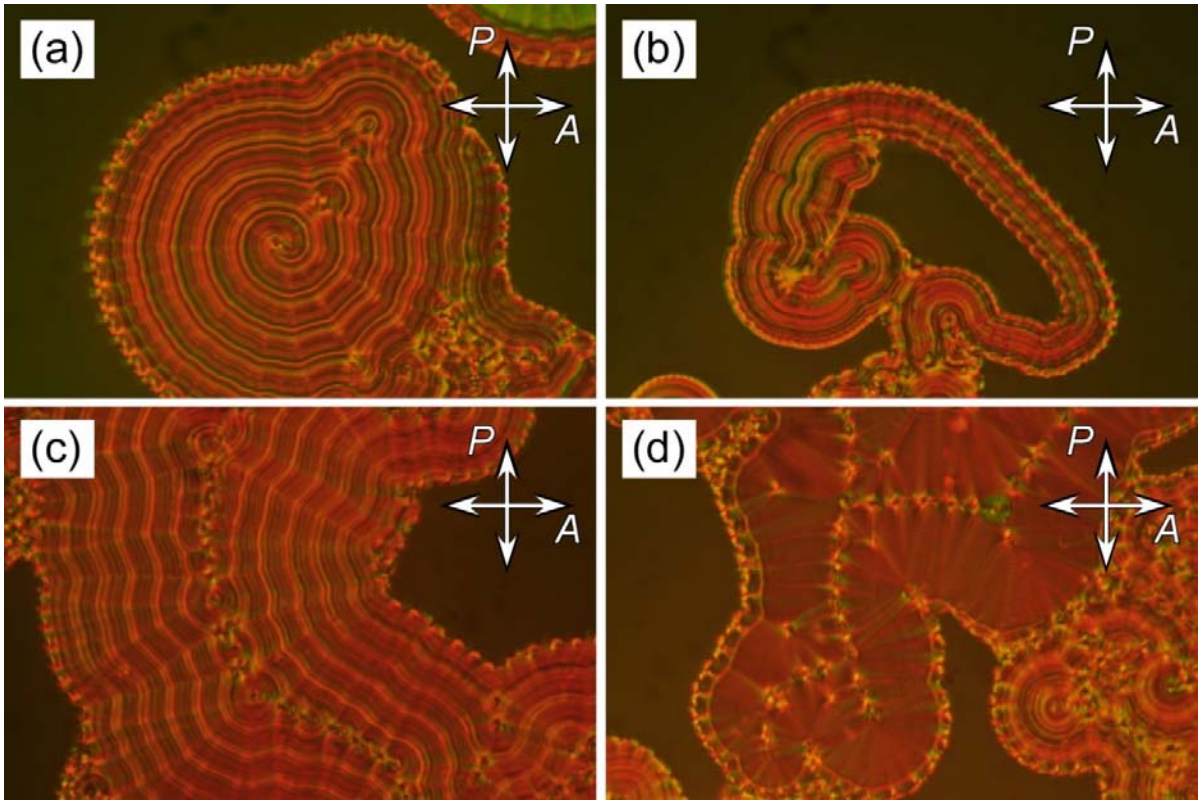

Figure 5.3.3: Optical textures of the B2 phase of a c=10% 8CB/NOBOW mixture taken at T=160°C, cooling from isotropic at 0.02°C/min. (a) The spiral texture of the B2 phase. (b) The ribbon texture of the B2 phase. (c) and (d) The ribbon texture of the B2 phase, where series of defects are observed.

Bibliography

[1] D. R. Link, G. Natale, R. Shao, J. E. Maclennan, N. A. Clark, E. Körblova, and D. M. Walba: Spontaneous formation of macroscopic chiral domains in a fluid smectic phase of achiral molecules. *Science* 1997, **278**, 1924-1927.

[2] D. A. Coleman, J. Fernsler, N. Chattham, M. Nakata, Y. Takanishi, E. Körblova, D. R. Link, R.-F. Shao, W. G. Jang, J. E. Maclennan, O. Mondainn-Monval, C. Boyer, W. Weissflog, G. Pelzl, L.-C. Chien, J. Zasadzinski, J. Watanabe, D. M. Walba, H. Takezoe, and N. A. Clark: Polarization-modulated smectic liquid crystal phases. *Science* 2003, **301**, 1204-1211.

[3] G. Pelzl, S. Diele, A. Jákli, and W. Weissflog: The mysterious B7 phase: From its discovery up to the present state of research. *Liquid Crystal* 2006, **33**, 1513-1518.

[4] Michi Nakata, Darren R. Link, Yoichi Takanishi, Yumiko Takahasi, Jirakorn Thisayukta, Hiroko Niwano, David A. Coleman, Junji Watanabe, Atsuo Iida, Noel A. Clark, and Hideo Takezoe: Electric-field-induced transition between the polarization-modulated and ferroelectric smectic-C_SP_F* liquid crystalline states studied using microbeam x-ray diffraction. *Phys. Rev. E* 2005, **71**, 011705/1-6.

[5] D. R. Link, N. Chattham, N. A. Clark, E. Korblova, and D. M. Walba, *European Conference on Liquid Crystals*, Hersonissos, 1999, O-32, Abstracts.

[6] A. Nemeş, A. Eremin, R. Stannarius, M. Schulz, H. Nádasi, and W. Weissflog: Structure characterization of free-standing filaments drawn in the liquid crystal state. *Phys. Chem. Chem. Phys.* 2006, **8**, 469-476.

[7] A. Eremin, A. Nemeş, R. Stannarius, M. Schulz, H. Nádasi, and W. Weissflog: Structure and mechanical properties of liquid crystalline filaments. *Phys. Rev. E* 2005, **71**, 031705/1-5.

[8] J. Fontana, C. Bailey, W. Weissflog, I. Jánossy, and A. Jákli: Optical waveguiding in bent-core liquid crystal filaments. *Phys. Rev. E* 2009, **80**, 032701/1-4.

[9] D. Pociecha, E. Gorecka, M. Čepič, N. Vaupotič, and W. Weissflog: Polar order and tilt in achiral smectic phases. *Phys. Rev. E* 2006, **74**, 021702/1-6.

[10] A. Jákli, Ch. Lischka, W. Weissflog, G. Pelzl, and A. Saupe: Helical filamentary growth in liquid crystals consisting of banana-shaped molecules, *Liquid Crystal* 2000, **27**, 1405-1409.

[11] A. Eremin, A. Nemes, R. Stannarius, G. Pelzl, and W. Weissflog: Spontaneous bend patterns in homochiral ferroelectric SmCP films: Evidence for a negative effective bend constant. *Soft Matter* 2008, **4**, 2186-2191.

Chapter 6

Achiral Structure of the B4 Phase

6.1 Introduction

Bent-core liquid crystals have attracted intense interest over the years, exhibiting a wide variety of novel structural phenomena involving the interplay of chirality, molecular bend and molecular tilt. It has been shown that bent-core molecules have a strong tendency for saddle-splay layer deformations attributed to the orthogonal tilt directions of the two molecular half-arms, which cause dilation in one half-layer and compression in the other and produce a frustrated state that can be relieved by saddle-splay curvature. If this tendency is strong enough, the smectic layers form catenoids or helicoids. In the B4 phase, the tendency for saddle-splay curvature coupled with the polarization leads to the formation of chiral helical nanofilaments with either clockwise or anticlockwise twist [1]. On the other hand, the dark conglomerate (DC) phase driven by the same underlying mechanism forms disordered focal conic domains [2]. Both of the B4 and DC phases show macroscopic left- and right-handed chiral domains and diffused x-ray scattering peak of the smectic layers with several sub harmonics. However, the DC phase usually appears directly from the isotropic medium, while the B4 phase is usually the lowest liquid crystal phase in the sample and is still stable at room temperature. The microscopic structures of these two phases are totally different, where the B4 phase is made of helical nanofilaments and the DC phase is made of disordered focal conics. One possible explanation for this is that the B4 phase is entropy favored while the DC phase is enthalpy favored.

Therefore, it would be interesting to further investigate these phases and understand the nature of them. By doing freeze-fracture transmission electron microscopy (FFTEM), we have studied the microstructure of many low temperature bent-core liquid crystal phases. Those low temperature liquid crystal phases are the lowest liquid crystal phases of the samples and are stable at room temperature (among all the liquid crystal phases formed by bent-core molecules, only the B4 phase is stable at room temperature). Thus, these phases are supposed to be the B4 phase. However, some interesting microstructures of those phases have been revealed by FFTEM images, which will be discussed in detail in the following sections.

6.2 P-12-OPIMB: Achiral B4 structure

The P-n-OPIMB series first synthesized by Prof. Junji Watanabe was reported as the first material indicating helical structure in the bent-core molecular systems [3]. The chemical structure and the phase sequence of the P-n-OPIMB series are shown in Figure 6.2.1. The molecules are symmetric and possess typical Schiff bases. In the P-n-OPIMB series, from the short alkyl tail bent-core molecule (n=6) to the long alkyl tail bent-core molecule (n=16), the molecular length increases as the alkyl tail becomes longer and the increase of molecular length shows typical odd-even effects, as shown in Table 6.2.1. Corresponding to the increase of the molecular length, the range of the B3 phase becomes smaller and smaller and disappears at P-12-OPIMB. In spite of the difference in the phase sequence between molecules with short and long alkyl tails, helical nanofilaments of the B4 phase have been confirmed in the P-n-OPIMB series. Figures 6.2.2a-c show unambiguous helical nanofilaments in the B4 phase of P-8-OPIMB, P-12-OPIMB and P-16-OPIMB, respectively.

However, in the study of the P-n-OPIMB series, we observe a coexistence of helical nanofilaments and another microstructure in the B4 phase of P-12-OPIMB. This microstructure which we call achiral B4 structure is dominated by saddle-splay curvature and shows no helical twist. Though we have shown in Chapter 3 that at the interface of the glass substrate, due to the geometry confinement, parabolic focal conic or toric focal conic structures are observed in the B4 phase, where the surface structures are achiral and yet the smectic layers are still chiral with specific twist of helical nanofilament growing epitaxial on top of the surface structures, the achiral B4 structure is observed in the bulk and has three-dimensional structure.

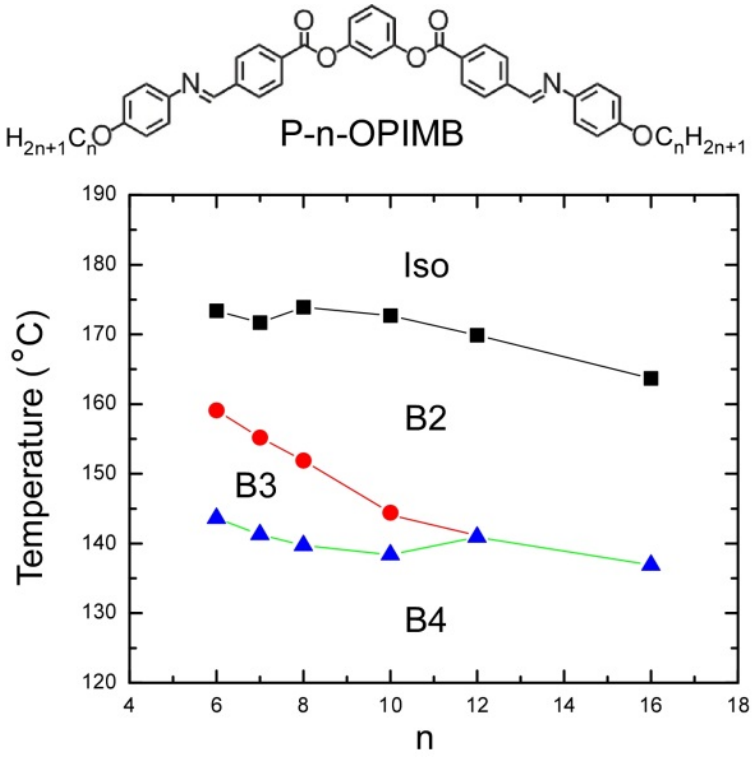

Figure 6.2.1: Chemical structure and phase sequence of the P-n-OPIMB homolog series. The phase sequence is reproduced from reference [3].

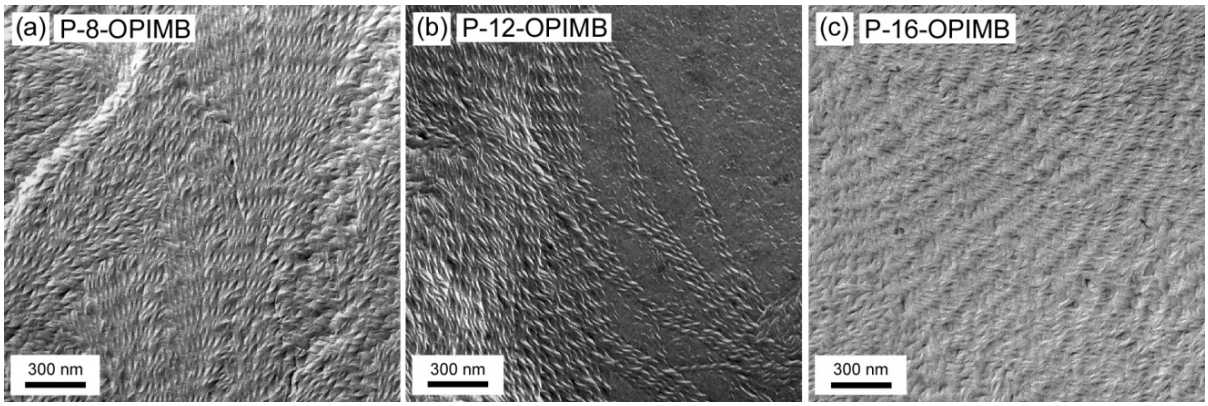

Figure 6.2.2: Helical nanofilaments of the B4 phase. (a), (b), (c) FFTEM images of P-8-OPIMB, P-12-OPIMB and P-16-OPIMB, respectively, showing the conventional helical nanofilaments of the B4 phase. All three materials are quenched at room temperature and fractured in the bulk.

	n=6	n=7	n=8	n=9	n=10	n=11	n=12	n=13	n=14	n=15	n=16
Length (Å)	38.0	38.0	40.4	40.7	43.4	43.7	46.3	46.7	49.3	49.6	52.3

Table 6.2.1: Molecular length of P-n-OPIMB obtained by Chem3D, MM2 energy minimization. As the alkyl tails become longer, the molecular lengths become larger and the typical odd-even effect is observed.

Because the achiral B4 structure coexists with the helical nanofilaments in the bulk phase of P-12-OPIMB, we cannot distinguish them using the depolarized transmission light microscopy (DTLM). Therefore, FFTEM is mainly used here to reveal the achiral B4 structure at nm scale for detailed analysis. As shown in Figure 6.2.3a, the achiral microstructure shows a coffee-bean-like texture while conventional helical nanofilaments show the flame-tip-like texture (Figures 6.2.2a-c). With higher magnification (Figure 6.2.3b), we can see clearly that the achiral B4 structure is made of smectic layers curved in saddle-splay shapes. Segments of saddle-splayed layers dominate the image and no macroscopic chiral structure can be observed. However, different from the disordered focal conics observed in the DC phase, these saddle-splay segments are locally arranged with hexagonal packing.

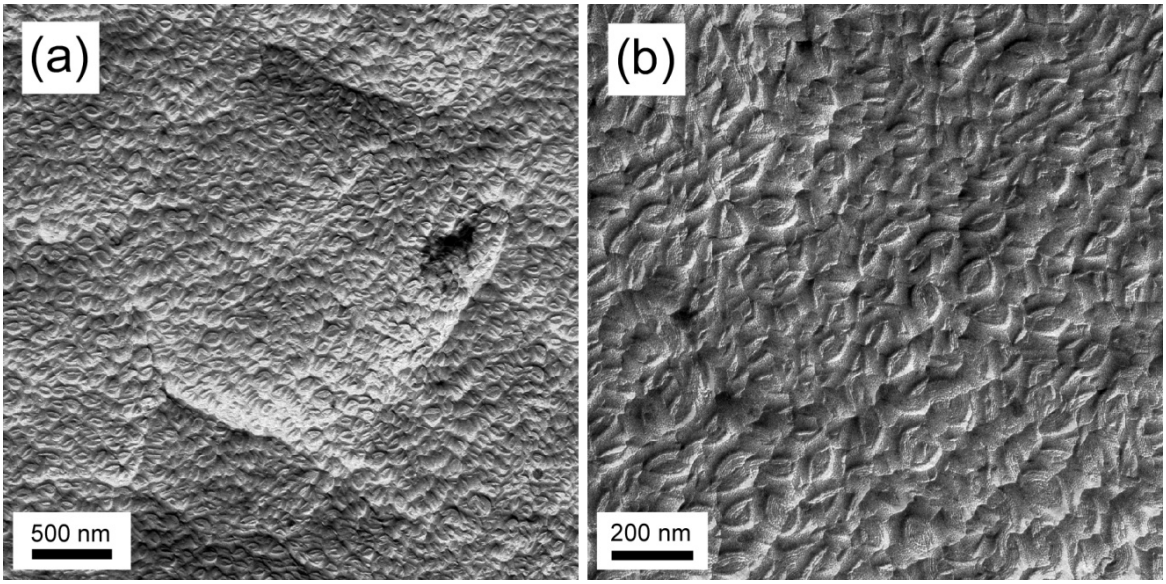

Figure 6.2.3: FFTEM images of the achiral B4 structure of P-12-OPIMB quenched at room temperature and fractured in the bulk. (a) The achiral B4 structure shows the coffee-bean-like texture. (b) Higher magnification of (a). The achiral B4 structure is dominated by saddle-slay curvature and segments of saddle-splay layers are locally arranged in a hexagonal lattice.

In order to unambiguously clarify the difference between the achiral B4 structure and that of the DC phase, as both phases are dominated by saddle-splay curvature, the free surface topography of the achiral B4 structure is shown in Figures 6.2.4a and b. At the air/liquid crystal interface, the achiral B4 structure is essentially the same as that observed in the bulk. On the other hand, the DC phase which shows disordered focal conics in the bulk forms quasi ordered toric focal conic domains at the air/liquid crystal interface (Chapter 4). This quasi ordered free surface structure is a common feature of the DC phase, having been observed in different materials forming the DC phase. Thus, the surface topography of the achiral B4 structure is totally different from that of the DC phase and we conclude that the achiral B4 structure is another kind of microstructure, different from the B4 helical nanofilaments and the DC

disordered focal conics. The consistent topography of the achiral B4 structure observed in the bulk and at the free surface indicates the continuous three-dimensional organization of those smectic layers. Different kinds of three-dimensional periodic minimal surfaces with saddle-splay curvature have been demonstrated by mathematicians and the three-dimensional arrangements of the Schwarz's P surface and the Schoen's GW surface are shown in Figures 6.2.5a and b, respectively. The Schwarz's P surface has been used to calculate the elastic energy of the focal conic in the DC phase. Due to the locally hexagonal arrange of the saddle-splay segments, the Schoen's GW surface may better describe the three-dimensional arrangement of the achiral B4 structure.

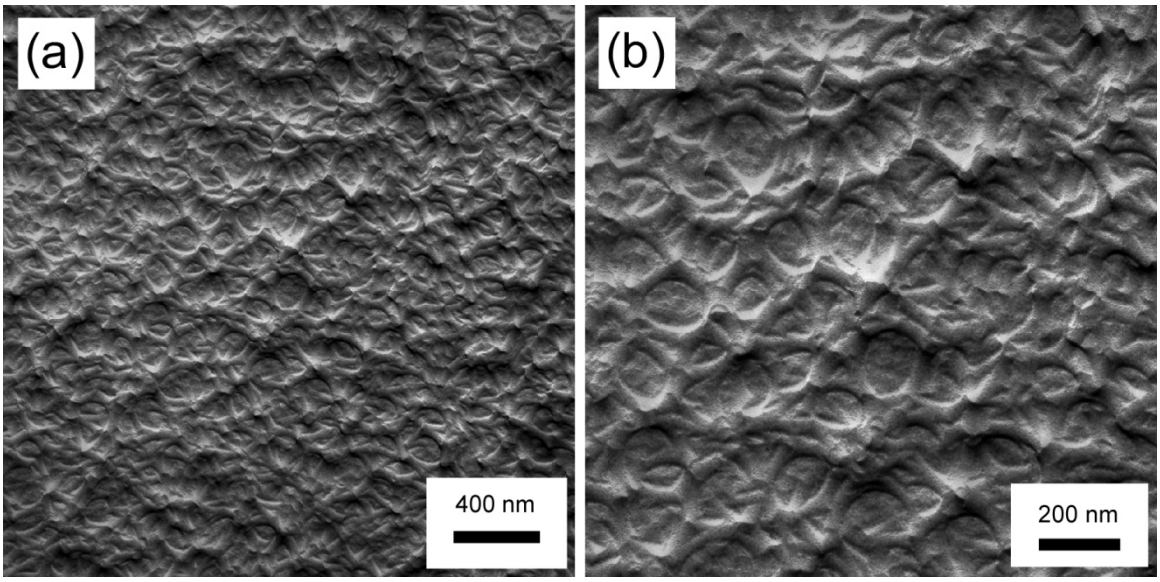

Figure 6.2.4: FFTEM images of the achiral B4 structure of P-12-OPIMB at the air/liquid crystal interface, quenched at T=120°C. (a) The free surface topography of the achiral B4 structure is similar to those observed in the bulk, indicating the three-dimensional organization of the smectic layers from the bulk to the surface. (b) Higher magnification of (a).

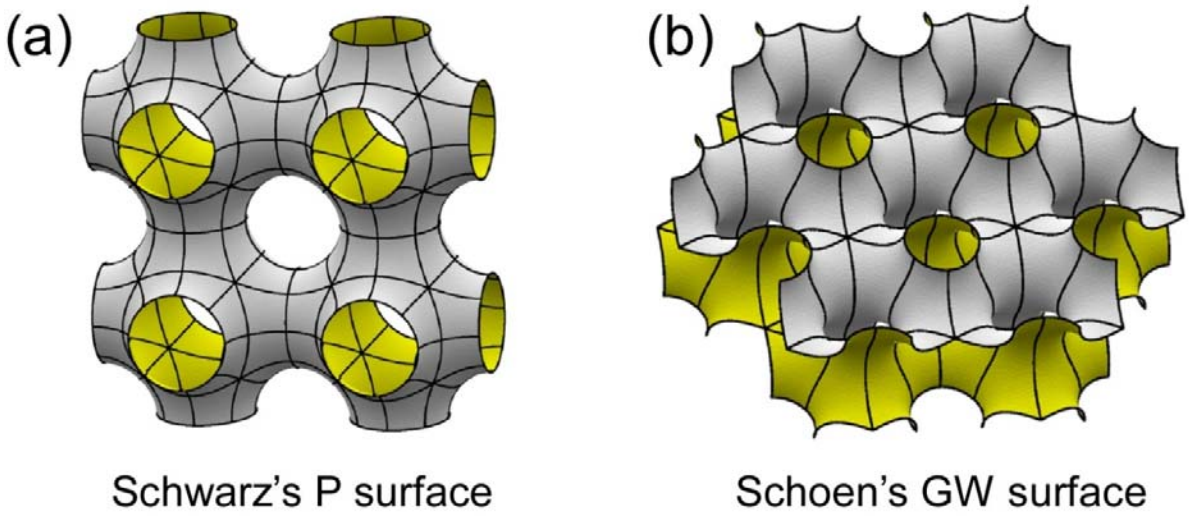

Figure 6.2.5: Examples of three-dimensional periodic minimal surfaces. (a) Three-dimensional periodic Schwarz's P surface, which is used to calculate the elastic energy of focal conic in the DC phase. (b) Three-dimensional periodic Schoen's GW surface, which can better explain the achiral B4 structure.

In order to further understand the nature of the achiral B4 structure, we will first compare the preferred radius of the saddle-splay curvature in the helical nanofilaments and that in the disordered focal conics. For helical nanofilaments, the preferred radius of the saddle-splay curvature is $r=p/2\pi\sim30$ nm (the pitch p can be measured from FFTEM images of helical nanofilaments). For the disordered focal conic structure of the dark conglomerate phase, the minimum elastic free energy corresponds to r~200 nm (measured from the distance between two toric focal conic at the air/liquid crystal interface). However, the preferred radius estimated from the achiral B4 structure is r~100 nm, which is in between the preferred radius of helical nanofilaments and that of disordered focal conics. The difference in preferred radius of the saddle-splay curvature may be an intrinsic reason for forming the achiral B4 structure. On the

other hand, in hundreds of FFTEM images studied, the achiral B4 structure is only observed in P-12-OPIMB and has never been observed in other P-n-OPIMB homologs. Compared with other P-n-OPIMB compounds in the phase diagram (Figure 6.2.1), P-12-OPIMB is the one where the B3 phase starts to disappear or appear. As we know, interesting things usually happen around regions where changes take place. So the unique phase sequence of P-12-OPIMB may also play an important role in the formation of the achiral B4 phase.

In a summary, in the B4 phase, the tendency for saddle-splay curvature coupled with the polarization usually leads to the formation of chiral helical nanofilaments with either clockwise or anticlockwise twist. However, in addition to the helical nanofilaments, we observe another microstructure in P-12-OPIMB with no helical twist, which we call achiral B4 structure. This achiral B4 structure is dominated by saddle-splay curvature and shows a coffee-bean-like texture. The achiral B4 structure is consistent in the bulk and at the free surface and appears to have three-dimensional order. Examples of three-dimensional periodic minimal surfaces have been shown to be the potential model of this phase.

6.3 W513: Enhanced formation of helical nanofilaments in the mixtures with 8CB

Until now most of the liquid crystal materials showing the B4 phase possess the classic double Schiff bases, which is hydrolytically unstable. W513 is a new bent-core mesogen synthesized by Dr. Ethan Tsai in Prof. David M. Walba's group, possessing an unsymmetrically substituted bisphenol unit as a rigid central linker. The chemical structure and the phase sequence of W513 are shown in Figure 6.3.1. Detailed characterization of the B4 phase will be published elsewhere. Here we will focus on the difference between the microstructure of pure W513 and that of 8CB/W513 mixtures observed in the B4 phase.

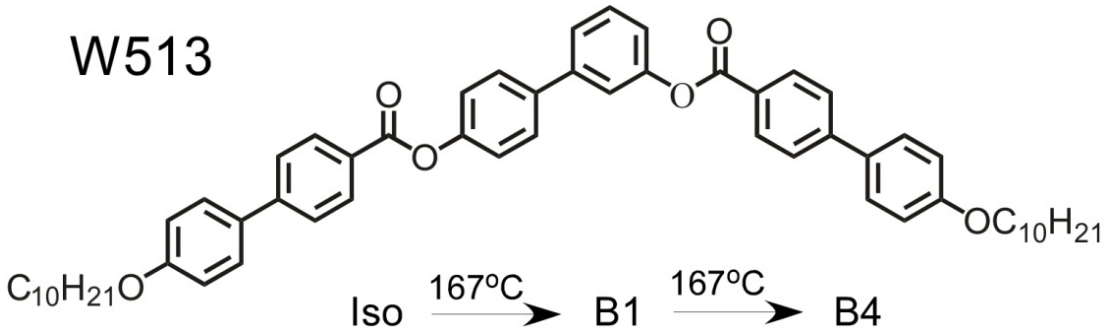

Figure 6.3.1: Chemical structure and phase sequence of pure W513. There is a B1 phase of very narrow temperature range, between the Iso and B4 phases.

Figures 6.3.2a-d show the DTLM images of the B1 and B4 phases of pure W513 during the B1-B4 phase transition. The B1 phase shows the conventional banana-leaf-like texture with dark brushes parallel to the polarizers (Figure 6.3.2a). Upon cooling, the B4 phase comes in as dark regions under crossed polarizers (Figures 6.3.2b and c), different from the texture of the conventional B4 phase such as that in NOBOW (Chapter 3) which shows a bluish color. When

the sample totally changes to the B4 phase, some bright, birefringent regions can still be observed (Figure 6.3.2d). We will show later that the birefringent regions correspond to the lock-in of the B1 phase. Interestingly, when decrossing the polarizers, we cannot observe left- and right-handed chiral domains in the B4 phase.

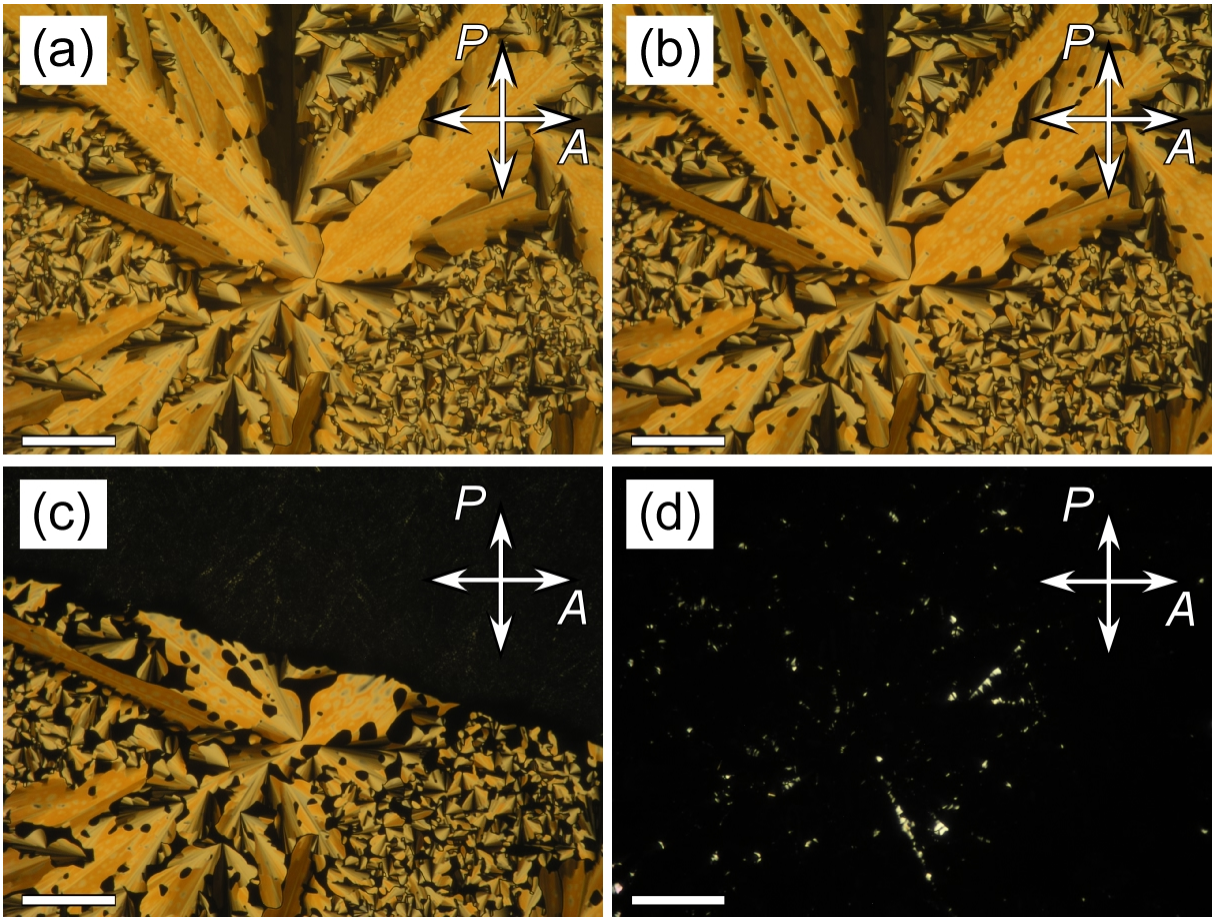

Figure 6.3.2: DTLM images of pure W513 during the B1-B4 phase transition around T=170°C. (a) DTLM image of the B1 phase of pure W513. (b) and (c) The B4 phase appears as dark regions under crossed polarizers. (d) DTLM image of the B4 phase of pure W513 with crossed polarizers. The birefringent regions are attributed to the lock-in of the B1 phase. The scale bar is 100 μm in all images.

In order to study the microstructure of the low temperature B4 phase, FFTEM and free surface TEM have been carried out. The results are shown in Figures 6.3.3a-d. Figure 6.3.3a shows the bulk structure of the B4 phase. Though individual helical nanofilaments cannot be distinguished in the image, the texture which is made of aggregates of helical nanofilaments resembles those observed in other materials. In the same sample, we also observed the two-dimensional periodic structure (the smectic layers and the layer undulations, as shown in Figure 6.3.3b), which indicates the coexistence of the B1 phase (two-dimensional periodic structure is characteristic of the B1 phase). The free surface TEM images show similar textures. The free surface topography of the B4 phase at the air/liquid crystal interface is shown in Figure 6.3.3c. Coexisting with the B4 phase, the microstructure of the B1 phase which lock-in at the low temperature B4 phase is also observed, as shown in Figure 6.3.3d.

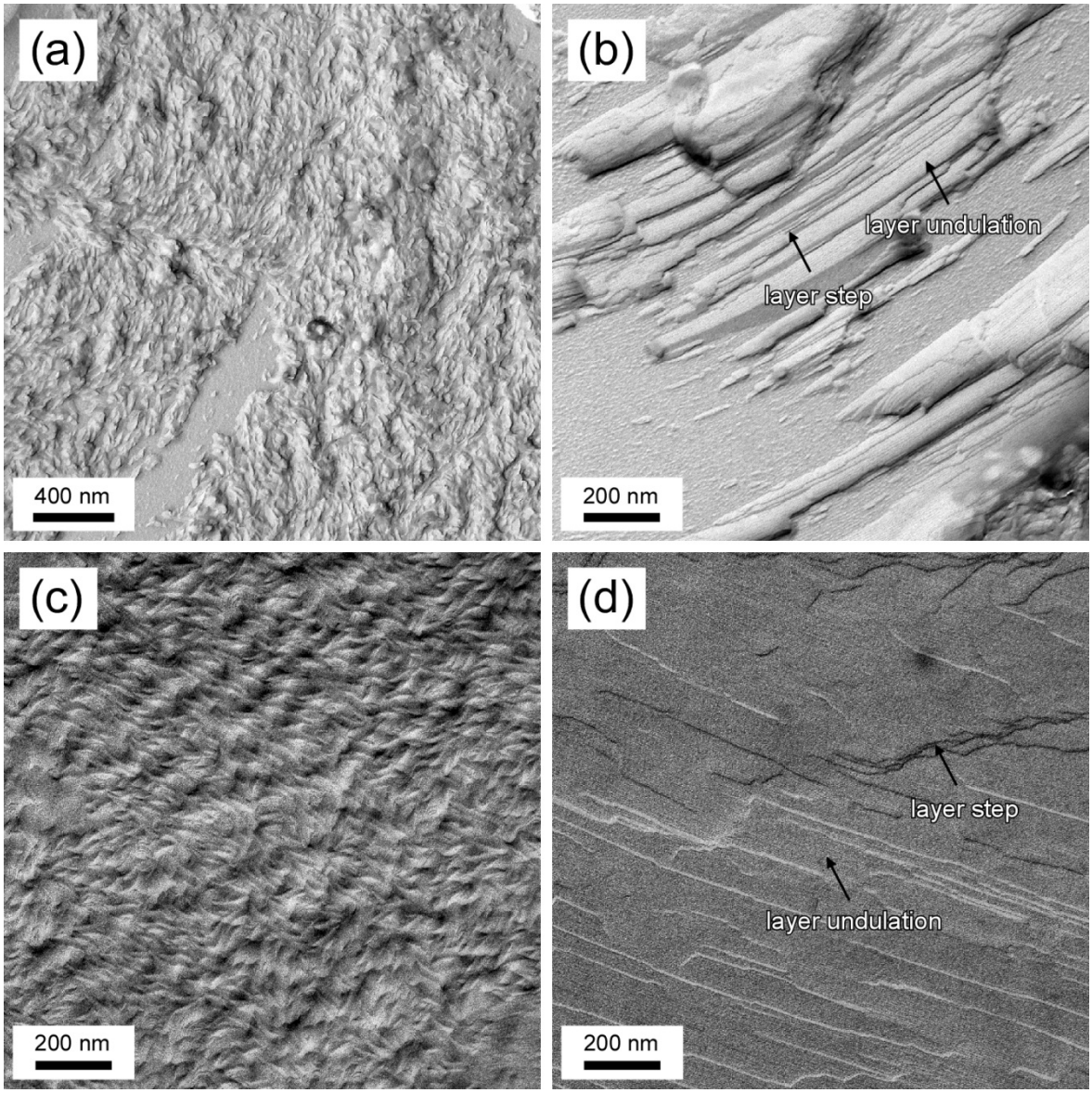

Figure 6.3.3: Microstructures of pure W513 in the bulk and at the air/liquid crystal interface. (a) FFTEM image of the B4 phase showing the topography of helical nanofilament aggregates. (b) FFTEM image of the B1 phase coexisting with the B4 phase at low temperature, showing two-dimensional periodic structure, the smectic layers and the layer undulations. (a) and (b) are taken from the same sample, quenched at T=160°C and then fractured in the bulk. (c) TEM image of the B4 phase at the air/liquid crystal interface. (d) TEM image of the B1 phase at the air/liquid crystal interface. (c) and (d) are taken from the same sample, quenched at T=155°C. The free surface structure is imaged in (c) and (d).

In order to further characterize the B4 phase of W513, three different concentrations of 8CB/W513 mixtures (c=10%, 40%, and 76%, c is the weight percent of 8CB) were prepared. Due to the freezing point depression, which is similar to the 8CB/NOBOW systems, there is no B1 phase in the mixtures. W513 molecules first undergo a complete phase separation into the B4 phase from the isotropic medium, while the 8CB is still isotropic. In all three mixtures, left and right-handed chiral domains are observed under decrossed polarizers, as shown in Figures 6.3.4a-f. Interestingly, the left- and right-handed chiral domains shown in the c=40% 8CB/W513 mixture present a unique boundary texture between different chiral domains. Under the optical microscope, we can directly observe how the boundary texture develops after different chiral domains meet. Currently, the appearance of the boundary texture is still a mystery.

Corresponding to the left and right-handed chiral domains, helical nanofilaments have been clearly observed in the mixtures. Figure 6.3.5a show the helical nanofilaments observed in a c=40% 8CB/W513 mixture. Individual helical nanofilament left on the replica appears as a dark, faint line in the image. An FFTEM image of a c=76% 8CB/W513 mixture is shown in Figure 6.3.5b, which also clearly shows the helical nanofilaments of the B4 phase. The width of the helical nanofilaments of W513 is similar as that of NOBOW, w~35 nm. However, the helical pitch of W513 is p~150 nm, while the helical pitch of NOBOW is p~210 nm. As we know, the filament width and helical pitch are determined by the minimization of the total elastic energy of the filament, which strongly depends on the elastic constants. Therefore, the difference in helical pitch indicates different elastic constants of W513 and NOBOW.

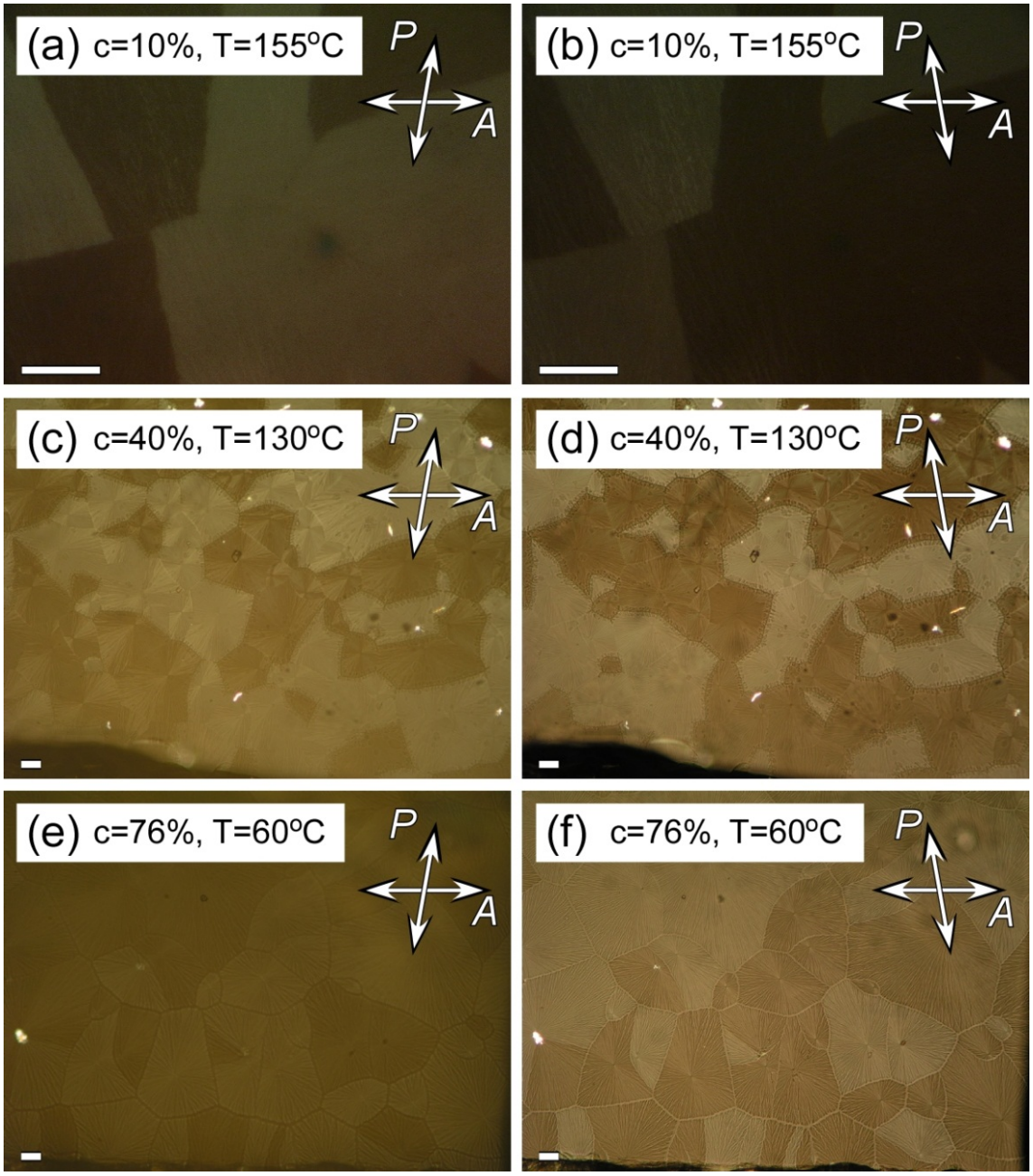

Figure 6.3.4: DTLM images of 8CB/W513 mixtures. (a) and (b) DTLM images of a c=10% 8CB/W513 mixture, showing left- and right-handed chiral domains with decrossed polarizers. (c) and (d) DTLM images of a c=40% 8CB/W513 mixture. (e) and (f) DTLM images of a c=76% 8CB/W513 mixture. The scale bar is 100 μm in all images.

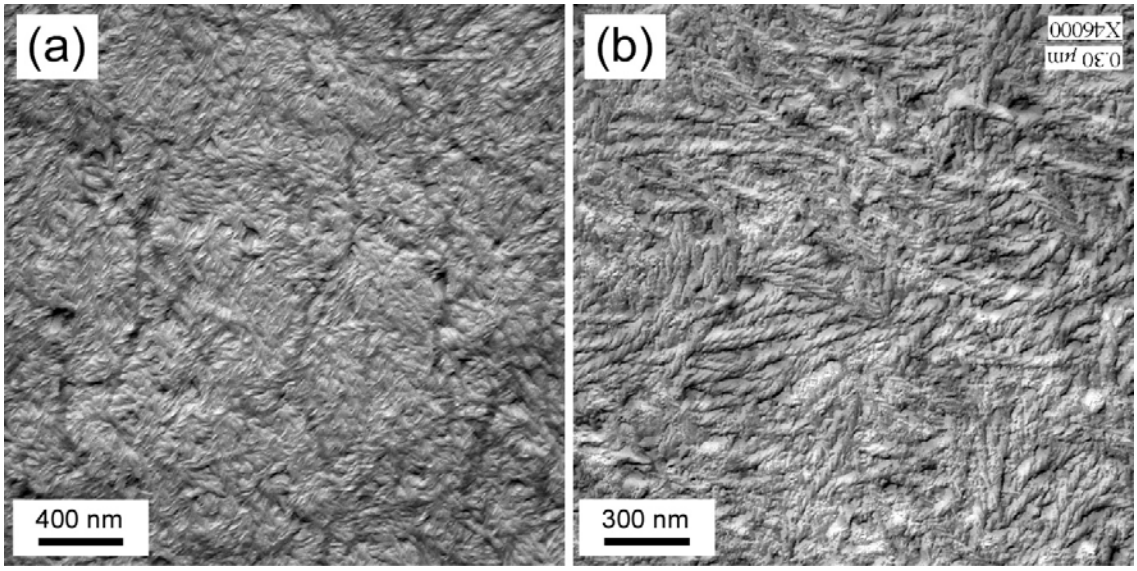

Figure 6.3.5: Distinct helical nanofilaments observed in mixtures of 8CB and W513. (a) FFTEM image of a c=40% 8CB/W513 mixture quenched at T=60°C when 8CB is still isotropic and fractured in the bulk. Helical nanofilaments can be observed in the mixture. The dark, faint lines are helical nanofilaments left on the replica. (b) FFTEM image of a c=76% 8CB/W513 mixture quenched at T=37°C when 8CB is in the nematic phase and fractured in the bulk. Individual helical nanofilaments can be identified.

Based on the above discussion, we notice that there are three main differences between pure samples and the mixtures: (1) There is coexistence of the B4 and B1 phases at low temperature in pure W513, while there is no B1 phase in the mixtures. (2) No optical rotation is observed in pure W513, while left- and right-handed chiral domains are distinguished in the mixtures. (3) Though the bulk texture of pure W513 resembles that of B4 helical nanofilament aggregates, distinct helical nanofilaments can only be observed in the mixtures. We believe that the high temperature B1 phase plays an important role here. It is possible that the B1 phase hinders the formation of helical nanofilaments when the B4 phase comes in and this is strongly supported by the lock-in of the B1 phase at low temperature. In this case, nucleation and growth of helical

nanofilaments in pure W513 may be confined in a small volume and no macroscopic chiral domains can be formed. To further test the idea, NMR has been carried out on pure W513 and 8CB/W513 mixtures, for the molecular environment in the B4 phase of pure W513 should be different from that of 8CB/W513 mixtures if the formation of helical nanofilament is hindered by the high temperature B1 phase in pure W513.

Figure 6.3.6 shows the NMR spectra of pure W513 (red curve) and a c=10% 8CB/W513 mixture (blue curve). By comparing the two NMR signals carefully, we notice three small differences between them: (1) In the mixture, the NMR peaks become sharper. (2) The positions of some NMR peaks have shifted a little bit in the mixture, for example, the two peaks around 27 ppm. (3) The NMR peak of C=O group (around 66 ppm) splits into two peaks in the mixture. The broad line width in the solid-state ^{13}C NMR of W513 is most likely due to a distribution of isotropic chemical shifts (as observed under Magic Angle Spinning), that is a distribution of local environments. When the B4 phase grows in from the isotropic in the mixture, it is much easier to get larger domains, which have fewer inherent inhomogeneities than the small saddles that grow in from the B1 phase in pure W513. Therefore, the carbons should be in more uniform shielding environments for each different carbon atom in the mixture and give a sharper peak. The small shifts of peak position also reflect the slightly different molecular environments in pure W513 and in the mixture. The single NMR peak of C=O group in the pure sample (around 66 ppm) splits into two peaks in the mixture, indicating the chiral confirmation of the molecular arms in the mixture, which is typical in the NOBOW B4 phase [4]. Thus, we conclude that due to the high temperature B1 phase, the formation of the B4 phase is hindered in pure samples. In the mixture, the B1 phase disappears and the formation of helical nanofilaments is enhanced in the B4 phase.

In a summary, we have shown a new bent-core material W513 without Schiff bases which forms the B4 phase. However, because of the high temperature B1 phase, the formation of the B4 phase is hindered to some extent. In the mixtures of W513 with 8CB, the formation of helical nanofilaments is enhanced. The overall behavior of W513 in 8CB mixtures is similar to that of NOBOW.

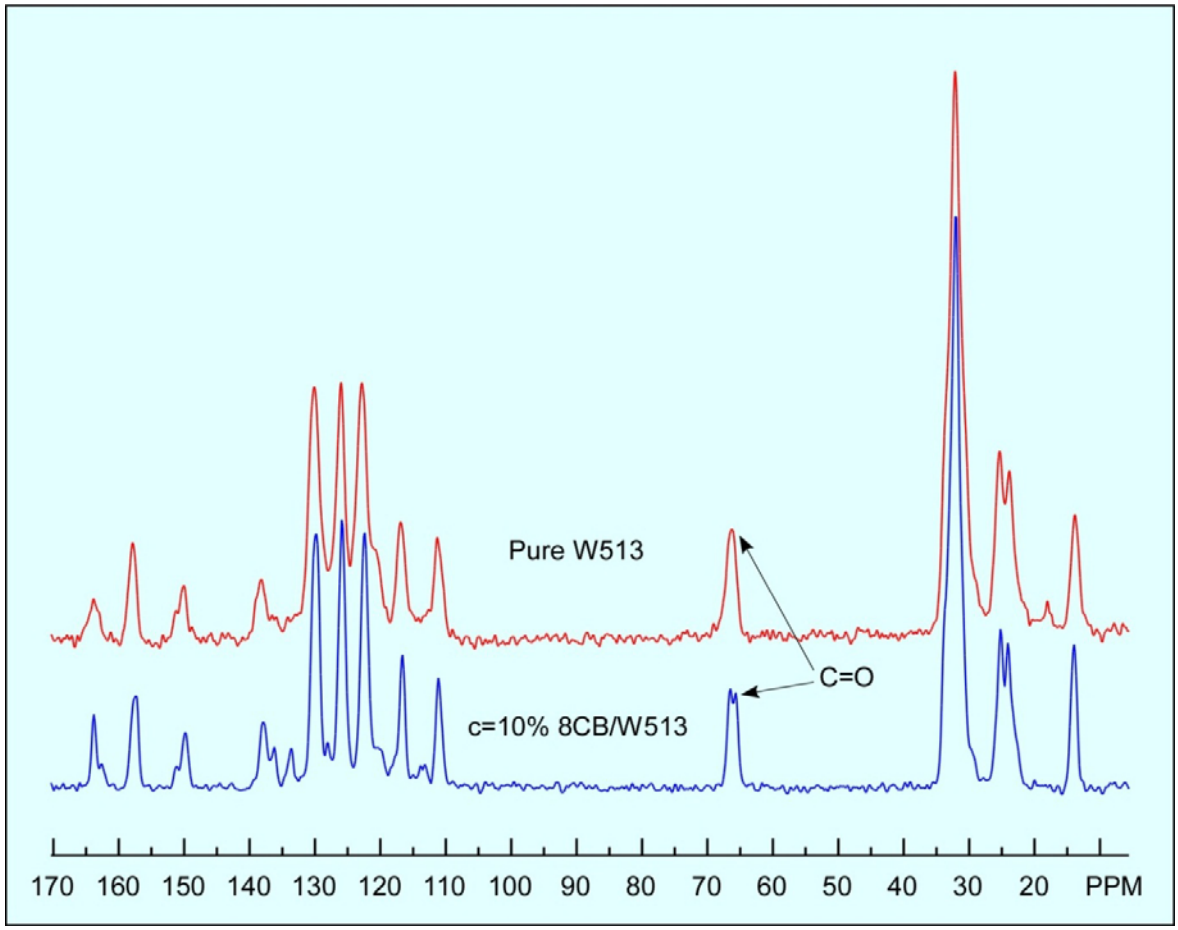

Figure 6.3.6: NMR spectra of pure W513 and a c=10% 8CB/W513 mixture. The red curve shows the NMR of pure W513 and the blue curve shows the NMR of a c=10% 8CB/W513 mixture. Some small peaks evident in the mixture are probably from 8CB.

6.4 W624: The disordered B4 phase or the low temperature DC phase

W624 is one of the five-ring banana-shaped mesogens derived from isophthalaldehyde which are different from the P-n-OPIMB series. The chemical structure and the phase sequence of W624 are shown in Figure 6.4.1 [5]. W624 has a very similar phase sequence to P-12-OPIMB, changing from Iso to B2 then to B4. However, the wide angle x-ray scattering indicates a crystal phase below the B4 phase in W624. The high temperature B2 phase of W624 shows a diffuse x-ray scattering peak at wide angle, indicating the short-range intralayer molecular ordering. In the low temperature B4 phase, multiple diffuse x-ray scattering peaks are observed at wide angle, indicates the intralayer hexagonal molecular packing, as observed in the B4 phase of the P-n-OPIMB series. On further cooling, a lot of sharp x-ray scattering peaks are observed at wide angle, which is characteristic of crystal structure [1]. This peculiar phase sequence has motivated us to characterize the microstructure of the B4 phase in detail.

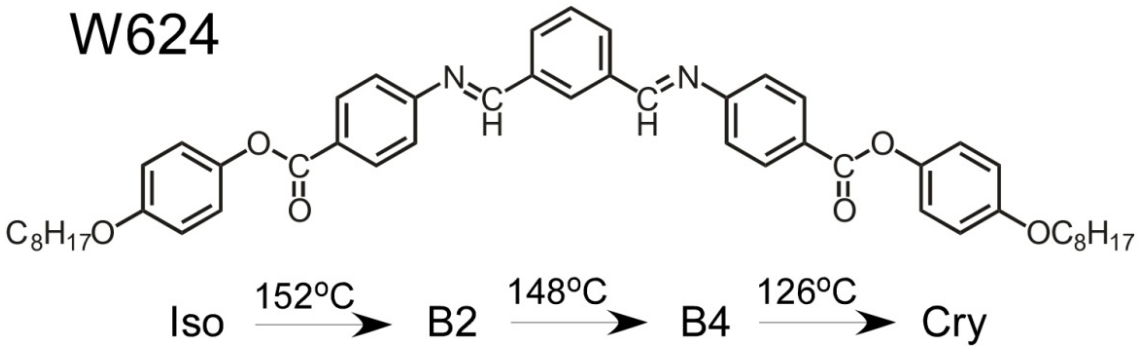

Figure 6.4.1: Chemical structure and phase sequence of W624 [5]. Interestingly, there is a crystal phase below the B4 phase, indicated by the x-ray scattering at wide angle.

Upon cooling, the B2 phase appears from the isotropic with an optical texture shown in Figure 6.4.2a (the growth dynamics and the optical texture of the B2 phase is very similar to that of the conventional B1 phase. Since we focus on the low temperature B4 phase here, we won't discuss whether the high temperature phase is the B1 or B2 phase here.). When further cooling down the sample, the texture totally changes, as shown in Figure 6.4.2b. Though no specific structure can be identified from the image, reminiscent of focal conic structure can be observed, which are totally different from that of P-n-OPIMB series. More interestingly, no left- or right-handed chiral domains can be observed in this phase when decrossing the polarizers. Though x-ray scattering indicates a crystal phase below the B4 phase, there is no observable change in the texture when the sample is cooled down to room temperature. This indicates that the microstructure of the B4 phase stays unchanged on further cooling and the appearance of multiple, sharp x-ray scattering peaks at wide angle may indicate a glass transition (glass transition of the B4 phase has been observed in the P-n-OPIMB series).

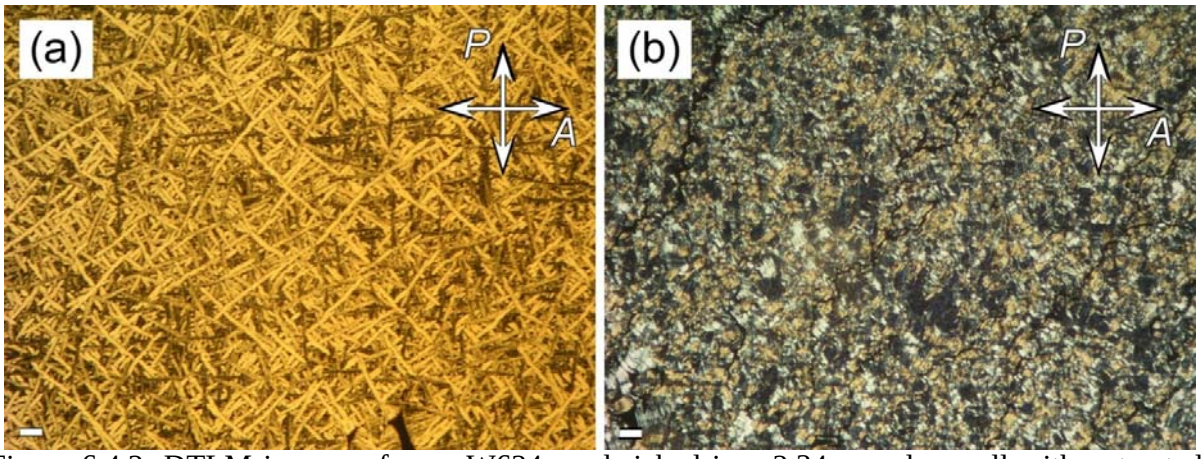

Figure 6.4.2: DTLM images of pure W624 sandwiched in a 2.34 μm glass cell with untreated clean surface. (a) Optical texture of the high temperature B2 phase (T=145°C), showing banana-leaf-like texture with the dark brushes parallel to the polarizers. (b) Optical texture of the low temperature B4 phase (T=135°C), which has a low birefringence. No left- or right-handed chiral domains can be observed when decrossing the polarizers.

FFTEM images of the B4 phase of W624 are shown in Figures 6.4.3a-d. Figures 6.4.3a and b show the microstructure near the glass substrate, where most layers terminate normally at the substrate, as continuous layer edges can be distinguished in the images. Occasionally, the smooth saddle-splay surfaces can also be observed in the fracture plane. This kind of surface topography strongly resembles that observed in the dark conglomerate (DC) phase (Chapter 4). To further confirm this idea, Figures 6.4.3c and d show, to some extent, the three-dimensional bulk structure, with a very rough fracture plane. No helical nanofilaments are visible in those images. Instead, only curved smectic layers, similar to those nested in disordered focal conics, are observed. The overall picture emerged from these FFTEM images is of disordered focal conics like those observed in the DC phase. Therefore, we call this phase, the disordered B4 phase or the low temperature DC phase (for convenience, we will use the low temperature DC phase for this phase).

In order to further confirm the microstructure of the low temperature DC phase, the free surface structures at the air/liquid crystal interface are shown in Figures 6.4.4a-d. Consistent with the microstructure observed in the bulk, there are no helical nanofilaments and the surface topography is dominated by saddle-splay curvature, as shown in Figures 6.4.4a and b. Figures 6.4.4c and d show the regions where most layers terminate at the interface and we can identify the long range continuity of those smectic layers through the layer edges. However, the low temperature DC phase is different from the high temperature DC phase which appears directly from isotropic, as the disordered focal conics anneal into quasi-ordered toric focal conic arrays in the high temperature DC phase at the air/liquid crystal interface (Chapter 4). It seems that the surface structure of the low temperature DC phase is also quenched in some disordered state.

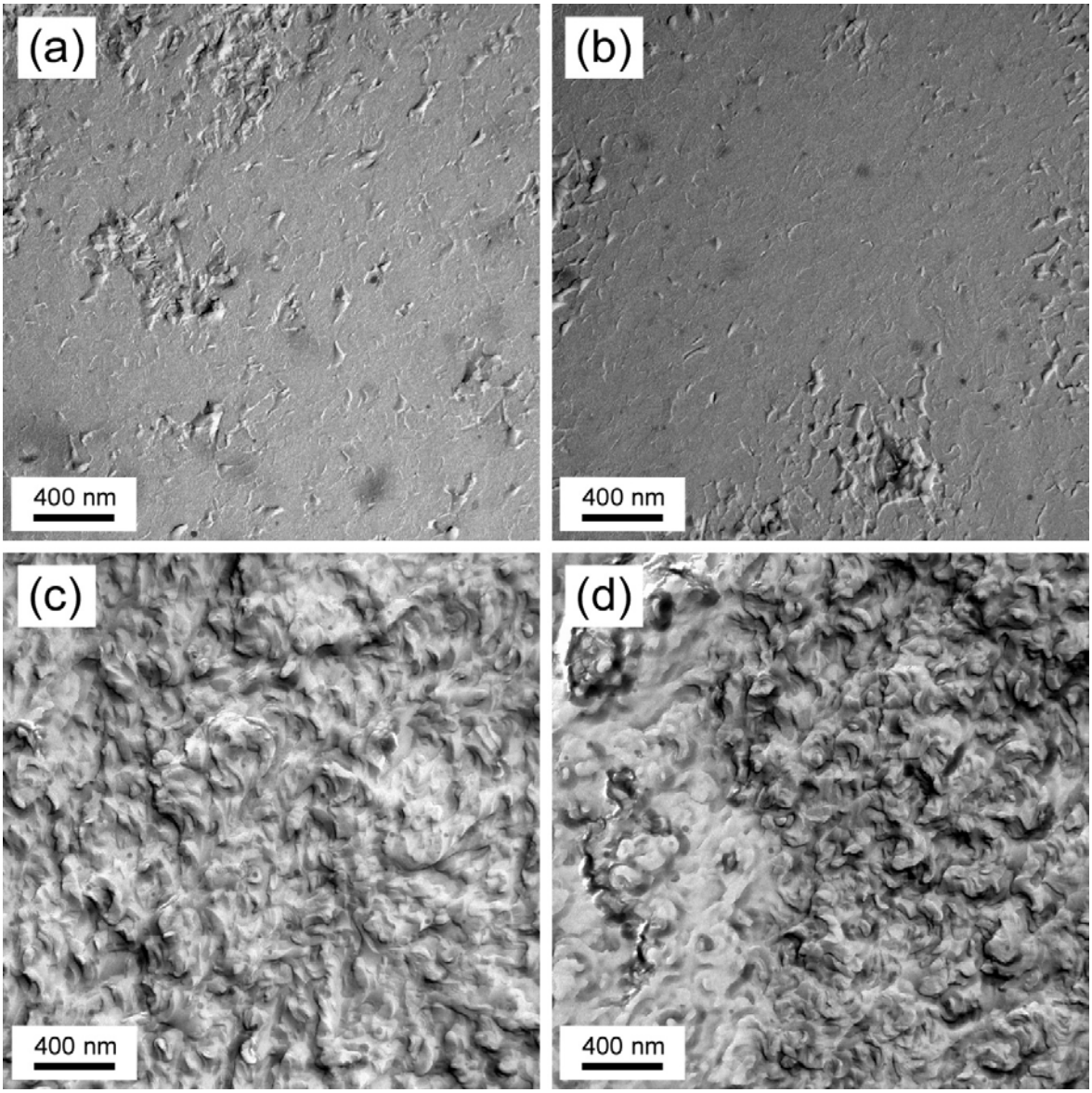

Figure 6.4.3: FFTEM images of W624 quenched at T=135°C and fractured in the bulk. (a) and (b) show the topography of the B4 phase fractured near the glass substrate. The texture is similar to that observed in the dark conglomerate phase, as continuous layer edges and smooth saddle-splay surfaces can be identified in the images. (c) and (d) Bulk arrangement of the smectic layers. No helical structure is observed, but disordered, curved smectic layers.

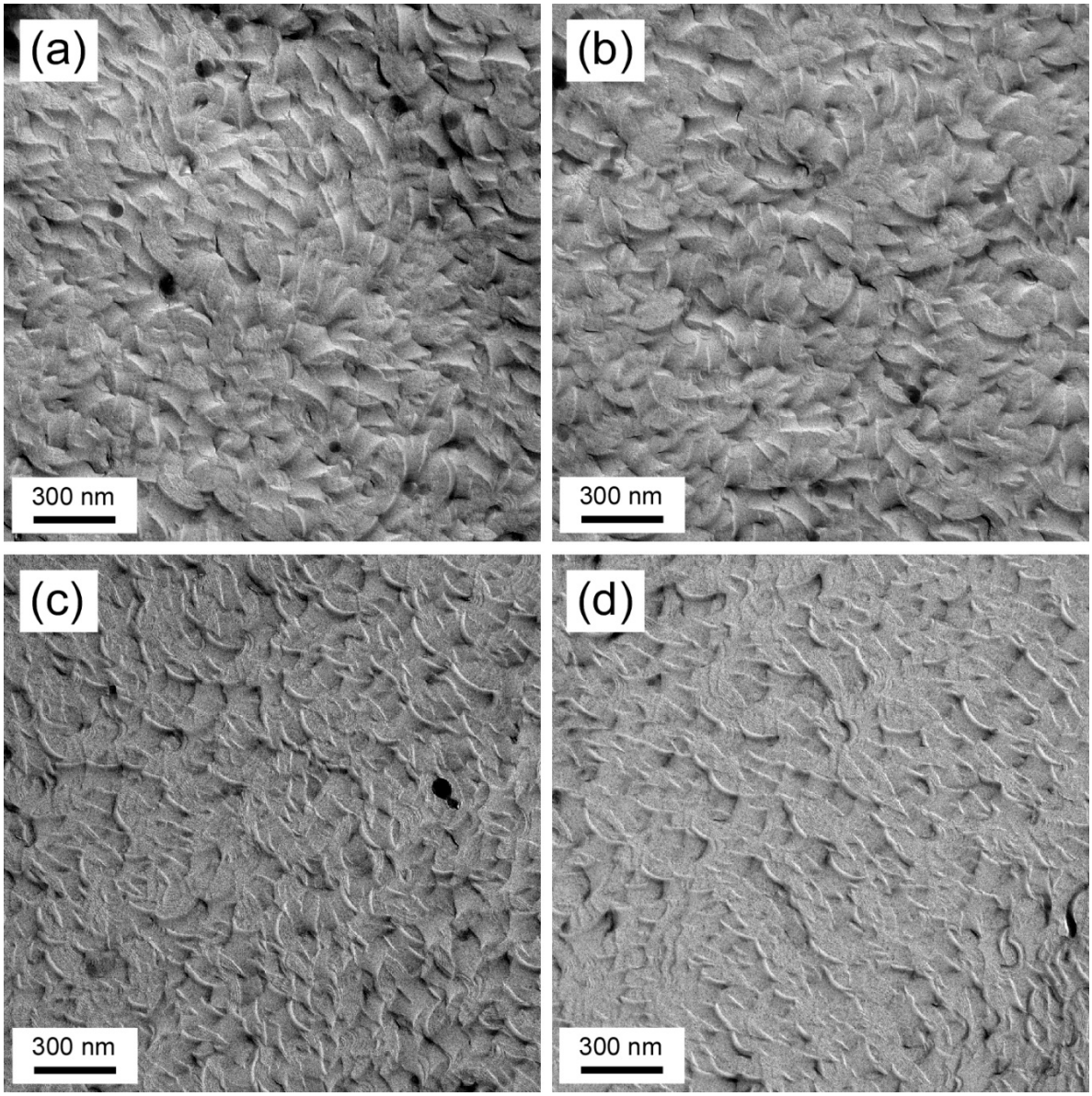

Figure 6.4.4: Free surface TEM images of W624 quenched at T=135°C. (a) and (b) show regions where smectic layers tend to be parallel to the surface. Saddle-splay curvature is the characteristic feature of those smectic layers. (c) and (d) show regions where most smectic layers terminate normally at the interface. Continuous smectic layers can be identified through the layer edges.

The conventional B4 phase is quite robust, forming individual helical nanofilaments in the mixtures same as those observed in pure samples. In order to further understand the property of the low temperature phase, mixtures of W624 with 8CB have been made. Figures 6.4.5a-d show the DTLM images of a c=23% 8CB/W624 mixture where c is the weight percent of 8CB in the mixture. When cooling from the isotropic, W624 first phase separates from the solution, forming the B2 phase, as shown in Figure 6.4.5a. Due to the freezing point depression, the Iso-B2 transition temperature has decreased. However, different from the conventional B4 materials (the P-n-OPIMB series), where the B2 phase disappears in the mixture when the Iso-B2 transition temperature decreases below the B2-B4 transition temperature of pure sample, the B2 phase of W624 still exist when the Iso-B2 transition temperature decreases below the B2-B4 transition temperature of pure sample. The temperature range of the B2 phase in the mixture is quite narrow, where the B2 phase comes in around T=110°C and then changes to the low temperature phase, as shown in Figure 6.4.5b. Left- and right-handed optical rotation can be observed in the low temperature DC phase when decrossing the polarizers, as shown in Figures 6.4.5c and d. The fine texture of the chiral domains is different from that usually observed in the B4 phase of the P-n-OPIMB series. However, the reason why the low temperature DC phase in pure samples has a different texture and doesn’t show any optical rotation is still unknown.

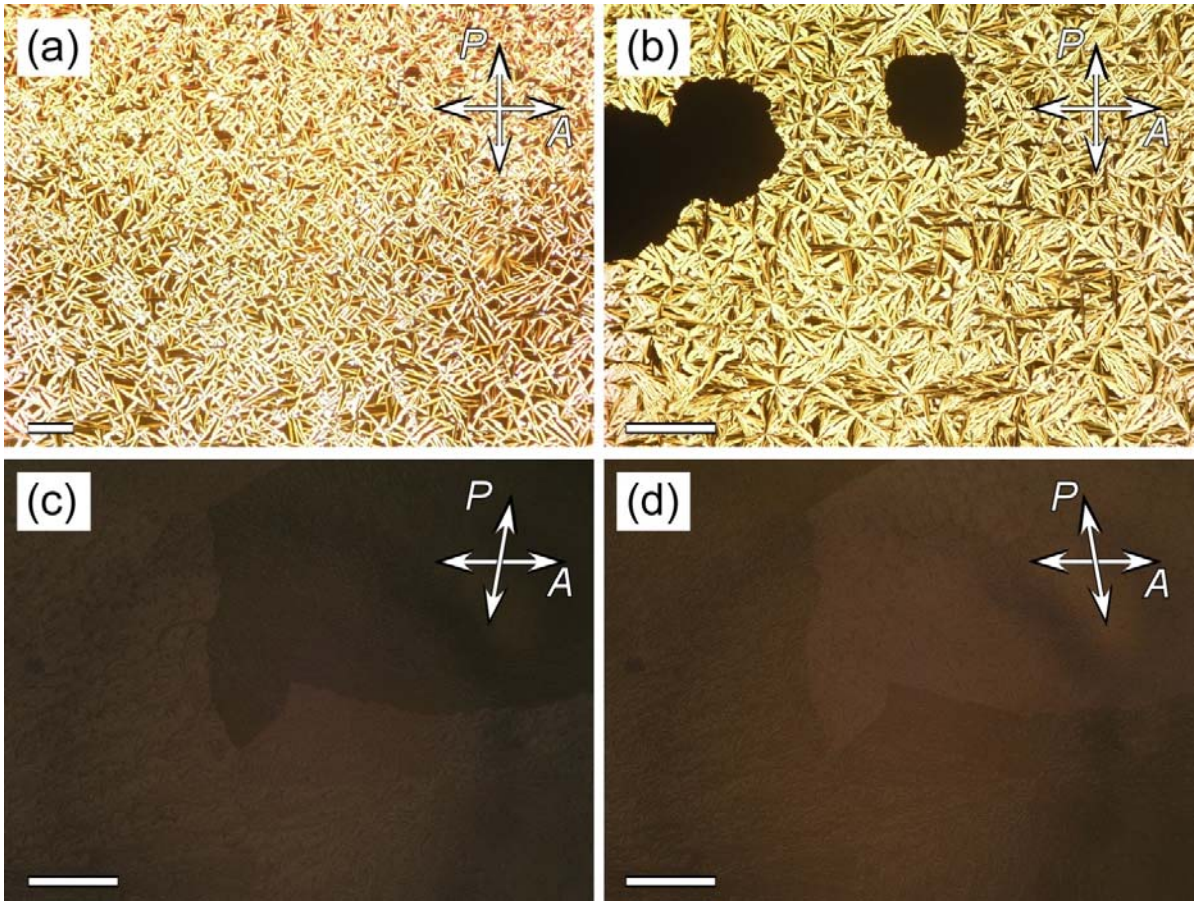

Figure 6.4.5: DTLM images of a c=23% 8CB/W624 mixture in a 4 μm thick cell with planar unidirectional alignment layers taken around T=110°C. (a) The B2 phase comes in from the isotropic on cooling, and shows the banana-leaf-like optical texture. (b) The low temperature DC phase comes in on further cooling, appearing as dark regions under crossed polarizers. (c) and (d) left- and right-handed chiral domains of the low temperature DC phase observed in the mixture, with decrossed polarizers. The B2 phase which has only a very short temperature range comes in around T=110°C and then changes to the B4 phase.

Beside the c=23% 8CB/W624 mixture, a c=50% 8CB/W624 mixture is also prepared. Figures 6.4.6a-f show the optical textures of the c=50% 8CB/W624 mixture heated from room temperature to isotropic, and then cooled down. Before heating, at T=30°C, 8CB is in the

nematic phase. Two different regions can be observed, where regions of the W624 low temperature DC phase appear as black lines and regions of 8CB aligned along the alignment layers show uniform birefringence (Figure 6.4.6a and magnified in Figure 6.4.6b). Upon heating, 8CB changes to isotropic, while W624 changes to a beautiful texture, shown in Figure 6.4.6c. When the mixture is heated to the isotropic and cooled down again, depending on the thermodynamics, different behaviors have been observed. Sometimes the low temperature DC phase appears below the B2 phase, and sometimes the low temperature DC phase appears directly below the isotropic. In the latter case, the DC phase shows a typical fractal growth pattern, as shown in Figure 6.4.6d. These fractal patterns also show left- and right-handed optical rotation as shown in Figures 6.4.6e and f. Overall, the phase behavior of the low temperature DC phase is different from that of the conventional B4 phase. However, as the 8CB concentration increases, the low temperature DC phase behaves more like the B4 phase in the mixture, evidenced by the formation of fractal patterns.

In a summary, we have shown that the disordered B4 structure or the low temperature DC phase of W624. The low temperature DC phase is quenched in some disordered state, compared with the high temperature DC phase. The phase behavior of W624 in mixtures with 8CB is different from the materials forming the conventional B4 phase. However, as the 8CB concentration increases, the low temperature DC phase behaves more like the B4 phase in the mixture, evidenced by the formation of fractal patterns.

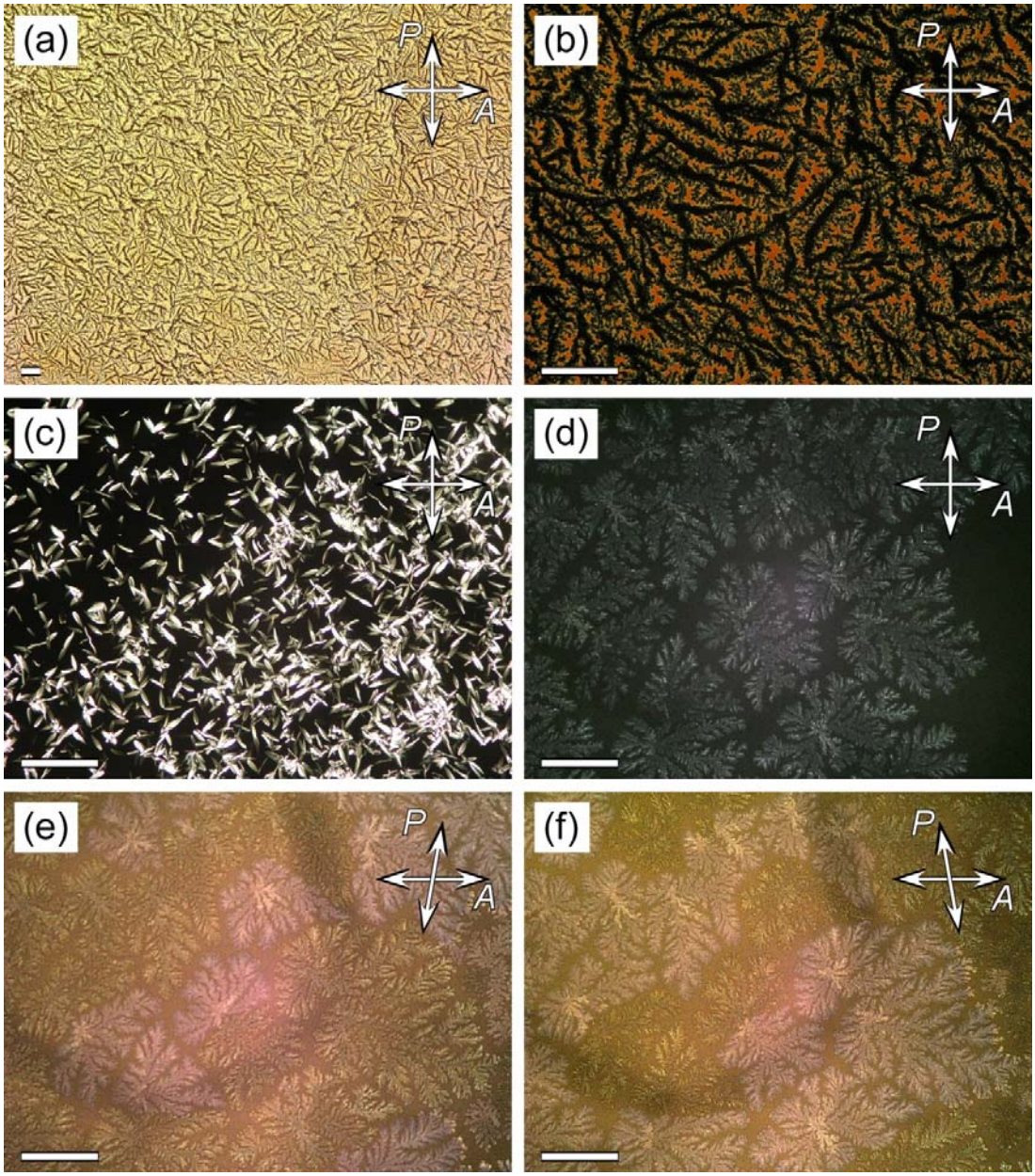

Figure 6.4.6: DTLM images of a c=50% 8CB/W624 mixture in a 4 μm thick cell with planar unidirectional alignment layers. (a) Before heating, at T=30°C, 8CB is in the nematic phase. Regions where 8CB is aligned along the alignment layers show very high birefringence. The low temperature DC phase of W624 shows the fractal-like texture (dark lines). (b) Higher magnification of (a). (c) When heating to T=80°C, 8CB changes to isotropic, while W624 changes to a beautiful texture. (d) Upon cooling from the isotropic, the low temperature DC phase of W624 nucleates and grows at different sites, and forms the fractal texture. (e) and (f) Left- and right-handed optical rotations of the fractal texture can be observed with decrossed polarizers. (d)-(f) are taken at T=90°C. The contrast in (d), (e) and (f) was enhanced using Canvas.

Bibliography

[1] L. E. Hough, H. T. Jung, D. Krüerke, M. S. Heberling, M. Nakata, C. D. Jones, D. Chen, D. R. Link, J. Zasadzinski, G. Heppke, J. P. Rabe, W. Stocker, E. Korblova, D. M. Walba, M. A. Glaser, and N. A. Clark: Helical nanofilament phases. *Science* **2009**, *325*, 456-460.

[2] L. E. Hough, M. Spannuth, M. Nakata, D. A. Coleman, C. D. Jones, G. Dantlgraber, C. Tschierske, J. Watanabe, E. Korblova, D. M. Walba, J. E. Maclennan, M. A. Glaser, and N. A. Clark: Chiral isotropic liquids from achiral molecules. *Science* **2009**, *325*, 452-456.

[3] T. Sekine, T. Niori, M. Sone, J. Watanabe, S.-W. Choi, Y. Takanishi, and H. Takezoe: Origin of helix in achiral banana-shaped molecular systems. *Jpn. J. Appl. Phys.* 1997, **36**, 6455-6463.

[4] D. M. Walba, L. Eshdat, E. Körblova, and R. K. Shoemaker: On the nature of the B4 banana phase: Crystal or not a crystal. *Crystal Growth & Design* **2005**, *5*, 2091-2099.

[5] H. Nádasi, Ch. Lischka, W. Weissflog, I. Wirth, S. Diele, G. Pelzl, and H. Kresse: B2-B4 dimorphism in a new series of banana-shaped mesogens. *Mol. Cryst. Liq. Cryst.* 2003, **399**, 69-84.

Chapter 7

Randomized Grain Boundary Phase

7.1 Introduction

Hockey-stick-like molecules, which are usually formed from a central core to which arms of a substantially different length are joined, are an interesting class of liquid crystal materials. Because of the unique molecular shape, hockey-stick-like molecules are on the border between classical rod-like molecules and conventional banana-shaped materials, where interesting phases and phenomena may emerge. Recently, the mesophases of several hockey-stick-like materials have been studied [1, 2, 3]. All these hockey-sticks like molecules show very similar phase sequences, e.g. N-SmC_S-SmC_A or SmA-SmC_S-SmC_A. The SmC_S-SmC_A phase transition seems to be a characteristic feature of the hockey-stick-like materials. A molecular conformation change has been observed across the SmC_S-SmC_A phase transition, where molecules change from more rod-like ones in the SmC_S phase to being more bent in the SmC_A phase, which leads to a different packing of the molecules within the layers [4]. In the study of COBOXD, a hockey-stick-like molecule synthesized by Dr. Haitao Wang, an interesting chiral phase has been observed. We will discuss this phase in detail below.

7.2 COBOXD: Randomized grain boundary phase

The chemical structure and the phase sequence of COBOXD are shown in Figure 7.2.1a. Similar to other hockey-stick-like molecules, COBOXD shows a SmA-SmX phase transition. Upon cooling, the SmA phase appears from isotropic, showing a typical focal conic texture, with the dark brushes parallel to the polarizers (Figure 7.2.1b). On cooling to the SmX phase, the birefringent texture disappears and it becomes dark under crossed polarizers. Interestingly, left- and right-handed chiral domains can be distinguished when decrossing the polarizers, as shown in Figures 7.2.1c and d. Below the SmX phase, there is a crystal phase, which shows colorful birefringence as it grows in, as shown in Figure 7.2.1d, bottom right. So far, only two phases showing macroscopic chiral domains under decrossed polarizers has been observed, the dark conglomerate phase which appears directly from the isotropic and the B4 phase which is the lowest liquid crystal phase and is still stable at room temperature. Both of these two liquid crystal phases are made of bent-core molecules and are dominated by the saddle-splay curvature driven by the intra-layer mismatch of the bent-core smectic layers. The chiral phase of COBOXD has a unique phase sequence, appearing below the SmA phase and followed by a crystal phase. We will show that the SmX phase is a new chiral structure different from any phases observed so far.

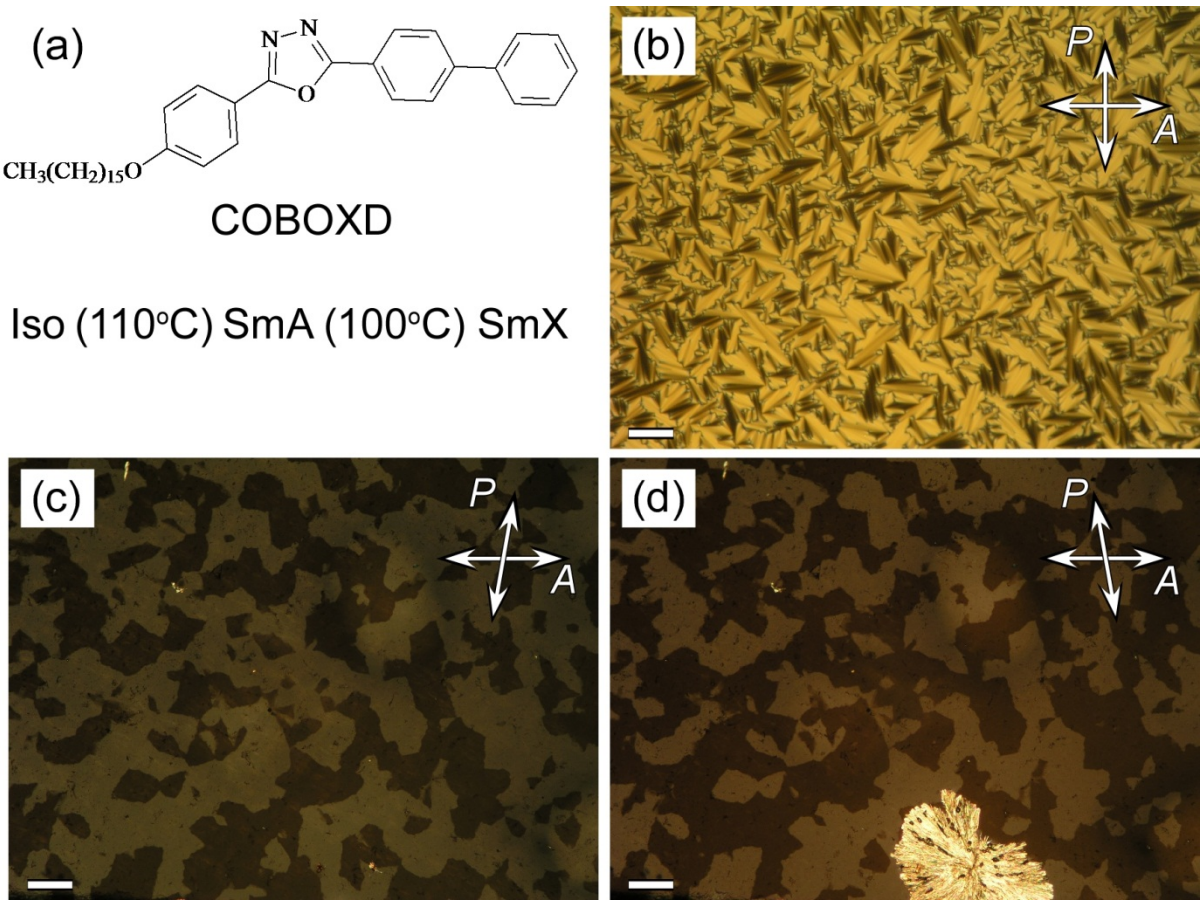

Figure 7.2.1: Chemical structure and phase sequence of COBOXD and the DTLM images of each liquid crystal phase. (a) Chemical structure and phase sequence of COBOXD. (b) Focal conic texture of the SmA phase observed below the isotropic at T=110°C. (c) and (d) Optical texture of the SmX phase below the SmA phase at T=100°C, showing left- and right-handed chiral domains. The scale is 100 μm in all images. The samples are sandwiched between clean, untreated glass planchettes.

In order to study the microstructure of the SmX phase, FFTEM and free surface TEM have been used. Figures 7.2.2a-d show the topography of the SmX phase at the air/liquid crystal interface. Before discussing the microstructure of the chiral phase, we will first illustrate an interesting aspect of human visual perception. Figures 7.2.2a and b are the same image rotated by

180°. However, Figures 7.2.2a and b give us a different impression about the surface topography that smectic blocks below the surface shown in Figure 7.2.2a appear to be above the surface in Figure 7.2.2b. Figures 7.2.2c and d give more examples of the surface structure of the SmX phase. The SmX phase is made of smectic blocks where locally the smectic layers are flat. Globally, the surface is rough, with the smectic blocks oriented in different directions. Instead of being dominated by saddle-splay curvature such as the B4 and DC phases, the chiral phase of COBOXD is made of flat smectic layers. However, those smectic layers self-assemble into small blocks oriented in different directions. Thus, we call this phase, a randomized grain boundary (TGB) phase.

When considering blocks of smectic layers, we are reminded of the famous twist grain boundary phase (the TGB phase), which is made of twisting blocks of smectic layers [5]. For comparison, Figures 7.2.3a-d shows the surface topography of the TGBA phase of the chiral rod-like molecule W371 with increasing magnification (the TGBA phase is one kind of the TGB phase, where the twisting smectic blocks are made of SmA layers). Though FFTEM images have revealed a twisted arrangement of the smectic blocks in the bulk, at the free surface, the smectic blocks are randomly oriented. In most cases, because of the rotational and translational symmetries imposed by the air/liquid crystal interface, more ordered structure is usually observed at the free surface than in the bulk (Chapter 4). The inverse case observed in the TGBA phase may be attributed to the competition between twist and the homeotropic alignment imposed by the air interface.

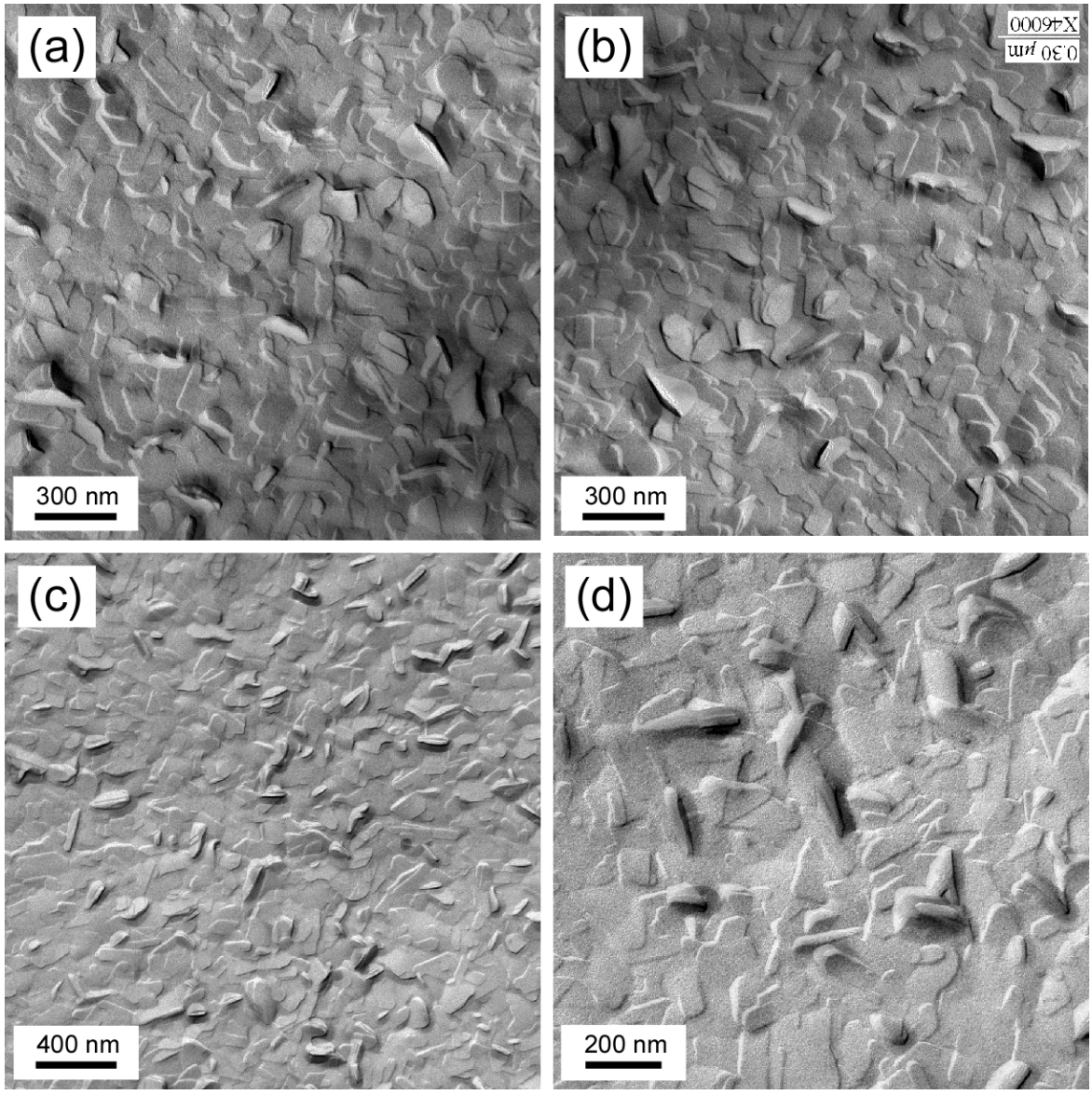

Figure 7.2.2: Free surface TEM images of the SmX phase at the air/liquid crystal interface, quenched at T=100°C. (a) Free surface TEM image of the SmX phase which shows the surface topography of the chiral phase, representing a rough surface of smectic blocks. (b) Image of (a) rotated by 180°. (c) Another example of the surface structure. At the air/liquid crystal interface, the free surface of the SmX phase is not flat and blocks of smectic layers are oriented at different directions. (d) Higher magnification of (c).

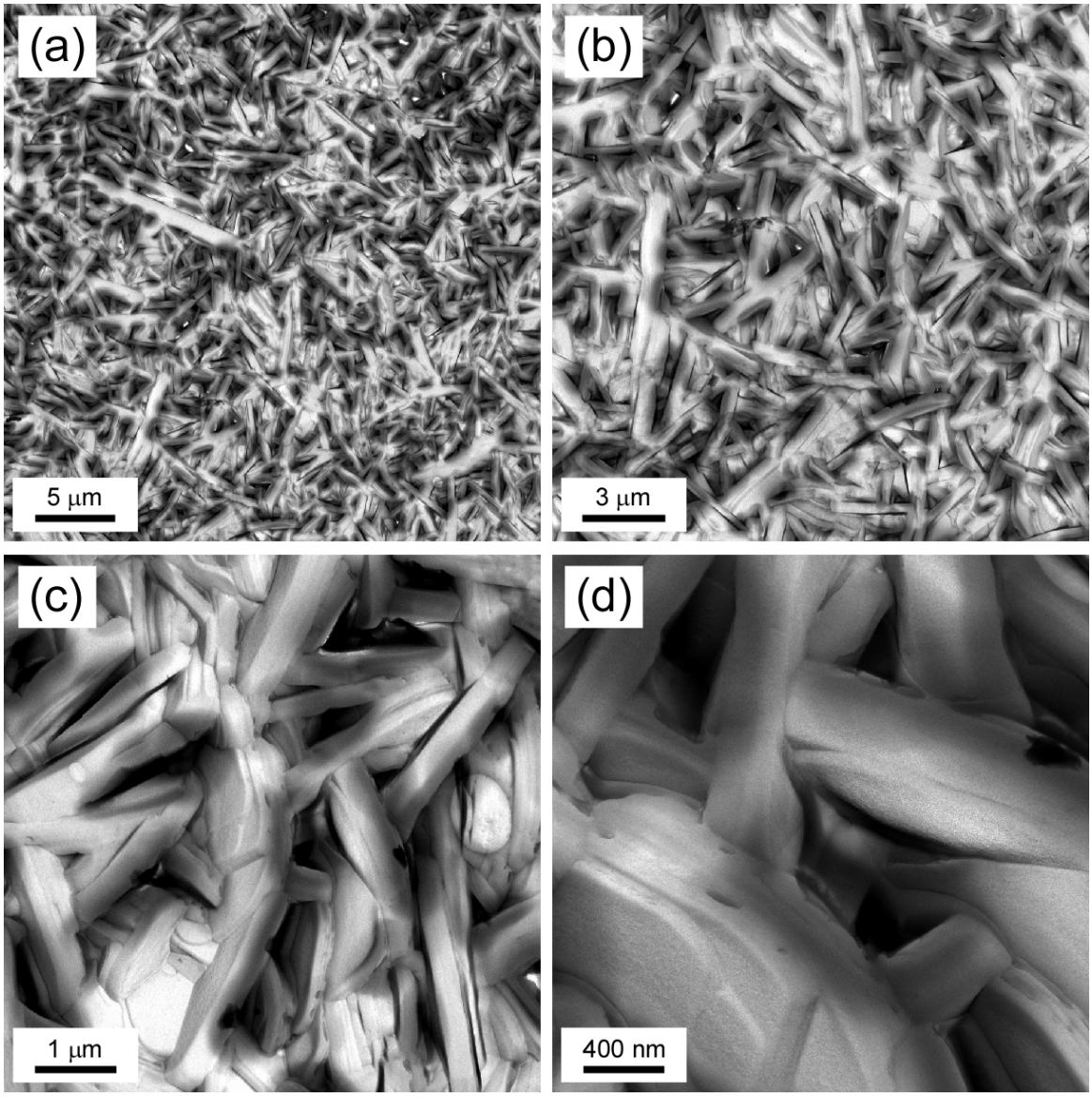

Figure 7.2.3: Free surface TEM images of the TGBA phase of W371 at the air/liquid crystal interface, quenched at T=55°C. (a) (b) (c) and (d) Free surface TEM images of the TGBA phase, showing the surface topography at the same region with increasing magnification. The TGBA phase is made of blocks of smectic layers. Though the smectic blocks are arranged in a twisting confirmation in the bulk, the smectic blocks at the free surface seem to randomly orient.

As discussed above, disordered smectic blocks of the TGBA phase have been observed at the air/liquid crystal interface phase. But the smectic blocks are much larger than those observed in the SmX phase and the surface topographies of those two phases are different. In order to further clarify the difference, the bulk structure of the SmX phase investigated by fracturing the sample is shown in Figures 7.2.4a-d. Consistent with the surface microstructure, the bulk topography also shows small blocks of randomly oriented smectic layers. In addition, some curved smectic layers are seen in the bulk. We believe that the curved layers connect different smectic blocks in the bulk. In Figures 7.2.4a and b, the curved layers are randomly distributed in the fracture plane. In Figures 7.2.4c and d, we see places where the curved smectic layers tend to make loops at the ends. The three-dimensional details of how the smectic blocks join with the curved smectic layers are still under investigation.

To distinguish the SmX phase from the low temperature crystal phase unambiguously, free surface TEM images of the crystal phase are shown in Figures 7.2.5a and b. Figure 7.2.5a shows the global surface topography of the crystal phase. At higher magnification, as shown in Figure 7.2.5b, the crystal phase is seen to be an ordered layer structure with long range correlation length. In order to further understand the molecular packing in the smectic layers of the SmX phase, we have carried out x-ray scattering on the powder samples.

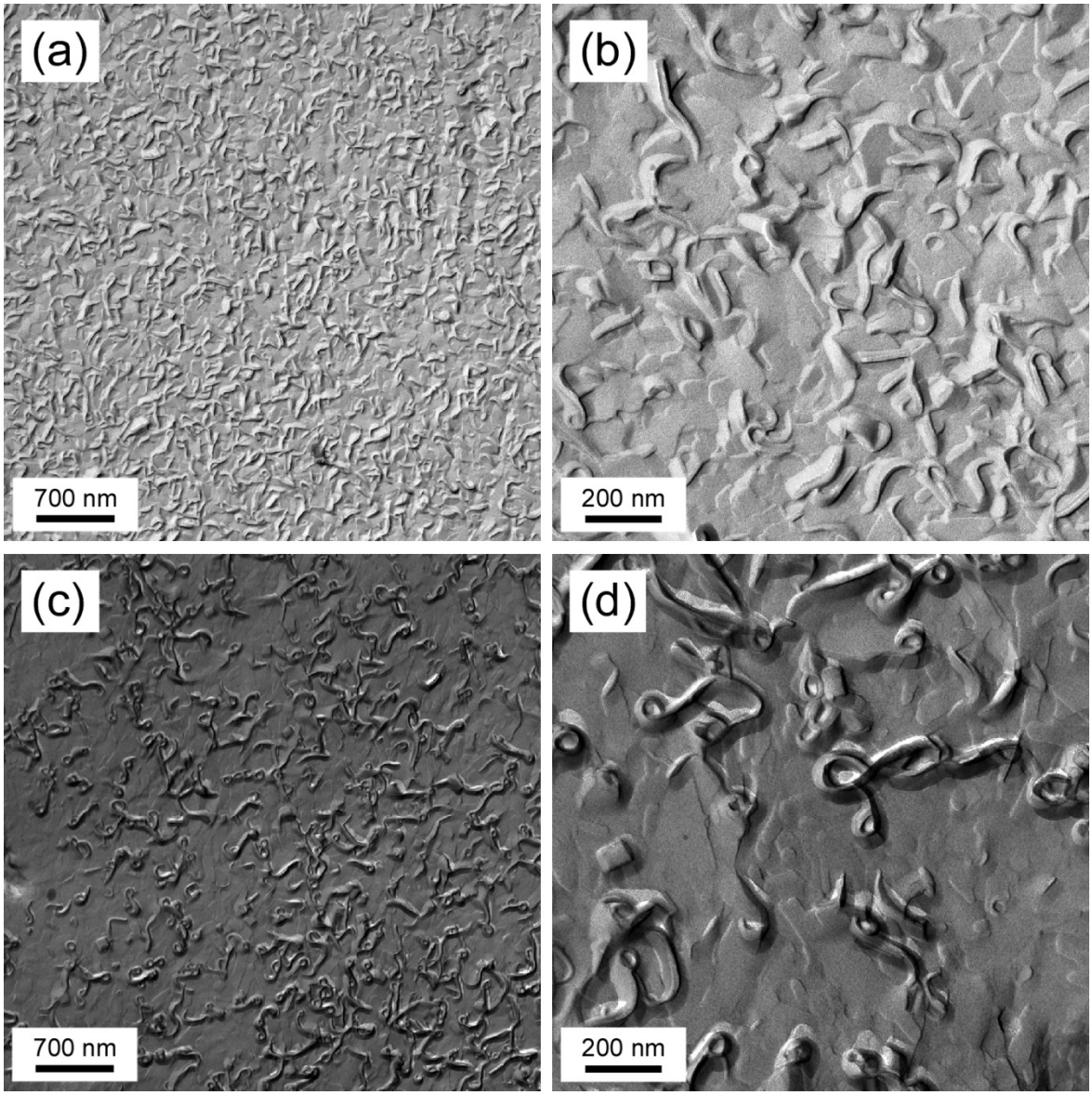

Figure 7.2.4: FFTEM images of the SmX phase quenched at T=100°C and fractured in the bulk. (a) Bulk structure of the SmX phase. Besides the randomly oriented smectic blocks, some curved smectic layers are revealed by fracturing the sample. (b) Higher magnification of (a). (c) Similar texture as (a). The curved smectic layers tend to make circles at the ends. (d) Higher magnification of (c).

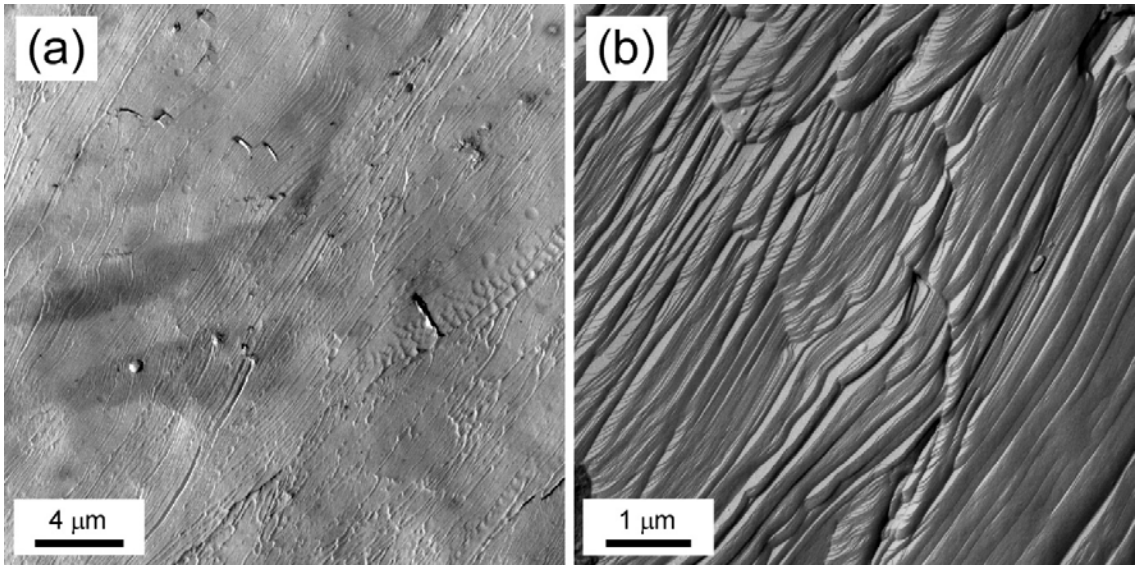

Figure 7.2.5: Free surface TEM images of the crystal phase of COBOXD below the SmX phase at the air/liquid crystal interface, quenched at T=90°C. (a) The overall surface texture of the crystal phase. (b) Higher magnification of (a). The low temperature crystal phase shows long range ordered structure.

The molecular configuration obtained from Chem3D (MM2, energy minimization) is shown in Figure 7.2.6a. The molecular length is l~30.2 Å. X-ray scattering shows a resolution limited peak of the SmA phase at q~0.1642 $Å^{-1}$, corresponding to d~38.0 Å, as shown in Figure 7.2.6b. The layer spacing of the SmA phase is therefore bigger than the molecular length, which suggests a bilayer structure of the SmA phase [6]. In the SmX phase, only a diffuse x-ray scattering peak is observed, as shown in Figure 7.2.6c. The peak position at q~0.2565 $Å^{-1}$ corresponds to d~24.5 Å. Because of the finite FWHM~0.0014 $Å^{-1}$, the correlation length of the smectic layers in the SmX phase is ξ~1428 Å, corresponding to about 58 smectic layers. This implies that each smectic block is made of about 58 smectic layers, which is consistent with the observation of the smectic blocks in the FFTEM or free surface TEM image. The layer spacing

of the SmX phase is much smaller than that in the SmA phase. If we assume the bilayer configuration of the molecules doesn't change in the SmX phase and the layer spacing shrinkage results from the molecular tilt, the molecular tilt is about θ~50° in the SmX phase, which is extremely large. However, this could be the intrinsic reason of forming the randomized grain boundary phase. As the phase changes from the SmA phase to the SmX phase, the layer spacing has deceased so much that the long range ordered smectic layers collapse into small smectic blocks oriented at different directions. The random orientation of the smectic blocks causes the birefringence to average out and the phase appears dark when observed under crossed polarizers. According to Neumann's principle, the symmetry of any physical property of a medium must include the symmetry elements of the point group of the medium. Therefore, the macroscopic chiral domains observed in the SmX phase indicate the chiral arrangement of the molecules. As there is no evidence of the molecules arranged in helical configuration, the macroscopic chirality may also come from the layer chirality, where the bilayer configuration shows the bent-shape and is tilted in the chiral phase,

In a summary, we have investigated the mesophases of a new hockey-stick-like molecule. Different from any previously known chiral phases, the chiral SmX phase is made of smectic blocks at different orientations, which we call the randomized grain boundary phase. The molecules are arranged in a bilayer structure in the SmA phase. At the transition to the SmX phase, there is a very large layer shrinkage, which may induce the collapsing of the smectic layers and form the randomly oriented smectic blocks.

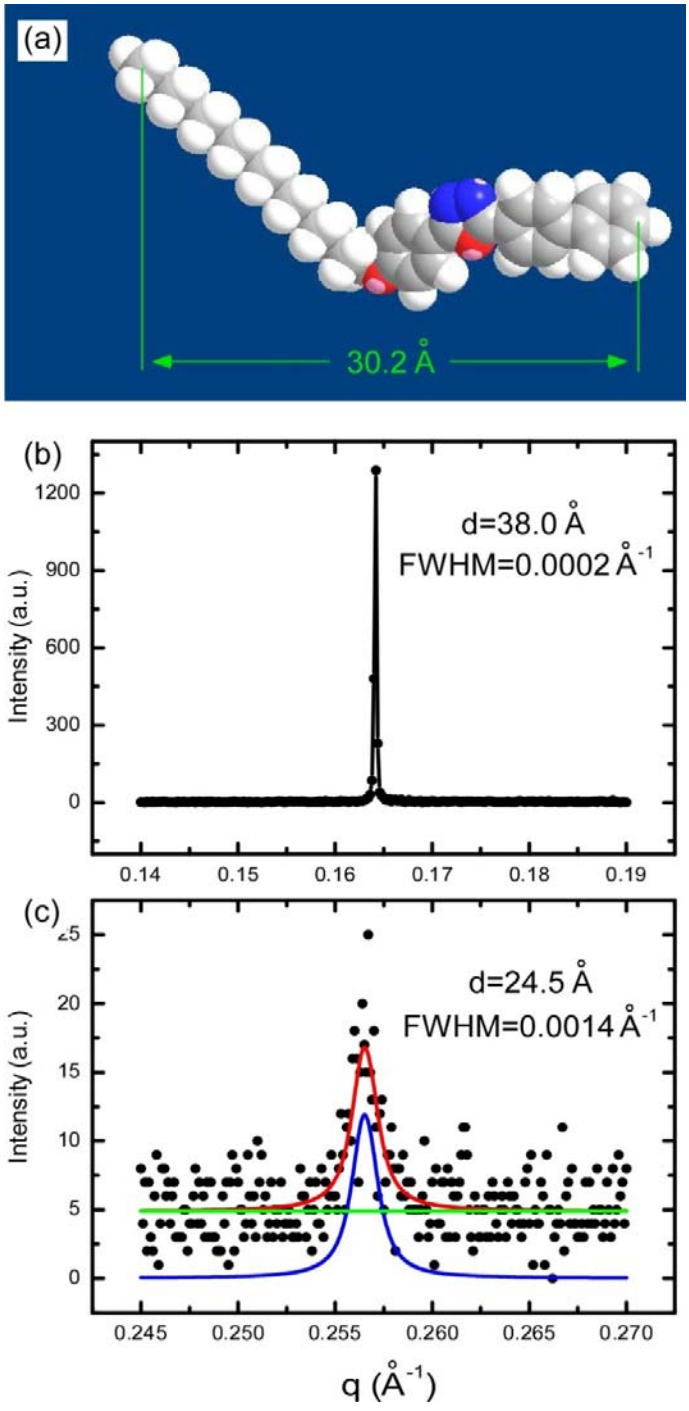

Figure 7.2.6: X-ray scattering in the SmA and SmX phases. (a) The molecular conformation and length of COBOXD obtained from Chem3D (MM2, energy minimization). (b) The x-ray scattering peak of the SmA phase, which is resolution limited. (c) The x-ray scattering peak of the SmX phase, which is very diffuse (the green curve is the background, the blue curve is a fitting to the peak after background subtraction and the red curve is the sum of the green and blue curves).

Bibliography

[1] E.-R. Cioanca, E. L. Epure, I. Carlescu, G. Lisa, D. Wilson, N. Hurduc, and D. Scutaru: Hockey stick liquid crystals based on a 2,5-asymmetric disubstituted [1,3,4]oxadiazole core. *Mol. Cryst. Liq. Cryst.* 2011, **537**, 51-63.

[2] V. Novotnáá, J. ŽŽurek, V. Kozmíík, J. Svoboda, M. Glogarováá, J. Kroupa, and D. Pociecha: Novel hockey-stick mesogens with the nematic, synclinic and anticlinic smectic C phase sequence. *Liq. Cryst.* 2008, **35**, 1023-1036.

[3] A. Chakraborty, B. Das, M. K. Das, S. Findeisen-Tandel, M.-G. Tamba, U. Baumeister, H. Kresse, and W. Weissflog: New hockey stick compounds with a lateral methyl group showing nematic, synclinic and anticlinic smectic C phases. *Liq. Cryst.* 2011, **38**, 1085-1097.

[4] B. Das, S. Grande, W. Weissflog, A. Eremin, M. W. Schröder, G. Pelzl, S. Diele and H. Kresse: Structural and conformational investigations in SmA and different SmC phases of new hockey stick-shaped compounds. *Liq. Cryst.* 2003, **30**, 529-539.

[5] J. Fernsler, L. Hough, R.-F. Shao, J. E. Maclennan, L. Navailles, M. Brunet, N. V. Madhusudana, O. Mondain-Monval, C. Boyer, J. Zasadzinski, J. A. Rego, D. M. Walba, and N. A. Clark: Giant-block twist grain boundary smectic phases. *PNAS* 2005, **102**, 14191-14196.

[6] R. A. Reddy, C. Zhu, R. Shao, E. Korblova, T. Gong, Y. Shen, E. Garcia, M. A. Glaser, J. E. Maclennan, D. M. Walba, and N. A. Clark: Spontaneous ferroelectric order in a bent-core smectic liquid crystal of fluid orthorhombic layers. *Science* 2011, **332**, 72-77.

Chapter 8

Gallery of microstructure shown by FFTEM images

8.1 Introduction

In the previous chapters, we have discussed the microstructures of the B4 phase, the DC phase, the B7 phase and other new, unidentified phases. In this chapter, we will show all the other microstructures which have been observed so far. We will focus on presenting those microstructures, with little detail. The related references are strongly suggested for detailed discussions of these systems. Therefore, this chapter will serve as a gallery of all the other microstructures.

8.2 SEM images of the dark conglomerate phase

In Chapter 4, we have shown disordered focal conics in the bulk and quasi-ordered toric focal conics at the air/liquid crystal interface of the dark conglomerate (DC) phase. Here we present disordered focal conics of the DC phase in the bulk, using SEM. As shown in Figures 8.2.1a-d, the bulk structure of the DC phase is made of disordered focal conics and the disordered focal conics vary in size. A characteristic feature of the topology is curved layers.

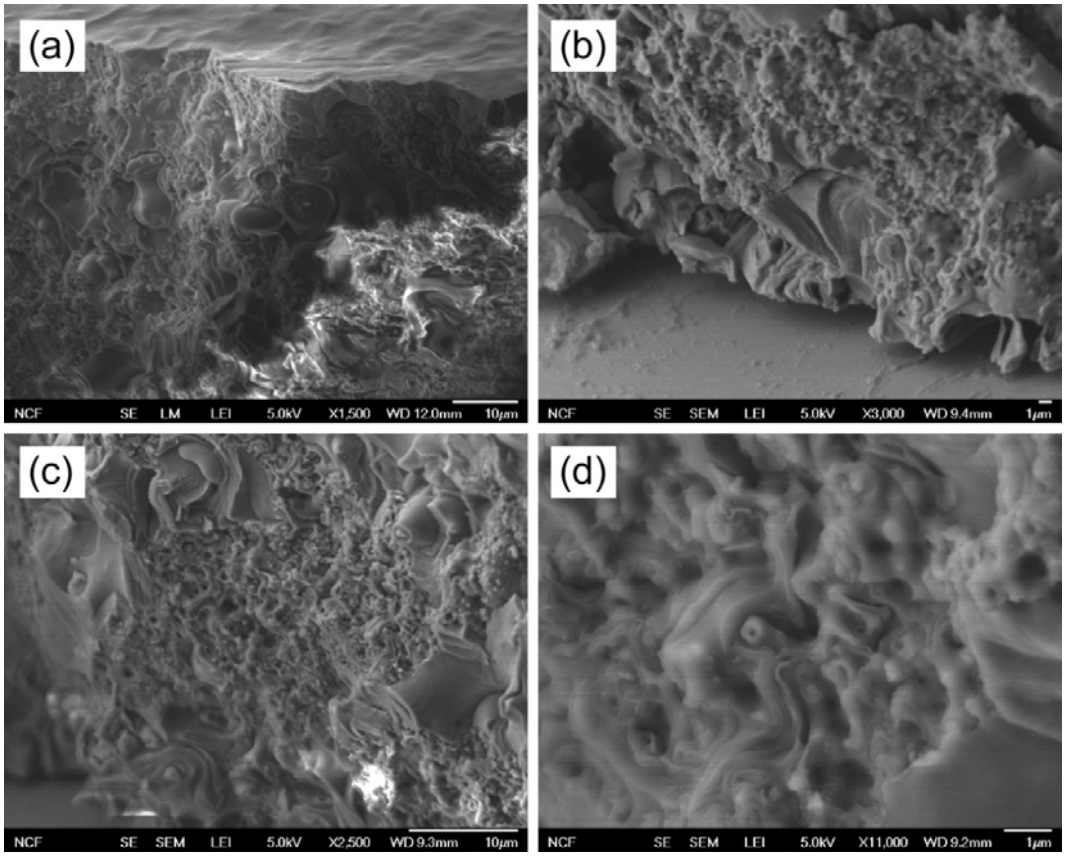

Figure 8.2.1: Bulk structure of the dark conglomerate phase of a c=50% W508 and No7 [1] mixture. (a), (b), (c) and (d) SEM images of the DC phase fractured in the bulk. The sample is quenched in the DC phase and then fractured in the bulk. After coating the surface with gold, the sample is visualized in SEM. Characteristic curved smectic layers are observed in all these images.

8.3 Two-dimensional nematic-smectic A phase transition of CT2

CT2 is a T-shaped molecule synthesized by Prof. Carsten Tschierske. The T-shaped molecules undergo very interesting self-assembly, as shown in Figure 8.3.1a [2]. Cooling from isotropic, the T-shaped molecules first form a 2D-Iso phase with layered structure and in-plane random order. On further cooling, the 2D-Iso phase transitions to a 2D-Nem phase of in-plane orientational order. In this phase, only one dimensional order is observed with typical layer steps appearing in the fracture plane as shown in Figure 8.3.1b. The layer surfaces are smooth and no finer structure can be observed (the in-plane orientational ordering cannot be distinguished in the FFTEM image) as magnified in Figure 8.3.1c. Below the 2D-Nem phase, the in-plane orientational order changes to smectic layering, where additional in-plane periodic structure appears, as shown in Figure 8.3.1d. This system provides a good example of a two-dimensional nematic-smectic A phase transition. With careful examination of the in-plane order, we notice that the periodicity of the 2D-Sm phase is not as ordered as those observed in the columnar phase (Figures 8.4.1a and b). When constructing the surface topography in three dimensions using Matlab software, as shown in Figure 8.3.1e, we can clearly identify the annihilation of the in-plane layers, mediated by dislocation lines [3].

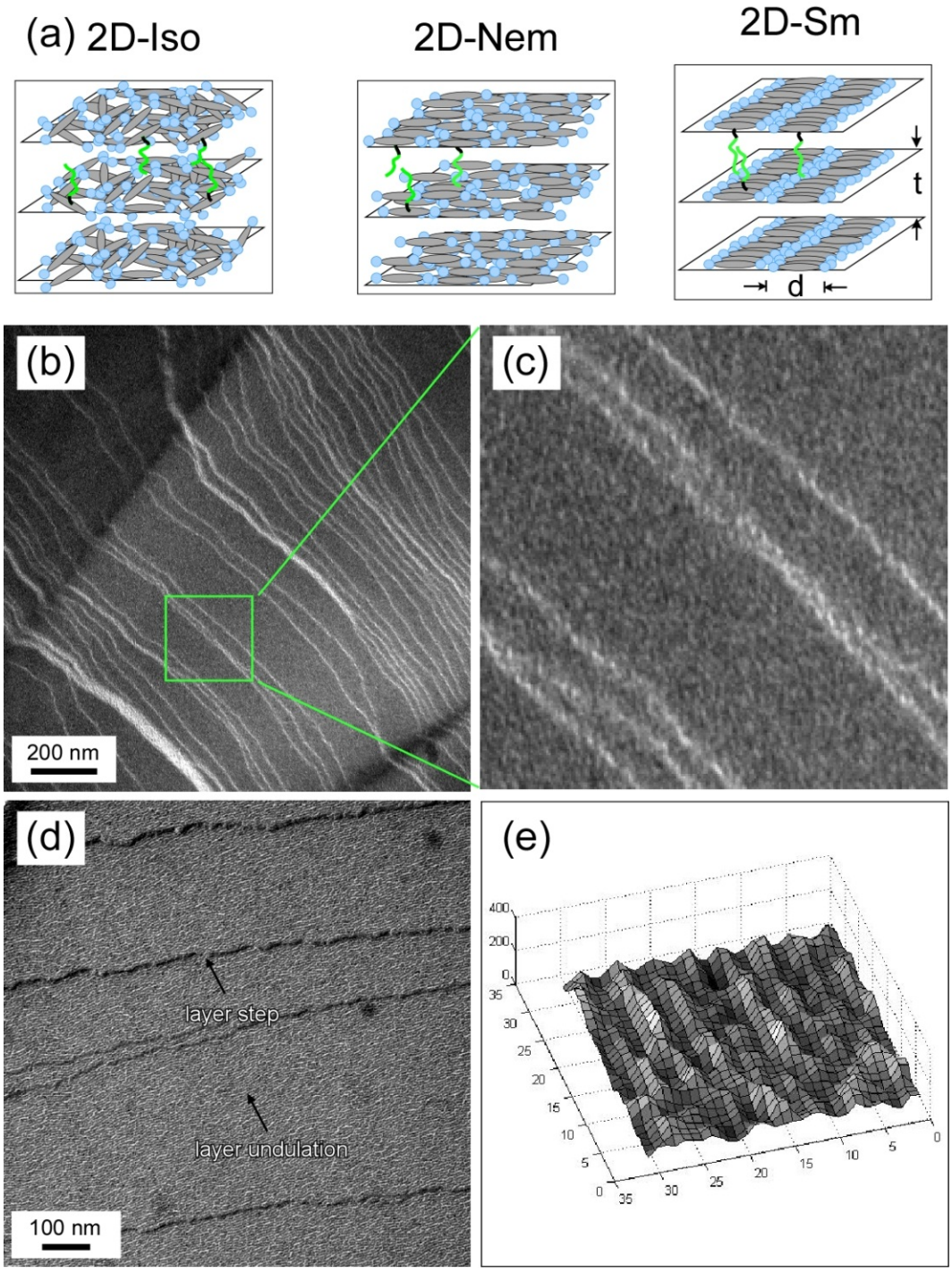

Figure 8.3.1: Two-dimensional nematic-smectic A phase transition of CT2. (a) Models of the 2D-Iso, 2D-Nem and 2D-Sm. (b) FFTEM image of the 2D-Nem phase, quenched at T=150°C and then fractured in the bulk. (c) Magnified region of (b). (d) FFTEM image of the 2D-Sm phase phase, showing in-plane periodic structure. (e) Construction of the three-dimensional structure of the fracture plane in (d).

8.4 Two-dimensional order of the columnar phases of the phasmidic indigoid liquid crystals

The molecular arrangement in the columnar phase of polycatenar mesogens has been well studied [4]. The two phasmidic indigoid liquid crystal materials, synthesized by Dr. Jan H. Porada, show very interesting optical textures [5], where the green sample (sample 1 in the reference) shows a B2 like texture and the blue sample (sample 2 in the reference) shows a B7 like texture. Multiple x-ray scattering peaks have been detected at small angle, indicating the two-dimensional order of these phases. In addition, FFTEM images of the green (Figure 8.4.1a) and blue (Figure 8.4.1b) samples, unambiguously show two-dimensional order of those phases, which are marked as layer step and layer undulation in the images. Therefore, despite of the unusual optical textures, these two phases are confirmed to be columnar phases. The reason why the columnar phases of these two liquid crystal materials show the B2 like and B7 like textures respectively is still unknown. The layer undulation of the columnar phases is quite ordered, which is different from that observed in two-dimensional smectic A phase of CT2 (Figure 8.3.1d) and indicates a long range correlation length within the two-dimensional lattices, consistent with sharp x-ray reflection peaks.

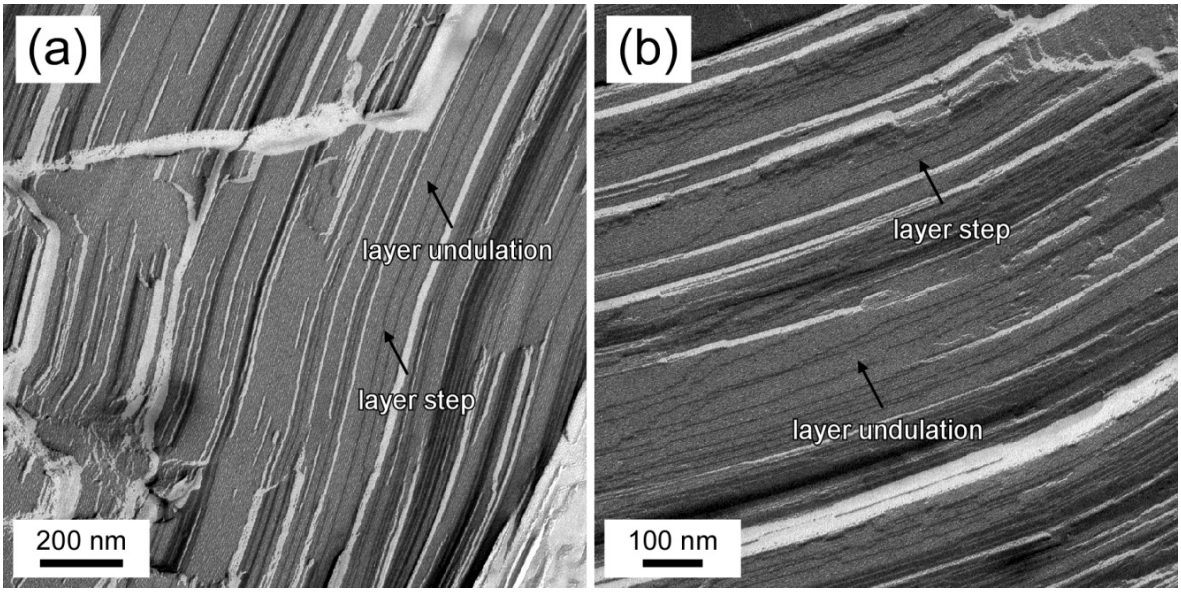

Figure 8.4.1: FFTEM images of the columnar phases of the phasmidic indigoid liquid crystal materials. (a) FFTEM image of the green sample (sample 1 in the reference), quenched at T=135°C and then fractured in the bulk. (b) FFTEM image of the blue sample (sample 2 in the reference), quenched at T=180°C and then fractured in the bulk. Two dimensional ordering is observed in these two phases.

8.5 Smectic layering of the De Vries phase of W530

Among smectic A phases, there is one class called the De Vries phase, where molecules are uniformly distributed in a tilt cone (the cone model). The layer spacing changes continuously when the smectic A phase transitions to the smectic C phase. Here, we show FFTEM images of the De Vries material W530 [6]. For the De Vries phase, only a typical layer structure can be observed, as shown in Figures 8.5.1. The layer structure is basically the same as those observed in the conventional smectic A phase, with no other feature.

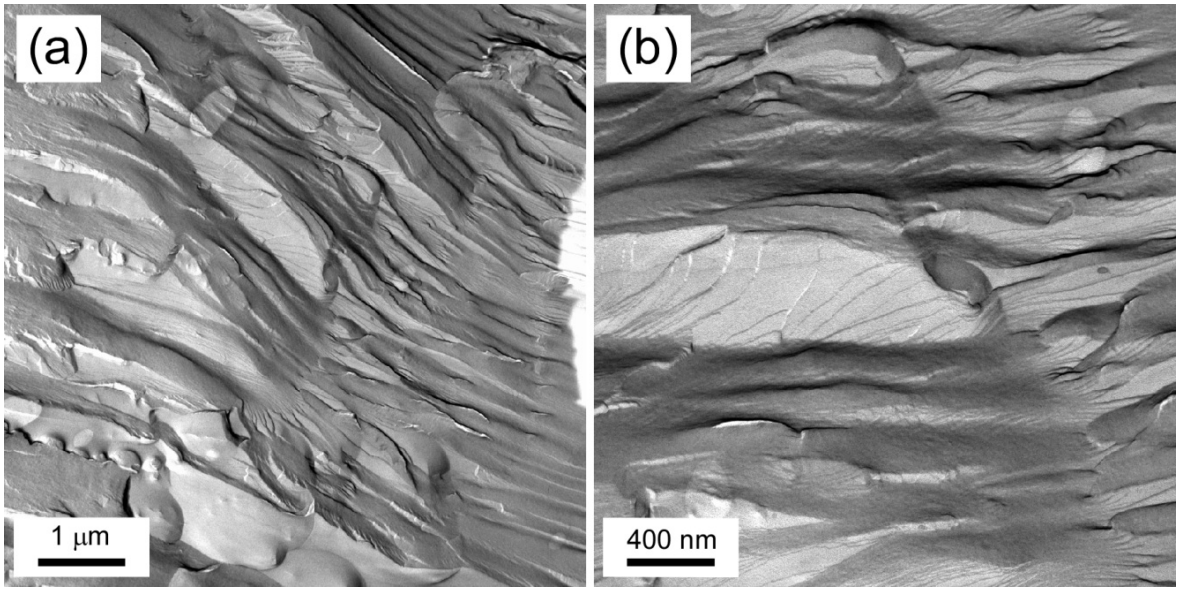

Figure 8.5.1 FFTEM images of the De Vries phase of W530. (a) FFTEM image of the De Vries phase, quenched at T=50°C and then fractured in the bulk. (b) Higher magnification of (a).

8.6 The $SmAP_F$ and $SmAP_{Fmod}$ phases of W596

Recently, a $SmAP_F$ phase of W586 has been discovered and characterized [7]. W596 is a derivative of W586 and was mainly characterized by Dr. Chenhui Zhu [8]. In the study of W596, a high temperature $SmAP_{Fmod}$ phase is observed and is followed by a low temperature $SmAP_F$ phase. In the $SmAP_{Fmod}$ phase, the polarization is splayed within each polarization modulation stripe, which forms the periodic layer undulations similar as those observed in the B7 phase, as shown in Figure 8.6.1a. While in the low temperature smectic AP_F phase, the layer surfaces are very flat, similar to those observed in a conventional smectic A phase, as shown in Figure 8.6.1b.

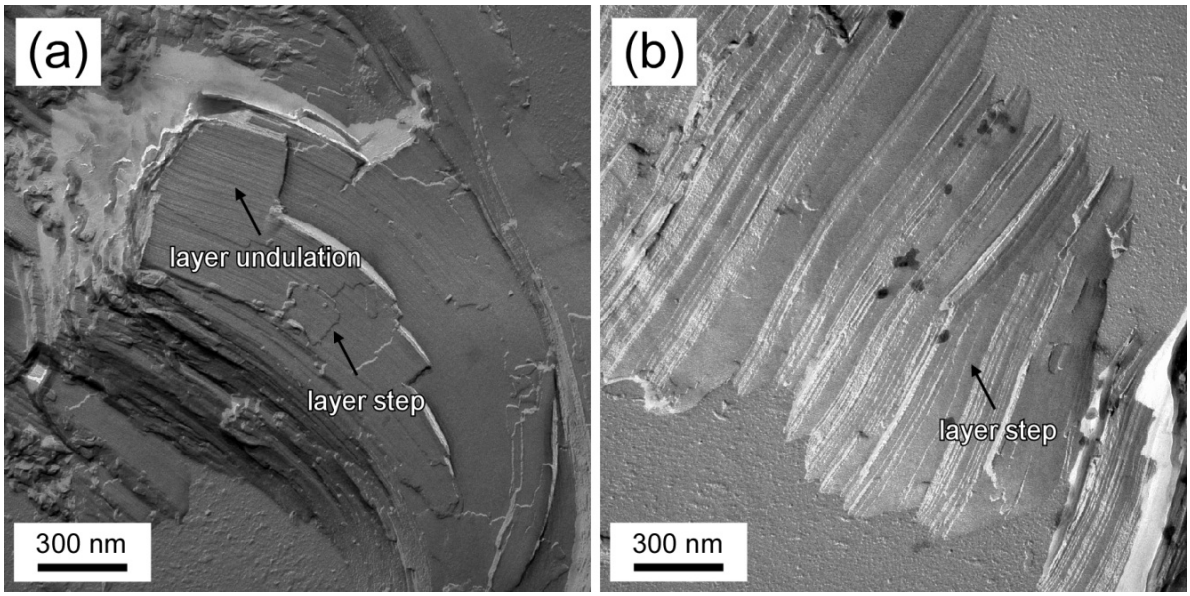

Figure 8.6.1: FFTEM images of the $SmAP_{Fmod}$ and $SmAP_F$ phases of W596. (a) FFTEM image of the $SmAP_{Fmod}$ phase, quenched at T=150°C and then fractured in the bulk. Two-dimensional ordering is observed in the $SmAP_{Fmod}$ phase. (b) FFTEM image of the $SmAP_F$ phase, quenched at T=120°C and then fractured near the glass substrate.

8.7 The $SmAP_F$ and SmX phases of W623

W623 is another derivative of W586, with the reversal of one carbonyl group in W623, which increases the polarization value of the molecules and shows continuous polarization reorientation in an electric field [9]. At high temperature, W623 shows the $SmAP_F$ phase, with characteristic smectic layers of flat surface, as shown in Figures 8.7.1a and b. Different from W596, W623 shows a low temperature SmX phase with two-dimensional periodicity, as shown in Figures 8.7.2a-d. Layer step and layer undulation can be clearly identified in Figure 8.7.2a, similar to those observed in the columnar phase (Figures 8.4.1a and b). However, the structure observed in the SmX phase is different from that of the columnar phase and shows fiber-like features, as shown in Figure 8.7.2b, where they are dramatically deformed due to fracturing. A single fiber can also be observed as shown in Figure 8.7.2c. In order to further understand this phase, mixtures of W623 with 8CB have been prepared. Similar two-dimensional structure is observed in the c=75% W623/8CB mixture, as shown in Figure 8.7.2d.

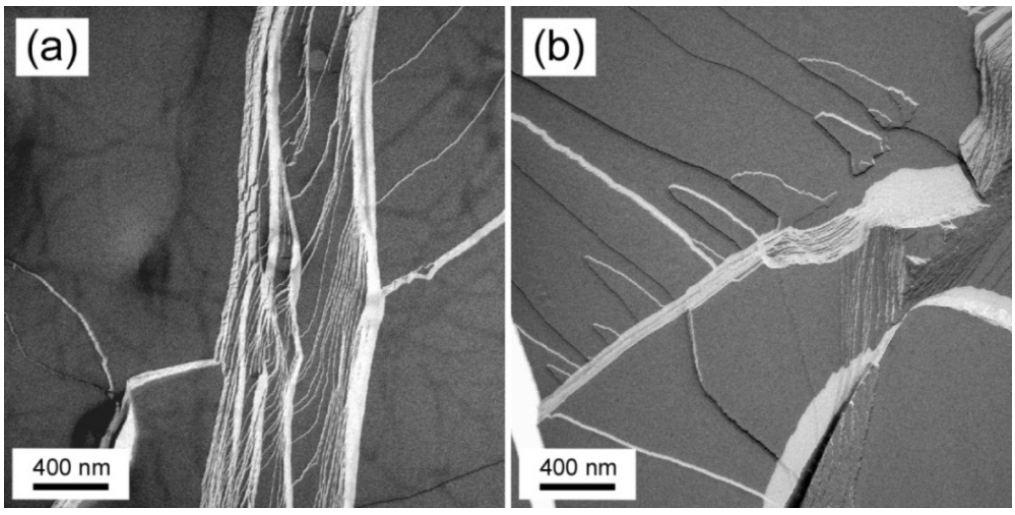

Figure 8.7.1: FFTEM images of the $SmAP_F$ phase of W623. (a) FFTEM of the $SmAP_F$ phase, quenched at T=160°C and then fractured in the bulk. (b) FFTEM image of the $SmAP_F$ phase, quenched at T=140°C and then fractured in the bulk. Typical smectic layers of flat surface are observed in the $SmAP_F$ phase.

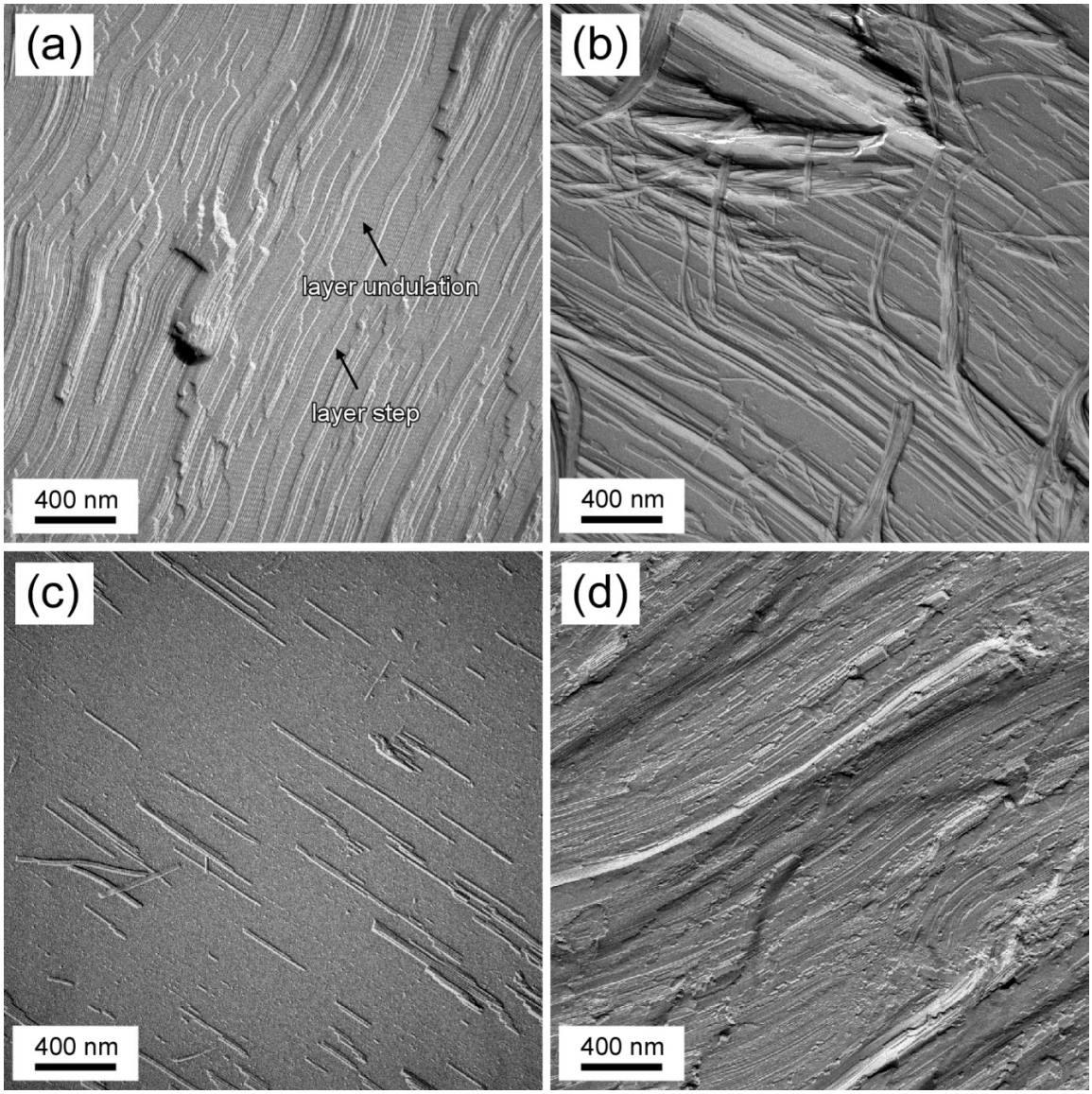

Figure 8.7.2: FFTEM images of the SmX phase of W623. (a) FFTEM image of the SmX phase, quenched at T=100°C and then fractured in the bulk. Two-dimensional periodicity is observed. (b) FFTEM image of the SmX phase, quenched at T=100°C and then fractured near the glass substrate, showing dramatically deformed fibers. (c) FFTEM image of the SmX phase quenched at T=100°C and then fractured near the glass substrate, showing individual fiber. (d) FFTEM image of the SmX phase in a c=75% W623/8CB mixture, quenched at T=110°C and then fractured in the bulk, showing collective organization of the fibers.

8.8 The cholesteric phase mixed with gold nanorods

Mixtures of cholesteric liquid crystals with gold nanorods have been prepared by Dennis F. Gardner to investigate the self-assembly and self-alignment of colloidal nanoparticle within the liquid crystals [10]. A typical example of gold nanorods are shown in Figure 8.8.1a (The gold nanorods prepared in solution are placed on a thin formvar, and the gold nanorods are directly imaged by TEM when the solution dries out). The gold nanorods are closely packed when the solution dries out. In the cholesteric phase mixed with the gold nanorods, periodicity of the cholesteric phase can be observed, as shown in Figure 8.8.1b. Unfortunately, since the liquid crystal molecules could not be distinguished and the gold nanorods were not identifiable, the bulk topology of the assembly is difficult to interpret.

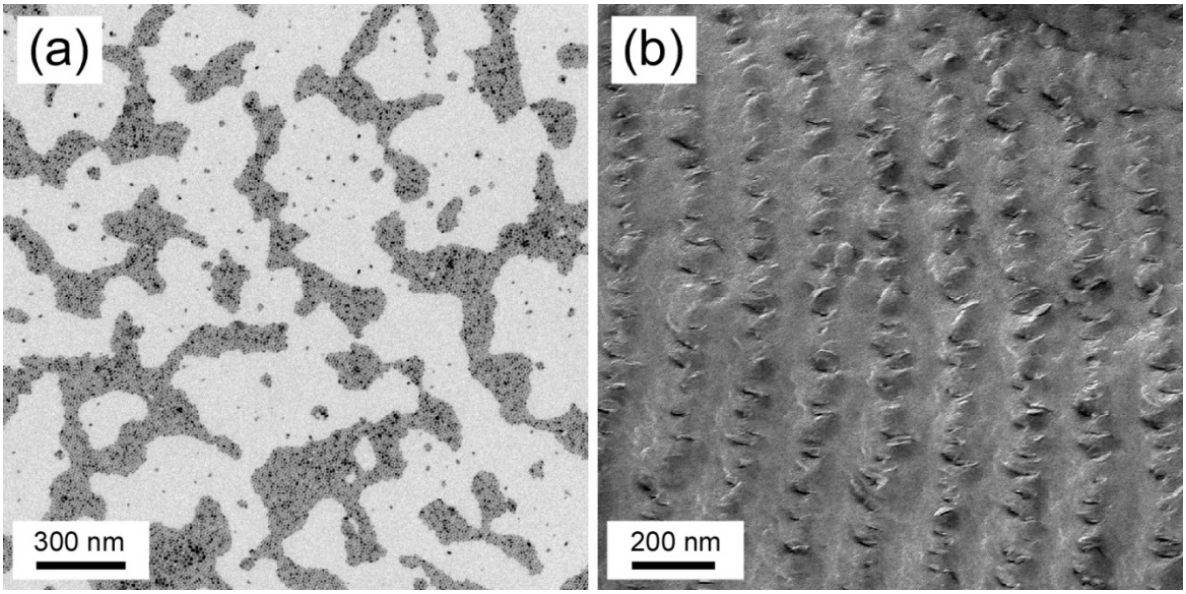

Figure 8.8.1: FFTEM images of the cholesteric phase mixed with the gold nanorods. (a) TEM image of the gold nanorods. (b) FFTEM image of the cholesteric phase mixed with 1% gold nanorods, quenched at T=35°C and then fractured in the bulk.

8.9 Mixtures of 8CB with gold nanoparticles

Mixtures of 8CB with gold nanoparticles have been made by Dr. R. Pratibha and the effect of the surrounding anisotropic liquid crystal medium on surface plasmon resonance exhibited by concentrated suspensions of gold nanoparticles has been studied [11]. The gold nanoparticles used in this mixture are shown in Figure 8.9.1a. When mixing 8CB with gold nanoparticles, the gold nanoparticles uniformly disperse in the mixture, as shown in Figure 8.9.1b. However, the 8CB smectic layers cannot be observed in the image, which is a mystery and is attributed to layer deformations induced by the nanoparticles [11].

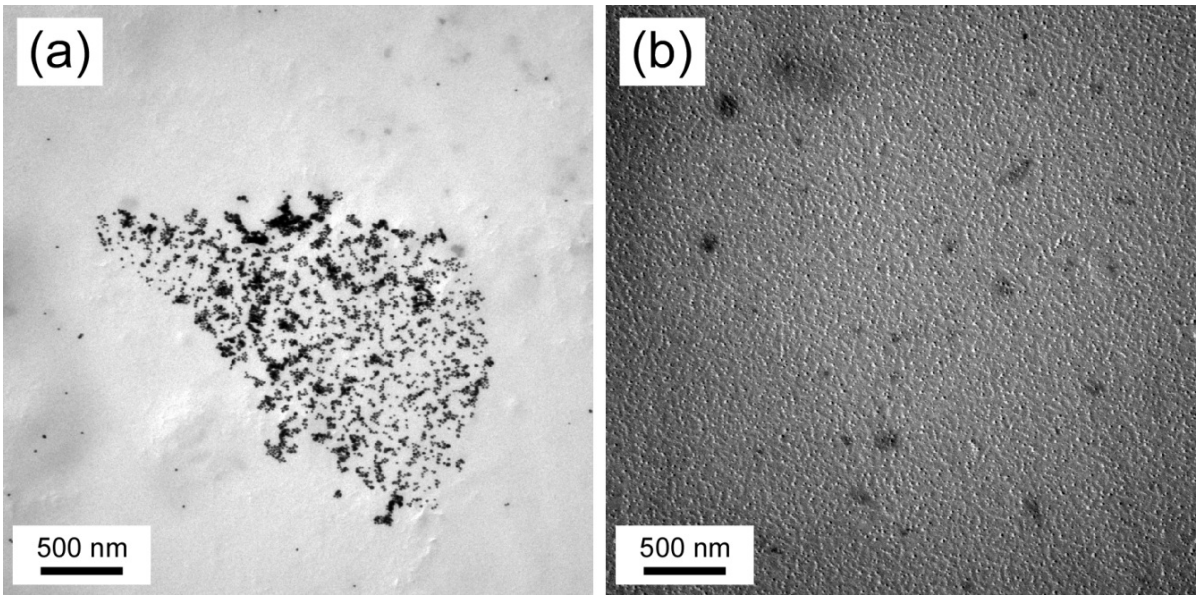

Figure 8.9.1: FFTEM images of 8CB mixed with gold nanoparticles. (a) TEM image of the gold nanoparticles. (b) FFTEM image of 8CB mixed with gold nanoparticles (the volume fraction of the gold nanoparticles in the mixture is 0.54), quenched at room temperature and then fractured in the bulk.

8.10 Gold nanorod with DMPC

Similar to mixtures of gold nanoparticles with calamitic liquid crystals, mixtures of gold nanoparticles with lyotropic liquid crystals show very promising properties [12]. Figure 8.10.1a shows an interesting fractal pattern of the gold nanorod which forms when the gold nanorods solution dries out. The ripple texture of DMPC in water [13] can be observed in Figure 8.10.1b. Because the gold nanorods are merged in the solution, they are difficult to identify in the image. Only a periodic ripple texture is obvious in this case.

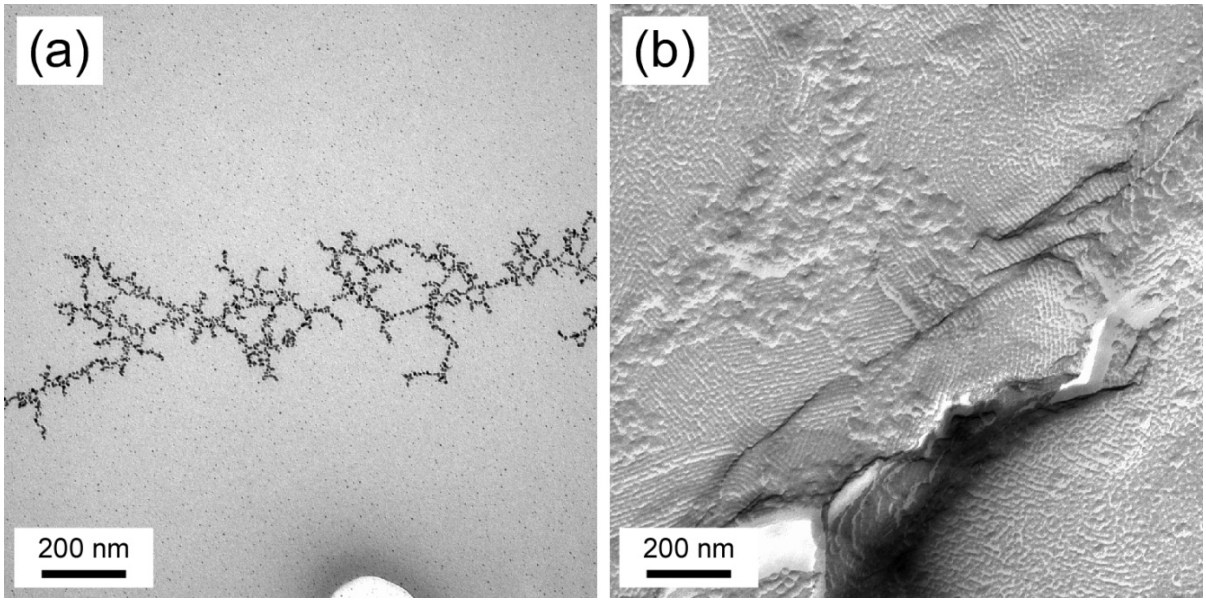

Figure 8.10.1: FFTEM images of the DMPC mixed with gold nanorods in water. (a) TEM image of gold nanorods. (b) FFTEM image of the DMPC mixed with gold nanorods in water, quenched at T=35°C and then fractured in the bulk, showing a ripple texture.

8.11 The crystal morphology of the complementary 12bp DNA

The appearance of liquid crystal phases of short complementary DNA due to end to end stacking has attracted a lot of interest, which may account for the origin of life [14]. In the work with Dr. Giuliano Zanchetta, we have observed some interesting phenomena in the 12 base pair (bp) self-complementary DNA system, which are not yet well understood. Solution of DNA is place on a clean glass substrate. Figures 8.11.1a and b show the free surface topography of the complementary 12bp DNA crystallizing at the glass substrate (When the DNA dries out, the surface is coated with platinum and then the replica is observed under TEM). It seems that the DNA self-assembles into nanofibers during crystallization. However, because we can't resolve individual molecules, the detailed molecular arrangement in those crystal fibers is still unknown.

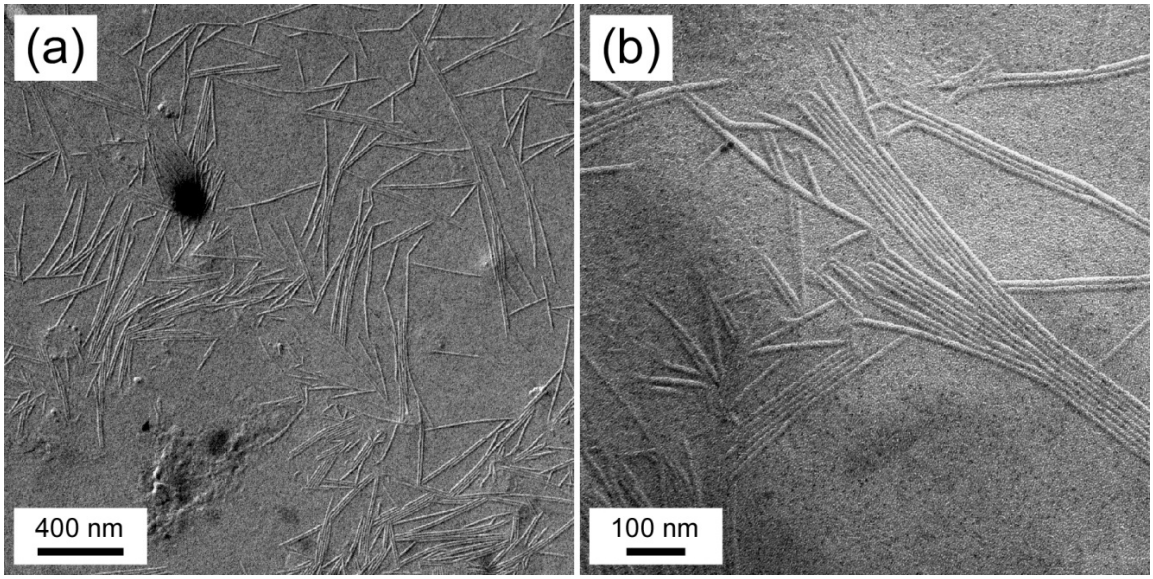

Figure 8.11.1 Free surface TEM images of self-complementary 12bp DNA dried on a glass substrate. (a) The crystal morphology of the complementary 12bp DNA dried on the clean glass substrate composed of bundles of nanofibers. (b) Higher magnification of (a).

8.12 Helical filaments observed in self-complementary 12bp DNA solution

When studying the liquid crystal phase, we observed helical filaments in the self-complementary 12bp DNA solution, as shown in Figures 8.12.1a-d. The width of the helical filaments is much larger than 3 nm (the width of a single duplex). Therefore, the helical filaments are an assembly of DNA duplexes. Still, the detailed molecular arrangement is unknown.

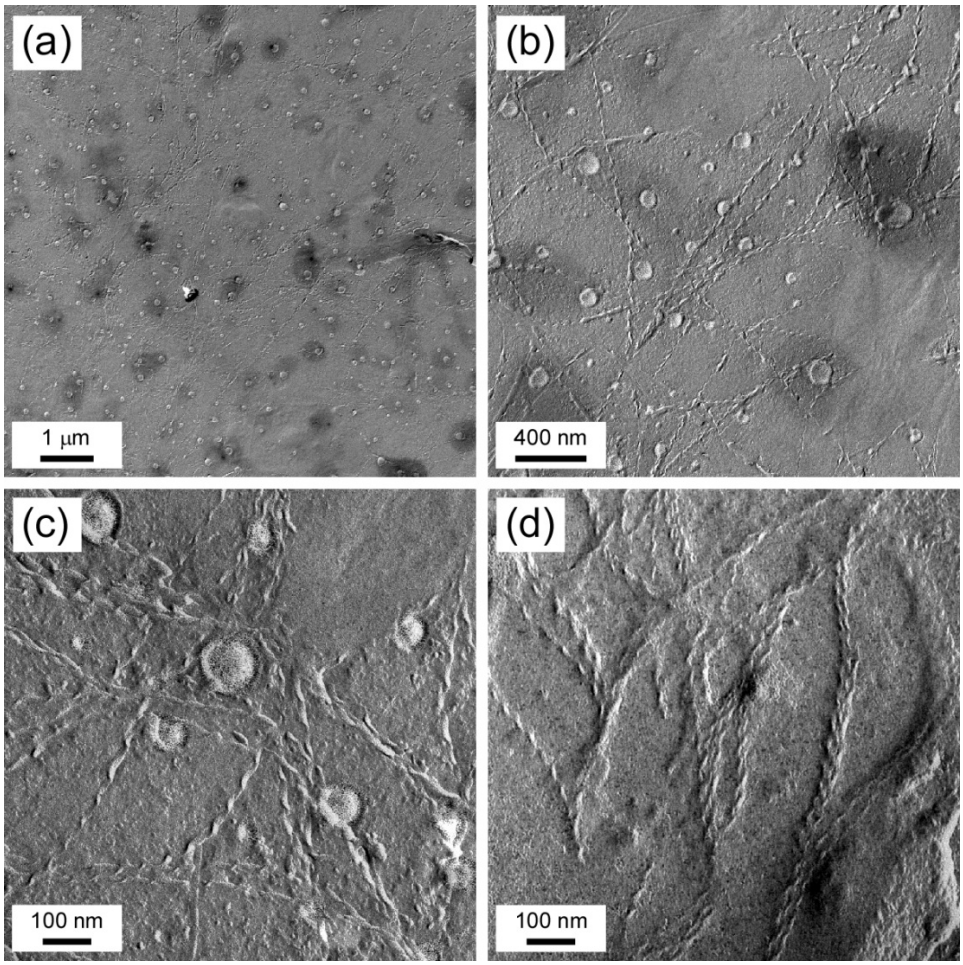

Figure 8.12.1: Helical filaments observed in the complementary 12bp DNA solution. (a), (b), (c) and (d) Series of FFTEM images with increasing magnification showing the helical filaments observed in the solution of the complementary 12bp DNA. The sample is quenched at room temperature.

8.13 FFTEM images of the cholesteric phase made from self-complementary 12bp DNA

The DNA solution is a typical lyotropic system, which shows isotropic, cholesteric and columnar phases, as the concentration of DNA increases. Because the DNA molecules are very small (width of a single DNA duplex ~3 nm) and the resolution of FFTEM is ~3 nm, individual molecule is hard to be distinguished in the FFTEM images. However, as shown in Figures 8.13.1a and b, the periodicity of the cholesteric phase can be observed, which identifies the liquid crystal phase.

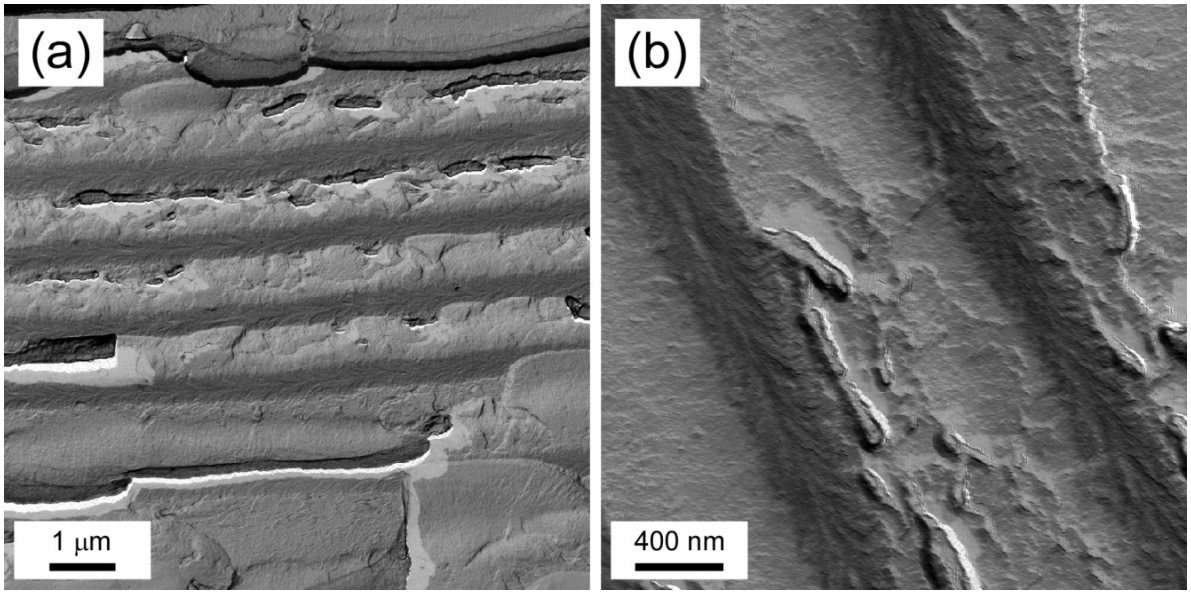

Figure 8.13.1: FFTEM images of the cholesteric phase of the complementary 12bp DNA solution. (a) FFTEM image of the cholesteric phase, showing the periodic topography. (b) Higher magnification of (a).

8.14 Liquid crystal phases of graphene oxide plates in water

Graphene is a material of broad interest. However, due to the difficulty of fabricating graphene in large amounts, graphene oxide plates have become another option [15]. Formation of the liquid crystal phase in a water solution of graphene oxide plates has attracted intense interest [16]. Figure 8.14.1a shows graphene oxide plates under TEM and Figure 8.14.1b shows the topography of the liquid crystal phase formed by graphene oxide plates in water, where graphene oxide plates tend to be parallel to each other. The beautiful story of "flexopolydispersity of nematic liquid crystals" will be presented by Yue Shi [17].

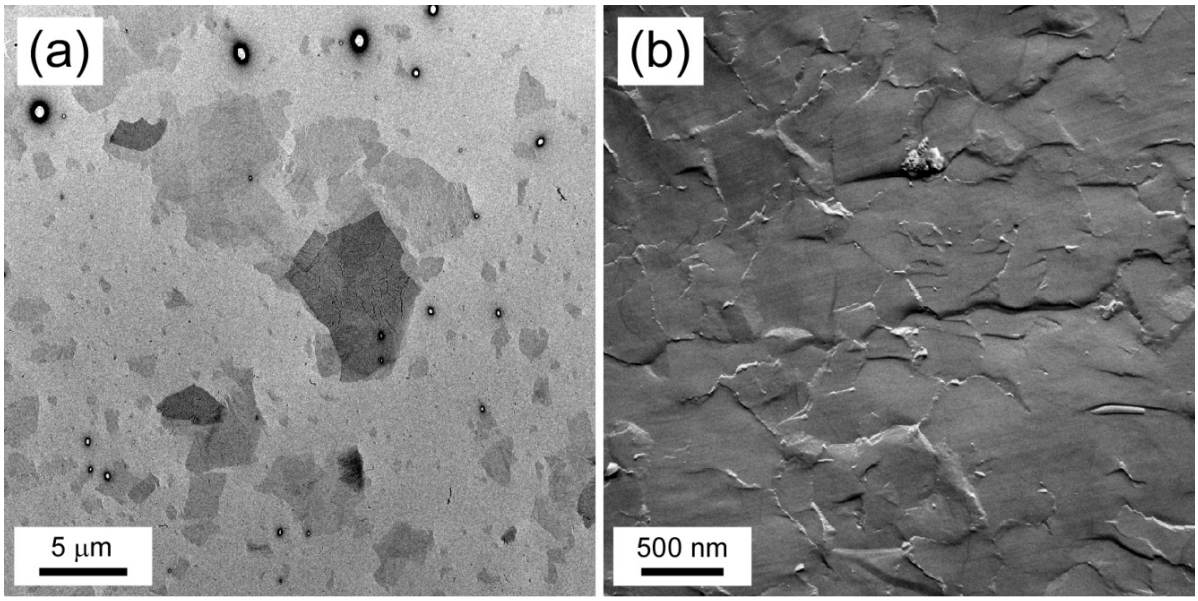

Figure 8.14.1: FFTEM images of graphene oxide plates in water. (a) TEM image of dry graphene oxide plates on a thin formvar. (b) FFTEM image of graphene oxide plates in water, quenched at room temperature and then fractured in the bulk, showing the arrangement of graphene oxide plates in the liquid crystal phase.

8.15 FFTEM images of the cybotactic nematic phase

The biaxial nematic phase has attracted a lot of attention recently [18]. Due to the observation of four diffuse peaks in 2D x-ray scattering at small angle from aligned samples, clusters of smectic C layers have been proposed in the biaxial nematic phase, which is also called the cybotactic nematic phase. In order to study those smectic C clusters in the cybotactic nematic phase, several materials provided by Prof. Tony Jakli have been investigated. Here are two examples. F493 shows very weak layering near the glass substrate, which may be the surface induced layer structure, as shown in Figure 8.15.1a. At the air/liquid crystal surface, no layer structure has been observed (Figure 8.15.1b). The bumps may associate with the local surface tension of the nematic phase. A131 is another example, which shows distinct layer structure, deep in the bulk, as shown in Figure 8.15.1c. This is supported by the surface structure, as shown in Figure 8.15.1d. However, these results are inconsistent with the XRD prediction that the smectic C cluster is about 30 nm in scale.

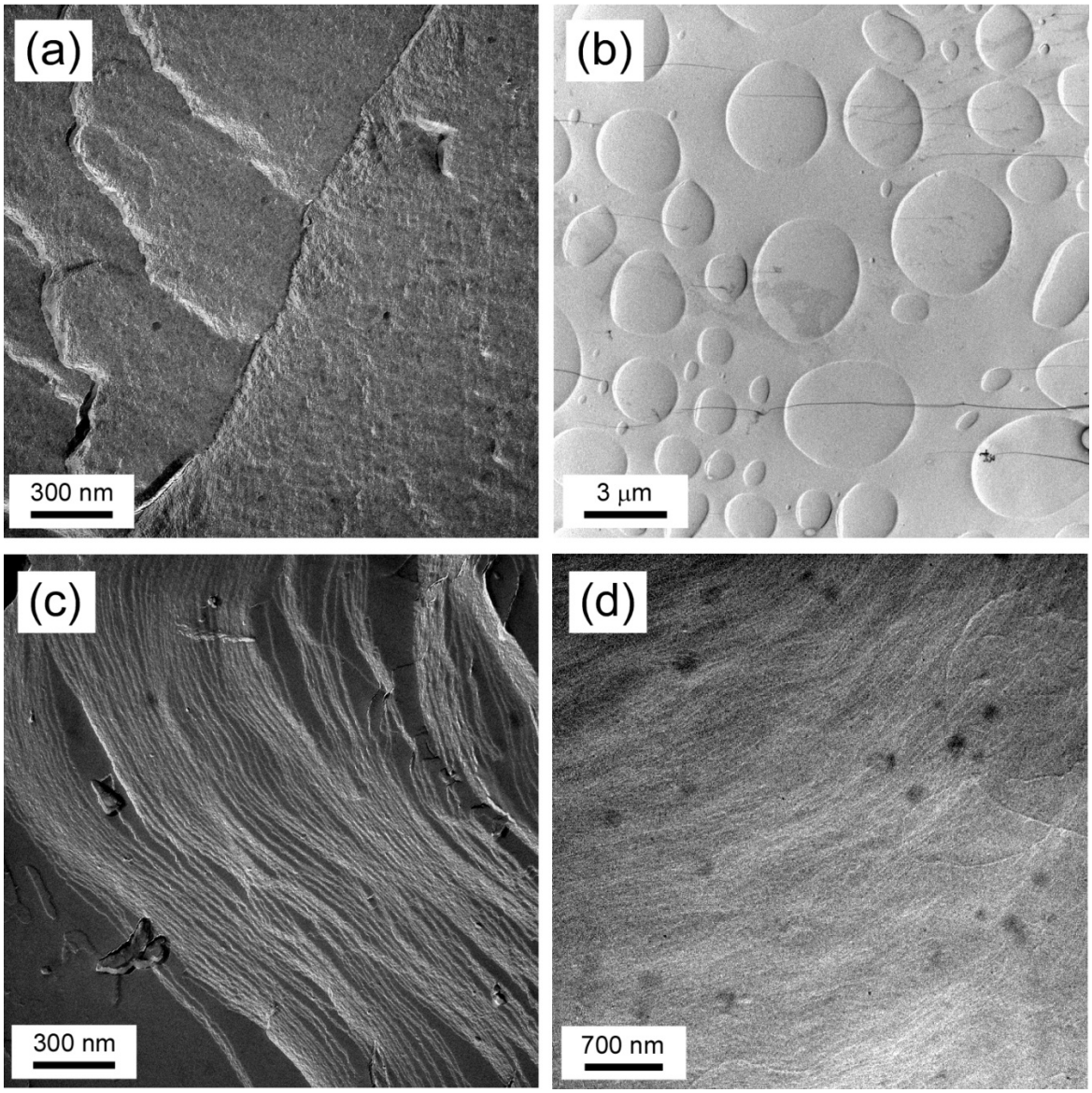

Figure 8.15.1: FFTEM images of the cybotactic nematic phases. (a) FFTEM image of F493, quenched at T=70°C and then fractured in the bulk. The weak layering may be the surface induced layer structure. (b) Free surface TEM image of F493, quenched at T=70°C. No layer can be observed, except large bumps. (c) FFTEM image of A131, quenched at T=70°C and then fractured in the bulk. Smectic layers are clearly observed, deep in the bulk. (d) Free surface TEM image of A131, quenched at T=130°C. Only weak layering is observed at the air/liquid crystal interface.

Bibliography

[1] D. K. Yoon, M. C. Choi, Y. H. Kim, M. W. Kim, O. D. Lavrentovich, and H. T. Jung: Internal structure visualization and lithographic use of periodic toric holes in liquid crystals. *Nature Mater*. 2007, **6**, 866-870.

[2] N. Chattham, C. Zhu, X. Cheng, J. Limtrakul, C. Tschierske, J. E. Maclennan, and N. A. Clark: Direct observation of two-dimensional nematic and smectic ordering in freely suspended films of a bolaamphiphilic liquid crystal. *Soft Matter* 2011, **7**, 9978-9982.

[3] S. Ostlund, and B. I. Halperin: Dislocation-mediated melting of anisotropic layers. *Phys. Rev. B* 1981, **23**, 335-358.

[4] S. Laschat, A. Baro, N. Steinke, F. Giesselmann, C. Hägele, G. Scalia, R. Judele, E. Kapatsina, S. Sauer, A. Schreivogel, and M. Tosoni: Discotic liquid crystals: From tailor-made synthesis to plastic electronics. *Angew. Chem. Int. Ed.* 2007, **46**, 4832-4887.

[5] J. H. Porada, and D. Blunk: Phasmidic indigoid liquid crystals. *J. Mater. Chem.* 2010, **20**, 2956-2958.

[6] R. Shao, L. Wang, C. D. Jones, D. A. Coleman, D. Nguyen, M. Nakata, J. E. Maclennan, P. Rudquist, D. M. Walba, and N. A. Clark: Observation of polarization current accompanying smetic A electroclinic reorientation. 2006 APS March Meeting Abstract, Baltimore, Maryland.

[7] R. A. Reddy, C. Zhu, R. Shao, E. Korblova, T. Gong, Y. Shen, E. Garcia, M. A. Glaser, J. E. Maclennan, D. M. Walba, and N. A. Clark: Spontaneous ferroelectric order in a bent-core smectic liquid crystal of fluid orthorhombic layers. *Science* 2011, **332**, 72-77.

[8] Chenhui Zhu: Novel Biaxial Smectic Phases. Thesis. 2009.

[9] Y. Shen, T. Gong, R. Shao, E. Korblova, J. E. Maclennan, D. M. Walba, and N. A. Clark: Effective conductivity due to continuous polarization reorientation in fluid ferroelectrics. *Rhys. Rev. E* 2011, **84**, 020701/1-4.

[10] D. F. Gardner, J. S. Evans, and I. I. Smalyukh: Towards reconfigurable optical metamaterials: Colloidal nanoparticle self-assembly and self-alignment in liquid crystals. *Mol. Cryst. Liq. Cryst.* 2011, **545**, 1227-1245.

[11] R. Pratibha, K. Park, I. I. Smalyukh, and W. Park: Tunable optical metamaterial based on liquid crystal-gold nanosphere composite. *Optical Express* 2009, **17**, 19459-19469.

[12] Q. Liu, Y. Cui, D. Gardner, X. Li, S. He, and I. I. Smalyukh: Self-alignment of plasmonic gold nanorods in reconfigurable anisotropic fluids for tunable bulk metamaterial applications. *Nano Lett.* 2010, **10**, 1347-1353.

[13] D. Needham, and E. Evans: Structure and mechanical properties of giant lipid (DMPC) vesicle bilayers from 20°C below to 10°c above the liquid crystal-crystalline phase transition at 24°C. *Biochemistry* 1988, **27**, 8261-8269.

[14] M. Nakata, G. Zanchetta, B. D. Chapman, C. D. Jones, J. O. Cross, R. Pindak, T. Bellini, and N. A. Clark: End-to-end stacking and liquid crystal condensation of 6-to-20-base pair DNA duplexes. *Science*, **318**, 1276-1279.

[15] D. R. Dreyer, S. Park, C. W. Bielawski, and R. S. Ruoff: The chemistry of graphene oxide. *Chem. Soc. Rev.* 2010, **39**, 228-240.

[16] J. E. Kim, T. H. Han, S. H. Lee, J. Y. Kim, C. W. Ahn, J. M. Yun, and S. O. Kim: Graphene Oxide Liquid Crystals. *Angew. Chem. Int. Ed.* 2011, **50**, 3043-3047.

[17] Y. Shi, D. Chen, R. Mahmood, N. Clark: Flexopolydispersity of nematic liquid crystals. 2012 APS March Meeting Abstract, Boston, Massachusetts.

[18] O. Francescangeli, F. Vita, F. Fauth, and E. T. Samulski: Extraordinary magnetic field effect in bent-core liquid crystals. *Phys. Rev. Lett.* 2011, **107**, 207801/1-5.